Electronic structure and vibrational properties of pristine and isotope engineered carbon nanostructures

Habilitationsschrift

**eingereicht zur Erlangung der *venia docendi* für Materialphysik an der
Fakultät für Physik der Universität Wien**

Ferenc Simon

Wien, Juli 2006

Contents

1

Introduction and experimental background

ABSTRACT
It is the purpose of this chapter to introduce the theoretical and experimental background of the experiments performed. We present an overview of the state-of-the-art of the carbon nanotube research and the open questions. We outline the sample preparation and spectroscopic techniques employed. This includes the synthesis of isotope engineered heteronuclear nanostructures and how information from Raman spectroscopy, nuclear magnetic resonance and theory can be combined to yield unprecedented insight into the electronic structure of carbon nanotubes.

1.1 Introduction

The era of nanotechnology received an enormous boost with the discovery of carbon nanotubes (CNTs) by Sumio Iijima in 1991 [1]. Before 1991 nano- and nanotechnology usually meant small clusters of atoms or molecules. The originally discovered CNTs contain several coaxial carbon shells and is called multi-wall CNTs (MWCNTs). Soon thereafter single-wall CNTs (SWCNTs), i.e. a carbon nanotube containing a single carbon shell were discovered [2, 3]. The principal interest in CNTs comes from the fact that they contain carbon only and all carbon are locally sp^2 bound, like in graphite, which provides unique mechanical and transport properties. This, combined with their huge, > 1000, aspect ratio (the diameters being 1-20 nm and their lengths over a few micron or even exceeding cms) gives them an enormous application potential. The not exhaustive list of applications includes field-emission displays (epxloiting their sharp tips) [4], cathode emitters for small sized x-ray tubes for medical applications [5], reinforcing elements for CNT-metal composites, tips for scanning probe microscopy [6], high current transmitting wires, cables for a future space elevator, elements of nano-transistors [7], and elements for quantum information processing [8].

Several fundamental questions need to be answered though before all the benefits of these novel nanostructures could be fully exploited. Recent theoretical and experimental efforts focused on the understanding of the electronic properties of carbon nanotubes. It has been long speculated that the one-dimensional structure of NTs renders their electronic properties inherently one-dimensional. This was suggested to result in a range of exotic correlated phenomenon such as the Tomonaga-Luttinger (TLL) state [9], the Peierls transition [10, 11], ballistic transport [12], and excitonic effects [13]. The presence of the TLL state is now firmly established [14–16], their is evidence for the ballistic transport properties [12] and there is growing experimental evidence for the presence of excitionic effects related to the one-dimensional structure of nanotubes [17]. The Peierls transition, however remains still to be seen.

An appealing tool to study the properties of materials is isotope engineering (IE). The change in phonon energies upon isotope substitution, while leaving the electronic properties unaffected, has been used to identify vibrational modes [18–20] and gave insight into underlying fundamental mechanisms, such as phonon-mediated superconductivity [21]. Applications of IE involve for instance the controlled doping of isotope engineered ready-prepared Si heterostructures by means of neutron irradiation [22], fabrication of mononuclear devices with controlled heat conducting properties [23], and the basic architecture for spintronics and quantum computing [24]. For carbon nanotubes, IE has been used[1] to clarify the role of phonons in the excitonic effects of SWCNTs [25]. Here, we use IE to study the vibrational and electronic properties of unique heteronuclear nanosctructures.

Another important aspect of the study of carbon nanostructures is the employed experimental methods. The most commonly used methods are advanced electron (such as electron energy loss spectroscopy [26] and photoemission spectroscopic [16]) and optical spectroscopic methods (Raman spectroscopy [27] or fluorescence spectroscopy [28]) and transport methods (contacted probe experiments [14] or scanning probe spectroscopy [29]). Another important family of spectroscopic methods is magnetic resonance (MR). Magnetic resonance can yield information on a variety of phenomena such as the density of states at the Fermi level, spin-lattice relaxation mechanisms, magnetic properties of materials and many more. Prior to the studies described herein there existed relatively few efforts focused on the use of MR for the studies of SWCNTs. To probe the SWCNT electronic properties with magnetic resonance, we encapsulated spin-probes inside SWCNTs and prepared ^{13}C isotope engineered nanostructures.

Here, the results related to the two major objectives are described: i.) to provide a better understanding of the SWCNT electronic properties by studying a model system, double-wall carbon nanotubes (DWCNTs) ii.) performing magnetic resonance experiments on novel nanostructures.

---

[1] Work done parallel to our studies

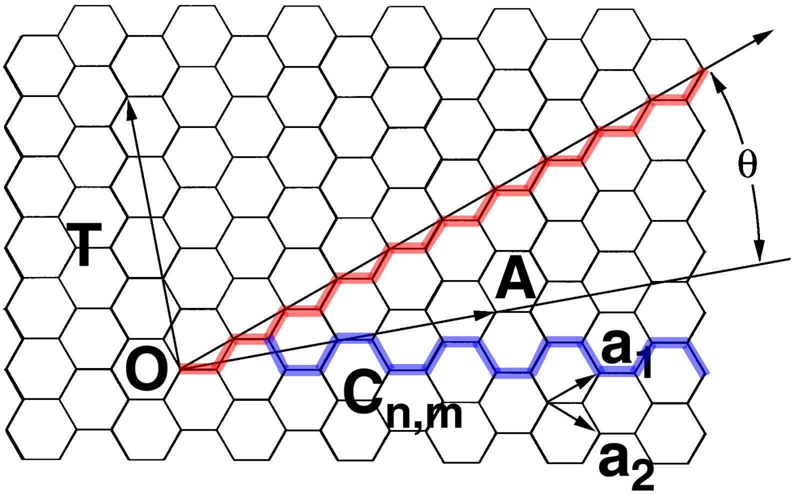

FIGURE 1.1. Geometry of a graphene sheet. a_1 and a_2 are the primitive lattice vectors. The Hamada vectors for an armchair (lower solid curve) and a zig-zag (upper solid curve) are indicated.

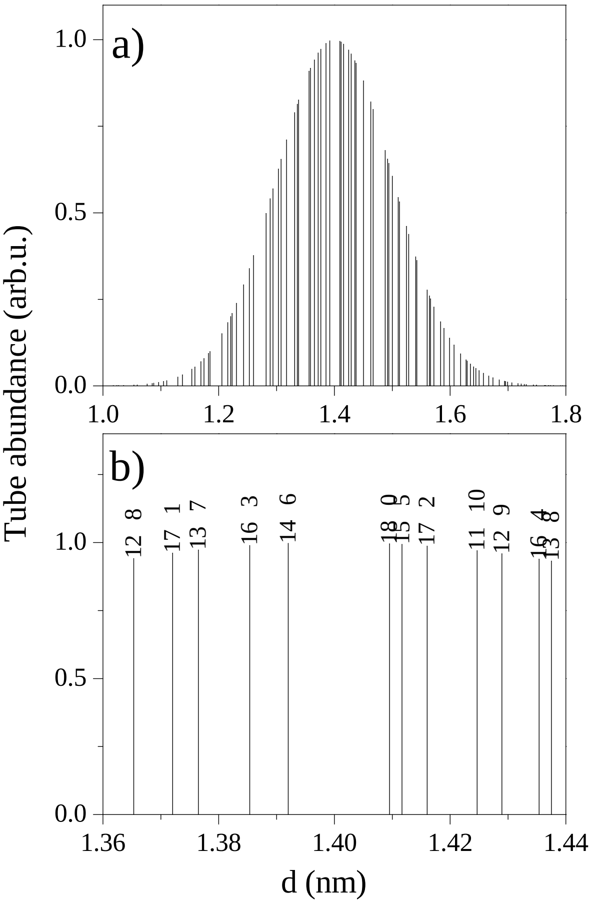

FIGURE 1.2. a) Tube diameter and b) chirality distribution in a real sample used in this study with parameters given in the text. Note the different diameter scale for the two graphs.

This introductory chapter is organized as follows. An overview on the vibrational and electronic properties of SWCNTs is given followed by a description of modified carbon nanostructures with a particular focus on double-wall carbon nanotubes (DWCNTs). The employed experimental methods are discussed and the results, which are detailed in the subsequent chapters, are summarized.

Recently, single-wall carbon nanotubes (SWCNTs) have been intensively studied as a result of the envisaged broad range of applicability and the unique physical properties related to their quasi one-dimensional electronic structure. Examples include the presence of Van Hove singularities in

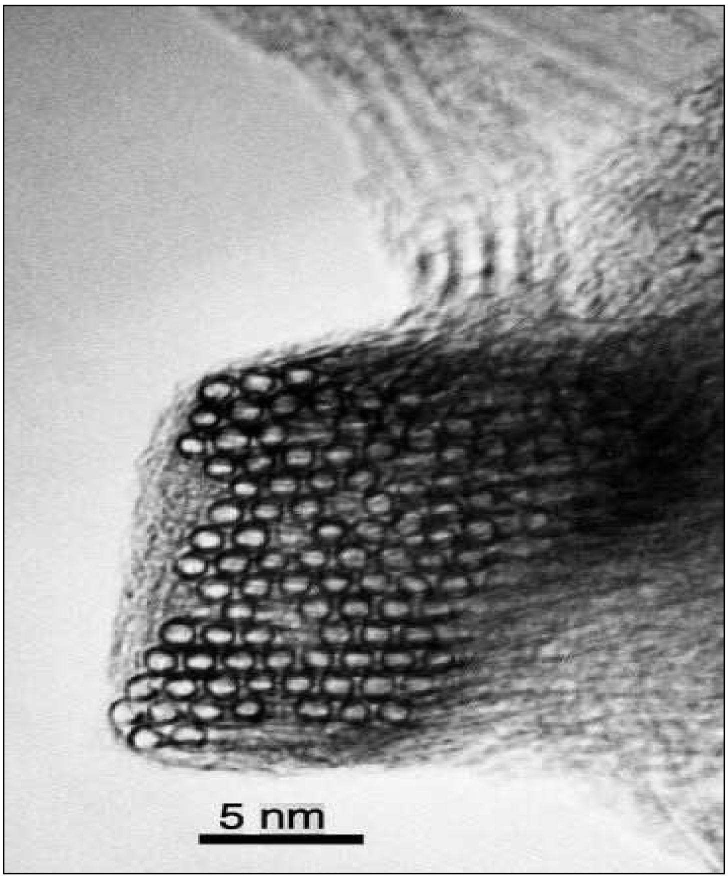

FIGURE 1.3. HR-TEM micrograph showing the SWCNTs in a bundle after Ref. [36]

the electronic density of states [30], and the Tomonaga-Luttinger liquid behavior [15]. IE of carbon nanotubes using isotope enriched graphite as the starting material was attempted in order to allow NMR spectroscopy [31, 32]. However, the NMR studies have been hampered by the fact that the ^{13}C NMR active nuclei can be found in all species of carbons, e.g. amorphous or graphitic carbon, inevitably present even in the purified SWCNT materials, and no nanotube selective enrichment or purification could be achieved until now. Vibrational spectroscopic methods are appropriate choices to study the effect of IE. For SWCNTs, Raman spectroscopy has proven to be most convenient to characterize their electronic and structural properties. In addition, Raman studies on double-wall carbon nanotubes (DWCNTs) [33], synthesized from fullerenes encapsulated inside the tubes (fullerene peapods) [34], provide a unique opportunity to study the small diameter inner tubes, while the outer ones are left intact during the synthesis.

1.1.1 *Geometry of single-wall carbon nanotubes*

SWCNTs are needle like graphitic tubules that can be visioned as a cut from a single graphite layer, a graphene sheet, rolled up along the cutting directions. The geometry of a graphene sheet is shown in Fig. 1.1. The (n,m) indeces of the rolling, Hamada, or chiral vector [35] denote the vector components in the coordinate system of the graphene basis vectors. The special (n,m)'s have distinguisehed names: when m=0 is called a zig-zag and when n=m is an armchair SWCNT, other tubes with arbitrary (n,m) are the chiral tubes as they have no plane of reflection. The (n,m) index is often referred to as chirality.

The growth of SWCNTs is a random process therefore the SWCNT diameters follow a Gaussian distribution. To date no efforts have been successful to yield a selected chirality instead of the tremendous efforts invested. In Fig. 1.2 the distribution of different chiralities is shown for a sample used in the current study with d=1.4 nm and σ= 0.1 nm for the mean diameter and the variance of the tube diameter distribution, respectively. As shown below, tubes with similar diameters have very different electronic properties, which severely limits the applicability of a

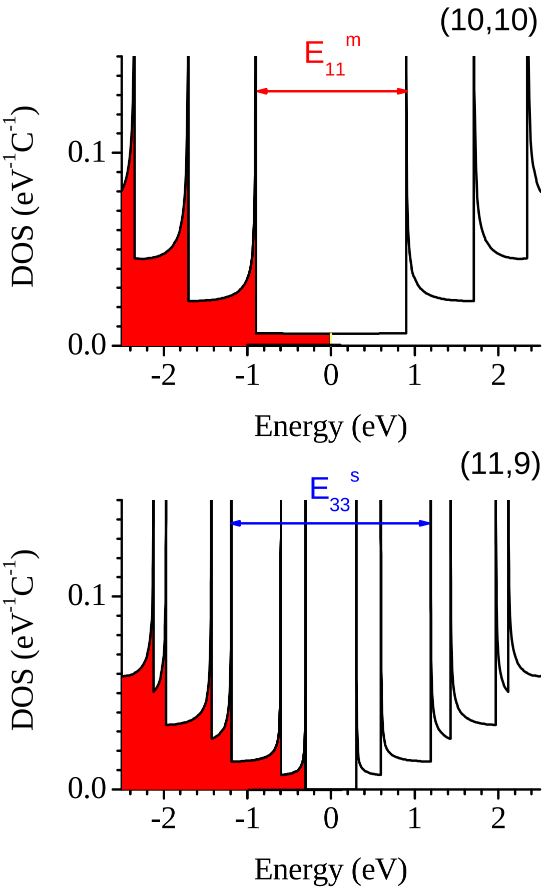

FIGURE 1.4. Density of states near the Fermi level for a (10,10) metallic and 11,9) semiconducting SWCNTs. Filled and open areas show the occupied and unoccupied states, respectively. The first, E_{11}^{m}, and the third E_{33}^{s} optical transitions are shown for the two kinds of tubes.

macroscopic amounts of SWCNTs where the ensemble of SWCNTs are present.

Attractive van der Waals force between SWCNTs makes them form bundles rather than isolated tubes. A typical high-resolution transmission electron micrograph is shown in Fig. 1.3 from Ref. [36].

1.1.2 Electronic properties of single-wall carbon nanotubes

The one-dimensional geometry of SWCNTs is reflected in their electronic structure: quasicontinuous electron states are found in k-space along the reciprocal vectors related to the tube axis, and discretized states for the other two directions which are related to the directions perpendicular to the tube axis. The band structure of SWCNTs can be derived from that of graphene. Graphene is a semi-metal with a zero energy-gap with touching bands at the K points. In the simplest nearest-neighbor tight-binding [35] approximation the electronic structure of the SWCNTs depends on simple geometry related rules: the resulting tube is semiconducting with gaps of a few eV when n-m mod 3=1,2 or metallic when n-m mod 3=0.

More recently, it has become known that the real band structure shows deviation from these rules [37]. The deviations include the so-called curvature induced gap for non-armchair metallic tubes with $d \lesssim 0.7$ nm and the re-entrant metallicity of very small tubes with $d \lesssim 0.5$ nm, which would be semiconducting according to the simple TB calculations [37]. These calculations all predict the existence of gaps above 100 meV. In addition, strong correlation effects, i.e. theories beyond one-electron models predict the existence of additional phenomena such as the Peierls effect resulting in a few 10 meV charge or spin-gaps [10, 11] for metallic carbon nanotubes.

As discussed in Chapter 12 our experiments provide the first experimental observations of a low energy ($\sim$ 3 meV) gap in small diameter carbon nanotubes ($d \sim 0.7$ nm), which may be interpreted as due to a Peierls transition [39]. Transport and recent photoemission experiments

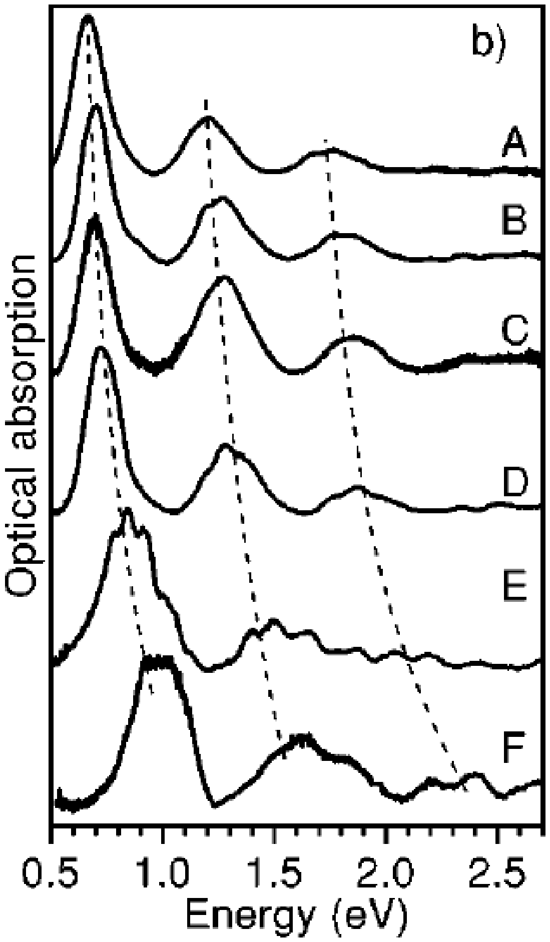

FIGURE 1.5. Optical absorption spectrum from Ref. [38] for different nanotube samples. The mean tube diameters increase from bottom to top.

have proven that the ground state of ∼ 1.4 nm tubes is a Tomonaga-Luttinger liquid (TLL) state [15, 16]. Clearly, it is a challange to both theory and experiments to reconcile the mutually exclusive Peierls and TLL ground states, which has initiated ongoing work.

The one-dimensionality of the SWCNT band structure renders van Hove singularities in their density of states (DOS). In Fig. 1.4 we show the DOS near the Fermi level for the (10,10) metallic armchair and the (11,9) semiconducting chiral tubes. The optically allowed transitions between occupied and unoccupied bands is also shown. In the simplest tight-binding approximation, the optical transition energies turn out to be inversely proportional to the tube diameter, d.

The presence of the van Hove singularities is one of the clearest experimental evidence proving the one-dimensional character of the electronic properties of tubes it was therefore studied in detail with several experimental methods. Optical absorption was first presented in the now classical work of Kataura *et al.* [40] and in Fig. 1.5 we show the optical absorption results from Ref. [38]. In the optical absorption spectrum absorption peaks broadened to up to 0.5 eV are observed rather than sharp van Hove singularities due to the presence of a large number of different chiralities, thus different optical transitions, present in a nanotube sample, which smears out any fine structures. The presence of DOS was also proven by scanning tunneling spectroscopy [29] and band-gap fluorescence [28, 41].

More recently, it has become evident that the single particle picture, i.e. neglecting the interaction between the optically excited electron-hole pair does not describe properly the optical properties of SWCNTs. It is now established theoretically [13, 42–44] and there is emerging experimental evidence [17, 25, 45, 46] that excitonic effects, i.e. the correlation of photoexcited electrons and holes, play an important role in the optical absorption and emission properties of single-wall carbon nanotubes (SWCNTs). However, it turned out that exciton binding ener-

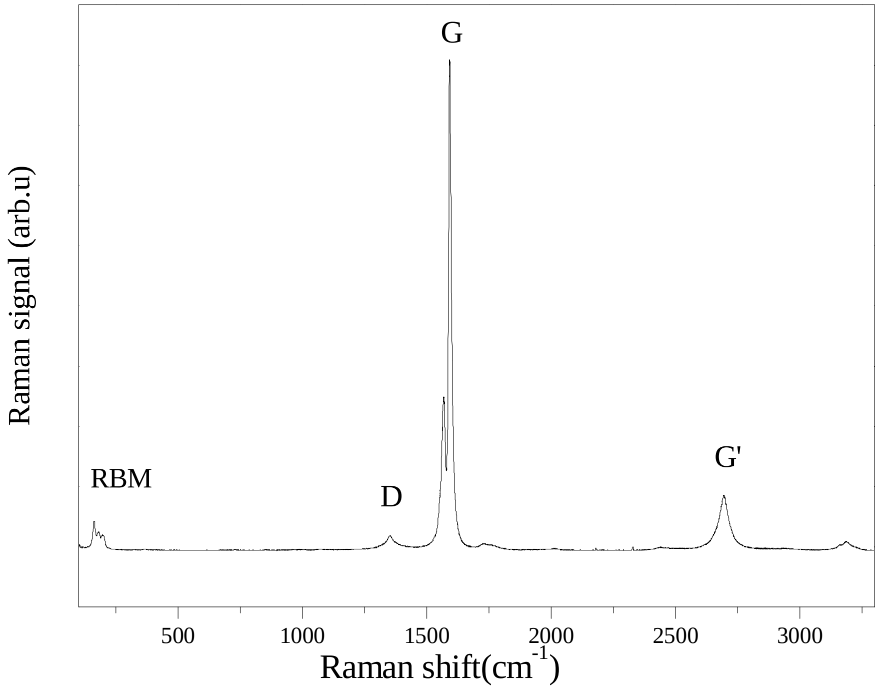

FIGURE 1.6. Raman spectrum of SWCNTs with the most significant Raman modes labeled when excited with a 488 nm laser.

gies and electron-electron interaction energies almost cancel [42], therefore it appears that the non-interacting optically excited state description works still acceptably at least phenomenologically. This justifies the use of the band structure shown in Fig. 1.4 to explain for e.g the optical absorption or Raman experiments.

1.1.3 Vibrational properties of SWCNTs and Raman spectroscopy

A great deal of information can be learned about SWCNTs using vibrational spectroscopy. SWCNTs have mainly Raman active modes, however recently the infrared active modes have also been detected [47]. In Fig. 1.6 the Raman spectrum of an SWCNT with the most significant modes is shown. The four major Raman modes, the radial breathing mode, RBM, the defect induced, D, mode, the graphite related tangential, G, mode and the overtone of the D mode, the D* or G' mode dominate the Raman spectrum [30]. The RBM mode is unique for SWCNTs and has an important practical use as its energy ν is inversely proportional to the tube diameter, d. This can be used to characterize the tube diameters in an SWCNT sample. The D mode also exists in graphite and is related to the back-scattering of an optically excited quasiparticle on defects [48–50].

The G mode is present in all graphitic like carbonaceous materials and is usually the strongest among all Raman active modes. The G' mode corresponds is the two phonon overtone of the D mode, i.e. no back-scattering on a defect is not required for this process to conserve momentum. This mode is studied and discussed in detail in Chapter 10.

Apart from the pure vibrational energies, Raman spectroscopy can be used to determined the electronic properties. The so-called resonance Raman scattering (RRS) allows to determine the optical transition energies from the Raman measurements. The RRS effect originates in the fact that the probability of the Raman process is increased by orders of magnitudes when either the incoming or the inelastically scattered outgoing photon [51] matches the energy of an optical transition. The guide to analyze Raman results and in particular data on the RBMs is the Kataura plot [40] that is shown in Fig. 1.7 calculated in the framework of a simple tight-binding. The Kataura plot describes the optical transition energies as a function of the tube diameter (or

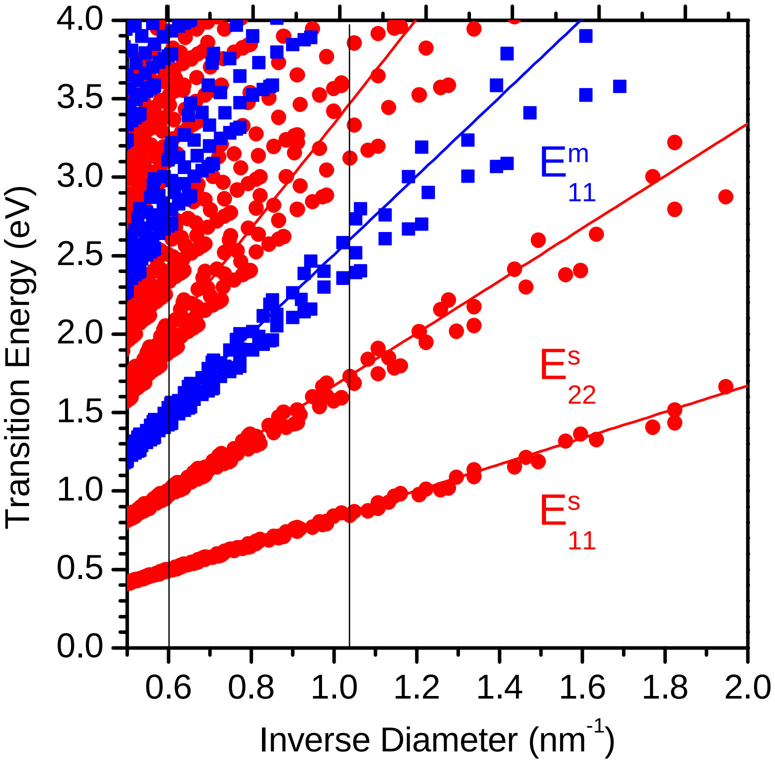

FIGURE 1.7. Kataura plot, i.e. optical transition energies as a function of the inverse tube diameter calculated with a nearest neighbor tight-binding. Squares and circles correspond to the optical absorptions of metallic and semiconducting tubes, respectively.

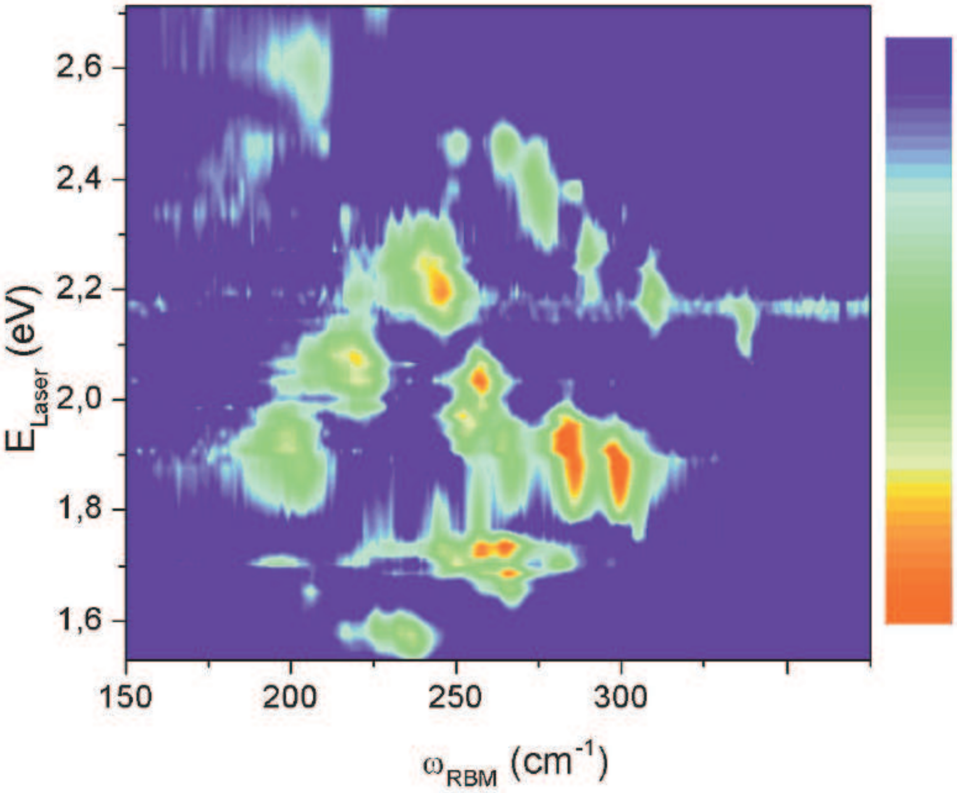

FIGURE 1.8. Raman map of SWCNT from Ref. [53]. Horizontal scale is the RBM frequencies.

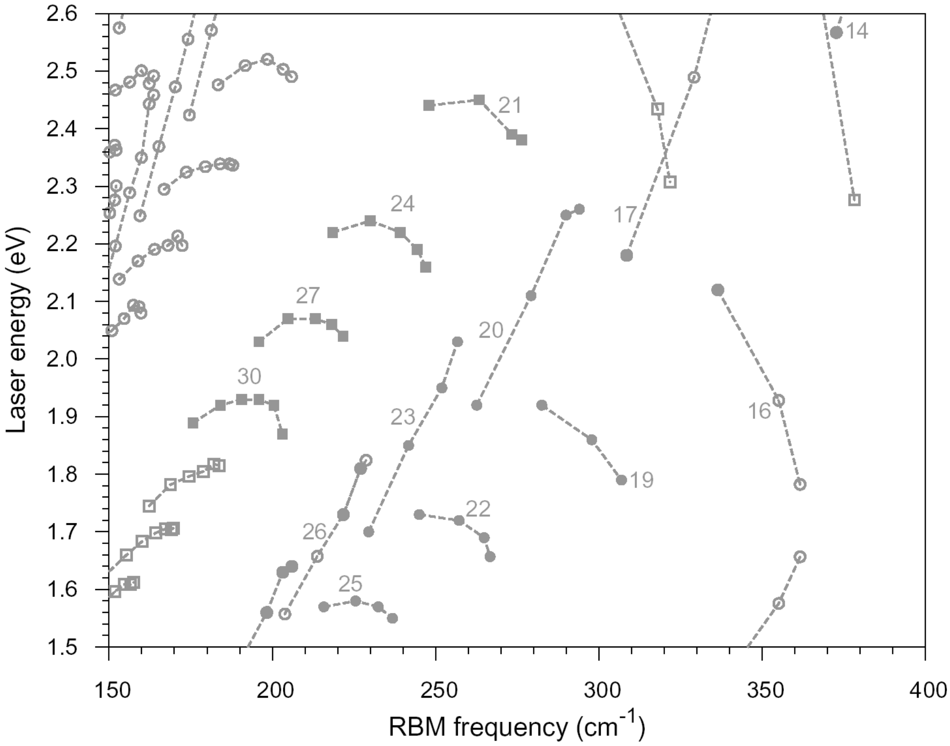

FIGURE 1.9. Assignment of the Raman map features to SWCNT chiralities. Solid curves join the chirality famililies with $2 \cdot n + m = const$ [56].

inverse tube diameter). The straight lines would correspond to a perfect $E_{ii} \propto 1/d$ rule, where E_{ii} is the optical transition energy for the ith transition. The deviation seen in Fig. 1.7 is known as the trigonal warping effect and is caused by the three-fold symmetry of the band structure around the Γ point [52].

More recent calculations have shown important corrections to the simple tight-binding calculations as it is discussed above. The Kataura plot immediately shows that for an SWCNT sample where a number of different diameters are present (see Fig. 1.2) those tube dominate the Raman spectrum whose optical transition is near the exciting laser energy (would be a horizontal line in Fig. 1.7). This strong photoselectvitiy can be exploited to selectively study a particular type of SWCNTs, e.g. nominally semiconducting tubes with a 1.6 eV excitation and nominally metallic tubes when excited with a 2.4 eV laser for an SWCNT sample with 1.0 nm mean diameter.

The one-to-one correspondence between the tube diameters and the RBM frequency allows to experimentally determine the so-called SWCNT Raman map where the optical transition energies are determined from the strength of the Raman signal as a function of the RBM Raman shift. Such a Raman map was determined for SWCNTs in Refs. [53, 54] and a result is shown in Fig. 1.8 as a 3D color plot after Ref. [53].

The detailed studies of the Raman map allows a comparison with theory and thus the assignment of the observed vibrational modes to tube chiralities. This has a great practical importance as it allows the use of Raman spectroscopy to characterize in detail the chirality distribution in a sample. In Fig. 1.9 we show the assignment of the chiralities to the Raman map features based on improved theoretical models by Popov [55].

1.1.4 Modifications of single-wall carbon nanotubes

An appealing tool to study the SWCNT properties originates from the discovery of fullerenes encapsulated inside SWCNTs by Smith, Monthioux, and Luzzi [34]. This peapod structure is particularly interesting as it combines two fundamental forms of carbon: fullerenes and carbon nanotubes. A high-resolution transmission electron microscopy (HR-TEM) image of a peapod is

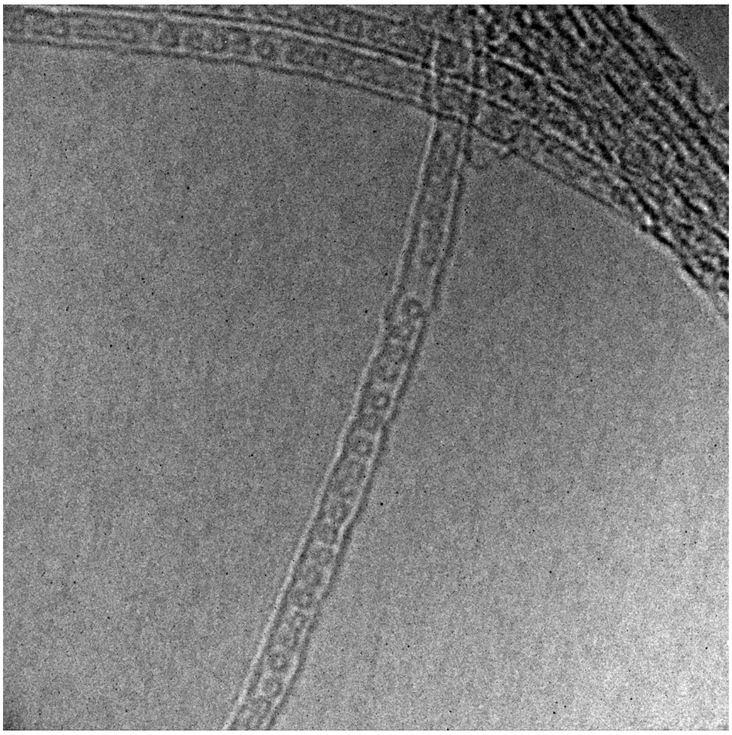

FIGURE 1.10. HR-TEM image of C_{60}@SWCNT peapods.

shown in Fig. 1.10. It was also shown that macroscopic filling with the fullerenes can be achieved [57, 58]. This opens the way to encapsulate magnetic fullerenes which enables to study the tube electronic properties using electron spin resonance as it is discussed here. Another interesting follow-up of the peapod structure discovery is that the encapsulated fullerenes can be fused into a smaller diameter inner tube [33, 59] thus producing a double-wall carbon nanotube (DWCNT). DWCNTs were first observed to form under intensive electron radiation [58] in a high resolution transmission electron microscope from C_{60} peapods.

Following the synthesis of C_{60} peapods in macroscopic amounts [57], bulk quantities of the DWCNT material are available using a high temperature annealing method [33]. Alternatively, DWCNTs can be produced with usual synthesis methods such as arc-discharge [60] or CVD [61] under special conditions. According to the number of shells, DWCNTs are between SWCNTs and MWCNTs. Thus, one expects that DWCNTs may provide a material where improved mechanical stability as compared to SWCNTs coexists with the rich variety of electronic properties of SWCNTs. There are, of course, a number of yet unanswered questions e.g. if the outer tube properties are unaffected by the presence of the inner tube or if the commensurability of the tube structures plays a role. These questions should be answered before the successful application of these materials.

The inner tubes grown inside SWCNTs from peapods turned out to be a particularly interesting system as they are remarkably defect free which results in very long phonon life-times, i.e. very narrow vibrational modes [62]. In addition, their smaller diameters results in a larger energy spread, i.e. larger spectral splitting, for diameter dependent phonon modes such as e.g. the radial breathing mode (RBM). These two effects make the inner tubes very suitable to study diameter dependent physics of the small diameter tubes with precision. Here, we show how to employ the inner tubes as *probes* of the outer tube properties. The additional benefit of the inner tube growth from fullerenes is that the starting carbon source can be tailored at wish, e.g. when ^{13}C isotope enriched fullerenes are encapsulated inside the SWCNT host tubes, ^{13}C isotope enriched inner tubes are grown. In Fig. 1.11 we show the schematics of such a DWCNT.

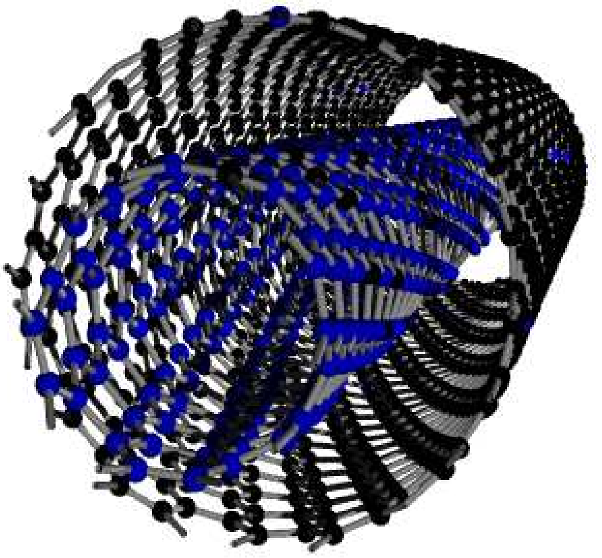

FIGURE 1.11. Schematic structure of an isotope engineered DWCNT with (14,6) outer and (6,4) inner tubes. ^{12}C and ^{13}C are shown in black and blue, respectively. The inner tube is 89 % ^{13}C enriched and the outer contains natural carbon (1.1 % ^{13}C abundance), which are randomly distributed for both shells.

1.1.5 Magnetic resonance in single-wall carbon nanotubes

Magnetic resonance is usually an excellent technique for probing the electronic properties at the Fermi level of metallic systems. In particular, nuclear magnetic resonance (NMR) has been extensively performed for such studies. The examples include conducting polymers, fullerenes, and high temperature superconductors. However the 1.1% natural abundance of ^{13}C with nuclear spin I=1/2 limits the sensitivity of such experiments. As a result, meaningful NMR experiments has to be performed on ^{13}C isotope enriched samples. NMR studies have been reported on carbon nanotubes prepared by using isotope enriched graphite as the starting material [31, 32]. However, these NMR studies have been hampered by the fact that the ^{13}C NMR active nuclei can be found in all species of carbons, e.g. amorphous or graphitic carbon, inevitably present even in the purified SWCNT materials, and no nanotube selective enrichment or purification could be achieved until now. Here, we discuss a different approach where only the inner nanotubes are enriched while other carbon phases including the outer tubes contain natural carbon only.

Observation of the intrinsic ESR signal of pristine SWCNTs remains elusive [63, 64]. Now, it is generally accepted that intrinsic ESR of the tubes can not be observed as conduction electrons on metallic tubes are relaxed by defects too fast to be observable. In addition, one always observes a number of ESR active species in a sample, such as graphitic carbon or magnetic catalyst particles, which prevent a meaningful analysis of the signal. In contrast, local probe studies could still allow an ESR study of tubes, provided the local spin probe can be selectively attached to the tubes. This goal can be achieved by using magnetic fullerenes, such as e.g. N@C_{60} or C_{59}N, since fullerenes are known to be selectively encapsulated inside SWCNTs [34] and can be washed from the outside using organic solvents [57]. This approach is discussed in detailed in this work.

1.2 Open questions prior to the discussed studies

Prior to the studies described herein a number of questions related to the synthesis of encapsulated nanostructures inside SWCNTs, the growth mechanism of inner tubes from encapsulated carbon, the electronic and vibrational properties of inner tubes, and the low energy excitations of SWCNT were yet unexplored fields.

In particular, it was not known whether temperature sensitive fullerenes, such as e.g. N@C_{60}, could be encapsulated inside SWCNTs to enable local probe ESR studies of the tubes. The growth mechanism of inner tubes from different carbon sources was not clarified, it was e.g. thought that the spherical geometry of fullerenes plays an important role. It was also unclear whether any carbon exchange might occur between the inner shell and that of the host outer tube. The behavior of openings on the SWCNTs under chemical treatments was not characterized in detail. It was also unclear whether the high perfectness of inner tubes is restricted to such tubes grown from fullerene templates or it is a general property of all tubes inside an outer one. The vibrational and electronic properties had not been studied in detail prior to the currently described works. In particular, the role of the outer tube on the vibrational and optical transition energies was not understood.

No conclusive and detailed NMR work had been presented on SWCNTs with a high nanotube specificity. The density of states near the Fermi level had not been studied in detail as a function of temperature using magnetic resonance.

1.3 Experimental methods

1.3.1 Sample preparation

The sample preparations are detailed at each chapter and is only briefly covered here. We obtained carbon nanotube samples from several commercial suppliers prepared with different methods. SWCNT sample prepared with the arc-discharge method from from Nanocarblab, Moscow, Russia, laser ablation prepared tubes from Tubes@ Rice, Rice University, Houston, Texas and nanotubes prepared with the chemical vapor deposition method (CCVD) from Nanocyl, Belgium. Fullerenes containing natural carbon were acquired from Hoechst AG, Frankfurt, Germany and ^{13}C isotope enriched fullerenes were obtained from Mercorp Inc., Tucson, USA. The tube diameter distribution was determined from multi-frequency Raman measurements [27] which gave the the mean diameter and the variance of the Gaussian tube diameter distribution.

Encapsulation of fullerenes at low temperatures inside SWCNTs was performed by sonicating the fullerene and SWCNT suspensions together in organic solvents. For fullerene encapsulation at high temperatures (the vapor method), the SWCNTs and the fullerenes were sealed under vacuum in a quartz ampoule and annealed at 650 °C for 2 hours [57]. Fullerenes enter the inside of the SWCNTs at this temperature due to their high vapor pressure that is maintained in the sealed environment. Non-encapsulated fullerenes were removed by dynamic vacuum annealing at the same temperature for 1 hour. The filling of SWCNTs with the fullerenes was characterized by observing the peapod structure in high-resolution transmission electron microscopy (HR-TEM), by X-ray studies of the one-dimensional array of fullerenes inside the SWCNTs and by the detection of the fullerene modes from the cages encapsulated inside the SWCNTs using Raman spectroscopy [57, 65]. The peapods were transformed to DWCNTs by a dynamic vacuum treatment at 1250 °C for 2 hours following Ref. [33]. Again, the DWCNT transformation was followed by HR-TEM and by the observation of the DWCNT structure factors using X-ray studies. In addition, new Raman modes emerge after the 1250 °C heat treatment particularly in a frequency range that is clearly upshifted from the outer tube RBMs.

1.3.2 Spectroscopic methods

Raman spectroscopy
Raman spectra were measured with a Dilor xy triple spectrometer using various lines of an Ar/Kr laser, a He/Ne laser and a Ti:sapphire laser in the 1.83-2.54 eV (676-488 nm) energy range. The spectra can be recorded in normal (NR) and high resolution (HR) mode, respectively ($\Delta\bar{\nu}_{\mathrm{NR}} = 1.3\,\mathrm{cm}^{-1}$ for blue and $\Delta\bar{\nu}_{\mathrm{HR}} = 0.4\,\mathrm{cm}^{-1}$ for red lasers). The samples in the form of bucky-paper are kept in dynamic vacuum and on a copper tip attached to a cryostat, which allows temperature variation in the 20-600 K temperature range. We used Raman spectroscopy

to characterize the diameter distribution of the SWCNT, to determine the peapod concentration, and to monitor the DWCNT transformation of the peapod samples.

Magnetic Resonance

Magnetic resonance, i.e. the resonant absorption of electromnagnetic waves between Zeeman levels whose degenerancy is lifted by a magnetic field, is a powerful method to study a range of phenomenon such as e.g. interaction between electron spins and density of states in a metal near the Fermi level.

Electron spin resonance (ESR) was performed on the N@C_{60}:C_{60} endohedral fullerene: fullerene solid solution, which was produced in a N_2 arc-discharge tube following Ref. [66] with a typical yield of 1-10 ppm [67]. After the solvent filling steps, excess fullerenes were removed by sonication in toluene and the filtered peapod material was dried at 100 °C in air. The peapod and the reference SWCNT materials were mixed with the ESR silent high purity SnO_2 in a mortar to separate the pieces of the conducting bucky-papers. The samples were sealed under dynamic vacuum. A typical microwave power of 10 μW and 0.01 mT magnetic field modulation at ambient temperature were used for the measurements in a Bruker Elexsys X-band spectrometer.

NMR was performed on tubes with selective enrichment of the inner shells using ^{13}C isotope enriched fullerenes [39, 68] in the "peapod" synthesis route. The ^{13}C enrichment allows to increase the ^{13}C NMR sensitivity by two orders of magnitude. This provides the possibility of singling out the electronic properties of the inner tubes NMR data were taken with the sample sealed in a 6 mm diameter glass tube filled with 200 mbar of high purity Helium gas. The ^{13}C-NMR spectra were obtained by a Fourier transformation of the free induction decay following the excitation pulse. We probed the low frequency spin dynamics (or low energy spin excitations, equivalently) of the inner-tubes using the spin lattice relaxation time, T_1, defined as the characteristic time it takes the ^{13}C nuclear magnetization to recover after saturation. The signal intensity after saturation, $S(t)$, was deduced by integrating the fast Fourier transform of half the spin-echo for different delay times t.

1.4 Summary

In Chapters 2, 3, and 4 the encapsulation and properties of magnetic fullerenes inside SWCNTs is presented. In Chapter 2, high filling of single wall carbon nanotubes (SWCNT) with C_{60} and C_{70} fullerenes in solvent is reported at temperatures as low as 69 ^{o}C. In Chapter 3, the synthesis of highly ^{13}C isotope enriched azafullerene, C_{59}N embedded in C_{60} is reported. The material enables the nuclear spin-labelling of heterofullerene complexes with a potential for biological applications. In Chapter 4, the filling of single-wall carbon nanotubes with C_{59}N azafullerene derivatives is reported from toluene solvent at ambient temperature.

In Chapters 5, 6, 7, and 8 the growth and the characterization of DWCNTs is presented. In Chapter 5 a method is presented which allows the study of diameter selective reactions in SWCNTs with an unprecedented accuracy. It is based on the transformation of fullerene peapods into double-wall carbon nanotubes and the study of the resulting diameter distribution of the inner nanotubes with Raman spectroscopy. An anomalous absence of mid-diameter inner tubes is explained by the suppressed amount of C_{70} peapods in the transition region between standing and lying C_{70} configurations. In Chapter 6, the reversible hole engineering of SWCNTs is studied. It is shown that opening on the nanotubes can be reversibly produced. The diameter dependence of the opening and closing mechanisms is studied using fullerene encapsulation and inner tube growth as diameter selective probes. In Chapter 7 the growth of inner tubes from organic solvents is presented. ^{13}C isotope labeled organic solvents, such as e.g. toluene was used to trace the source of carbon on the inner tube. In Chapter 8, the synthesis of double-wall carbon nanotubes (DWCNTs) with highly unperturbed inner shells is reported using the catalytic vapor deposition method. Temperature dependent and high resolution Raman measurements show an enhanced phonon life-time of the inner tubes with respect to the outer ones and similar diameter SWCNTs.

In Chapters 9, 10, and 11 a detailed study on the the vibrational properties of peadpod template grown DWCNTs is presented. In Chapter 9 a detailed investigation of the Raman response of the inner tube radial breathing modes (RBMs) in double-wall carbon nanotubes is reported. In Chapter 10, the resonance behavior and the dispersion of the G′ line in double-wall carbon nanotubes is investigated by multi-frequency Raman scattering. In Chapter 11, the Raman scattering cross section of the radial breathing modes of double-wall carbon nanotubes was used to determine the optical transitions of the inner tubes.

In Chapters 12, 13 the growth, vibrational and NMR spectroscopy of isotope engieneered DWCNTs is presented. In Chapter 12 the synthesis of a unique isotope engineered system, double-wall carbon nanotubes with natural carbon outer and highly ^{13}C enriched inner walls, is reported from isotope enriched fullerenes encapsulated in single-wall carbon nanotubes (SWCNTs). The material allows to observe the D-line of the highly defect free inner tubes that can be related to a curvature induced enhancement of the electron-phonon coupling. In Chapter 13 we report on the spin dynamics of ^{13}C isotope enriched inner-walls in double-wall carbon nanotubes (DWCNT) using ^{13}C nuclear magnetic resonance (NMR). Contrary to expectations, the data set implies that the spin-lattice relaxation time (T_1) has the same temperature (T) and magnetic field (H) dependence for most of the innerwall nanotubes detected by NMR. For $T \lesssim 150$ K we find a significant increase in $1/T_1T$ with decreasing T, followed by a sharp drop below $\simeq 20$ K. The data clearly indicates the formation of a gap in the spin excitation spectrum, where the gap value $2\Delta \simeq 40$ K ($\equiv 3.7$ meV) is H independent.

In Chapter 14 we review the properties of double wall carbon nanotubes (DWCNTs). In Chapter 15, the efforts to study the SWCNT properties using encapsulated probes is reviewed. In particular, inner tubes are shown to be efficient probes of the SWCNT properties, isotope labeled inner tubes are shown to be a unique system to perform NMR studies on the tubes and finally it is discussed how ESR on encapsulated magnetic fullerenes can be used to study the SWCNT properties.

References

[1] S. Iijima, Nature **354**, 56 (1991).
[2] S. Iijima and T. Ichihashi, Nature **363**, 603 (1993).
[3] D. S. Bethune, C. H. Kiang, M. S. DeVries, G. Gorman, S. R., and R. Beyers, Nature **363**, 605 (1993).
[4] A. N. Obraztsov, I. Pavlovsky, A. P. Volkov, E. D. Obraztsova, A. L. Chuvilin, and V. L. Kuznetsov, J. Vac. Sci. Techn. B **18**, 1059 (2000).
[5] G. Z. Yue, Q. Qiu, B. Gao, Y. Cheng, J. Zhang, H. Shimoda, S. Chang, J. P. Lu, and O. Zhou, Appl. Phys. Lett. **81**, 355 (2002).
[6] J. H. Hafner, C. L. Cheung, and C. M. Lieber, Nature **398**, 761 (1999).
[7] A. Bachtold, P. Hadley, T. Nakanishi, and C. Dekker, Science **294**, 1317 (2001).
[8] W. Harneit, C. Meyer, A. Weidinger, D. Suter, and J. Twamley, Phys. St. Solidi B **233**, 453 (2002).
[9] R. Egger and A. O. Gogolin, Nature **79**, 50825085 (1997).
[10] K. P. Bohnen, R. Heid, H. J. Liu, and C. T. Chan, Phys. Rev. Lett. **93**, 245501 (2004).
[11] D. Connétable, G.-M. Rignanese, J.-C. Charlier, and X. Blase, Phys. Rev. Lett. **94**, 015503 (2005).
[12] S. J. Tans, M. H. Devoret, H. Dai, A. Thess, R. E. Smalley, L. J. Geerligs, and C. Dekker, Nature **386**, 474 (1997).
[13] C. Kane and E. Mele, Phys. Rev. Lett. **90**, 207401 (2003).
[14] M. Bockrath, D. H. Cobden, J. Lu, R. A. G., R. E. Smalley, L. Balents, and P. L. McEuen, Nature **397**, 598 (1999).
[15] H. Ishii, H. Kataura, H. Shiozawa, H. Yoshioka, H. Otsubo, Y. Takayama, T. Miyahara, S. Suzuki, Y. Achiba, M. Nakatake, et al., Nature **426**, 540 (2003).
[16] H. Rauf, T. Pichler, M. Knupfer, J. Fink, and H. Kataura, Phys. Rev. Lett. **93**, 096805 (2004).
[17] F. Wang, G. Dukovic, , L. E. Brus, and T. F. Heinz, Science **308**, 838 (2005).
[18] M. C. Martin, J. Fabian, J. Godard, P. Bernier, J. M. Lambert, and L. Mihály, Phys. Rev. B **51**, 2844 (1995).
[19] A. Rosenberg and C. Kendziora, Phys. Rev. B **51**, 9321 (1995).
[20] P. J. Horoyski, M. L. W. Thewalt, and T. R. Anthony, Phys. Rev. B **54**, 920 (1996).

[21] J. Bardeen, L. N. Cooper, and J. R. Schrieffer, Phys. Rev. **108**, 1175 (1957).

[22] J. Meese, *Neutron Transmutation Doping of Semiconductors* (Plenum Press, NY, 1979).

[23] W. S. Capinski, H. J. Maris, E. Bauser, I. Silier, M. Asen-Palmer, T. Ruf, M. Cardona, and E. Gmelin, Appl. Phys. Lett. **71**, 2109 (1997).

[24] I. Shlimak, HAIT J. Sci. Eng. **1**, 196 (2004).

[25] Y. Miyauchi and S. Maruyama, *Identification of excitonic phonon sideband by photoluminescence spectroscopy of single-walled carbon-13 nanotubes*, cond-mat/0508232.

[26] T. Pichler, M. Knupfer, M. S. Golden, J. Fink, A. Rinzler, and R. E. Smalley, Phys. Rev. Lett. **80**, 4729 (1998).

[27] H. Kuzmany, W. Plank, M. Hulman, C. Kramberger, A. Grüneis, T. Pichler, H. Peterlik, H. Kataura, and Y. Achiba, Eur. Phys. J. B **22**, 307 (2001).

[28] M. J. O'Connell, S. M. Bachilo, C. B. Huffman, V. C. Moore, M. S. Strano, E. H. Haroz, K. L. Rialon, P. J. Boul, W. H. Noon, C. Kittrell, et al., Science **297**, 593 (2002).

[29] J. W. G. Wildör, L. C. Venema, A. G. Rinzler, R. E. Smalley, and C. Dekker, Nature **391**, 59 (1998).

[30] R. Saito, G. Dresselhaus, and M. Dresselhaus, *Physical Properties of Carbon Nanotubes* (Imperial College Press, 1998).

[31] X.-P. Tang, A. Kleinhammes, H. Shimoda, L. Fleming, K. Y. Bennoune, S. Sinha, C. Bower, O. Zhou, and Y. Wu, Science **288**, 492 (2000).

[32] C. Goze-Bac, S. Latil, P. Lauginie, V. Jourdain, J. Conard, L. Duclaux, A. Rubio, and P. Bernier, Carbon **40**, 1825 (2002).

[33] S. Bandow, M. Takizawa, K. Hirahara, M. Yudasaka, and S. Iijima, Chem. Phys. Lett. **337**, 48 (2001).

[34] B. W. Smith, M. Monthioux, and D. E. Luzzi, Nature **396**, 323 (1998).

[35] N. Hamada, S. Sawada, and A. Oshiyama, Phys. Rev. Lett. **68**, 1579.1581 (1992).

[36] A. Thess, R. Lee, P. Nikolaev, H. Dai, P. Petit, J. Robert, C. Xu, Y. H. Lee, S. G. Kim, A. G. Rinzler, et al., Science **273**, 483 (1996).

[37] V. Zólyomi and J. Kürti, Phys. Rev. B **70**, 085403 (2004).

[38] X. Liu, T. Pichler, M. Knupfer, M. S. Golden, J. Fink, H. Kataura, and Y. Achiba, Phys. Rev. B **66**, 045411 (2002).

[39] F. Simon, C. Kramberger, R. Pfeiffer, H. Kuzmany, J. Zólyomi, V. Kürti, P. M. Singer, and H. Alloul, Phys. Rev. Lett. **95**, 017401 (2005).

[40] H. Kataura, Y. Kumazawa, Y. Maniwa, I. Umezu, S. Suzuki, Y. Ohtsuka, and Y. Achiba, Synthetic Met. **103**, 2555 (1999).

[41] S. M. Bachilo, M. S. Strano, C. Kittrell, R. H. Hauge, R. E. Smalley, and R. B. Weisman, Science **298**, 2361 (2002).

[42] C. D. Spataru, S. Ismail-Beigi, L. X. Benedict, and S. G. Louie, Phys. Rev. Lett. **92**, 077402 (2004).

[43] V. Perebeinos, J. Tersoff, and P. Avouris, Phys. Phys. Lett. **92**, 257402 (2004).

[44] V. Perebeinos, J. Tersoff, and P. Avouris, Phys. Phys. Lett. **94**, 027402 (2005).

[45] J. Maultzsch, R. Pomraenke, S. Reich, E. Chang, D. Prezzi, A. Ruini, E. Molinari, M. S. Strano, C. Thomsen, and C. Lienau, Phys. Rev. B **72**, 241402 (2005).

[46] F. Plentz, H. B. Ribeiro, A. Jorio, M. A. Pimenta, and M. S. Strano, *Direct Experimental Evidence of Exciton-Phonon Bound States in Carbon Nanotubes*, cond-mat/0507104.

[47] U. J. Kim, X. M. Liu, C. A. Furtado, G. Chen, R. Saito, J. Jiang, M. S. Dresselhaus, and P. C. Eklund, Phys. Rev. Lett. **95**, 157402 (2005).

[48] C. Thomsen and S. Reich, Phys. Rev. Lett. **85**, 5214 (2000).

[49] J. Kürti, V. Zólyomi, A. Grüneis, and H. Kuzmany, Phys. Rev. B **65**, 165433 (2002).

[50] V. Zólyomi, J. Kürti, A. Grüneis, and H. Kuzmany, Phys. Rev. Lett. **90**, 157401 (2003).

[51] H. Kuzmany, *Solid-State Spectroscopy, An Introduction* (Springer Verlag, Berlin, 1998).

[52] R. Saito, G. Dresselhaus, and M. S. Dresselhaus, Phys. Rev. B **61**, 2981 (2000).

[53] C. Fantini, A. Jorio, M. Souza, M. S. Strano, M. S. Dresselhaus, and M. A. Pimenta, Phys. Rev. Lett. **93**, 147406 (2004).

[54] H. Telg, J. Maultzsch, S. Reich, F. Hennrich, and C. Thomsen, Phys. Rev. Lett. **93**, 177401 (2004).

[55] V. N. Popov, New J. Phys. **6**, 17 (2004).

[56] G. G. Samsonidze, R. Saito, N. Kobayashi, A. Grüneis, J. Jiang, A. Jorio, S. G. Chou, G. Dresselhaus, and M. S. Dresselhaus, Appl. Phys. Lett. **85**, 5703 (2004).

[57] H. Kataura, Y. Maniwa, T. Kodama, K. Kikuchi, K. Hirahara, K. Suenaga, S. Iijima, S. Suzuki, Y. Achiba, and W. Krätschmer, Synthetic Met. **121**, 1195 (2001).

[58] B. W. Smith, M. Monthioux, and D. Luzzi, Chem. Phys. Lett. **315**, 31 (1999).

[59] B. W. Smith and D. Luzzi, Chem. Phys. Lett. **321**, 169 (2000).

[60] J. L. Hutchison, N. A. Kiselev, E. P. Krinichnaya, A. V. Krestinin, R. O. Loutfy, A. P. Morawsky,

V. E. Muradyan, E. D. Obraztsova, J. Sloan, S. V. Terekhov, et al., Carbon **39**, 761 (2001).

[61] W. Ren, F. Li, J. Chen, S. Bai, and H.-M. Cheng, Chem. Phys. Lett. **359**, 196 (2002).

[62] R. Pfeiffer, H. Kuzmany, C. Kramberger, C. Schaman, T. Pichler, H. Kataura, Y. Achiba, J. Kürti, and V. Zólyomi, Phys. Rev. Lett. **90**, 225501 (2003).

[63] A. S. Claye, N. M. Nemes, A. Jánossy, and J. E. Fischer, Phys. Rev. B **62**, 4845 (2000).

[64] J.-P. Salvetat, T. Fehér, C. LHuillier, F. Beuneu, and L. Forró, Phys. Rev. B **72**, 075440 (2005).

[65] T. Pichler, H. Kuzmany, H. Kataura, and Y. Achiba, Phys. Rev. Lett. **87**, 267401 (2001).

[66] B. Pietzak, M. Waiblinger, T. Murphy, A. Weidinger, M. Hohne, E. Dietel, and A. Hirsch, Chem. Phys. Lett. **279**, 259 (1997).

[67] A. Jánossy, S. Pekker, F. Fülöp, F. Simon, and G. Oszlányi, in *Proceedings of the IWEPNM* (2000), p. 199.

[68] F. Simon, A. Kukovecz, C. Kramberger, R. Pfeiffer, F. Hasi, H. Kuzmany, and H. Kataura, Phys. Rev. B **71**, 165439 (2005).

2

Low temperature fullerene encapsulation in single wall carbon nanotubes: synthesis of N@C_{60}@SWCNT

F. Simon, H. Kuzmany, H. Rauf, T. Pichler, J. Bernardi, H. Peterlik, L. Korecz, F. Fülöp, and A. Jánossy

Chemical Physics Letters **383**, *362 (2004)*.

ABSTRACT High filling of single wall carbon nanotubes (SWCNT) with C_{60} and C_{70} fullerenes in solvent is reported at temperatures as low as 69 ^{o}C. A 2 hour long refluxing in n-hexane of the mixture of the fullerene and SWCNT results in a high yield of C_{60},C_{70}@SWCNT, fullerene peapod, material. The peapod filling is characterized by TEM, Raman and electron energy loss spectroscopy and X-ray scattering. We applied the method to synthesize the temperature sensitive (N@C_{60}:C_{60})@SWCNT as proved by electron spin resonance spectroscopy. The solvent prepared peapod samples can be transformed to double walled nanotubes enabling a high yield and industrially scalable production of DWCNT.

2.1 Introduction

Nanostructures based on carbon nanotubes [1] have been in the forefront of nanomaterial research in the last decade. Single wall carbon nanotube (SWCNT) is an even more exciting material as it represents the perfect, one-dimensional form of carbon. Fullerene encapsulating SWCNTs have attracted considerable interest after the discovery of C_{60}@SWCNT peapods [2]. More recently, several molecules have been successfully inserted into the interior of tubes such as other fullerenes, endohedral metallofullerenes or alkali halides [3]. It is believed that the inside filled structures can alter or enhance the mechanical and electronic properties of the SWCNTs or may allow the fine tuning of these parameters. However, all these synthesis methods required treatment at relatively high temperatures, above 400 °C. In particular, the peapod synthesis requires the heat treatment of SWCNT and fullerenes sealed together under vacuum, a method that appears impractical for large scale production purposes. Another important trend is the study of the behavior of the encapsulated materials under special conditions. It was recently shown that fullerene peapods are transformed into a double wall carbon nanotube (DWCNT) structure after high temperature annealing [4]. The fullerenes coalesce into an inner nanotube, which leaves the electronic properties unaffected but is expected to significantly enhance the mechanical properties of the tube system. This enhanced mechanical stability makes DWCNTs promising candidates for applications such as future electronics, probe tips for scanning probe microscopy, field emission devices and many more. Our aim in the current study was two-fold: i.) development of a peapod synthesis method that allows the use of low temperatures in order to obtain encapsulated materials which do not survive the usual high temperature synthesis methods, ii.) devising a simple method for the production of peapod starting materials to facilitate the large scale synthesis of DWCNT. In what follows, we describe the synthesis of fullerene peapods from SWCNT mixed with fullerene in solution. We present transmission electron microscopy, Raman spectroscopy, electron energy loss spectroscopy, and X-ray studies to prove that a high filling content of the peapods is achieved. We show electron spin resonance evidence that the temperature sensitive N@C_{60} survives the filling. We also present the transformation of the solvent prepared peapod samples into DWCNT.

2.2 Experimental

Sample preparation. Commercial SWCNT (NCL-SWCNT from Nanocarblab, Moscow, Russia and Rice-SWCNT from Tubes@Rice, Rice University, Houston, Texas) and fullerenes (Hoechst AG, Frankfurt, Germany), and n-hexane (Merck KGaA, Darmstadt, Germany) were used for the low temperature synthesis of fullerene peapods. The NCL-SWCNT material is prepared by the arc-discharge method and is purified to 50 % using repeated high temperature air and acid washing treatments by the manufacturer. The Rice SWCNT material had an initial purity of 15 % and is purified with a triple repetition of H_2O_2 refluxing and HCl acid etching. The material was then filtered and degassed in dynamic vacuum at 400 °C for 1 h. The filling levels discussed below are consistent with the effective tube-end opening side-effect of the SWCNT purification [5, 6]. Additional heat treatment in air or refluxing in H_2O_2 does not increase the fullerene filling levels in our samples. The mean value, d, and the variance, σ, of the tube diameters were determined from multifrequency Raman measurements [7] and it was found that $d = 1.50$ nm, $\sigma = 0.1$ nm and $d = 1.34$ nm, $\sigma = 0.09$ nm for the NCL- and purified Rice-SWCNT samples, respectively. We followed the method of Kataura et al. [6] to fill fullerenes from the vapor phase, denoted as vapor-filling in the following. This involves sealing of the SWCNT material with the fullerene in a quartz ampoule after degassing at 300 °C and keeping it at 650 °C for 2 hours. The resulting material was sonicated in toluene in order to remove non-reacted fullerenes, filtered, and dried from toluene at 400 °C in dynamic vacuum. Dynamic vacuum treatment at 700 ^oC is equivalent to this last step in removing non-reacted fullerene particles without an observable effect on the peapods. Fullerene filling into SWCNT in n-hexane, denoted as solvent-filling in the following, is achieved with mixing typically 5 mg of the SWCNT material with 10 ml n-hexane with 5 mg of

C_{60} or C_{70}. The as-received NCL-SWCNT materials were dried by the manufacturer and care was taken to keep it away from humidity. The 400 °C dynamic vacuum degassing of the Rice-SWCNT was also crucial for the solvent-filling: rinsing it in water prevents any further solvent-fillability probably because water enters into the nanotubes. The SWCNT, fullerene and n-hexane mixture was sonicated for 5 minutes resulting in the partial dissolution of C_{60} due to the relatively low room temperature solubility, 0.043 mg/ml [8], of C_{60} in n-hexane. The C_{60} solution, undissolved C_{60} and SWCNT mixture was then refluxed at 69 °C for 2 hours. After this treatment, the filtered bucky-papers were dried in air at 120 °C for 1 hour. Not encapsulated C_{60} that covers the bucky-paper is removed with the two methods mentioned above: sonication in toluene or by dynamic vacuum treatment at 700 °C. Our studies have shown that both methods yield identical materials. The same steps were followed for the production of the C_{70}@SWCNT peapod material. DWCNT transformation of the peapod samples was performed with a 2 h long dynamic vacuum treatment at 1250 °C following Ref.[4].

Transmission electron microscopy. High resolution transmission electron microscopic (HR-TEM) studies were performed on a TECNAI F20 field emission microscope equipped with a Gatan Image Filter (GIF 2001) operated at 120kV or 200 kV. Electron transparent samples were prepared by drying a suspension of peapod material and N,N-Dimethyl-formamide on a holey carbon grid.

Raman spectroscopy. Multi frequency Raman spectroscopy was studied on a Dilor xy triple spectrometer equipped with a cryostat for the 20-600 K temperature range in the 1.83-2.54 eV (676-488 nm) energy range using an Ar-Kr mixed-gas laser. We used Raman spectroscopy to characterize the diameter distribution of the SWCNT, to determine the peapod concentration, and to monitor the DWCNT transformation of the peapod samples.

Electron energy loss spectroscopy. EELS was performed in transmission at a 170 keV in a purpose built spectrometer which combines both high energy (180 meV) and momentum resolution (0.6 nm^{-1}). Details can be found in Ref. [9] and references therein. Free standing films of about 100 nm effective thickness, which is thin enough to avoid multiple scattering, were prepared as described in Ref. [10].

X-ray studies. X-ray diffraction images were measured with Cu K_α radiation from a rotating anode X-ray generator and a pinhole camera, equipped with a two-dimensional, position-sensitive detector [11]. The system works in a 10^{-4} mbar vacuum to avoid parasitic scattering from air. Radial averages of the two-dimensional spectra were evaluated to obtain the scattering curves $q = 4\pi/\lambda sin\theta$, with 2θ being the scattering angle and $\lambda = 0.1542$ nm being the X-ray wavelength. The strong increase in scattering intensity, that is always observed for SWCNT towards small q, is subtracted by a power-law [12].

Electron spin resonance spectroscopy. The N@C_{60}:C_{60} endohedral fullerene: fullerene solid solution was produced in a N_2 arc-discharge tube following Ref. [13] with a typical yield of 1-10 ppm [14]. After the solvent filling steps, excess fullerenes were removed by sonication in toluene and the filtered peapod material was dried at 100 ^oC in air. The peapod and the reference SWCNT materials were mixed with the ESR silent high purity SnO_2 in a mortar to separate the pieces of the conducting bucky-papers. The samples were sealed under dynamic vacuum. A typical microwave power of 10 μW and 0.01 mT magnetic field modulation at ambient temperature were used for the measurements in a Bruker Elexsys X-band spectrometer.

2.3 Results and discussion

We performed TEM studies on our vapor and solvent prepared samples. For both kinds of materials TEM micrographs (not shown) proved that an abundant peapod concentration was achieved. However, it is not representative of the bulk of the sample thus filling efficiency has to be determined from spectroscopic investigations. In Figure 2.1., we show the comparison of the Raman spectra of vapor- and solvent-filled C_{60} peapod samples. The Raman spectra of peapod samples in the plotted frequency range consist of the SWCNT G and D modes at 1590 and 1355 cm^{-1},

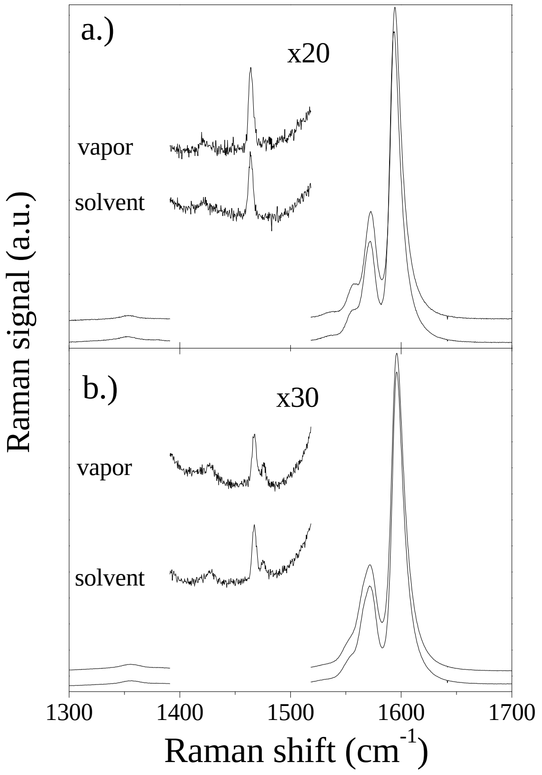

FIGURE 2.1. a.) Raman spectra of vapor and solvent filled C_{60}@NCL-SWCNT and b.) vapor and solvent filled C_{60}@Rice-SWCNT at $\lambda = 488$ nm and 90 K. The spectra are normalized to the amplitude of the SWCNT G mode.

respectively and narrow lines related to the Raman active modes of the C_{60} inside the SWCNT [6, 15]. We show enlarged the most significant Raman active line of C_{60} peapod, the $A_g(2)$ mode. For the NCL-SWCNT peapod sample, we observe a single $A_g(2)$ line at 1466 cm^{-1} and for the Rice-SWCNT the well known doublet peapod signal at 1466 and 1474 cm^{-1} [15]. The absence of an extra line at 1469 cm^{-1}, that is the Raman shift of the $A_g(2)$ of crystalline C_{60} and the observation of the characteristic double $A_g(2)$ line structure in the Rice-SWCNT peapod sample are evidence that no C_{60} is present apart from those encapsulated in the nanotubes. The larger mean tube diameter of the NCL-SWCNT is consistent with the absence of the weaker satellite of the $A_g(2)$ at 1474 cm^{-1} in this sample as this signal is associated with the presence of immobile C_{60} molecules in the smaller diameter nanotubes [16]. We have also observed that the Raman spectra of vapor and solvent prepared C_{70}@SWCNT (spectra not shown) are identical also.

We determined the peapod concentration quantitatively from EELS measurements using the method described in Ref. [10] for both the vapor and solvent prepared samples. The C1s core level spectrum (not shown) contains contributions from carbon in C_{60} and in the SWCNT starting material and additional carbon in the sample. When compared to a non C_{60} encapsulating SWCNT reference, the excess C1s signal related to C_{60} can be determined in the peapod samples. This yields the number of C_{60} related carbon atoms that is directly translated to the filling level. Carbon in some impurity phases also affects the measurement. Thus, the values provided by this technique are only higher limits of the C_{60} filling. Nevertheless, the current samples are of comparable quality than in the previous study [10] so any effect related to impurities gives the same order of error. Following Ref. [10], the C_{60} related C1s contributions can be translated to the volume filling with simple geometrical considerations taking into account the mean tube diameter and the 0.97 nm interfullerene distance [5]. We found that within experimental precision both the vapor and solvent prepared peapod materials have an overall C_{60} filling of 55±5 % for the NCL-SWCNT. This has to be compared with 61±5 % found in a previous study on highly filled samples prepared with the vapor method [10]. The Rice-SWCNT has a smaller peapod content as seen from the Raman spectra that is most probably related to the smaller tube diameters in this sample as C_{60} can only enter into nanotubes with $d \gtrsim 1.2$ nm [10]. Nevertheless, the similar

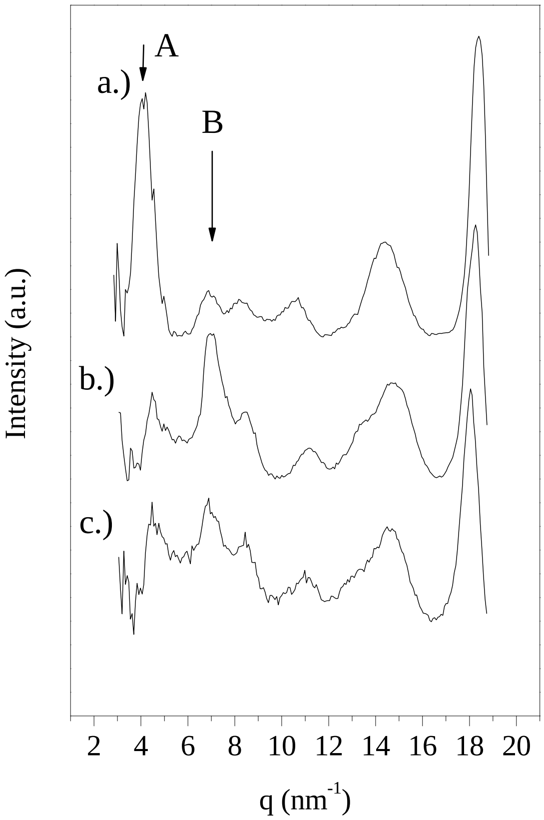

FIGURE 2.2. X-ray diffraction profile of a.) pristine NCL-SWCNT, b.) vapor and c.) solvent prepared C_{60}@NCL-SWCNT samples. The relative intensity of the A and B peaks is a measure of the peapod concentration. The scattering peak observed at 18 nm^{-1} comes from residual graphitic carbon.

peapod content of the vapor and solvent prepared materials emphasizes the effectiveness of the solvent filling method.

We also checked the consistency of the peapod filling content from X-ray diffraction. In Fig. 2.2., X-ray diffraction patterns of the pristine NCL-SWCNT, the peapod sample prepared by the vapor and the solvent method are shown. The encapsulation with C_{60} strongly modifies the intensity of the peaks, in particular the 10 peak around $q = 4.5$ nm^{-1} is strongly depressed in comparison to the other peaks [17]. The intensity modulation of the hexagonal lattice peaks by the different form factor of filled and empty SWCNT can be related to the filling content of the encapsulated peapods [17, 18]. The first peak (A) decreases for filled nanotubes in comparison to the pristine SWCNT material and a second peak (B) appears, which is related to the one-dimensional lattice of the encapsulated C_{60} molecules. The X-ray spectra of the vapor and the solvent prepared peapod samples are nearly identical, which proves that a similar, high peapod filling is achieved with the two methods. Moreover, it proves that the solvent prepared peapod samples possess a similarly well ordered one-dimensional peapod structure. A numerical simulation following [17, 18] leads for the inter-C_{60} distance and the coherence length of 0.95 nm and 25 nm, respectively, in agreement with previous electron diffraction studies [10].

In Fig. 2.3., we show the ESR spectra of the starting NCL-SWCNT, (N@C_{60}:C_{60})@NCL-SWCNT, and N@C_{60}:C_{60}. The ESR spectrum of the pristine NCL-SWCNT for the magnetic field range shown is dominated by a signal that is assigned to some residual carbonaceous material, probably graphite. Fig. 2.3c. shows, that after the solvent encapsulation of N@C_{60}:C_{60} in the NCL-SWCNT, we observe a hyperfine N triplet ESR, similar to that in pristine N@C_{60}:C_{60}, superimposed on the broad signal present in the pristine nanotube material. Fig. 2.3d. shows the triplet component of this signal after subtracting the signal observed in pristine SWCNT. The hiperfine triplet in N@C_{60}:C_{60} is the result of the overlap of the $^4S_{3/2}$ state of the three 2p electrons of the N atom and the ^{14}N nucleus, with nuclear spin, I =1. The isotropic hyperfine coupling of N@C_{60}:C_{60} is unusually high as a result of the strongly compressed N atomic 2p^3 orbitals in the C_{60} cage thus it unambiguously identifies this material [19]. The hyperfine cou-

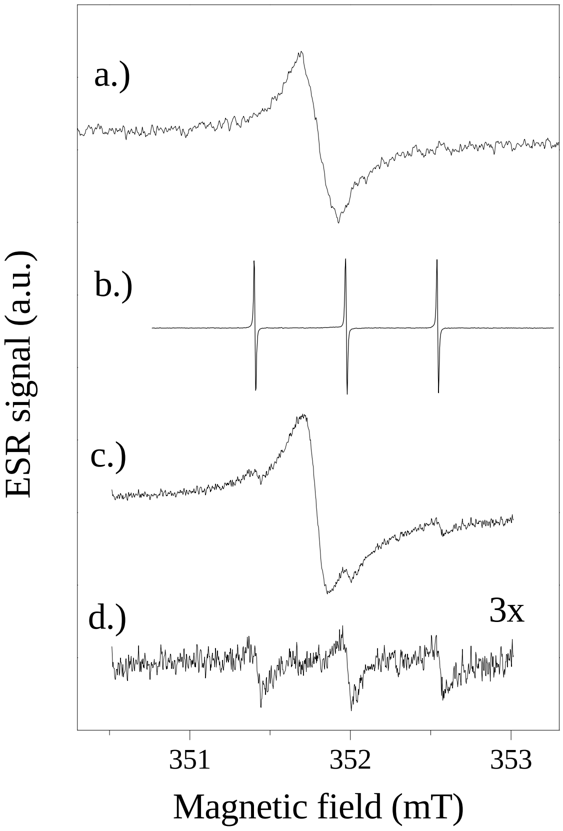

FIGURE 2.3. X-band electron spin resonance spectrum of the a.) pristine SWCNT, b.) crystalline N@C_{60}:C_{60}, c.) (N@C_{60}:C_{60})@SWCNT and d.) the triplet component of the (N@C_{60}:C_{60})@SWCNT ESR spectrum at ambient temperature.

pling constant observed for the triplet structure in the encapsulated material, A =0.57±0.01 mT, agrees within experimental precision with that observed in N@C_{60}:C_{60} [19], which proves that the encapsulated material is (N@C_{60}:C_{60})@SWCNT. The preparation procedure, as detailed above, guarantees that non-encapsulated N@C_{60} is not present in our samples. The ESR linewidth for the encapsulated material, ΔH_{pp} = 0.07 mT, is significantly larger than the resolution limited ΔH_{pp} =0.01 mT in the pristine N@C_{60}:C_{60} material, the lines being Lorentzian. The most probable cause for the broadening is static magnetic fields from residual magnetic impurities in the SWCNT [20]. The ESR signal intensity is proportional to the number of N spins, and this allows the quantitative comparison of N concentrations in (N@C_{60}:C_{60})@SWCNT and N@C_{60}:C_{60}. Taking the filling value from the EELS measurement, we obtain that the N spin concentration in (N@C_{60}:C_{60})@SWCNT is ~2.5 times smaller than in the starting N@C_{60}:C_{60} material. This cannot be due to a loss of N spins during the synthesis as N@C_{60}:C_{60} is stable below 100 ^{o}C and N loss becomes rapid above 220 °C only [21]. However, the observed difference may be caused by the limited accuracy of the ESR intensity measurement also caused by microwave losses as the conducting bucky-paper pieces are separated from each-other in a poorly controlled way.

In Figure 2.4., we show the Raman spectra of DWCNT prepared from vapor and solvent prepared C_{60}@NCL-SWCNT peapod samples. For both spectra, the narrow Raman lines in the 250-350 cm^{-1} spectral range correspond to the inner tubes[22]. Similar patterns were observed at other laser lines (not shown) proving that the inner tube diameter distributions are identical in the two kinds of samples irrespective of the peapod synthesis method. This shows that peapod materials can be produced with the solvent method that are suitable for the production of DWCNT materials.

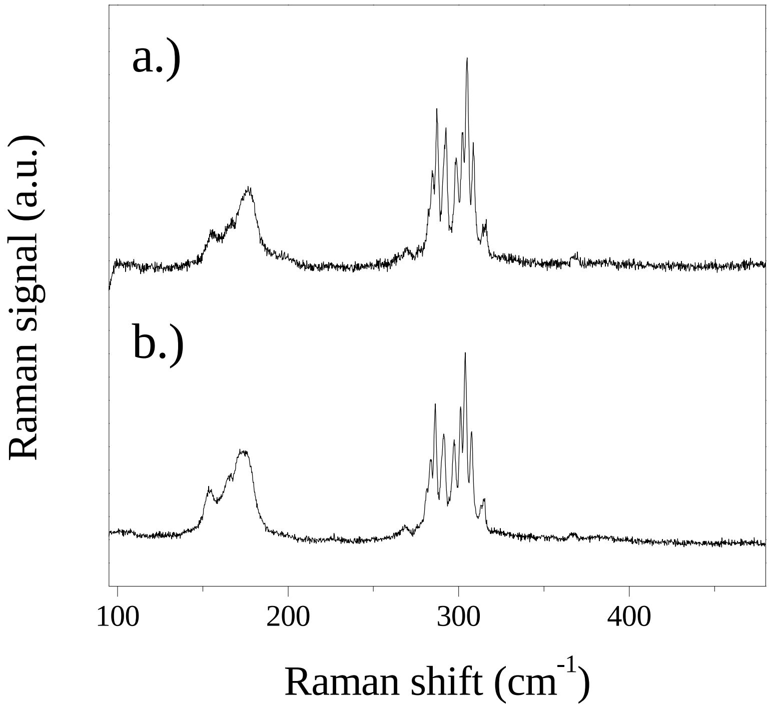

FIGURE 2.4. Raman spectra of DWCNT obtained from a.) vapor and b.) solvent filled C_{60}@NCL-SWCNT at $\lambda = 676$ nm and ambient temperature.

2.4 Conclusion

We presented the preparation of fullerene encapsulated SWCNT at temperatures slightly above room temperature. This method produces very high filling and provides a simple alternative to the commonly used vapor filling method. Its advantage is the relative simplicity and the possibility to scale it up to larger amounts. The mechanism by which C_{60} enters the tubes from solution at low T's needs further exploration. At the moment, we argue that the low concentration of dissolved C_{60} in n-hexane behaves as a continuous source of C_{60} similar to the C_{60} vapor. The encapsulation itself is an exothermal process [23] and the loss of some degrees of freedom is compensated by the gain in potential energy. We have encapsulated a temperature senstive material, N@C_{60}:C_{60}, and observed its ESR signal. To our knowledge it is the first successful magnetic resonance experiment on an SWCNT encapsulated spin-probe. It has been speculated that such materials, when available in higher spin concentrations, may be fundamental elements of quantum-computering [24]. The solvent prepared peapod samples are transformed to DWCNT with a yield identical to that from vapor prepared materials. This opens the way for the production of high purity and highly perfect DWCNT in industrial amounts.

Acknowledgement: The authors gratefully acknowledge useful discussions with Christian Kramberger and Rudolf Pfeiffer. This work was supported by the Austrian Science Funds (FWF) project Nr. P16315 and Nr. 14893, by the EU project NANOTEMP MPRN-CT-2002-00192, by the Deutsche Forschungsgemeinschaft DFG project PI 440, by the Hochschuljubiläums-stiftung der Stadt Wien project H-175/2001 and by the Hungarian State Grant OTKA T043255. The Budapest ESR Laboratory is member of the SENTINEL European Infrastructural Network.

Note added. After preparing this manuscript for publication we learned about a similar low temperature C_{60} encapsulation method from Ref.[25] using ethanol as solvent.

References

[1] S. Iijima, Nature **354**, 56 (1991).

[2] B. W. Smith, M. Monthioux, and D. E. Luzzi, Nature **396**, 323 (1998).

[3] M. Monthioux, Carbon **40**, 1809 (2002).

[4] S. Bandow, M. Takizawa, K. Hirahara, M. Yudasaka, and S. Iijima, Chem. Phys. Lett. **337**, 48 (2001).

[5] K. Hirahara, K. Bandow, S. Suenaga, H. Kato, T. Okazaki, T. Shinohara, and S. Iijima, Phys. Rev. B **64**, 115420 (2001).

[6] H. Kataura, Y. Maniwa, T. Kodama, K. Kikuchi, K. Hirahara, K. Suenaga, S. Iijima, S. Suzuki, Y. Achiba, and W. Krätschmer, Synthetic Met. **121**, 1195 (2001).

[7] H. Kuzmany, W. Plank, M. Hulman, C. Kramberger, A. Grüneis, T. Pichler, H. Peterlik, H. Kataura, and Y. Achiba, Eur. Phys. J. B **22**, 307 (2001).

[8] M. Dresselhaus, G. Dresselhaus, and P. C. Ecklund, *Science of Fullerenes and Carbon Nanotubes* (Academic Press, 1996).

[9] J. Fink, Adv. Electron. Electron Phys. **75**, 121 (1989).

[10] X. Liu, T. Pichler, M. Knupfer, M. S. Golden, J. Fink, H. Kataura, Y. Achiba, K. Hirahara, and S. Iijima, Phys. Rev. B **65**, 045419 (2002).

[11] H. Peterlik, P. Fratzl, and K. Kromp, Carbon **32**, 939 (1994).

[12] A. Rinzler, J. Liu, H. Dai, P. Nikolaev, C. Huffman, F. Rodriguez-Macias, P. Boul, A. Lu, D. Heymann, D. Colbert, et al., Appl. Phys. A **67**, 29 (1998).

[13] B. Pietzak, M. Waiblinger, T. Murphy, A. Weidinger, M. Hohne, E. Dietel, and A. Hirsch, Chem. Phys. Lett. **279**, 259 (1997).

[14] A. Jánossy, S. Pekker, F. Fülöp, F. Simon, and G. Oszlányi, in *Proceedings of the IWEPNM* (2000), p. 199.

[15] T. Pichler, H. Kuzmany, H. Kataura, and Y. Achiba, Phys. Rev. Lett. **87**, 267401 (2001).

[16] R. Pfeiffer, H. Kuzmany, T. Pichler, H. Kataura, Y. Achiba, M. Melle-Franco, and F. Zerbetto, Phys. Rev. B **69**, 035404 (2004).

[17] M. Abe, H. Kataura, H. Kira, T. Kodama, S. Suzuki, Y. Achiba, K.-i. Kato, M. Takata, A. Fujiwara, K. Matsuda, et al., Phys. Rev. B **68**, 041405(R) (2003).

[18] H. Kataura, Y. Maniwa, M. Abe, A. Fujiwara, T. Kodama, K. Kikuchi, J. Imahori, Y. Misaki, S. Suzuki, and Y. Achiba, Appl. Phys. A **74**, 349 (2002).

[19] T. Almeida Murphy, T. Pawlik, A. Weidinger, M. Hhne, R. Alcala, and J.-M. Spaeth, Phys. Rev. Lett. **77**, 1075 (1996).

[20] X.-P. Tang, A. Kleinhammes, H. Shimoda, L. Fleming, K. Y. Bennoune, S. Sinha, C. Bower, O. Zhou, and Y. Wu, Science **288**, 492 (2000).

[21] M. Waiblinger, K. Lips, W. Harneit, A. Weidinger, E. Dietel, and A. Hirsch, Phys. Rev. B **64**, 159901 (2001).

[22] R. Pfeiffer, H. Kuzmany, C. Kramberger, C. Schaman, T. Pichler, H. Kataura, Y. Achiba, J. Kürti, and V. Zólyomi, Phys. Rev. Lett. **90**, 225501 (2003).

[23] S. Berber, Y.-K. Kwon, and D. Tománek, Phys. Rev. Lett. **88**, 185502 (2002).

[24] W. Harneit, C. Meyer, A. Weidinger, D. Suter, and J. Twamley, Phys. St. Solidi B **233**, 453 (2002).

[25] M. Yudasaka, K. Ajima, K. Suenaga, T. Ichihashi, A. Hashimoto, and S. Iijima, Chem. Phys. Lett. **380**, 42 (2003).

3

Highly ^{13}C isotope enriched azafullerene, $C_{59}N$, for nuclear spin labelling

F. Simon, F. Fülöp, A. Rockenbauer, L. Korecz, and H. Kuzmany

Chemical Physics Letters **404**, *85 (2005).*

ABSTRACT Synthesis of highly ^{13}C isotope enriched azafullerene, $C_{59}N$ embedded in C_{60} is reported. ^{13}C enriched fullerenes, produced with the Krätschmer-Huffmann process, were subject to a N_2 discharge that produces $C_{59}N$ with a low probability. Raman spectroscopy indicates a homogeneous ^{13}C distribution. Electron spin resonance measurement (ESR) proves that the $C_{59}N$ concentration, 0.2 %, is similar as in non-enriched fullerenes. The ESR spectrum is simulated accurately with the known ^{14}N and ^{13}C hyperfine coupling constants. The material enables the nuclear spin-labelling of heterofullerene complexes with a potential for biological applications. It might also find applications as a building element for quantum computation.

3.1 Introduction

Isotope controlled synthesis (ICS) of molecular nanostructures provides an important degree of freedom to characterize fundamental and application oriented properties. ICS is generally considered as a tool to e.g. enhance nuclear magnetic resonance signals, to provide improved information when specific isotope labelling is possible or to trace biological processes using radioactive nuclei. For fullerenes [1], ICS was applied to improve the NMR data [2], to identify the origin of different vibrational modes in crystalline C_{60} [3], and to yield an insight into underlying physical phenomenon such as the mechanism of the superconductivity in alkali doped fullerides [4] by means of ^{13}C enrichment. More recently, ^{13}C enriched fullerenes were used to produce ^{13}C enriched single wall carbon nanotubes [5].

Properties of fullerenes can be also studied through the synthesis of on-ball doped modifications. The $C_{59}N$ or $C_{59}B$ heterofullerenes were predicted to provide a doping opportunity for C_{60} [6, 7]. In general, heterofullerenes possess a rich chemistry due to their enhanced reactivity as compared to pristine fullerenes [7]. The $C_{59}N$ azafullerene can be synthesized in macroscopic amounts [7, 8] and in a solid form it is an insulator consisting of $(C_{59}N)_2$ dimer units where the extra electrons are localized in the dimer bonds as singlet states [9]. The $C_{59}N$ monomer radical can be observed by light [10, 11] or thermal induced homolysis of $(C_{59}N)_2$ [12] or when the $C_{59}N$ monomer is embedded in a low concentration in the C_{60} crystal [13]. This $C_{59}N$:C_{60} solid solution was synthesized in a discharge tube designed for the production of N@C_{60} [13]. The advantages of the latter synthesis method over the chemical synthesis [8] are its relative simplicity and the ability of providing an isotope control option by changing the $^{14}N_2$ gas to $^{15}N_2$. Recently, it was shown that the extra electron on the $C_{59}N$ is transferred toward the C_{60}'s at high temperatures and it provides a controllable electron doping of the crystalline C_{60} [14].

Here, we report the synthesis of the $C_{59}N$ monomer radical with controlled ^{13}C isotope content. The material was prepared from C_{60} containing isotopically controlled amounts of ^{13}C using the N_2 discharge method. Raman spectroscopy indicates a uniform ^{13}C enrichment of the fullerenes. The ^{13}C enriched $C_{59}N$:C_{60} material was studied with electron spin resonance. The ^{14}N hyperfine triplet, that dominates the spectrum for non isotope enriched $C_{59}N$:C_{60}, collapses into a broad line in agreement with the isotope content and the ^{13}C nuclear hyperfine couplings determined previously in $C_{59}N$ [13]. A minority phase that is poor in ^{13}C was also observed underlying the sensitivity of the ESR method in characterizing this material.

3.2 Experimental

Sample preparation. Commercial ^{13}C isotope enriched fullerene mixture (MER Corp., Tucson, USA) was used for the synthesis of $C_{59}N$. The isotope enriched fullerenes were produced by the Krätschmer-Huffmann process [15] using ^{13}C enriched graphite rods. The supplier provided a ^{13}C enrichment of nominal 25 % that was determined using mass spectrometry. The isotope enriched fullerenes are denoted as $\left(^{13}C_x\right)_{60}$ and $\left(^{13}C_x\right)_{59}N$ in the following. We refer to the material with the nominal $x = 0.25$ ^{13}C content, although this value is slightly refined in this work. Apart from the C_{70} and other higher fullerenes with contents up to 20 %, the dominant impurity in the material is a $\left(^{13}C_x\right)_{60}$ phase with $x \approx 0.05$ and a content below 2 %. The high purity C_{60} (> 99.9 %) used for comparison was obtained from Hoechst (Hoechst AG, Frankfurt, Germany). $C_{59}N$ production was performed in the same N_2 discharge tube as previously [13] following the original design of Pietzak *et al.* [16] for the production of N@C_{60}:C_{60}. In brief, fullerenes are sublimed into a nitrogen discharge that is maintained by a high voltage between two electrodes inside a quartz tube filled with a low pressure of N_2 gas. $C_{59}N$:C_{60} deposits on surfaces with temperatures between 200-400 °C of the quartz tube, whereas N@C_{60}:C_{60} deposits on the water-cooled cathode. The resulting material is collected from the tube walls and is resublimed at 500 °C twice in order to remove impurities that are usually produced during the synthesis and to reduce the amount of higher fullerenes [17]. However, the less ^{13}C enriched C_{60} phase can not be removed from the

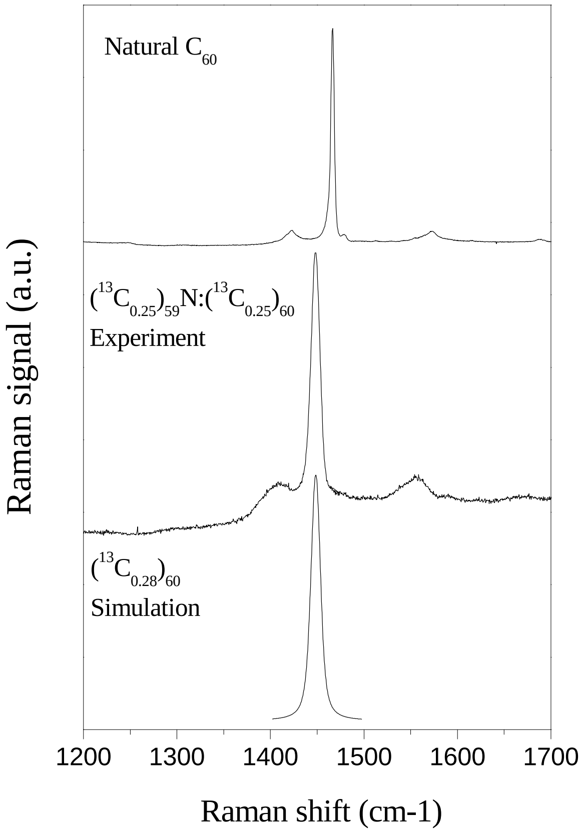

FIGURE 3.1. Raman spectra of natural C$_{60}$ and $\left(^{13}\mathrm{C}_{0.25}\right)_{59}$N:$\left(^{13}\mathrm{C}_{0.25}\right)_{60}$ at λ = 488 nm excitation. The lowest solid curve show the simulated C$_{60}$ A$_g$(2) mode with 28 % ^{13}C enrichment as explained in the text.

sample with this method. Typically 10 mg of final material containing $\left(^{13}\mathrm{C}_{0.25}\right)_{59}$N at 2000 ppm concentrations in $\left(^{13}\mathrm{C}_{0.25}\right)_{60}$ is produced from 100 mg starting fullerene material. The samples were sealed in quartz tubes under vacuum for the ESR and Raman measurements. Among the higher fullerenes, C$_{70}$ can be best observed using Raman spectroscopy and its amount was found to be below 1 % in the final material.

Raman spectroscopy. Multi frequency Raman spectroscopy was studied on a Dilor xy triple spectrometer at 488 nm excitation energy using an Ar-Kr mixed-gas laser.

Electron spin resonance spectroscopy. The ESR experiments were performed with a Bruker Elexsys X-band spectrometer. A typical microwave power of 1 mW and 0.01 mT magnetic field modulation at ambient temperature were used.

3.3 Results and discussion

In Fig. 3.1., we show the Raman spectra of $\left(^{13}\mathrm{C}_{0.25}\right)_{59}$N:$\left(^{13}\mathrm{C}_{0.25}\right)_{60}$ and C$_{60}$ with natural carbon isotope contents at ambient conditions and excited with a 488 nm laser. The spectrum of $\left(^{13}\mathrm{C}_{0.25}\right)_{59}$N:$\left(^{13}\mathrm{C}_{0.25}\right)_{60}$ is identical to that of $\left(^{13}\mathrm{C}_{0.25}\right)_{60}$ as the Raman technique is not sensitive to the 2000 ppm amounts of $\left(^{13}\mathrm{C}_{0.25}\right)_{59}$N. We focus our attention on the totally symmetric A$_g$(2) mode that appears with the largest intensity for this laser excitation [17]. Analysis of this mode enables us to determine the ^{13}C enrichment level with precision and provides information on its homogeneity. A similar analysis was performed previously [18, 19]. As the ^{13}C build-in in the C$_{60}$'s is a random process, the number of ^{13}C nuclei on a given $\left(^{13}\mathrm{C}_x\right)_{60}$ fullerene is expected to follow a binomial distribution with $x \cdot 60$ expectation value. The vibrational frequency of the ^{13}C enriched fullerenes downshifts as a result of the heavier ^{13}C. In a continuum approximation the amount of the downshift is given by: $\left(\nu_0 - \nu\right)/\nu_0 = 1 - \sqrt{\frac{12+c_0}{12+c}}$, where ν_0 and ν are the Raman shifts of the corresponding modes in the natural carbon and enriched materials, respectively, c is the concentration of the ^{13}C enrichment, and c_0 = 0.011 is the natural abundance of ^{13}C in

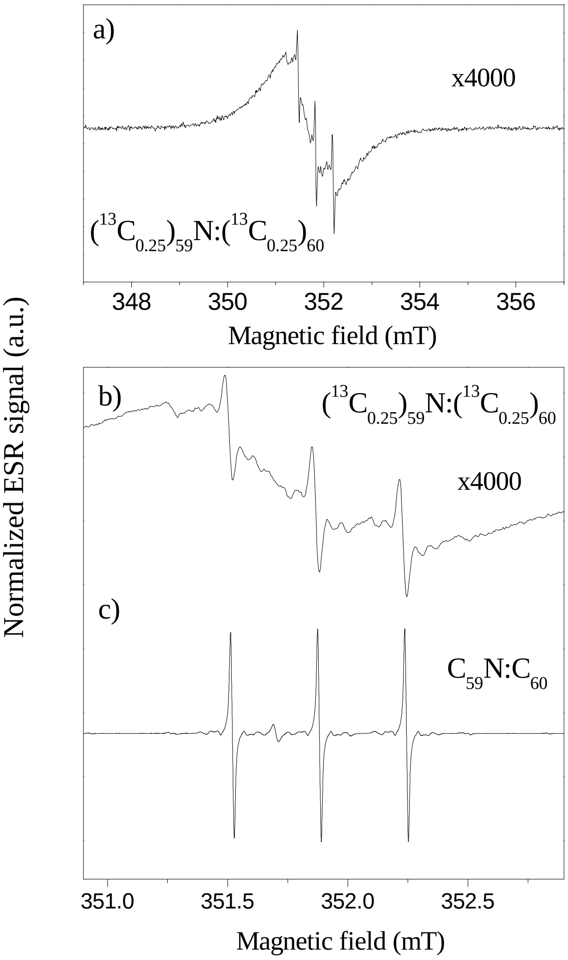

FIGURE 3.2. ESR spectra of $C_{59}N:C_{60}$ produced from a-b) ^{13}C enriched and c) natural carbon normalized by the sample mass. Note the different field scales for a) and b-c) and the enlarged scaling for the enriched materials.

carbon. The experimentally observed 16.0(5) cm^{-1} downshift of the first moment of the $A_g(2)$ mode, corresponds to $c = 0.28(1)$. In addition, the full line-shape was simulated from the convolution of the binomial distribution with the line-shape of this mode in the natural C_{60}. A good agreement between the experimentally observed line-shape and the simulation (lowest solid curve in Fig. 3.1) was obtained using the above value for c. This proves that the distribution of the ^{13}C nuclei follows the statistical expectation and is therefore homogeneous. The current $c = 0.28(1)$ is slightly different from the value, $c = 0.25$, given by the supplier underlining the difficulty of the ^{13}C content determination.

In order to further characterize the material, we compared its Raman spectra with that of the starting fullerene mixture (not shown). The absence of the C_{70} peaks puts a 2 % upper limit on the total amount of residual higher fullerenes in our material as compared to the starting value of about 20 %. This proves that the double sublimation procedure at 500 °C is indeed very effective in purifying the material from higher fullerenes. The $\left(^{13}C_x\right)_{60}$ phase with $x \approx 0.05$ that was observed with mass spectroscopy by the supplier is not removed by the double sublimation, however its content is below the detectability limit. In contrast, electron spin resonance spectroscopy can detect the fraction of the sample that belongs to the different $\left(^{13}C_x\right)_{59}N$ radicals.

In Fig. 3.2., we show the room temperature ESR spectrum of the $\left(^{13}C_{0.25}\right)_{59}N$: $\left(^{13}C_{0.25}\right)_{60}$ material with two different magnetic field scales. We also show the spectrum of non-enriched $C_{59}N:C_{60}$ for comparison. The spectra of the latter was analyzed in detail previously [13] and is recalled here. The dominating triplet component was identified as due to the ^{14}N ($I = 1$) hyperfine interaction. The free tumbling of the molecule above the *sc-fcc* structural transition of the C_{60}, $T_c = 261$ K [17], averages out the anisotropic part of this hyperfine coupling. However, the electron is delocalized on the $C_{59}N$ cage and a number of well defined ^{13}C ($I = 1/2$) satellite doublets appear as a result of the finite electron density on the different C positions and the 1.1 % abundance

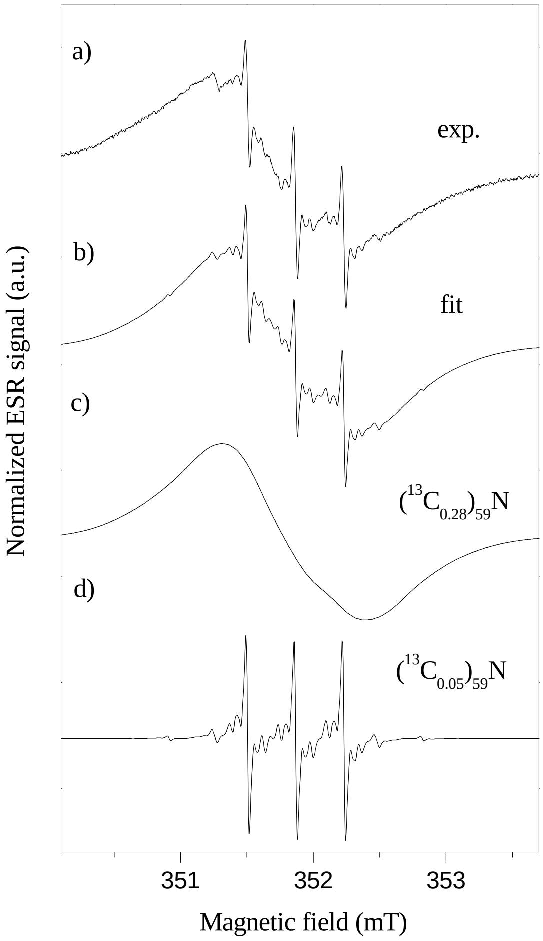

FIGURE 3.3. Comparison of the experimental ESR spectra of $(^{13}C_{0.25})_{59}N:(^{13}C_{0.25})_{60}$ (a) with the simulation as explained in the text (b). Simulated spectra for the two levels of isotope enrichments, $(^{13}C_{0.28})_{59}N:(^{13}C_{0.25})_{60}$ (c) and $(^{13}C_{0.05})_{59}N:(^{13}C_{0.25})_{60}$ (d) are also shown.

of ^{13}C in carbon. The hyperfine couplings were determined for eight non-equivalent carbon sites corresponding to twenty-three sites on the $C_{59}N$ molecule. An additional small intensity signal between the two low-field ^{14}N triplet lines was identified as a $C_{59}N^+$-C_{60}^- heterodimer due to a partial charge transfer from $C_{59}N$ [14].

The $(^{13}C_x)_{59}N$ spectrum is simulated for arbitrary x by using a recursive build-up technique [20]. The effect of the first ^{13}C coupling is computed by superimposing a doublet pattern with intensity x onto each components of the original nitrogen triplet signal with intensity of $1-x$. In the next step, this superimposed spectrum is considered as a starting signal and the next superimposition is carried out in the same way by using the next carbon splitting constant. The new carbon splitting could have the same value as the preceding one in the case of equivalent carbons. The procedure is repeated for all the 23 carbon nuclei with resolved splitting. The impact of the 36 non-resolved carbon splittings can be considered by using an increased intrinsic line-width in the primer spectrum. Similarly, the small intensity $C_{59}N^+$-C_{60}^- heterodimer signal becomes unobservable due to its broadening.

The ESR spectrum of the $(^{13}C_{0.25})_{59}N:(^{13}C_{0.25})_{60}$ consists of apparently two overlapping signals: a broad component and a triplet signal together with a ^{13}C hyperfine pattern. The ^{13}C hyperfine structure is similar to that observed in the non-enriched $C_{59}N$, however its components have an increased line-width that results from the hyperfine interaction of the non-resolved C sites. The double integrated and mass normalized intensities, that measures the number of spins in the sample, are similar for the natural and enriched materials suggesting that the complicated pattern in the enriched sample also originates from the $C_{59}N$ radicals, however, the presence of ^{13}C broadens its spectrum. Below, we show that the observed ESR pattern reflects the inhomogeneity in our sample. The narrow triplet and the broader components originate from the less and highly ^{13}C enriched phases, respectively.

In Fig. 3.3a. we show the experimental spectrum again together with a simulation for a sample containing a mixture of $\left({}^{13}\mathrm{C}_x\right)_{59}\mathrm{N}$ molecules with $x = 0.28$ and $x = 0.045$ enrichments (Fig. 3.3b.) with intensity ratios of 98.2:1.8, respectively. The g-factors of the two components were taken to be identical with that of the non-enriched $\mathrm{C}_{59}\mathrm{N}$ of $g = 2.0014(2)$. A residual 0.04 mT line-width was assumed to account for the hyperfine interactions of the non-resolved C sites. The combination of these spectra was found to simulate best the experimental curve. It was assumed that the molecules are freely rotating and the spectra can be described using the previously determined hyperfine coupling constants. The simulated spectra are shown separately for the two types of molecules in Fig. 3.3c. and d., respectively. Although, the two kinds of molecules have a similar ESR amplitude, they have very different integrated intensities. We recall that the ESR signal intensity is inversely proportional to the square of the linewidth due to the field modulation technique employed. As a result, the narrow structure is only a tiny, < 2 % fraction of the total ESR signal intensity. This small amount of ${}^{13}\mathrm{C}$ poorer phase is an unwanted side-product of the production of the higher ${}^{13}\mathrm{C}$ enriched material, however, its amount may not be a limiting factor for practical applications.

3.4 Conclusion

In conclusion, we presented the preparation of a ${}^{13}\mathrm{C}$ enriched heterofullerene, the ${}^{13}\mathrm{C}_{59}\mathrm{N}$ azafullerene, from ${}^{13}\mathrm{C}$ enriched fullerenes. Raman and ESR spectroscopy was used to characterize the enrichment and its homogeneity. The material was produced in a nitrogen discharge tube with the same yield as the non-enriched material. This synthesis method opens new prospects for applications of the chemically active heterofullerenes. These include nuclear spin-labelling of bio-molecules with heterofullerenes or the nuclear spin labelling of the biologically active fullerene itself such as in the HIV-1 inhibitor fullerene derivatives [21]. In addition, an emerging field where application of the current system is envisaged is the use of molecules with well defined interaction configurations between electron and nuclear spins for the purpose of quantum computing [22, 23].

Acknowledgement: This work was supported by the Austrian Science Funds (FWF) project Nr. 17365, by the EU project NANOTEMP BIN2-2001-00580, PATONN MEIF-CT-2003-501099 and the Hungarian State Grants OTKA T043255 and T046953.

References

[1] H. W. Kroto, J. R. Heath, S. C. O'Brien, R. F. Curl, and R. E. Smalley, Nature **318**, 162 (1985).
[2] C. H. Pennington and V. A. Stenger, Rev. Mod. Phys. **68**, 885 (1996).
[3] M. C. Martin, J. Fabian, J. Godard, P. Bernier, J. M. Lambert, and L. Mihály, Phys. Rev. B **51**, 2844 (1995).
[4] O. Gunnarsson, Rev. Mod. Phys. **69**, 575 (1997).
[5] F. Simon, A. Kukovecz, C. Kramberger, R. Pfeiffer, F. Hasi, H. Kuzmany, and H. Kataura, Phys. Rev. Lett. **95**, 017401 (2005).
[6] W. Andreoni, F. Gygi, and M. Parrinello, Chem. Phys. Lett. **190**, 159 (1992).
[7] J. C. Hummelen, C. Bellavia-Lund, and F. Wudl, *Heterofullerenes* (Springer, Berlin, Heidelberg, 1999), vol. 199, p. 93.
[8] J. C. Hummelen, B. Knight, J. Pavlovich, R. Gonzalez, and F. Wudl, Science **269**, 1554 (1995).
[9] T. Pichler, M. Knupfer, M. S. Golden, S. Haffner, R. Friedlein, J. Fink, W. Andreoni, A. Curioni, M. Keshavarz-K, C. Bellavia-Lund, et al., Phys. Rev. Lett. **79**, 3026 (1997).
[10] A. Gruss, K.-P. Dinse, A. Hirsch, B. Nuber, and U. Reuther, J. Am. Chem. Soc. **119**, 8728 (1997).
[11] K. Hasharoni, C. Bellavia-Lund, M. Keshavarz-K, G. Srdanov, and F. Wudl, J. Am. Chem. Soc. **119**, 11128 (1997).
[12] F. Simon, D. Arčon, N. Tagmatarchis, S. Garaj, L. Forró, and K. Prassides, J. Phys. Chem. A. **103**, 6969 (1999).
[13] F. Fülöp, A. Rockenbauer, F. Simon, S. Pekker, L. Korecz, S. Garaj, and A. Jánossy, Chem. Phys. Lett. **334**, 223 (2001).

[14] A. Rockenbauer, G. Csányi, F. Fülöp, S. Garaj, L. Korecz, R. Lukács, F. Simon, L. Forró, S. Pekker, and A. Jánossy, Phys. Rev. Lett. **94**, 066603 (2005).

[15] W. Krätschmer, L. D. Lamb, K. Fostiropoulos, and D. R. Huffmann, Nature **347**, 354 (1990).

[16] B. Pietzak, M. Waiblinger, T. Murphy, A. Weidinger, M. Hohne, E. Dietel, and A. Hirsch, Chem. Phys. Lett. **279**, 259 (1997).

[17] M. Dresselhaus, G. Dresselhaus, and P. C. Ecklund, *Science of Fullerenes and Carbon Nanotubes* (Academic Press, 1996).

[18] A. Rosenberg and C. Kendziora, Phys. Rev. B **51**, 9321 (1995).

[19] P. J. Horoyski, M. L. W. Thewalt, and T. R. Anthony, Phys. Rev. B **54**, 920 (1996).

[20] A. Rockenbauer and L. Korecz, Appl. Magn. Reson. **10**, 29 (1996).

[21] S. H. Friedman, D. L. DeCamp, R. P. Sijbesma, G. Srdanov, F. Wudl, and G. L. Kenyon, J. Am. Chem. Soc. **115**, 6506 (1993).

[22] W. Harneit, C. Meyer, A. Weidinger, D. Suter, and J. Twamley, Phys. St. Solidi B **233**, 453 (2002).

[23] M. Mehring, J. Mende, and W. Scherer, Phys. Rev. Lett. **90**, 153001 (2003).

4

Encapsulating $C_{59}N$ azafullerene derivatives inside single-wall carbon nanotubes

F. Simon, H. Kuzmany, J. Bernardi, F. Hauke, and A. Hirsch

Carbon **44** *1958 (2006).*

ABSTRACT Filling of single-wall carbon nanotubes with $C_{59}N$ azafullerene derivatives is reported from toluene solvent at ambient temperature. The filling is characterized by high resolution transmission electron microscopy and Raman spectroscopy. The filling efficiency is the same as for C_{60} fullerenes and the tube-azafullerene interaction is similar to the tube-C_{60} interaction. Vacuum annealing of the encapsulated azafullerene results in the growth of inner tubes, however no spectroscopic signature of nitrogen built in the inner walls is detected.

4.1 Introduction

The hollow space inside single-wall carbon nanotubes (SWCNTs) have attracted considerable attention recently. The field was opened by the discovery of C_{60} fullerenes encapsulated inside SWCNTs, the peapods [1]. Later it was found that chemical reactions can take place inside the tube such as charging induced polymerization [2] or fusion of the C_{60} spheres to inner tubes [3, 4]. The resulting inner tubes in the double-wall carbon nanotubes (DWCNTs) were shown to be exceptionally defect free [5] which apostrophizes the inside the of the tube as "nano clean-room chemical reactor". We recently found that chemical reactions are not restricted to fullerenes but organic solvents such as benzene or toluene can also participate [6]. The breakthrough to further explore the in-the-tube chemistry was the discovery of encapsulating fullerenes or fullerene derivatives at ambient temperatures [7–9]. Conventional peapod synthesis involves heating the sample above 400-500 °C [10, 11], which most fullerene derivatives do not tolerate. $C_{59}N$, the on-ball nitrogen doped modification of fullerenes, has a rich chemistry due to its enhanced reactivity as compared to pristine fullerenes and can be synthesized in macroscopic amounts chemically [12, 13]. The electronic state of $C_{59}N$ and its derivatives is strongly modified compared to C_{60} [14]. Encapsulating azafullerene peapods would be advantageous as they are expected to go preferably inside the SWCNTs similarly to all-carbon fullerenes, however their sizeable dipole moment adds a further degree of freedom for their applications such as e.g. ambipolar transistor [15]. In addition, the presence of the nitrogen enables to explore the in-the-tube chemistry with heteroatoms.

Here, we present the encapsulation of azafullerene derivatives inside SWCNTs. We use a low temperature synthesis method at ambient conditions. The encapsulation is proven by high-resolution transmission microscopy and Raman spectroscopy. The latter method shows that azafullerenes enter the tube with the same efficiency as C_{60}. Inner tubes grown from the azafullerene adduct are spectroscopically identical to all-carbon inner tubes.

4.2 Experimental

Sample preparation. Commercial SWCNT (Nanocarblab, Moscow, Russia) was used in the current study. The SWCNT material is prepared by the arc-discharge method and is purified to 50 wt% by the manufacturer. The mean value, $d = 1.40$ nm, and the variance, $\sigma = 0.1$ nm, of the tube diameters were determined from multi-laser Raman measurements [16]. The starting azafullerene, $(C_{59}N)_2$, was prepared according to literature procedures [12]. The 4-Hydroxy-3,5-dimethyl-phenyl-hydroazafullerene ($C_{59}N$-der in the following) was prepared from 60 mg (41.66 mol) $(C_{59}N)_2$ and 135 mg (0.7 mmol, 10 eq.) p-Touluenesulfonic acid dissolved in 100 ml 1,2-Dichlorobenzene. 43 mg (351 μmol, 5 eq.) 2,6-dimethylpenol was added to this solution. The reaction mixture was heated to 150 °C for 15 min while passing a constant stream of air through the solution. The formed product was isolated by flash chromatography using toluene as eluent. The product was precipitated from CS_2/pentane, washed three times with pentane and dried in high vacuum and its molecular structure is shown in Fig. 4.1. The material was characterized by ^{1}H and ^{13}C NMR and mass spectroscopy. Fullerene encapsulation was performed with the modification of the low temperature solvent method [8]: open SWCNTs were added to 1 mg/1 ml fullerene-toluene solutions and sonicated for 1 hour. The resulting material was filtered from the solvent, re-suspended in excess toluene to remove non-encapsulated fullerenes and re-filtered. Raman spectroscopy was performed on the bucky-papers. The material was then vacuum annealed at 1250 °C for 2 hours for the growth of inner tubes from the encapsulated material following Refs. [3, 4].

HR-TEM. High resolution transmission electron microscopic (HR-TEM) studies were performed on a TECNAI F20 field emission microscope at 120 kV. The use of this voltage combined with low exposition times of 1 s allows to take good quality pictures without observable irradiation damage to the sample. HR-TEM samples were prepared from a suspension of the peapod material in N,N-Dimethylformamide.

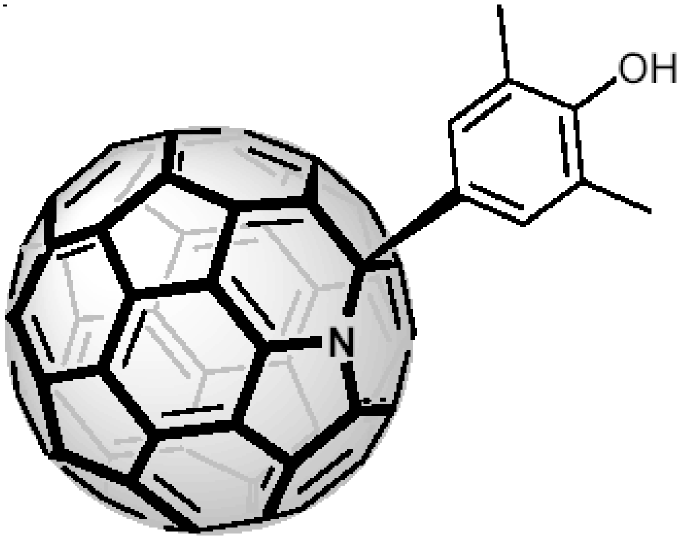

FIGURE 4.1. Schematic structure of the 4-Hydroxy-3,5-dimethyl-phenyl-hydro-azafullerene.

Raman spectroscopy. Raman spectroscopy was studied on a Dilor xy triple spectrometer in the 488-676 nm range with an Ar-Kr laser at room temperature. We used Raman spectroscopy to characterize the diameter distribution of the SWCNTs, to determine the concentration of encapsulated fullerenes, and to study the resulting DWCNT samples.

4.3 Results and discussion

In Figure 4.2., we show a HR-TEM micrograph of the $C_{59}N$-der encapsulated inside SWCNTs. HR-TEM shows an abundant filling of the tubes with the azafullerene, however it does not provide a quantitative measurement on the filling efficiency that is determined from Raman spectroscopy. A cross section profile through the center of the encapsulated azafullerenes enables to determine their separation as the low and high values of the profile indicate bright and dark parts, respectively. Interestingly, we found 0.7-0.8 nm separation for several $C_{59}N$-der pairs (indicated by arrows in Fig. 4.2) in contrast to the ~ 1 nm separation that is usual for encapsulated C_{60} peapods [1, 17]. Although the data does not allow to determine the accurate configuration of the $C_{59}N$-der pairs, it indicates that the presence of the strongly polar side-group gives rise to a structure that is markedly different from the ordered structure found for the spherically symmetric and apolar C_{60}s.

In Figure 4.3., we show the Raman spectra of the pristine and encapsulated $C_{59}N$-der. The Raman spectra of the peapod sample (lower curve in Fig. 4.3) in the plotted frequency range consist of the SWCNT G modes around 1550 cm^{-1} and additional lines related to the Raman active modes of the encapsulated azafullerene derivative [2]. The major Raman modes of the pristine $C_{59}N$-der are similar to those of the $(C_{59}N)_2$ dimer [18]. Here, we focus on the strongest mode that is observed at 1459.2 cm^{-1}. This mode is derived from the C_{60} $A_g(2)$ mode and is downshifted to 1457 cm^{-1} after the encapsulation procedure. The 2.2 cm^{-1} downshift proves the encapsulation of the molecule inside the SWCNT. When encapsulated inside SWCNTs, the corresponding $A_g(2)$ mode of C_{60} downshifts with 3 cm^{-1} , which is assigned to the softening of the C_{60} $A_g(2)$ vibrational mode due to the interaction between the ball and the SWCNT wall [2]. The slight difference between the downshift for the azafullerene and for the C_{60} peapods might be attributed to the different structure of the two molecules. The encapsulation also manifests in a line broadening: the main component of the 1457 cm^{-1} mode is broadened from 4.5 cm^{-1} FWHM in the pristine material to 10 cm^{-1} FWHM in the encapsulated one. This is similar to the values found for encapsulated C_{60} [2].

The integrated intensity of the observed $A_g(2)$ derived mode of the $C_{59}N$ is approximately 5

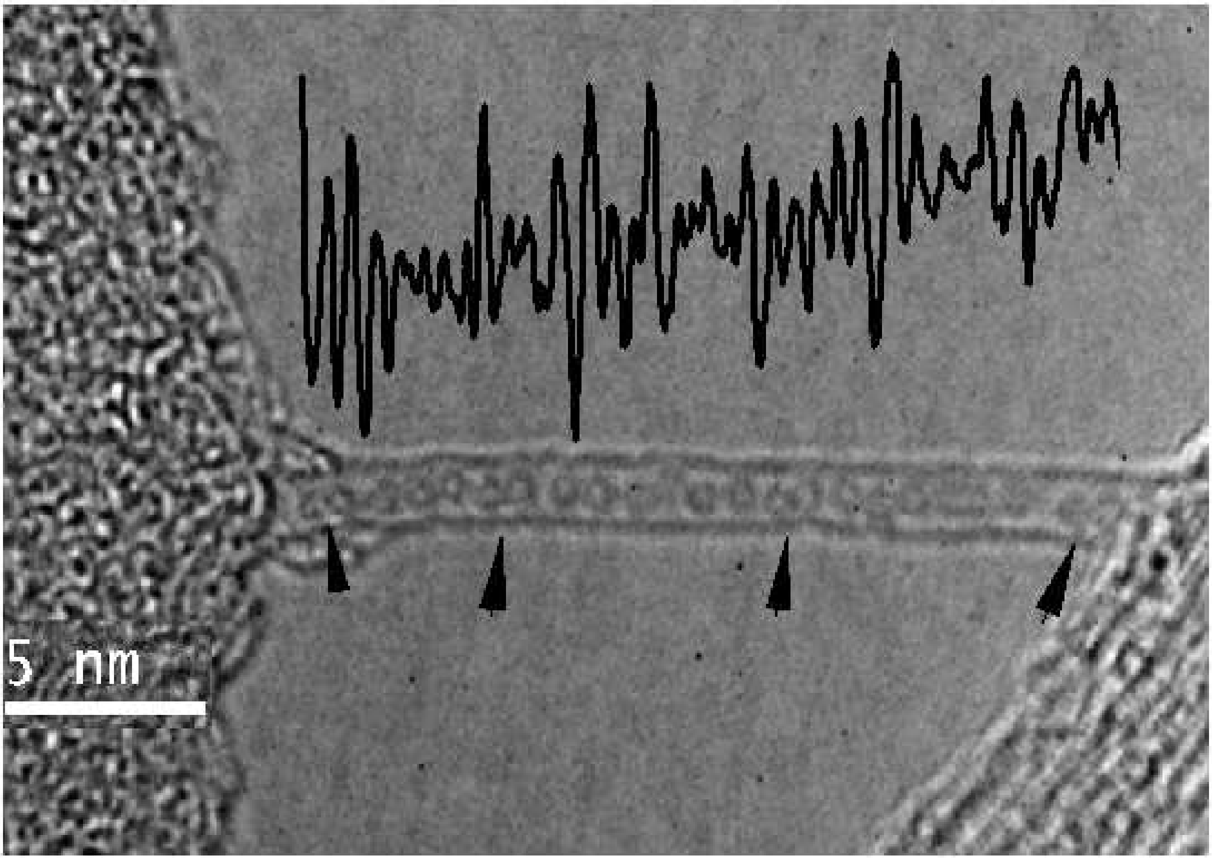

FIGURE 4.2. HR-TEM micrograph of C_{59}N-der encapsulated inside SWCNTs. The solid line shows a cross-section profile of the micrograph. Arrows indicate CC_{59}N-der pairs whose centers are only 0.7-0.8 nm apart.

times larger than that of a C_{60} peapod prepared identically when normalized by the SWCNT G mode intensity. This, however, can not be used to measure the encapsulation efficiency as Raman intensities depend on the strength of the Raman resonance enhancement and the Raman scattering matrix elements [19]. For C_{60} peapods the Raman signal was calibrated with independent and carbon number sensitive measurements: EELS studies gave the total number of C_{60} related and non-C_{60} related carbons [20] and the mass of encapsulated C_{60}s was determined from NMR studies using ^{13}C enriched fullerenes [21]. In the current case, neither methods can be employed and we determined the filling efficiency for the azafullerene by encapsulating a mixture of the azafullerene and C_{60}.

In Fig. 4.4., we show the Raman spectra of the encapsulated C_{59}N-der:C_{60} mixture with weight ratios of 1:9 in the starting solvent. The Raman spectrum of the encapsulated mixture was simulated with a weighted sum of the separately recorded spectra for encapsulated C_{59}N-der and C_{60}. The best agreement between the simulated and the experimental spectra is for a C_{59}N-der content of 0.12(2). This value is close to the expected value of 0.1 and it proves that the azafullerene enters the tubes with the same efficiency as C_{60}. The filling efficiency for C_{60} using the toluene stirring method was found to yield 48(1) % filling of the total available volume by comparing the Raman signal with the previous calibration [22]. This corresponds to ~6 % fraction of the total sample mass as the 100 % encapsulation corresponds to 13 % mass fraction of the encapsulated fullerenes [21].

Encapsulating an azafullerene inside SWCNTs provides a unique opportunity to explore the in-the-tube chemistry with a heteroatom. Peapod samples with toluene encapsulated C_{59}N-der and C_{60} were subject to 1250 °C for 2 hours. In Fig. 4.5, we show the Raman response of the resulting DWCNT made from C_{60} and the C_{59}N-der peapod samples. The radial breathing mode (RBM) range [23] is shown in Fig. 4.5a at 647 nm laser excitation and the Raman G' mode range

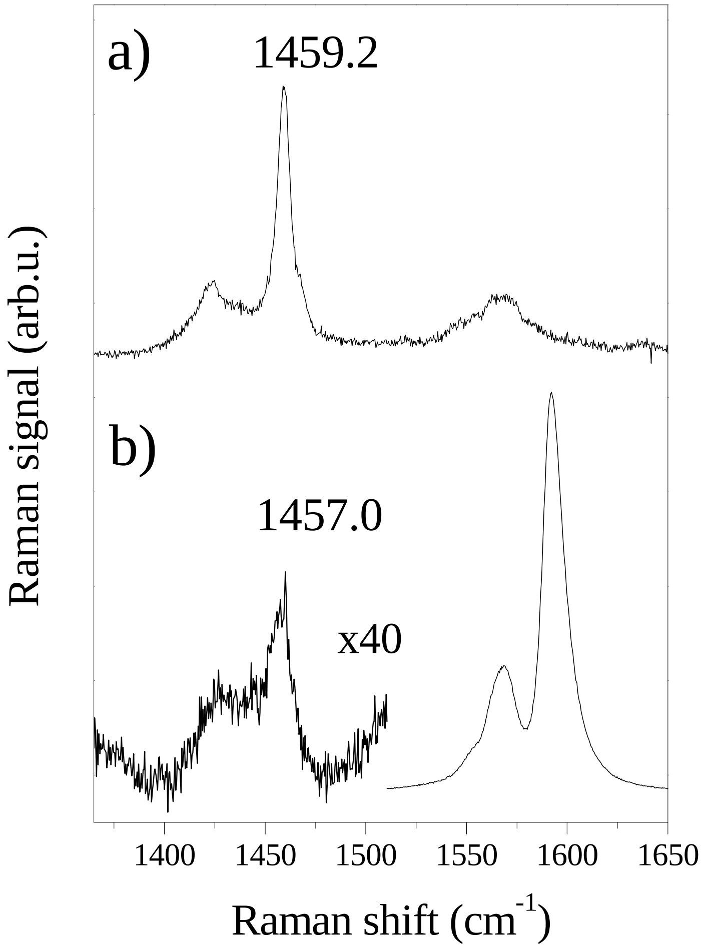

FIGURE 4.3. Tangential mode of the Raman spectra of the $C_{59}N$-der before (a) and after encapsulation (b) excited with a 488 nm laser. Labels mark the position of the strongest $C_{59}N$-der mode in the two samples. The Raman G-mode of SWCNT dominates the peapod spectrum in the 1550-1650 cm^{-1} range.

in Fig. 4.5b with the 515 nm laser. For both materials, the narrow Raman lines in the 250-350 cm^{-1} spectral range correspond to the RBMs of inner tubes [5, 24] and the lower frequency G' mode component (marked by an asterisk in Fig. 4.5b.) to the inner tube G' mode [25]. The emergence of the inner tube RBMs and G' mode in the $C_{59}N$-der peapod material is a further proof that the azafullerenes are indeed encapsulated inside SWCNTs. The G' mode is on of the most energetic vibrational modes of SWCNTs. Therefore any effect related to the modification of the phonon energies would markedly manifest for this mode. We observe no change for the inner tube G' mode for the $C_{59}N$-der based DWCNT as compared to the C_{60} peapod based DWCNTs. Thus, our result suggests that either nitrogen is not entering to the inner tube walls or it has no observable effect on the Raman spectrum.

The only difference observed for the $C_{59}N$-der based DWCNT is the absence of some modes, corresponding to very small diameter inner tubes (shown by arrow in Fig. 4.5a.). This can be understood by the somewhat larger effective size of the $C_{59}N$-der compared to C_{60} and by its inability to enter in very small diameter SWCNTs. Since these tubes remain unfilled, they do not have an inner tube after the heat-treatment.

4.4 Conclusion

In conclusion, we presented the preparation of fullerene peapods containing a derivative of the azafullerene $C_{59}N$ with a low temperature synthesis method. The encapsulation efficiency of the azafullerene is the same as that of C_{60} fullerenes. Although no spectroscopic evidence for nitrogen on the inner tube walls was observed, our material is a starting point to explore the in-the-tube chemistry with heteroatoms. The material might find applications in nano-electronics as

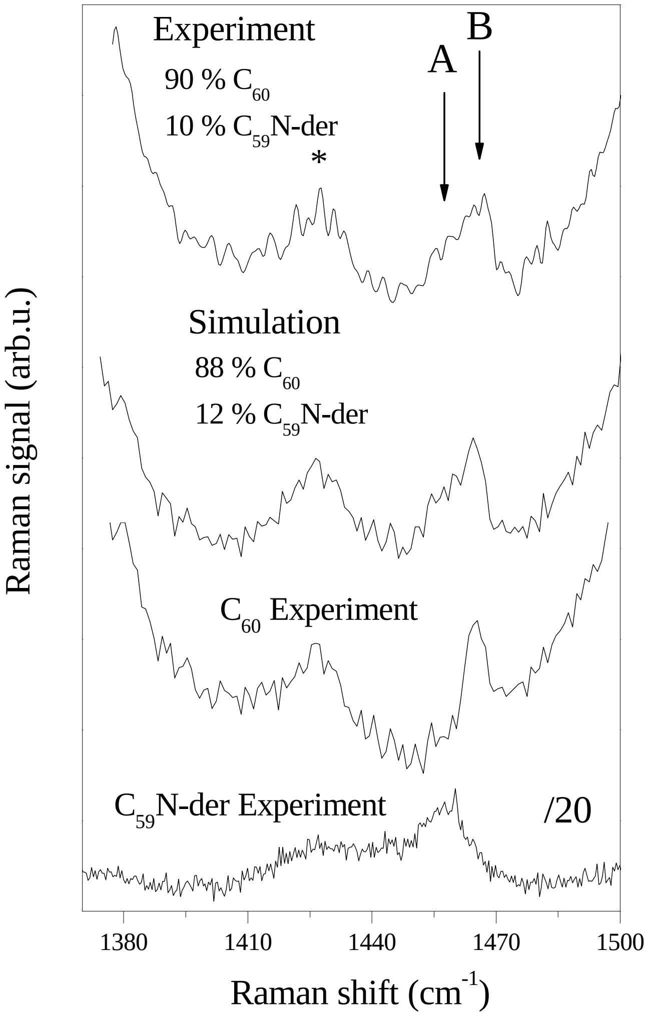

FIGURE 4.4. Raman spectra of the encapsulated $C_{59}N$-der:C_{60} mixture at the 488 nm laser excitation. The spectra for the $C_{59}N$-der and C_{60} peapods is shown together with their weighted sum as explained in the text. A and B mark the componenents coming nominally from the superposing two phases. The asterisk marks a mode that is present in the pristine SWCNT material. Note the different scale for the $C_{59}N$-der peapod material.

the presence of the sizeable electric dipole moment of the molecule allows to fine-tune the nanotube properties. Currently, we investigate the possibility of removing the sidegroup by thermal treatment to produce $C_{59}N$ monomer radicals embedded inside SWCNTs.

Acknowledgement: Work supported by the FWF project 17345, by the Deutsche Forschungsgemeinschaft (DFG) and by the BIN2-2001-00580 and MEIF-CT-2003-501099 EU grants. FS acknowledges the Zoltán Magyary fellowship for support.

References

[1] B. W. Smith, M. Monthioux, and D. E. Luzzi, Nature **396**, 323 (1998).
[2] T. Pichler, H. Kuzmany, H. Kataura, and Y. Achiba, Phys. Rev. Lett. **87**, 267401 (2001).
[3] B. W. Smith and D. Luzzi, Chem. Phys. Lett. **321**, 169 (2000).
[4] S. Bandow, M. Takizawa, K. Hirahara, M. Yudasaka, and S. Iijima, Chem. Phys. Lett. **337**, 48 (2001).
[5] R. Pfeiffer, H. Kuzmany, C. Kramberger, C. Schaman, T. Pichler, H. Kataura, Y. Achiba, J. Kürti, and V. Zólyomi, Phys. Rev. Lett. **90**, 225501 (2003).
[6] F. Simon and H. Kuzmany, *unpublished.*
[7] M. Yudasaka, K. Ajima, K. Suenaga, T. Ichihashi, A. Hashimoto, and S. Iijima, Chem. Phys. Lett. **380**, 42 (2003).
[8] F. Simon, H. Kuzmany, H. Rauf, T. Pichler, J. Bernardi, H. Peterlik, L. Korecz, F. Fülöp, and A. Jánossy, Chem. Phys. Lett. **383**, 362 (2003).
[9] A. N. Khlobystov, D. A. Britz, J. W. Wang, S. A. O'Neil, M. Poliakoff, and G. A. D. Briggs, J. Mat. Chem. **14**, 2852 (2004).
[10] B. W. Smith, M. Monthioux, and D. Luzzi, Chem. Phys. Lett. **315**, 31 (1999).

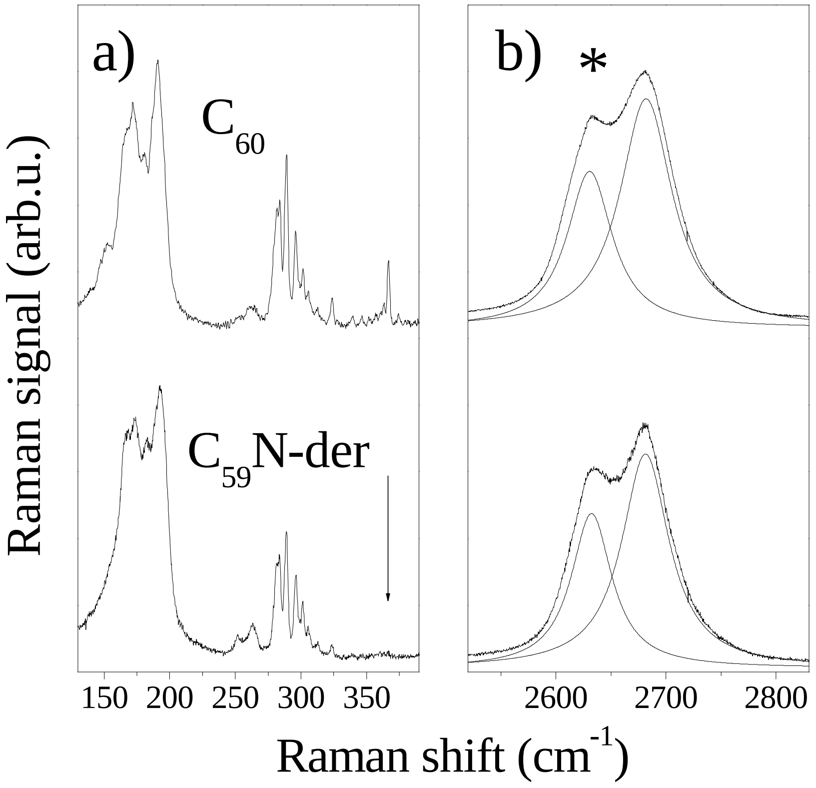

FIGURE 4.5. Raman spectra of the DWCNTs made from C_{60} and C_{59}N-der peapods with a) 647 nm and b) 515 nm laser excitation. Arrow indicates a small diameter RBM mode that is missing from the C_{59}N-der based DWCNT sample. Solid curves show the deconvolution of the G' mode spectra into inner (marked by an asterisk) and outer tube mode components on b).

[11] H. Kataura, Y. Maniwa, T. Kodama, K. Kikuchi, K. Hirahara, K. Suenaga, S. Iijima, S. Suzuki, Y. Achiba, and W. Krätschmer, Synthetic Met. **121**, 1195 (2001).

[12] J. C. Hummelen, C. Bellavia-Lund, and F. Wudl, *Heterofullerenes* (Springer, Berlin, Heidelberg, 1999), vol. 199, p. 93.

[13] A. Hirsch and B. Nuber, Acc. Chem. Res. **32**, 795 (1999).

[14] T. Pichler, M. Knupfer, M. S. Golden, S. Haffner, R. Friedlein, J. Fink, W. Andreoni, A. Curioni, M. Keshavarz-K, C. Bellavia-Lund, et al., Phys. Rev. Lett. **79**, 3026 (1997).

[15] T. Shimada, T. Okazaki, R. Taniguchi, T. Sugai, H. Shinohara, K. Suenaga, Y. Ohno, S. Mizuno, S. Kishimoto, and T. Mizutani, Appl. Phys. Lett. **81**, 4067 (2002).

[16] H. Kuzmany, W. Plank, M. Hulman, C. Kramberger, A. Grüneis, T. Pichler, H. Peterlik, H. Kataura, and Y. Achiba, Eur. Phys. J. B **22**, 307 (2001).

[17] K. Hirahara, K. Bandow, S. Suenaga, H. Kato, T. Okazaki, T. Shinohara, and S. Iijima, Phys. Rev. B **64**, 115420 (2001).

[18] H. Kuzmany, W. Plank, J. Winter, O. Dubay, N. Tagmatarchis, and K. Prassides, Phys. Rev. B **60**, 1005 (1999).

[19] H. Kuzmany, *Solid-State Spectroscopy, An Introduction* (Springer Verlag, Berlin, 1998).

[20] X. Liu, T. Pichler, M. Knupfer, M. S. Golden, J. Fink, H. Kataura, Y. Achiba, K. Hirahara, and S. Iijima, Phys. Rev. B **65**, 045419 (2002).

[21] F. Simon, A. Kukovecz, C. Kramberger, R. Pfeiffer, F. Hasi, H. Kuzmany, and H. Kataura, Phys. Rev. Lett. **95**, 017401 (2005).

[22] H. Kuzmany, R. Pfeiffer, C. Kramberger, T. Pichler, X. Liu, M. Knupfer, J. Fink, H. Kataura, Y. Achiba, B. W. Smith, et al., Appl. Phys. A **76**, 449 (2003).

[23] M. Dresselhaus, G. Dresselhaus, and P. C. Ecklund, *Science of Fullerenes and Carbon Nanotubes* (Academic Press, 1996).

[24] F. Simon, R. Pfeiffer, C. Kramberger, M. Holzweber, and H. Kuzmany, *The Raman response of double wall carbon nanotubes* (Springer New York, 2005), pp. 203–224.

[25] R. Pfeiffer, H. Kuzmany, F. Simon, S. N. Bokova, and E. Obraztsova, Phys. Rev. B **71**, 155409 (2005).

5

Diameter selective reaction processes of single-wall carbon nanotubes

F. Simon, Á. Kukovecz, C. Kramberger, R. Pfeiffer, F. Hasi, and H. Kuzmany

Physical Review B **71**, *165439 (2005).*

ABSTRACT A method is presented which allows the study of diameter selective reactions in SWCNTs with an unprecedented accuracy. It is based on the transformation of fullerene peapods into double-wall carbon nanotubes and the study of the resulting diameter distribution of the inner nanotubes with Raman spectroscopy. This yields a spectral resolution increase of about forty for the modes of different tubes. The method is demonstrated for the diameter selective healing of nanotube defects and yield from C_{70} peapod samples. The growth of very small diameter inner tubes from C_{70} peapods is demonstrated, which challenges the models of inner nanotube formation. An anomalous absence of mid-diameter inner tubes is explained by the suppressed amount of C_{70} peapods in the transition region between standing and lying C_{70} configurations.

5.1 Introduction

Nanostructures based on carbon nanotubes [1] have been in the forefront of nanomaterial research in the last decade. However, there still remains a number of open questions before one of the most promising candidates, single-wall carbon nanotubes (SWCNTs) will have wide-spread applications. The major obstacle is the large number of electronically different nanotubes produced with varying diameters and chiralities [2]. Directed growth or separation efforts are hindered by the lack of accurate chiral vector identification methods in bulk samples. In addition, little is known about chirality and diameter sensitive reactions. Band-gap fluorescence was successfully applied to assign chiral indices to semiconducting SWCNTs [3]. Similarly, assignment of small diameter nanotubes to chiral vectors was performed in double-wall carbon nanotubes (DWCNTs) using Raman spectroscopy [4, 5]. DWCNTs are SWCNTs containing a coaxial, smaller diameter CNT. The material is produced from fullerenes encapsulated in SWCNT (peapods [6]), by a high temperature treatment [7]. The growth process in such systems is of fundamental interest, since it proceeds without catalytic particle support.

The growth process of DWCNTs from fullerene peapods is not yet understood. Computer simulations have suggested that C_{60}@SWCNT based DWCNTs are formed by Stone-Wales transformations from C_{60} dimer precursors at high temperature by cyclo-addition [8, 9]. The free rotation of C_{60} molecules is a prerequisite for the dimer formation as it enables the molecules to have facing double bonds. The ellipsoidal shaped C_{70} were found to be present in both standing or lying configurations i.e. with the longer C_{70} axis perpendicular or parallel to the tube axis [10, 11].

At a first glance, the above mentioned assignment by Raman spectroscopy of the inner tubes in DWCNTs is not applicable to study properties of the outer tubes. However, we show in this report that assignment of chiralities to the inner tubes of DWCNTs is a new and so far unique tool for a diameter selective or even chirality selective analysis of the outer tube reactions. This possibility originates from the correlation between inner and outer tube abundances and from the robustness of this correlation against the different types of SWCNTs used for the inner tube growth. Due to the larger spectral splitting and narrower linewidths of the inner tube radial breathing modes [4], the inner tube diameter distribution can be characterized with a spectral resolution that is about 40 times larger as compared to the analysis on the outer tubes. Thus, the analysis of the inner tubes allows the characterization of diameter selective reactions in the starting material with an unprecedented accuracy. The method is demonstrated on the diameter selective healing of the SWCNT openings. A dramatic exception in the equivalency of the C_{60} and C_{70} grown tubes is also presented for the $d \approx 0.67$ nm inner nanotubes for which the corresponding outer tubes are on the border between lying and standing C_{70} configurations.

5.2 Experimental details

C_{60} and C_{70} based DWCNTs (60-DWCNT and 70-DWCNT, respectively) were prepared from two arc-discharge grown commercial SWCNTs (SWCNT-N1 and N2 from Nanocarblab, Russia) and two laser ablation grown tubes. From the latter, one was commercial (SWCNT-R from Tubes@Rice, Houston, USA) and the other was laboratory prepared (SWCNT-L). The SWCNT-N1, N2 materials were purified to 50 % by the manufacturer. SWCNT-R and SWCNT-L materials were purified following Ref. [12]. Peapod samples were prepared by annealing SWCNT with C_{60} in a quartz tube following Ref. [12] and were transformed to DWCNT at high temperature following Ref. [7]. The diameter distributions of the SWCNT materials were determined from Raman spectroscopy [13] giving $d_{\mathrm{N1}} = 1.50$ nm, $\sigma_{\mathrm{N1}} = 0.10$ nm, $d_{\mathrm{N2}} = 1.45$ nm, $\sigma_{\mathrm{N1}} = 0.10$ nm, $d_{\mathrm{R}} = 1.35$ nm, $\sigma_{\mathrm{R}} = 0.09$ nm, and $d_{\mathrm{L}} = 1.39$ nm, $\sigma_{\mathrm{L}} = 0.09$ nm for the mean diameters and the variances of the distributions, respectively. The results described here were observed for all samples. Multi frequency Raman spectroscopy was performed on a Dilor xy triple axis spectrometer in the 1.64-2.54 eV (755-488 nm) energy range and in a Bruker FT-Raman spectrometer for the 1.16 eV (1064 nm) excitation at 90 K. The spectral resolution was 1-2 cm^{-1} depending on the laser

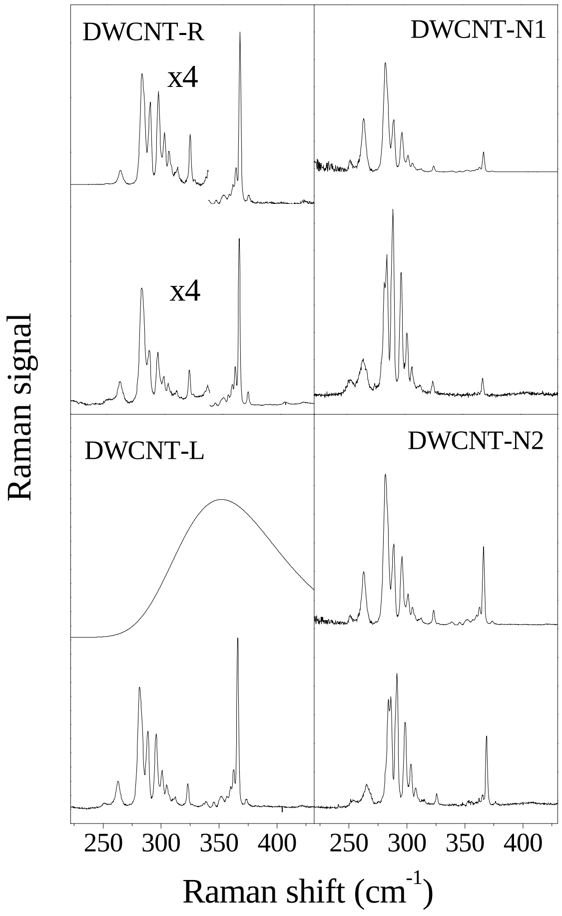

FIGURE 5.1. As measured Raman spectra of the inner nanotube RBMs for four 60-DWCNT samples (lower curves in each quarter) at λ=647 nm laser excitation. The upper spectra are smart scaled from the lower left spectrum. The Gaussian diameter distribution is shown for the DWCNT-L sample.

wavelength. Raman shifts were calibrated against a series of spectral calibration lamps.

5.3 Experimental results and discussion

In Fig. 5.1., we compare Raman spectra of the different 60-DWCNT materials for the 647 nm excitation. The spectra are representative for excitations with other laser energies and represent the response from the radial breathing mode (RBM) of inner tubes. The RBMs of all the observable inner tubes, including the split components [4], can be found at the same position in all DWCNT samples within the ± 0.5 cm^{-1} experimental precision of our measurement for the whole laser energy range studied here. This proves that vibrational modes of DWCNT samples are robust against the starting material.

As the four samples have different diameter distributions, the overall Raman patterns look different. However, scaling the patterns with the ratio of the distribution functions (smart scaling) allows to generate the overall pattern for all systems, starting from e.g. DWCNT-L in the bottom-left corner of Fig. 5.1. It was assumed that the inner tube diameter distributions follow a Gaussian function with a mean diameter 0.72 nm smaller than those of the outer tubes [14] and with the same variance as the outer tubes. We used the empirical constants from Ref. [5] for the RBM mode Raman shift versus inner tube diameter expression. The corresponding Gaussian diameter distribution of inner tubes is shown for the DWCNT-L sample in Fig. 5.1. We observe a good agreement between the experimental and simulated patterns for the DWCNT-R sample. A somewhat less accurate agreement is observed for the DWCNT-N1, N2 samples, which may be related to the different growth method: arc discharge for the latter, as compared to laser ablation for the R and L samples. The observed agreement has important consequences for the understanding of the inner tube properties. As a result of the photoselectivity of the Raman

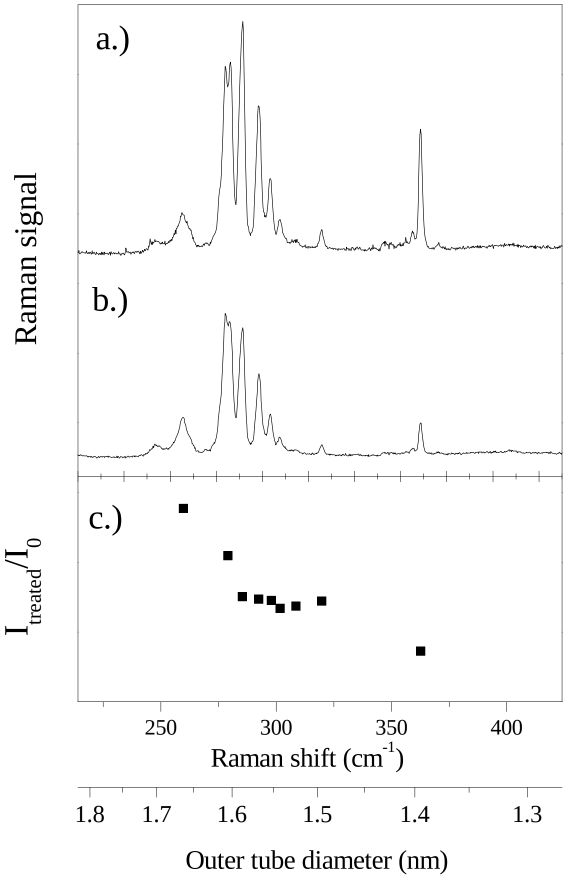

FIGURE 5.2. Raman spectra of untreated tubes (a), tubes heated at 800 °C prior to filling (b), and ratio of the inner tube signal intensity for the heat treated ($I_{treated}$) and the untreated material (I_0) (c). The lowest scale shows the diameters of the corresponding outer tubes.

experiment, it proves that the electronic structure of the inner tubes is identical in the different starting SWCNT materials.

The RBM frequencies of neighboring inner tubes are on the average four times more separated from each other than those of the outer ones [5]. In addition, the outer tube RBMs have a typical FWHM of 5-10 cm^{-1} [15] as compared to the FWHM of the inner tube RBMs of 0.5 cm^{-1} [4]. As a result, the available spectral resolution is at least 40 times larger when the RBMs of the inner tubes are investigated. This allows to study chirality or at least diameter selective reactions of the outer tubes by analyzing the inner tube response.

In Fig. 5.2., we show the Raman spectra of the 60-DWCNT-N2 heat treated at 800 °C in dynamic vacuum for 40 minutes prior to the C_{60} encapsulation and DWCNT transformation as compared to an untreated sample. The spectra are normalized by the amplitude of the corresponding outer tubes. The weaker response at higher Raman shifted lines, i.e. inner tubes with smaller diameters is apparent in Fig. 5.2b. and is shown quantitatively in Fig. 5.2c. The result is evidence for an annealing induced closing of the outer tubes with small diameters, which prevents the C_{60} encapsulation. It relates to the higher reactivity for healing of openings in small diameter SWCNTs, which provide the host for the narrower inner tubes. To exclude other effects, such as coalescence observed at similar temperatures under intensive electron radiation [16], we checked that the full inner tube signal can be obtained for samples subject to a 30 minute long 500 °C oxidation treatment in air (re-opening) after the vacuum annealing. Although, the overall healing effect and the more rapid closing of smaller nanotubes has been long anticipated, to our knowledge this is the first example when it is observed with an individual tube sensitivity. The technique allows a quantitative determination of the healing speed of the different SWCNTs.

Fig. 5.3. compares the Raman spectra of 60- and 70-DWCNT-R for some representative laser energies. The RBMs of all the observable inner tubes, including the split components, can be found at the same position for all the 60-DWCNT and 70-DWCNT samples within our experimental precision. This reinforces the previous finding that the inner tube formation is robust against the

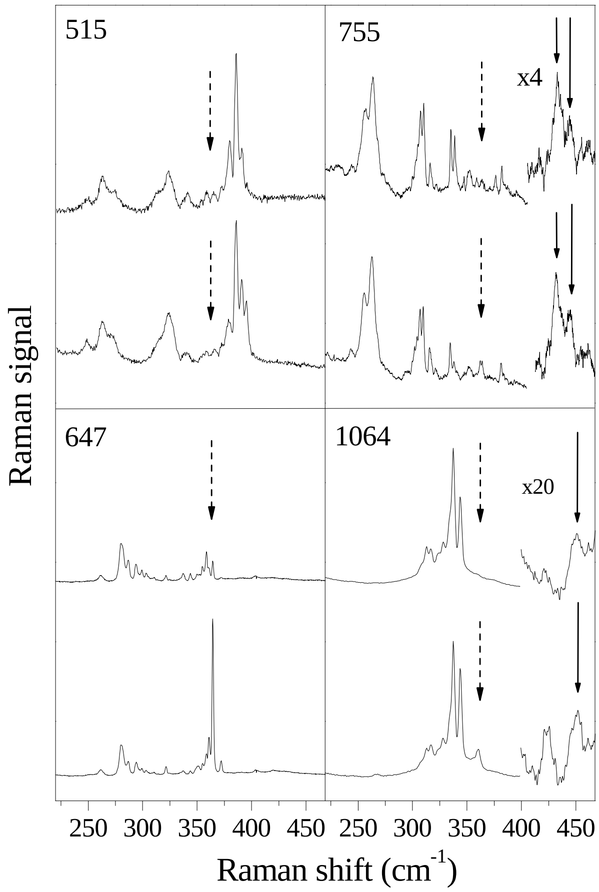

FIGURE 5.3. Comparison of the Raman spectra of 60-DWCNT-R (lower spectra) and 70-DWCNT-R (upper spectra) for λ=515, 647, 755, and 1064 nm, respectively. Solid arrows indicate the (7,5) and (5,3) nanotubes in the 755 nm spectra and the (4,4) nanotube on the 1064 spectra. Dashed arrows mark the vicinity of the 362±3 cm^{-1} spectral range.

starting SWCNT material or fullerene. The spectra shown in Fig. 5.3. are pair-wise normalized by the intensity of a selected inner tube from the 300-340 cm^{-1} spectral range.

The observation of the very small inner tubes, with Raman shifts ranging up to 450 cm^{-1} for 70-DWCNTs is important. The smallest observable inner tubes for 60-SWCNT were found to be [4] the (7,0), (5,3), (4,4) and (6,1) with diameters of 0.553, 0.553, 0.547, and 0.519 nm, respectively [5]. As indicated by solid arrows in Fig. 5.3., we clearly observe the (7,0), (5,3) and (4,4) for the 70-DWCNT-R sample with intensities similar as in 60-DWCNT. The identification of the (6,1) tube is less certain as it appears with very small intensity already for the 60-DWCNT sample in the previous report [4].

Using the experimentally determined 0.72 nm inner and outer tube diameter difference [14], the cut-off of the inner tube distribution at the (6,1) tube for 60-DWCNT can be related to the smallest outer tube with $d_{\text{cut-off, C}_{60}} \approx 1.239$ nm where C_{60} can enter. This value is in reasonable agreement with theoretical estimates where $d_{\text{cut-off, C}_{60}} \approx 1.2$ nm was found for the smallest tube diameter where C_{60} peapod formation is energetically favored [17–19]. Similarly, the energetics of the C_{70} encapsulation was calculated and $d_{\text{critical}} \approx 1.35$ nm was found for the SWCNT diameter which separates the standing and lying configurations [20]. Based on this value, inner tubes with $d \lesssim 0.63$ nm can only be formed from C_{70} peapods in the lying configuration. The diameter of the above mentioned and arrow-indicated tubes in Fig. 5.3. are all well below this value. Thus, the smallest observed inner tubes for the 70-DWCNT are made nominally from lying C_{70} peapod molecules.

The above result has important implications on the theoretical models of the inner tube formation. It has been suggested that the route to inner tube growth is the formation of cyclo-additionally bonded precursor C_{60} dimers [8, 9]. Once the dimers are formed, Stone-Wales transformations proceed till the completely formed inner tubes are developed. As cyclo-addition needs facing parallel double bonds, the lying C_{70} molecules are geometrically hindered to establish this reaction due to the facing pentagons [21]. Therefore, a different process must be anticipated for

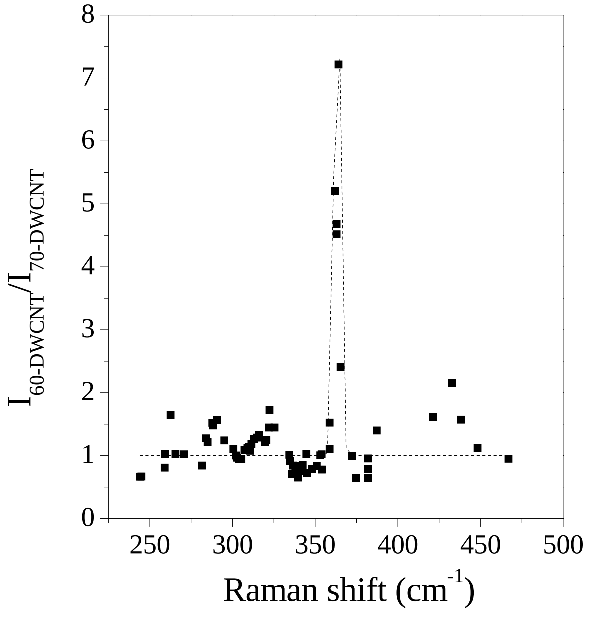

FIGURE 5.4. Normalized intensity ratios of the Raman RBM modes of inner tubes in 60-, and 70-DWCNT-R materials at all laser lines studied. The data are sliding averaged as explained in the text. The dashed curve is guide to the eye.

the formation of very small diameter inner tubes. This means the theory of inner tube formation requires revision. As an alternative possibility for the formation of inner tubes, a complete decay of the fullerenes into e.g. C_2 units may take place. In this case the particular geometry of the given fullerene does not play a role.

In what follows, an anomalous behavior observed for 70-DWCNTs with $d_{\text{outer}} \approx d_{\text{critical}}$ is discussed. The dashed arrows in Fig. 5.3. mark the vicinity of the 363±3 cm^{-1} Raman shifted RBMs which were previously identified to originate from the (5,5) metallic (d = 0.68 nm) and the (8,1) semiconducting (d = 0.671 nm) inner tubes along with their split components [4, 5]. For the 647 nm excitation an unusual and unexpected behavior is observed. Within the Raman shift range indicated by the dashed arrows, some inner tube RBM components are significantly weaker for the 70-DWCNT samples as compared to the 60-DWCNT samples. This is consistent with the results of the 755 and 1064 nm excitations where weaker RBM modes are observed for the 70-DWCNT-R sample. The spectra recorded for 515 nm excitation did not exhibit a relevant signal in the Raman shift region under discussion [4]. The same anomalous behavior was observed for 70-DWCNT samples prepared from other SWCNT materials.

To quantify this effect, we compared the intensity ratio of the inner tube RBMs in 60-, and 70-DWCNTs for all measured laser lines and for all observed tubes. Voigtian lines were fitted to the observed spectra with a Gaussian width determined by the spectrometer response to the elastically scattered light and with a Lorentzian line-width of the corresponding RBM mode. As discussed above, we chose a particular tube in the 300-340 cm^{-1} spectral range to normalize the observed inner tube RBM intensities before dividing the so-obtained values for the 60-, and 70-DWCNT by each other. Data points were collected for the RBM from each tube for excitations with 8 different lasers and smoothed with a 3-point sliding averaging. This procedure reduces the noise of the intensity ratio and makes a data point more reliable when the same tube is observed at different laser energies. The result is summarized in Fig. 5.4. The anomaly of the intensity ratio is clearly observed in the 363±3 cm^{-1} spectral range. This spectral range corresponds to inner tubes with $d_{\text{inner}} \approx 0.67$ nm and $d_{\text{outer}} \approx 1.39$ nm. As the latter value is close to the critical diameter, it is tempting to associate the anomaly with the competition between the two configurations. In this case the critical diameter to allow for standing C_{70} encapsulates is refined by the experiment to 1.39 nm. We discuss two possible origins of the missing inner tubes: i) inability to form inner tubes from peapods filled with mixed lying and standing C_{70} configurations, ii) inability of C_{70} to enter into SWCNTs with $d_{\text{outer}} \approx d_{\text{critical}}$. Concerning the first case, SWCNTs with $d_{\text{outer}} \approx d_{\text{critical}}$ can be filled with mixed lying and standing C_{70} molecules, which makes a cyclo-addition reaction difficult. However, we have shown that inner tubes are also formed from lying C_{70} molecules alone, which disfavors the idea that the precursor dimer is indeed necessary for the inner tube formation. Thus, it is argued that the absence of inner tubes when $d_{\text{outer}} \approx d_{\text{critical}}$ is rather caused by the absence of C_{70} molecules for peapods with this diameter.

A mechanism involving impurities or side-wall defects can explain the observation: for the critical outer tube diameter one can expect that for a perfect tube the lying configuration is preferred. However, when side-wall defects or impurities are present, a C_{70} may change its configuration to a standing geometry that would immobilize it thus preventing other C_{70} from entering the tube. Alternatively, a C_{70} molecule entering at the critical diameter may get trapped at a tube defect as e.g. a bend or kink and thus prevents further filling. The diameter selective filling may provide a way to mass-separate the unfilled and filled C_{70} peapod tubes. Interestingly, the outer tubes which remain unfilled are close to the well studied (10,10) tube.

5.4 Conclusions

In conclusion, DWCNT formation from peapods enables the study of diameter selective phenomena in SWCNT materials. The method provides a new and accurate tool for the characterization of controlled nanotube growth and the effects of subsequent treatments or diameter selective separation. The diameter selective closing of tube openings was observed for the first time. Comparison of C_{60}, C_{70} peapod based DWCNTs proves that the inner tube formation is a conservative process against the starting SWCNT or fullerene material. The presence of very small inner nanotubes in 70-DWCNT presents a challenge to the current theoretical models. The absence of mid-diameter inner tubes in 70-DWCNT is explained by the absence of C_{70} peapods for the corresponding nanotube diameter due to the borderline between the lying and standing C_{70} configurations.

Acknowledgement: Support from the FWF Nr. 14893, the EU NANOTEMP BIN2-2001-00580 and PATONN MEIF-CT-2003-501099 grants, the Hungarian State Grant OTKA F46361, and from the Industrial Technology Research Grant Program in '03 from the NEDO of Japan are acknowledged. Á. K. acknowledges support from the AMFK foundation in the framework of the Zoltán Magyary programme.

References

[1] S. Iijima, Nature **354**, 56 (1991).

[2] R. Saito, G. Dresselhaus, and M. Dresselhaus, *Physical Properties of Carbon Nanotubes* (Imperial College Press, 1998).

[3] S. M. Bachilo, M. S. Strano, C. Kittrell, R. H. Hauge, R. E. Smalley, and R. B. Weisman, Science **298**, 2361 (2002).

[4] R. Pfeiffer, H. Kuzmany, C. Kramberger, C. Schaman, T. Pichler, H. Kataura, Y. Achiba, J. Kürti, and V. Zólyomi, Phys. Rev. Lett. **90**, 225501 (2003).

[5] C. Kramberger, R. Pfeiffer, H. Kuzmany, V. Zólyomi, and J. Kürti, Phys. Rev. B **68**, 235404 (2003).

[6] B. W. Smith, M. Monthioux, and D. E. Luzzi, Nature **396**, 323 (1998).

[7] S. Bandow, M. Takizawa, K. Hirahara, M. Yudasaka, and S. Iijima, Chem. Phys. Lett. **337**, 48 (2001).

[8] S. W. Han, M. Yoon, S. Berber, N. Park, E. Osawa, J. Ihm, and D. Tománek, Phys. Rev. B **70**, 113402 (2004).

[9] Y. Zhao, B. I. Yakobson, and R. E. Smalley, Phys. Rev. Lett. **88**, 185501 (2002).

[10] K. Hirahara, K. Bandow, S. Suenaga, H. Kato, T. Okazaki, T. Shinohara, and S. Iijima, Phys. Rev. B **64**, 115420 (2001).

[11] H. Kataura, Y. Maniwa, M. Abe, A. Fujiwara, T. Kodama, K. Kikuchi, J. Imahori, Y. Misaki, S. Suzuki, and Y. Achiba, Appl. Phys. A **74**, 349 (2002).

[12] H. Kataura, Y. Maniwa, T. Kodama, K. Kikuchi, K. Hirahara, K. Suenaga, S. Iijima, S. Suzuki, Y. Achiba, and W. Krätschmer, Synthetic Met. **121**, 1195 (2001).

[13] H. Kuzmany, W. Plank, M. Hulman, C. Kramberger, A. Grüneis, T. Pichler, H. Peterlik, H. Kataura, and Y. Achiba, Eur. Phys. J. B **22**, 307 (2001).

[14] M. Abe, H. Kataura, H. Kira, T. Kodama, S. Suzuki, Y. Achiba, K.-i. Kato, M. Takata, A. Fujiwara, K. Matsuda, et al., Phys. Rev. B **68**, 041405(R) (2003).

[15] A. Jorio, R. Saito, J. H. Hafner, C. M. Lieber, M. Hunter, T. McClure, G. Dresselhaus, and M. S. Dresselhaus, Phys. Rev. Lett. **86**, 1118 (2001).

[16] M. Terrones, H. Terrones, F. Banhart, J. C. Charlier, and P. M. Ajayan, Phys. Rev. B **288**, 1226 (2000).

[17] M. Melle-Franco, H. Kuzmany, and F. Zerbetto, J. Phys. Chem. B **109**, 6986 (2003).

[18] S. Berber, Y.-K. Kwon, and D. Tománek, Phys. Rev. Lett. **88**, 185502 (2002).

[19] M. Otani, S. Okada, and A. Oshiyama, Phys. Rev. B **68**, 125424 (2003).

[20] S. Okada, M. Otani, and A. Oshiyama, New J. Phys. **5**, 122 (2003).

[21] M. Dresselhaus, G. Dresselhaus, and P. C. Ecklund, *Science of Fullerenes and Carbon Nanotubes* (Academic Press, 1996).

6

Reversible Hole Engineering for Single Wall Carbon Nanotubes

F. Hasi, F. Simon, and H. Kuzmany

J. Nanoscience and Nanotechnology **5**, *1785 (2005).*

ABSTRACT Experimental results are provided for reversible generation of holes on single wall carbon nanotubes and their closing by temperature treatment. The generation of the holes was analyzed by checking the amount of C_{60} fullerenes that can be filled into the tubes and subsequently transformed to an inner-shell tube. The concentration of the latter was determined from the Raman response of the radial breathing mode. The tube opening process was performed by exposure of the tubes to air at elevated temperatures. This process was found to be independent from the tube diameters. In contrast, the tube closing process was found to depend strongly of the tube diameter. For large diameter tubes ($d = 1.8$ nm) the activation energy was 1.7 eV whereas for the small diameter tubes this energy was only 0.33 eV. Optimum conditions for tube closing were found to be one hour at 800 °C or 10 minutes at 1000 °C. From the almost identical Raman spectra for the tubes before and after engineering, a predominant generation of the holes at the tube ends is concluded.

6.1 Introduction

The inside of carbon cages has been attracting the interest of chemists and physicists ever since the discovery of the fullerenes in 1985 by H. Kroto *et al.* [1]. To develop an endohedral or concave chemistry was one of the dreams of the scientists in the early days of fullerene research. New materials and new chemical reactions, which do not exist outside the cages, were expected to be discovered. It was indeed demonstrated in a large number of experiments that atoms or even groups of atoms can be encaged into the fullerenes [2–4] and revealed so far unobserved systems. However, a reversible opening, filling and re-closing of the cages was not possible. Only very recently such a process was demonstrated to operate for the filling of a fullerene cage with hydrogen atoms [5]. In contrast to this, filling of carbon nanotubes had been demonstrated already in 1994 [6] shortly after the discovery of the tubes [7]. At that time, filling of multi-wall carbon nanotubes was studied in some detail. Since the inner diameter of such tubes is rather large, of the order of 10 to 20 nm, fillers such as lead or iron was expected and was observed to behave almost like bulk material. The situation changed when Smith et al. discovered the filling of single wall carbon nanotubes (SWCNTs) with C_{60} fullerenes [8] by electron beam irradiation. The resulting structures were called peapods. Shortly later it was reported by several groups that different types of fullerenes, including higher fullerenes or endohedral fullerenes can be filled into the SWCNTs [9–11] if the tubes were treated in a special way in order to generate holes in the side walls or to open the caps of the tubes. The filling of the SWCNTs attracted considerable attention, since the inner diameter of the tubes is at least an order of magnitude smaller than the inner diameter of the multi-wall tubes and reaches values where quantum confinement becomes noticeable. Also, the highly shielded inside of the tubes were demonstrated to provide clean room conditions where highly defect free material can be grown [12]. Special recipes were reported for efficient filling but it turned out that any cleaning of the as grown tube material by chemical etching allows for filling with fullerenes or other inorganic or organic material. Attractive forces between the fullerenes and the inside of the cages were considered as the driving mechanism for the filling process. However, details of the filling mechanism remained not understood so far. Model calculations were able to demonstrate that the fullerenes can enter the tubes through holes in the side walls [13] but filling from the tube ends seems also possible, and even more likely, since after the etching procedure there are natural holes of large enough size.

The filling process was reported to be less efficient if the tubes were annealed at moderate temperatures before the filling procedure, at least as far as filling with fullerenes is concerned. Partial or complete closing of the holes was considered as the reason for such behavior. Since the growth of nanomaterials within the one-dimensional nanospace inside the tubes is of fundamental interest, we report in this paper on a detailed study of the opening and closing processes for the SWCNTs. To do this, we make use of another interesting property of the fullerenes inside the tubes. At rather high temperatures of the order of 1400 K the fullerenes can be fused to a second tube, inside the master tube [14, 15]. These inner tubes exhibit an unusual strong Raman spectrum for the radial breathing mode [12] and therefore serve as a very sensitive probe of whether the filling was successful or not [16]. The inner shell tubes are interesting by themselves as they have a very small diameter of the order of 0.7 nm, which implies rather strong deviation of structural and electronic properties from a flat graphene sheet. Applying the analytical technique of C_{60} transformation we found critical temperatures where tubes with holes generated from a chemical treatment start to close. Such temperatures were found to depend on the diameter of the tubes. Small diameter tubes close first with a much lower thermal activation. In contrast, the opening of the tubes occurs with only a weak dependence on the diameter. Reversible closing and reopening is demonstrated.

6.2 Experimental Details

SWCNTs were purchased from Med Chem Labs with a nominal diameter of 1.4 nm and a purity of 50 %. Raman analysis revealed a Gaussian diameter distribution with peak value and width (variance) of 1.45 nm and 0.1 nm, respectively. The tubes could be filled with c fullerenes as purchased by tempering them at 600 °C in a sealed and evacuated quartz tube for two hours together with excess amounts of C_{60}. Outside fullerenes were removed by dynamic vacuum annealing at 800 °C. This filling procedure was used throughout in the work presented here and will be called standardized filling in the following. After filling, the C_{60} could be detected inside the tubes by Raman scattering and high-resolution transmission electron microscopy. However, neither technique allows for a diameter selective detection of the filling process. In order to obtain information on the latter, the peapods were transformed to double wall carbon nanotubes by tempering in high vacuum at 1250 °C for two hours and subsequent slow cooling in the furnace. This procedure of inner shell tube growth from the peapods was used throughout in this work and will be assigned as standardized transformation in the following. The transformed material was then checked by Raman spectroscopy in the range of the radial breathing mode (RBM) for double wall carbon nanotubes (DWCNTs). Since the Raman response in the diameter range of the inner shell tubes is highly diameter selective, this yields diameter selective information on the filling process.

All Raman experiments were carried out at liquid nitrogen temperature with a Dilor xy triple spectrometer in the normal resolution mode, unless indicated otherwise. Detection of scattered light was performed with a blue enhanced and back-thinned CCD chip. For the excitation various laser lines were used in the red and yellow spectral range. Scattering intensities were evaluated as peak intensities of the Raman lines.

Annealing of as purchased or opened tubes was performed at various temperatures between 800 °C and 1200 °C in a sealed and evacuated quartz tube at a rest gas pressure of 10^{-6} mbar. Opening of the tubes was performed by exposure to air at various temperatures between 350 °C and 500 °C.

6.3 Results and Discussion

Figure 6.1 depicts the Raman spectrum of DWCNTs in the spectral range of the RBM as obtained from a filling of pristine tubes and standardized transformation. The broad and only weakly structured line around 180 cm^{-1} represents the response from the outer tubes. The group of narrow lines extending from 250 cm^{-1} to 400 cm^{-1} originates from the RBM of the inner shell tubes. According to our present understanding, each peak represents one tube or at least one pair of inner and outer tubes. Due to the low spectral resolution used, the well known splitting of the lines [17] is not or only hardly resolved.

In the lower part of the figure the resulting diameter distribution is depicted on a $1/d$ scale. The narrower peak for the smaller $1/d$-values was obtained from the Raman analysis of the diameter distribution of the outer tubes. The broad peak for the larger $1/d$-values was obtained from a down scaling of the outer tube diameters by 0.7 nm which is considered as twice the relevant wall to wall distance between inner and outer tubes. The cut-off at 440 cm^{-1} (0.5 nm diameter) reflects the limiting diameter value of 1.2 nm below which outer tubes cannot be filled with C_{60} due to geometrical constraints. The relative scaling between the x-axis for the frequencies and the x-axis for the inverse diameters was obtained from the frequency to diameter scaling of the form

$$\nu_{RBM} = C_1/d + C_2 \tag{6.1}$$

where C_1 and C_2 have the values 223 cm^{-1} nm and 13 cm^{-1}, respectively. These parameters were recently obtained from a detailed analysis of resonance Raman excitations of HiPCo SWCNTs dispersed in solution [18]. The values differ slightly from previous results obtained from a pure

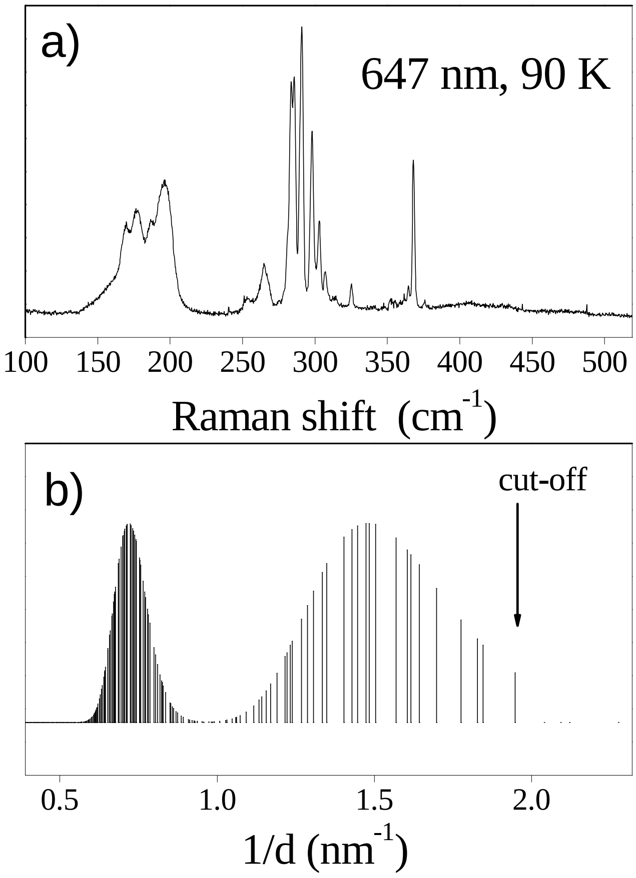

FIGURE 6.1. Raman spectrum of DWCNTs as prepared from pristine SWCNTs filled with C_{60} (a). Excitation was for 647 nm laser and 2 mW. Part (b) of the figure displays the concentration of the diameters d on a $1/d$ scale.

vibronic analysis of DWCNTs [19] but are in good agreement with parameters obtained from an analysis of optical spectra and resonance Raman spectra from HiPCo tubes [20, 21]. Note the difference of the center of gravity for the $1/d$ distribution and for the Raman line distribution for both the inner tubes and the outer tubes. This is a consequence of resonance enhanced scattering for selected tubes. Comparing the peak intensities in the spectrum and in the $1/d$ distribution yields an enhancement factor > 100.

Figure 6.2 shows the Raman response of tubes after standardized transformation conditions but different pre-treatment. Only the spectral range of the inner tube is depicted in the main part of the figure. The spectrum at the bottom is an expanded version of the spectrum in Fig. 6.1. The spectrum at the center was recorded under identical conditions but the as purchased material was pre-annealed before the standardized filling and standardized transformation. As can be seen almost no response from inner shell tubes is observed which means no fullerenes had entered the tubes. The tubes were very efficiently closed by the annealing process.

The small response just below 300 cm^{-1} could originate from some small leaks in the cage were a few C_{60} molecules or even more likely some carbon contamination had entered the primary tubes on a level which leads to less than 20 % inner tubes for the larger diameter tubes and less than 3 % for the smaller diameter tubes. Also, these tubes were not grown under clean room conditions as the width of the Raman lines is rather broad. The insert in the figure depicts the RBM response from the outer tubes before and after annealing. The two spectra are almost identical which indicates that no tube coalescence had occurred at the temperature applied. The similarity of the two spectra allows on the other hand for a convenient way of intensity calibration for the spectra recorded after various sample pre-treatments. This calibration was used throughout the work presented here if not otherwise specified. The spectrum at the top in Fig. 6.2 was recorded after reopening the annealed tubes at 500 °C on air and standard filling and transformation. As can be seen, the spectra derived from the pristine and from the reopened tubes are identical in all details. This means no dramatic damages by cutting a large number of holes into the sidewalls

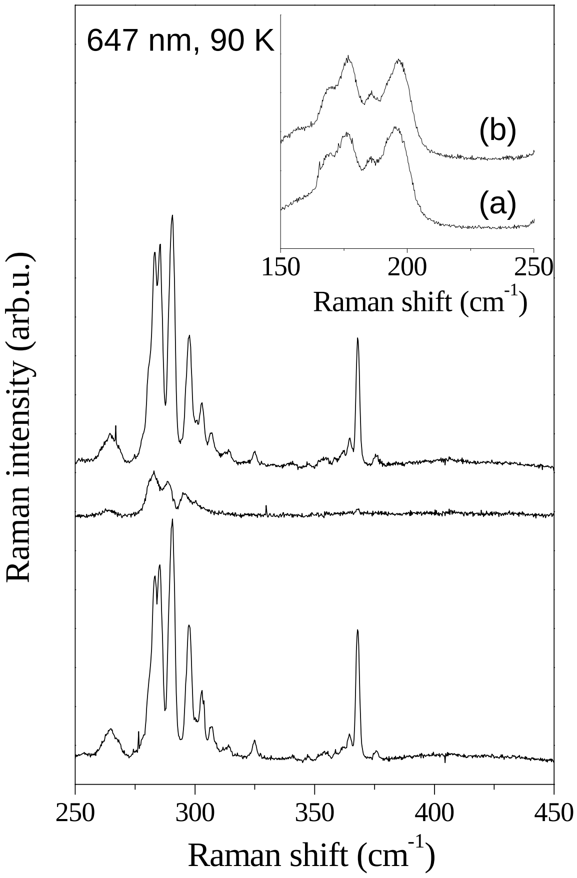

FIGURE 6.2. Raman spectra in the spectral range of the inner shell tube RBM for nanotubes after special pre-treatment. Bottom: after filling as purchased tubes with C_{60} and standard transformation; Center: after annealing the as purchased tubes at 1000 °C for two hours and standard transformation; Top: after re-opening the annealed samples, filling with C_{60}, and standard transformation. All spectra recorded at 90 K for 647 nm, 2 mW excitation, 30 minutes sampling, and normalized to the response of the outer tube RBM of the pristine tubes. Insert: the RBM of the outer tubes before (a) and after (b) annealing at 1000 °C.

have happened. Consequently, the sidewalls of the tubes remain highly untouched by the opening process. Thus, it is strongly suggested that the fullerenes enter the tubes through holes at the tube ends.

Figure 6.3 depicts some examples for the efficiency of the tube closing for various annealing conditions. All spectra were now recorded with 568 nm excitation. The top spectrum represents the pristine tubes after standard filling and standard transformation. The three spectra below depict the response of the inner tube RBM for samples which were annealed under the conditions indicated in the figure before filling and transformation. As can be seen 800 °C annealing has almost no effect on the filling for the large diameter tubes but efficiently reduces filling of the smaller tubes with RBM frequencies larger than 300 cm^{-1}.

After 20 minutes annealing, the signal at 340 cm^{-1} has reduced to 35 % of the signal of the pristine sample. This means 65 % of this particular tube species was closed by the annealing process. After 10 minutes annealing at 1200 °C only a very small response from the inner shell tubes (less than 10 % at 310 cm^{-1}) is left which again may be interpreted as the response from a small fraction of carbon atoms entering the tubes during the annealing process.

The dependence of tube closing on annealing temperature and time was studied in more detail. Spectra for the RBM response were recorded for standard filling and standard transformation after various annealing temperatures and annealing times. The most important lines were evaluated with respect to their peak intensity. This intensity was related to the peak intensity of inner shell modes of DWCNTs grown from untreated starting material. This ratio is a quantitative measure for the fraction of tubes which remain open after the annealing procedure. Results are depicted in Fig. 6.3 for annealing at 800 °C (1073 K), 1000 °C (1273 K) and 1200 °C (1473 K). A dramatic decrease of concentration for tubes remaining open after the annealing treatment is immediately recognized on Fig. 6.3 with decreasing tube diameter (increasing RBM frequency).

For tubes with 1.8 nm diameter (240 cm^{-1}) 98 % remain open for a 20 min annealing at 800 °C whereas for the same annealing conditions and tubes with 1.3 nm diameter (345 cm^{-1}) only 15

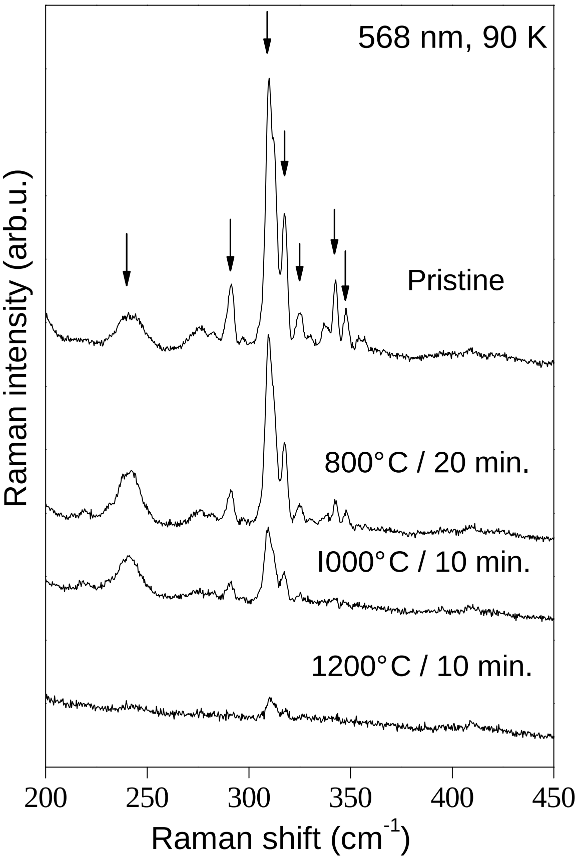

FIGURE 6.3. Raman response of the inner tube RBM of the untreated and standardized filled and transformed tube material (top) and after various annealing treatments as indicated before the filling and transformation processes. All spectra recorded at 90 K for 568 nm, 2 mW excitation, 30 minutes sampling, and normalized to the response of the outer tube RBM of the pristine tubes. The arrows assign Raman peaks which were used for a detailed analysis shown in Fig. 6.3

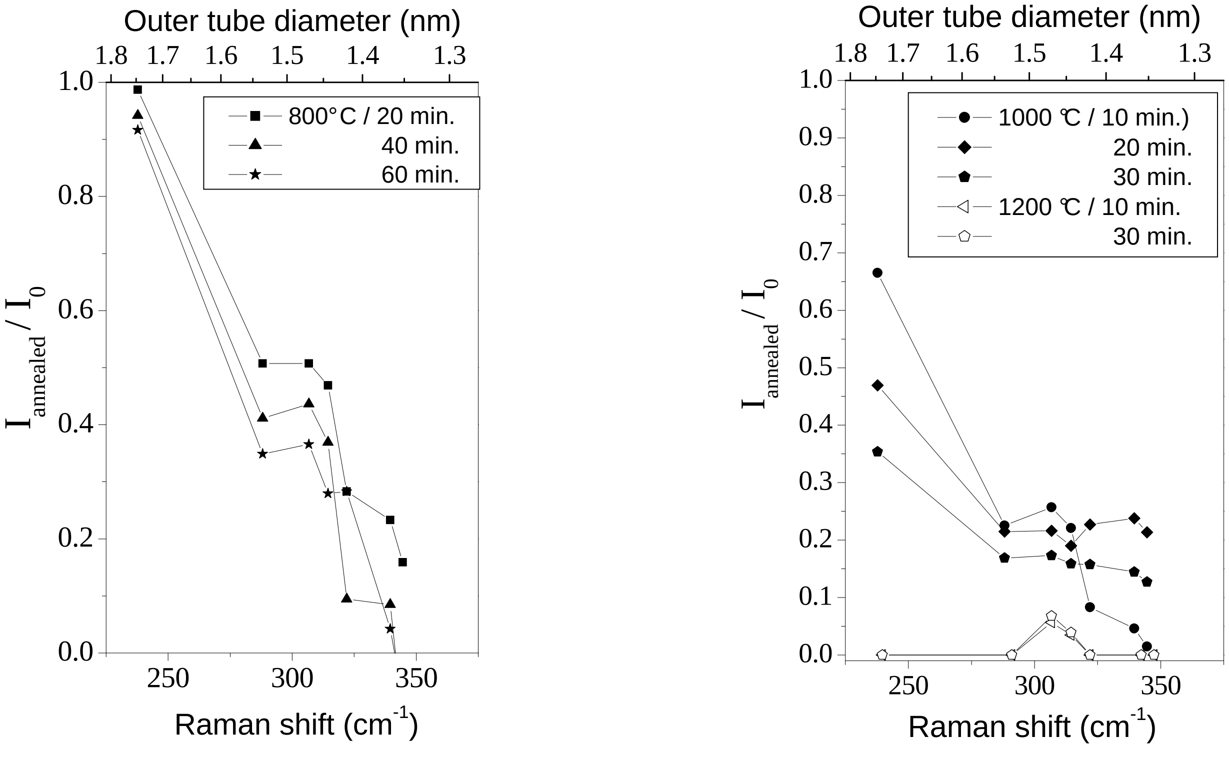

FIGURE 6.4. Relative intensities I_{annealed}/I_0 of RBM Raman lines of the inner tubes versus frequency (tube diameter) after various annealing conditions as indicated in the inserted legend. All spectra were recorded and normalized as in Fig. 3. The scale below the main figures gives tube diameters from Eq. 6.1.

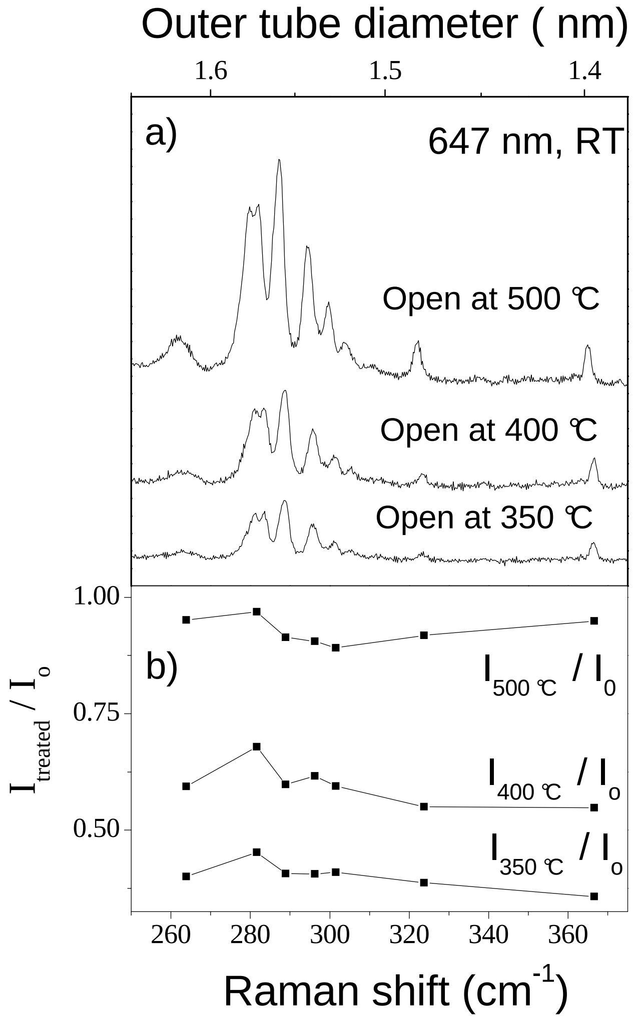

FIGURE 6.5. Raman response of the RBM of inner shell CNTs for standard filling and transformation procedures after the pristine tubes had been closed and reopened at temperatures indicated (a). Part (b) depicts evaluated relative intensities versus Raman shift for the three different opening conditions. I0 is the intensity for the pristine tubes after standard filling and transformation. The scale below the mainfigure provides tube diameters from Eq. 6.1. All spectra recorded at RT for 647 nm, 2 mW excitation,30 minutes sampling, and normalized to the response of the outer tube RBM of the pristine tubes.

% remain open. A similar dramatic dependence of the tube closing on the tube diameter can be recognized for annealing at 1000 °C even though in this case after 10 minutes the concentration of open tubes has already decreased to 67 % even for the largest diameter tubes studied. From the smallest diameter tubes analyzed only 2 % remain open under these conditions. The strong temperature dependence of the tube closing process can be recognized from the behavior of the large diameter tubes. For the species with 240 cm^{-1} RBM the values are 98 % and 47 % after 20 minutes annealing at 800 °C and 1000 °C, respectively. This indicates a strong thermal activation of the closing process. The closing as a function of annealing time can also be deduced from the figure. With increasing annealing time, the process of tube closing proceeds but slows down as annealing time increases. This is particularly obvious for annealing at 1000 °C. Interestingly, for annealing at 800 °C the intensity ratios for the different annealing times always decrease with annealing time throughout the frequency range studied, with some noise at high frequencies. This is not so for annealing at 1000 °C. Here the annealing isotherms recorded for different annealing times cross as a function of RBM frequency (tube diameter). As a consequence, short time annealing is more efficient for the narrow diameter tubes than long time annealing. For example for 1000 °C annealing the fraction of tubes with 345 cm^{-1} RBM that remain open after 10 min, 20 min, and 30 min are 2 %, 22 %, and 14 %, respectively.

For 1200 °C annealing any response from inner shell RBM for very large and very small tubes remains below the detection limit which is of the order of 1 %. Only in the intermediate diameter range a very small and annealing time independent signal from inner shell tubes could be detected.

Finally, the analytical technique developed here can also be used to study the diameter selective tube opening process. Figure 6.5 depicts Raman spectra of the RBM recorded for 647 nm excitation for tubes which were closed at 1000 °C for two hours and then reopened by exposure to air at temperatures indicated.

As an overall result, the opening process becomes less and less efficient with decreasing temperature. However, the reduction in efficiency is hardly depending on the tube diameter. The latter behavior is more evidently seen from an analysis of the response for the individual peaks as depicted in part (b) of Fig. 6.5. For opening at 500 °C 95 % of the closed tubes could be reopened, nominally independent of tube diameter. For opening at 400 °C only about 60 % of the tubes could be opened. Surprisingly, as plotted this fraction is even slightly decreasing with decreasing tube diameter. Similarly, for opening at 350 °C only 45 % of the tubes could be opened again, with a slight decrease of this fraction for small diameter tubes.

The analytical technique used here anticipates that the Raman intensity for the RBM of a particular inner shell tube equals the concentration of the tube in the sample. This is justified, since for each measurement exactly the same resonance conditions and spectrometer sensitivity hold and all spectra are normalized to the RBM response of the outer shell tube.

Concerning the closing of holes which are required to allow the fullerene molecules to enter, three main results were obtained, namely: i) The closing process is thermally activated with an increasing efficiency for low diameter tubes, ii) The closing process is time dependent with saturation for long annealing times, iii) For small diameter tubes the time dependence of the effective closing is more complex.

Result iii) makes the analysis of the dynamical processes more difficult for the small diameter tubes. Thus, for the discussion of the thermal activation and for the time dependence we will concentrate on the large and medium diameter tubes. The temperature dependence of the closing process is indeed dramatic. Note that for a change in temperature of only 18 % (from 1073 K to 1273 K) the closing fraction for the tubes with a RBM at 240 cm^{-1} ($d = 1.78$ nm) after 20 minutes annealing changes by a factor of more than 25. The activation energy α for this process can be evaluated from

$$\alpha = k_B T_1 T_2 \ln[1 - I(T_1)/I(T_2)]/(T_1 - T_2) \tag{6.2}$$

where k$_B$ is the Boltzmann constant and $I(T)$ are the relative intensities from Fig. 6.3. For $T_1 = 1073K$ ($I(T_1)/I_0 = 0.98$) and $T_2 = 1273K$ ($I(T_2)/I_0 = 0.67$), we obtain $\alpha = 1.72$ eV. If we do the same analysis for a medium diameter tube, e.g. with an RBM at 285 cm^{-1} ($I(T_1)/I_0 = 0.52$, $I(T_2)/I_0 = 0.23$) the activation energy is only 0.33 eV. This value may be slightly underestimated, since for medium diameter tubes secondary processes to be discussed below start to become noticeable. For still smaller diameter tubes the activation is obviously further reduced but cannot be analyzed directly due to other competing processes. The dramatic decrease of the activation energy with tube diameter must be a consequence of tube wall or tube cap curvature and higher mobility of carbon atoms on the tube surface.

Similar to the thermal activation, the time dependence of the closing process may be described by an exponential law with a relaxation time τ obtained from

$$I(\mathrm{t})/I_0 = \exp^{-t/\tau} \tag{6.3}$$

where $I(\mathrm{t})/I_0$ is the fraction of open tubes after annealing time t. Table 6.1 lists some of the experimental results for 1000 °C annealing at 240 cm^{-1} and 305 cm^{-1}.

For the tubes with the largest diameters (1.8 nm) evaluation of the time constants for the three different annealing times reveal values in good agreement, which supports the exponential time dependence. For the averaged time constant of 26 minutes a two hour annealing at 1000 °C would leave only 1 % of the tubes open.

As expected for the smaller tubes with $d = 1.45$ nm (RBM at 305 cm^{-1}) the evaluated time constants are much shorter. The value of about 8 minutes may still be all right but for longer annealing times secondary processes obviously influence the evaluated time constant. The value of about 13 min for a 20 minutes annealing process is noticeably larger than the value for ten minutes annealing. It even increases to 17 min for 30 min annealing. Therefore the latter values

TABLE 6.1. Experimental data and relaxation time τ for the tube closing process at 1273 K and two selected tube diameters. The concentrations for open and closed tubes after 120 min (1.8 nm diameter) and 60 min (1.45 nm diameter) annealing is as calculated for 26 and 8 min time constants, T, respectively.

d [nm]/ RBM [cm^{-1}]	Annealing [min]	Open tubes [%]	Closed tubes [%]	T [min]
1.8/ 240	10	0.67	0.33	25
	20	0.47	0.53	26
	30	0.35	0.65	28
	120	0.01	0.99	Calc. for $\tau = 26$
1.45/ 305	10	0.26	0.72	7.5
	20	0.22	0.78	13.2
	30	0.17	0.83	17
	60	$5 \cdot 10^{-4}$	~ 1	Calc. for $\tau = 8$

should not be considered as intrinsic for the tube closing process. The much shorter time constants for the closing of the smaller diameter tubes is again a consequence of the higher tube curvature and consistent with the lower activation energy.

The increase of the time constant for tube opening or eventually the crossing of the annealing isotherms for different annealing times is surprising. One possibility to describe such a behavior is by proposing two processes with complimentary effects on the hole-concentration in the tubes. One process is responsible for the hole-closing and the other with a considerably larger time constant generates holes into the tube walls or tube caps. Then, only for long time annealing the opening process becomes relevant. The opening process could e.g. be a very slow reaction of the tubes with rest gas concentration of oxygen in the annealing experiment. For a quantitative analysis of the behavior more detailed results are needed.

The results for the tube opening as a function of tube diameter and reaction temperature in Fig. 6.5 must be analyzed with some care. It would be very difficult to understand why small diameter tubes open less efficient than large diameter tubes as one might conclude from the low temperature (350 °C and 400 °C process temperatures) reactions depicted in Fig. 6.5. For a more realistic interpretation we can assume that the starting situation for the tube opening process is not the same for the large diameter tubes and the small diameter tubes. The former may not have closed completely by the annealing process whereas the smaller diameter tubes have. Such a behavior can be depicted form the 30 minutes annealing at 1000 °C shown in Fig. 6.3. The annealing isotherm shows that for the small diameter tubes still 15 % remain open. The effect is, however, weakened by the slow tube opening process noticeable for small diameter tubes. Even though, with the corrected starting situation at least the opening reaction at 500 °C may be more sensitive to the smaller diameter tubes. In spite of these corrections the tube opening processes are definitely much less sensitive to the tube diameter as compared to the tube closing processes. The thermodynamic background for this different behavior may be related to the fact that tube opening is a very local process whereas tube closing needs long distance carbon motion and long distance carbon rearrangements. After all for a small tube almost 50 % of the side wall or the total cap must be etched away in the opening process and at least partly replaced by the closing process.

6.4 Summary

The reaction activity of holes in SWCNTs was investigated by studying the process of filling the tubes with C_{60} fullerenes and transforming the latter to a set of small diameter inner shell tubes. A standardized process for tube opening by exposing the tubes at elevated temperatures to air and for tube filling by heating the opened tubes in C_{60} vapor was developed. The process of tube opening was found to be sensitive to temperature but highly insensitive to tube diameter. The almost identical Raman spectra for the pristine and for the opened tubes with respect to line positions, line widths and line intensities suggest that the tube walls remain highly untouched and the holes for the tube filling are concentrated at the tube ends. Tube closing can be performed to a very high degree. After such processes, only a very small amount of inner tubes can be grown, mostly in high defect areas of the tubes. In contrast to tube opening, the tube closing process is highly diameter sensitive with a strongly diameter dependent activation energy and a temperature dependent reaction time. A reversible closing and opening of the tubes was demonstrated.

6.5 Acknowledgements

This work was supported by the Fonds zur Förderung der Wissenschaftlichen Forschung in Austria, project 17345 and by the EU project PATONN Marie Curie MEIF - CT- 2003 - 501099 grants. Valuable discussions with R. Pfeiffer are gratefully acknowledged.

References

[1] H. W. Kroto, J. R. Heath, S. C. O'Brien, R. F. Curl, and R. E. Smalley, Nature **318**, 162 (1985).
[2] Y. Chai, T. Guo, C. Jin, R. E. Haufler, L. P. F. Chibante, J. Fure, L. Wang, J. M. Alford, and R. E. Smalley, J. Phys. Chem. **95**, 7564 (1991).
[3] D. S. Bethune, R. D. Johnson, J. R. Salem, M. S. de Vries, and C. S. Yannoni, Nature **363**, 123 (1993).
[4] H. Shinohara, H. Yamaguchi, N. Hayashi, H. Sato, M. Ohkohchi, Y. Ando, and Y. Saito, J. Phys. Chem. **97**, 4259 (1993).
[5] K. Komatsu, M. Murata, and Y. Murata, Science **307**, 238 (2005).
[6] C. Guerret-Piécourt, Y. Le Bouar, A. Loiseau, and H. Pascard, Nature **372**, 761 (1994).
[7] S. Iijima, Nature **354**, 56 (1991).
[8] B. W. Smith, M. Monthioux, and D. E. Luzzi, Nature **396**, 323 (1998).
[9] K. Hirahara, K. Bandow, S. Suenaga, H. Kato, T. Okazaki, H. Shinohara, and S. Iijima, Phys. Rev. B **64**, 115420 (2001).
[10] K. Hirahara, K. Suenaga, S. Bandow, H. Kato, T. Okazaki, H. Shinohara, and S. Iijima, Phys. Rev. Lett. **85**, 5384 (2000).
[11] T. Okazaki, K. Suenaga, K. Hirahara, S. Bandow, I. S., and H. Shinohara, J. Am. Chem. Soc. **123**, 9673 (2001).
[12] R. Pfeiffer, H. Kuzmany, C. Kramberger, C. Schaman, T. Pichler, H. Kataura, Y. Achiba, J. Kürti, and V. Zólyomi, Phys. Rev. Lett. **90**, 225501 (2003).
[13] S. Berber, Y.-K. Kwon, and D. Tománek, Phys. Rev. Lett. **88**, 185502 (2002).
[14] S. Bandow, M. Takizawa, K. Hirahara, M. Yudasaka, and S. Iijima, Chem. Phys. Lett. **337**, 48 (2001).
[15] F. Simon, H. Kuzmany, H. Rauf, T. Pichler, J. Bernardi, H. Peterlik, L. Korecz, F. Fülöp, and A. Jánossy, Chem. Phys. Lett. **383**, 362 (2004).
[16] F. Simon, A. Kukovecz, C. Kramberger, R. Pfeiffer, F. Hasi, H. Kuzmany, and H. Kataura, Phys. Rev. B **71**, 165439 (2005).
[17] R. Pfeiffer, C. Kramberger, F. Simon, H. Kuzmany, V. N. Popov, and H. Kataura, Eur. Phys. J. B **42**, 345 (2004).
[18] C. Fantini, A. Jorio, M. Souza, M. S. Strano, M. S. Dresselhaus, and M. A. Pimenta, Phys. Rev. Lett. **93**, 147406 (2004).
[19] C. Kramberger, R. Pfeiffer, H. Kuzmany, V. Zólyomi, and J. Kürti, Phys. Rev. B **68**, 235404 (2003).
[20] S. M. Bachilo, M. S. Strano, C. Kittrell, R. H. Hauge, R. E. Smalley, and R. B. Weisman, Science **298**, 2361 (2002).
[21] H. Telg, J. Maultzsch, S. Reich, F. Hennrich, and C. Thomsen, Phys. Rev. Lett. **93**, 177401 (2004).

7

Growth of single wall carbon nanotubes from ^{13}C isotope labelled organic solvents inside single wall carbon nanotube hosts

F. Simon and H. Kuzmany

Chemical Physics Letters **425** *85 (2006).*

ABSTRACT Exploring the synthesis of novel molecular nanostructures has been in the forefront of material research in the last decade. One of the most interesting nanostructures are single wall carbon nanotubes (SWCNTs). Their catalyst free growth, however, remains an elusive goal. Here, we present the growth of single wall carbon nanotubes from organic solvents such as benzene and toluene in a confined environment, inside a host SWCNT. The solvents encapsulated in SWCNTs are transformed to an inner tube when subject to a heat treatment under dynamic vacuum at 1270 °C. We used isotope labeling of the different carbon sources to prove that the source of the inner tubes is indeed the solvent. Our results put constraints on the models explaining the inner tube growth and provides a simple alternative for the fullerene based inner tube growth. It also provides the possibility to study a completely new field of in-the-tube chemistry.

7.1 Introduction

Catalyst free growth of single wall carbon nanotubes (SWCNT) has been intensively attempted since their discovery in 1993 [1, 2]. The efforts resulted in novel nanostructures such as e.g. the nano-horns [3] but the metal catalyst-free synthesis remains elusive. Recently, catalyst free growth of SWCNTs was achieved from fullerenes encapsulated in SWCNTs, when these so-called peapods [4] are subject to a high temperature annealing at 1270 °C [5, 6].

In this paper the synthesis of inner tubes is reported from ^{13}C isotope labeled organic solvents such as benzene and toluene encapsulated in SWCNTs. This is demonstrated to work when fullerenes are co-encapsulated preventing the solvents from evaporation. Isotope labeling proves unambiguously that the solvents contribute to the inner tubes and gives a measure on the yield. The current result opens new perspectives for the catalyst free synthesis of SWCNTs in other confined environments such as zeolite [7] and allows further exploration of the in-the-tube chemistry.

7.2 Experimental

Sample preparation. Commercial SWCNT material (50 weight % purity, Nanocarblab), fullerenes of natural carbon (Hoechst AG), benzene and toluene (Sigma Aldrich) and isotope labeled benzene and toluene (Euriso-Top SA) were used. The purification of the SWCNTs by the supplier in the form of repeated air oxidation at 400 °C and acid washing results in purified and opened SWCNTs. The tube diameter distribution was determined from Raman spectroscopy [8] and we obtained $d = 1.40$ nm and $\sigma = 0.10$ nm for the mean diameter and the variance of the Gaussian distribution, respectively. Vapor filling with fullerenes was performed by subjecting the SWCNT flakes to fullerene vapor in a sealed quartz ampoule at 650 °C following Ref. [9]. Non-encapsulated fullerenes were removed by a 650 °C dynamic vacuum treatment. Typically 150 μg fullerenes in 100 μl solvent was sonicated for 1 h with 1 mg SWCNT in an Eppendorf tube for the solvent peapod preparation. The weight uptake of the SWCNT is ~15 % [10] that is shared between the solvent and the fullerenes. The peapod was separated from the solvent by centrifuging and the peapod material was greased on a sapphire substrate. The vapor or solvent prepared peapods were treated in dynamic vacuum at 1270 °C for 2 hours for the inner tube growth. The inner tube growth efficiency was found independent of the speed of warming.

Raman spectroscopy. Vibrational analysis was performed on a Dilor xy triple Raman spectrometer in the 1.64-2.54 eV (676-488 nm) energy range at ambient conditions.

7.3 Results and discussion

The growth of inner carbon nanotubes can be monitored by Raman spectroscopy. We use extensively the response from the overtone of the SWCNT D-line, known as the G' mode [11], since this mode exhibits the largest absolute isotope shift. Fig. 7.1 shows the G' mode for a SWCNT (a) and two DWCNT samples that were obtained by high temperature annealing from vapor prepared C_{60} peapods (b) and toluene+C_{60} peapods (c) by a 1270 °C heat treatment. The vapor method involves placing the SWCNT in a fullerene vapor in a sealed ampoule, while the solvent method involves sonicating the solvent+C_{60} solution together with the nanotubes which results in the encapsulation of both the fullerene and the solvent [12]. All results reported here are identical when C_{70} fullerenes were used. The G' mode provides a convenient measure of the inner tube growth as the inner and outer tube response are separated in the DWCNT samples: the mode on the low Raman shifted side comes from the inner tubes [13]. The ratio of the inner to outer tube mode intensities strongly depends on the exciting laser energy with a maximum around 2.41 eV [13], that is used in the current study.

The relative intensity of the inner tube mode in the vapor-C_{60} and solvent+C_{60} peapod based

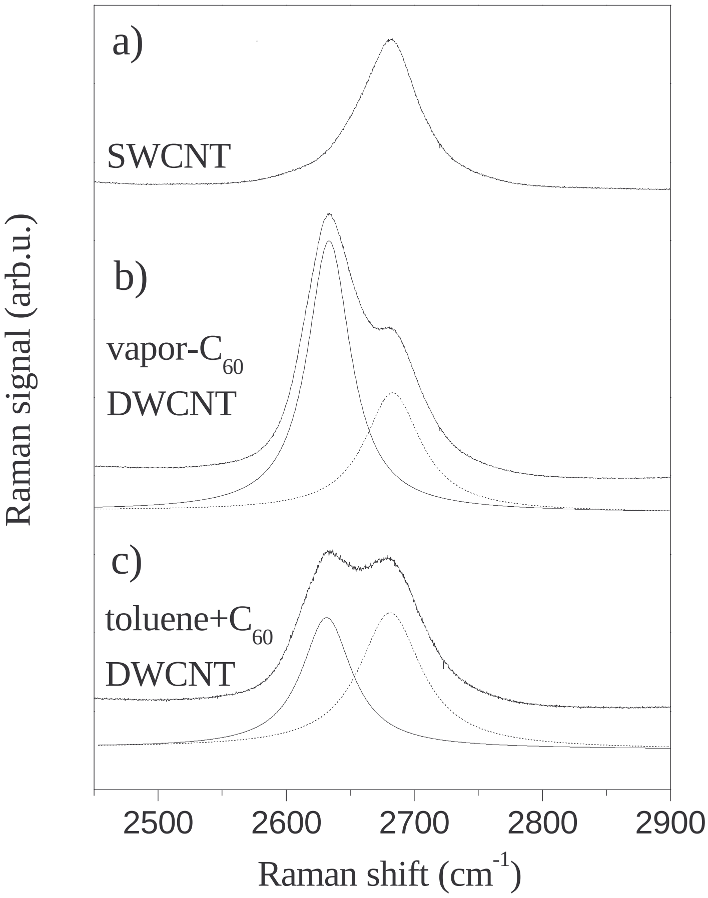

FIGURE 7.1. The G' Raman mode of a) SWCNTs, b) vapor-C_{60} peapod and c) toluene+C_{60} peapod based DWCNTs at λ=515 nm laser excitation (2.41 eV). Smooth solid and dashed curves show the deconvolution to inner and outer tube modes, respectively.

DWCNTs measures the inner tube content in the two samples. This can be quantified by deconvolution of the DWCNT signal into inner and outer tube components as shown in Fig. 7.1. The smaller inner tube signal in the solvent+C_{60} sample is the result of a partial evaporation of the solvent before the inner tubes are formed. It is known that encapsulation of the fullerene is energetically preferred and thus it cannot escape from the tubes [14]. However, a small molecule such as benzene and toluene can leave the tube at higher temperatures. We found that the yield of inner tubes grown from the benzene- (spectrum not shown) and toluene+C_{60} peapods is 44(1) % and 48(1) % of that from the vapor-C_{60} sample, respectively. To separate the contribution to the inner tubes from the solvents and C_{60}, the encapsulated C_{60} content can be determined in the solvent+C_{60} peapod samples. In Fig. 7.2, we show the spectral range that contains the C_{60} pentagonal pinch mode (PPM) at 1466 cm^{-1} [15] and the nanotube G modes around 1650 cm^{-1} [11] for the vapor-C_{60} and solvent+C_{60} peapod sample. It was demonstrated [16] that the encapsulated C_{60} content can be determined from the relative intensity of the PPM and G modes. Assuming 100 % filling of the available volume with C_{60} for the vapor-C_{60} peapod sample [17], the results of Fig. 7.2 demonstrates only 40(1) % fullerene filling for the toluene+C_{60} sample. The same value was obtained for benzene as a solvent.

In summary, from the 44 % inner tube content in the benzene+C_{60} peapod based sample, 91 % of the carbon originates from C_{60}. Thus benzene contributes only to approximately 9(4) % of the carbon. Similarly, toluene contributes to approximately 17(4) % fraction of the total carbon amount on the inner tubes. If we assume that solvents fill all available volume apart from that filled with C_{60}, the current result means that a significant portion, over 80 %, is evaporated from both solvents without contributing to the inner tube growth.

Based on the current analysis, it can not be ruled out that e.g. amorphous carbon is also inside the tubes or enters the tubes and thus contributes to the inner tube growth. Therefore the crucial statement on the growth of inner tubes from organic solvents requires further reinforcement. To

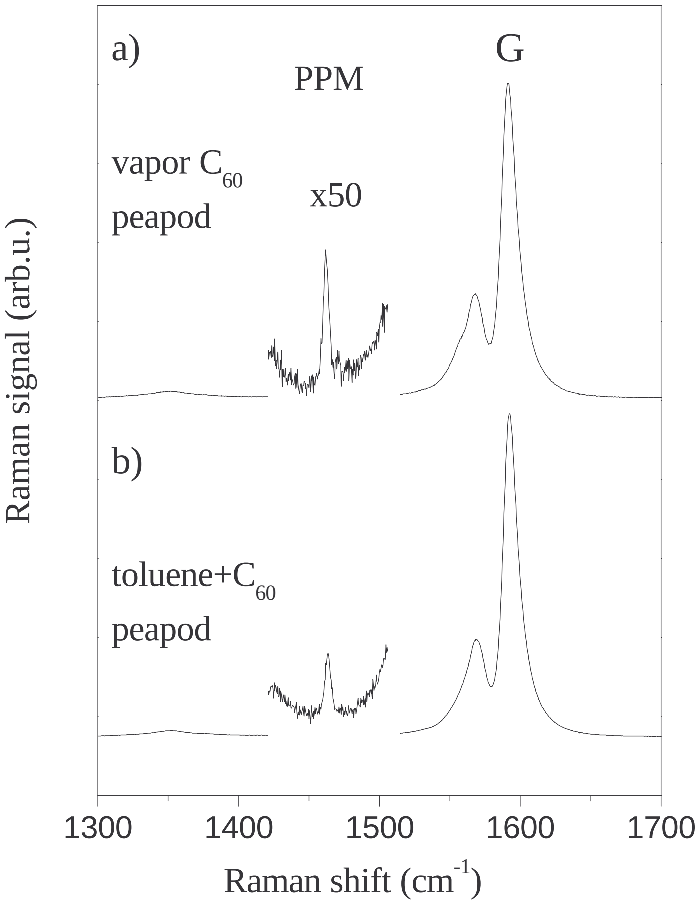

FIGURE 7.2. The C_{60} PPM mode and the nanotube G mode in a) vapor-C_{60} peapod and b) toluene+C_{60} peapod sample at λ=488 nm laser excitation (2.54 eV). Note the 50 times magnified scale for the PPM range.

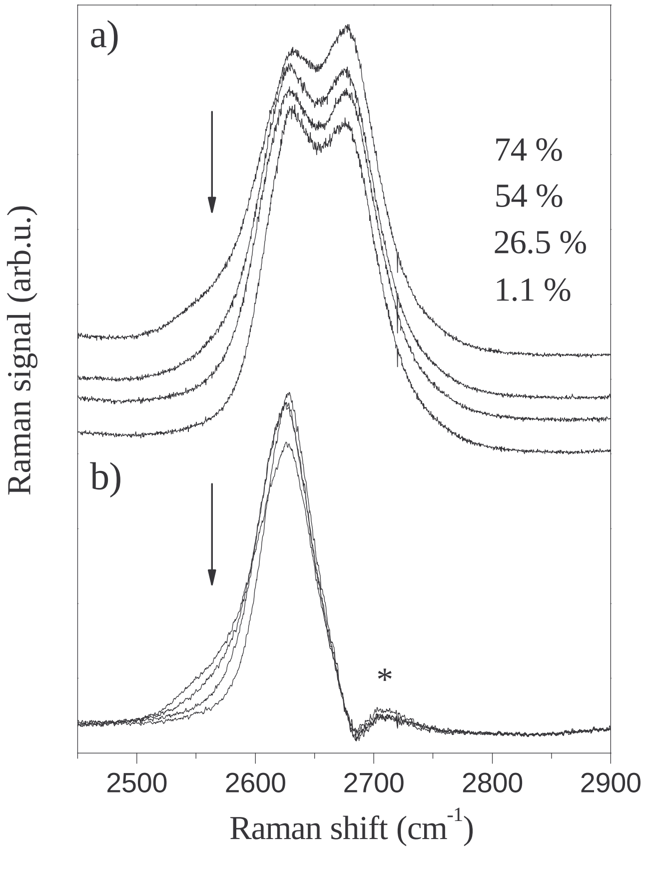

FIGURE 7.3. a) The G' mode of toluene+C_{60} peapod based DWCNTs with varying ^{13}C enrichment at λ=515 nm laser excitation (2.41 eV). From top to bottom: 74 %, 54 %, 26.5 % and natural ^{13}C content. b) The G' mode of the inner tubes after subtracting the experimental SWCNT spectrum. Arrows indicate the spectral weight shifted toward lower frequencies. A small residual peak is observed around 2710 cm^{-1} (denoted by an asterisk) due to the imperfect subtraction.

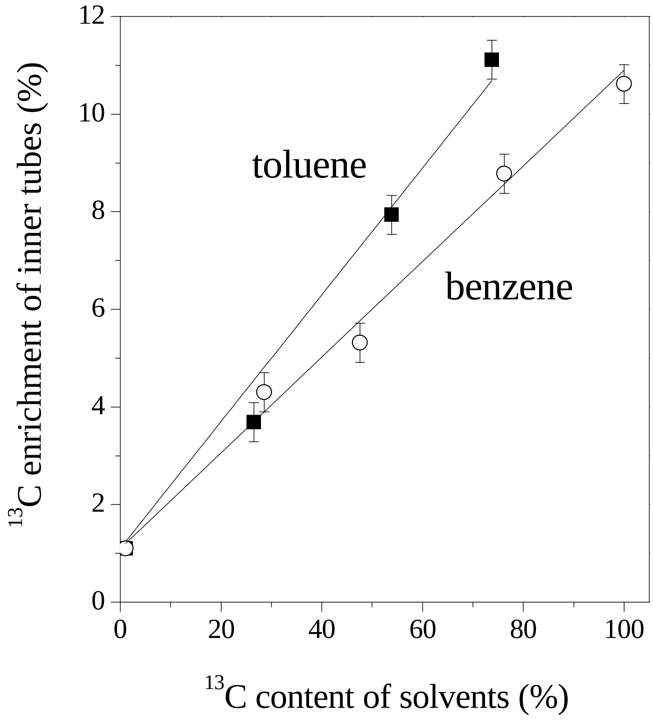

FIGURE 7.4. ^{13}C content of inner tubes based on the first moment analysis as explained in the text as a function of ^{13}C enrichement of benzene and toluene. Lines are linear fits to the data as explained in the text.

provide this, we studied the inner tube growth from solvent+C_{60} peapods where the solvent was a mixture of ^{13}C isotope labeled and natural solvents with varying concentrations. Toluene was a mixture of ring ^{13}C labeled ($^{13}C_6H_6$-CH_3) and natural toluene (C_7H_8). Benzene was a mixture of ^{13}C enriched and natural benzene. The labeled site was $>$ 99 % ^{13}C labeled for both types of molecules. The ^{13}C content, x, of the solvent mixtures was calculated from the concentration of the two types of solvents and by taking into account the presence of the naturally enriched methyl-group for the toluene. In Fig. 7.3a, we show the G' modes of DWCNTs with varying ^{13}C labeled content in toluene-C_{60} based samples and in Fig. 7.3b, we show the same spectra after subtracting the outer SWCNT component. A shoulder appears for larger values of x on the low frequency side of the inner tube mode, whereas the outer tube mode is unchanged. Similar behavior was observed for the benzene+C_{60} based peapod samples (spectra not shown) although with a somewhat smaller spectral intensity of the shoulder. The appearance of this low frequency shoulder is evidence for the presence of a significant ^{13}C content in the inner tubes. This proves that the solvent indeed contributes to the inner tube formation as it is the only sizeable source of ^{13}C in the current samples. The appearance of the low frequency shoulder rather than the shift of the full mode indicates an inhomogeneous ^{13}C enrichment. A possible explanation is that smaller diameter nanotubes might be higher ^{13}C enriched as they retain the solvent better than larger tubes.

To quantify the ^{13}C enrichment of the inner tubes, the downshifted spectral weight of the inner tube G' mode was determined from the subtracted spectra in Fig. 7.3b. The subtraction does not give a flat background above 2685 cm^{-1}, however it is the same for all samples and has a small spectral weight, thus it does not affect the current analysis. The line-shapes strongly deviate from an ideal Lorentzian profile. Therefore the line positions cannot be determined by fitting, whereas the first moments are well defined quantities. The effective ^{13}C enrichment of the inner tubes, c, is calculated from $(\nu_0 - \nu)/\nu_0 = 1 - \sqrt{\frac{12+c_0}{12+c}}$, where ν_0 and ν are the first moments of the inner tube G' mode in the natural carbon and enriched materials, respectively, and $c_0 = 0.011$ is the natural abundance of ^{13}C in carbon. The validity of this "text-book formula" was previously verified by *ab-initio* calculations for enriched inner tubes [10].

In Fig. 7.4, we show the effective ^{13}C content in the inner tubes as a function of the ^{13}C content in the starting solvents. The scaling of the ^{13}C content of the inner tubes with that in the starting solvents proves that the source of the ^{13}C is indeed the solvents. The highest value of the relative shift for the toluene based material, $(\nu_0 - \nu)/\nu_0 = 0.0041(2)$, corresponds to about 11 cm^{-1} shift in the first moment of the inner tube mode. The shift in the radial breathing mode range (around 300 cm^{-1}) [11] would be only 1 cm^{-1}. This underlines why the high energy G' mode is convenient for the observation of the moderate ^{13}C enrichment of the inner tubes.

When fit with a linear curve with $c_0 + A * x$, the slope, A directly measures the carbon fraction in the inner tubes that originates from the solvents. The values, $A = 0.098(5)$ and $A = 0.130(6)$ agree with the solvent related carbon fractions on the inner tubes of 9 and 17 % as determined from the intensity of the inner tube modes for benzene and toluene, respectively.

The synthesis of inner tubes from organic solvent proves that any form of carbon that is encapsulated inside SWCNTs contributes to the growth of inner tubes. As mentioned above, inner tubes are not formed in the absence of fullerenes but whether the fullerene is C_{60} or C_{70} does not play a role. It suggests that fullerenes act only as a stopper to prevent the solvent from evaporating before the synthesis of the inner tube takes place. It also clarifies that the geometry of fullerenes do not play a distinguished role in the inner tube synthesis as it was originally suggested [18]. It also proves that inner tube growth can be achieved irrespective of the carbon source, which opens a new prospective to explore the in-the-tube chemistry with other organic materials.

7.4 Acknowledgement

FS acknowledges the Zoltán Magyary programme for support. Work supported by the Austrian Science Funds (FWF) project Nr. 17345, by the EU projects MERG-CT-2005-022103 and BIN2-2001-00580, and by the Hungarian State Grants (OTKA) No. TS049881, F61733 and NK60984.

‡ Corresponding author, email: ferenc.simon@univie.ac.at, Present address: Budapest University of Technology and Economics, Institute of Physics and Solids in Magnetic Fields Research Group of the Hungarian Academy of Sciences, H-1521, Budapest P.O.Box 91, Hungary

References

[1] S. Iijima and T. Ichihashi, Nature **363**, 603 (1993).

[2] D. S. Bethune, C. H. Kiang, M. S. DeVries, G. Gorman, S. R., and R. Beyers, Nature **363**, 605 (1993).

[3] S. Iijima, M. Yudasaka, R. Yamada, S. Bandow, K. Suenaga, F. Kokai, and K. Takahashi, Chem. Phys. Lett. **309**, 165 (1999).

[4] B. W. Smith, M. Monthioux, and D. E. Luzzi, Nature **396**, 323 (1998).

[5] S. Bandow, M. Takizawa, K. Hirahara, M. Yudasaka, and S. Iijima, Chem. Phys. Lett. **337**, 48 (2001).

[6] R. Pfeiffer, H. Kuzmany, C. Kramberger, C. Schaman, T. Pichler, H. Kataura, Y. Achiba, J. Kürti, and V. Zólyomi, Phys. Rev. Lett. **90**, 225501 (2003).

[7] Z. K. Tang, L. Y. Zhang, N. Wang, X. X. Zhang, G. H. Wen, G. D. Li, J. N. Wang, C. T. Chan, and P. Sheng, Science **292**, 2462 (2001).

[8] H. Kuzmany, W. Plank, M. Hulman, C. Kramberger, A. Grüneis, T. Pichler, H. Peterlik, H. Kataura, and Y. Achiba, Eur. Phys. J. B **22**, 307 (2001).

[9] H. Kataura, Y. Maniwa, T. Kodama, K. Kikuchi, K. Hirahara, K. Suenaga, S. Iijima, S. Suzuki, Y. Achiba, and W. Krätschmer, Synthetic Met. **121**, 1195 (2001).

[10] F. Simon, C. Kramberger, R. Pfeiffer, H. Kuzmany, J. Zólyomi, V. Kürti, P. M. Singer, and H. Alloul, Phys. Rev. Lett. **95**, 017401 (2005).

[11] M. S. Dresselhaus, G. Dresselhaus, and P. Avouris, *Carbon Nanotubes: Synthesis, Structure, Properties, and Applications* (Springer, Berlin, Heidelberg, New York, 2001).

[12] F. Simon, H. Kuzmany, H. Rauf, T. Pichler, J. Bernardi, H. Peterlik, L. Korecz, F. Fülöp, and A. Jánossy, Chem. Phys. Lett. **383**, 362 (2004).

[13] R. Pfeiffer, H. Kuzmany, F. Simon, S. N. Bokova, and E. Obraztsova, Phys. Rev. B **71**, 155409 (2005).

[14] S. Berber, Y.-K. Kwon, and D. Tománek, Phys. Rev. Lett. **88**, 185502 (2002).

[15] T. Pichler, H. Kuzmany, H. Kataura, and Y. Achiba, Phys. Rev. Lett. **87**, 267401 (2001).

[16] H. Kuzmany, R. Pfeiffer, C. Kramberger, T. Pichler, X. Liu, M. Knupfer, J. Fink, H. Kataura, Y. Achiba, B. W. Smith, et al., Appl. Phys. A **76**, 449 (2003).

[17] X. Liu, T. Pichler, M. Knupfer, M. S. Golden, J. Fink, H. Kataura, Y. Achiba, K. Hirahara, and S. Iijima, Phys. Rev. B **65**, 045419 (2002).

[18] Y. Zhao, B. I. Yakobson, and R. E. Smalley, Phys. Rev. Lett. **88**, 185501 (2002).

8

Highly perfect inner tubes in CVD grown double-wall carbon nanotubes

F. Simon, Á. Kukovecz, Z. Kónya, R. Pfeiffer, and H. Kuzmany

Chemical Physics Letters **404**, *85 (2005).*

ABSTRACT The synthesis of double-wall carbon nanotubes (DWCNTs) with highly unperturbed inner shells is reported using the catalytic vapor deposition method. Temperature dependent and high resolution Raman measurements show an enhanced phonon life-time of the inner tubes with respect to the outer ones and similar diameter SWCNTs. This proves that the inner tubes are unperturbed similar to the inner tubes in peapod-grown DWCNTs. The presence of the outer tube is argued to protect the inner tube from interaction with impurities and also to stabilize the growth of defect free inner tubes. The current material underlines the application potential of DWCNTs.

8.1 Introduction

Double-wall carbon nanotubes (DWCNTs) are on the borderline between single-wall (SWCNTs) and multi-wall carbon nanotubes (MWCNTs). As a result, they share common features with both classes of materials. Generally, SWCNTs are considered to be of fundamental interest and MWCNTs are known to be more application-friendly. SWCNTs exhibit a number of compelling physical properties such as superconductivity [1], the Tomonaga-Luttinger liquid state [2, 3] and a predicted Peierls state [4, 5]. DWCNTs are fundamentally interesting as their physical properties are determined by the well defined inner and outer tube chiralities [6, 7] and are candidates for applications such as e.g. reinforcing composites or scanning microscopy probeheads due to the improved elastic properties as compared to the SWCNTs but still of smaller diameter than MWCNTs. In addition, the small diameter inner tubes enable to study the behavior of highly curved nanostructures such as curvature induced deviations from the electronic structure of graphite [8, 9].

DWCNTs can be grown from fullerenes encapsulated inside SWCNTs, peapods [10] (PEA-DWCNTs) by a high temperature treatment [11, 12] without any catalysts. Raman studies on the inner tubes in PEA-DWCNTs indicated at least an order of magnitude longer phonon lifetimes, i.e. narrower line-widths, as compared to the outer tubes [6]. This was associated with the highly unperturbed nature of the inner tubes, that are grown in the nano clean-room interior of SWCNTs. The defect content of the tube shells is crucial for applications such as the possibility of ballistic transport and improved mechanical properties.

An alternative DWCNT synthesis is based on catalytic SWCNT growth methods such as arc-discharge [13] and Catalytic Chemical Vapor Deposition (CCVD) methods [14–20]. So far, Raman studies on such samples have given a similar linewidth for the inner and outer tubes indicating comparable number of defects for the two shells [15, 18–21]. However, no low temperature and high resolution Raman data have been reported that is needed for the accurate observation of the inner tube line-widths. As a result, inner tubes in PEA-DWCNTs are the only tubes known to be highly defect free among all kinds of CNT materials.

Here, we report that CCVD grown DWCNTs (CVD-DWCNTs) can also have very narrow Raman line-widths indicating their high perfectness as the inner tubes in PEA-DWCNTs. Interestingly, the inner tube diameter distribution in the current CVD-DWCNT is very similar to the PEA-DWCNT samples and it is discussed whether perfectness of small diameter inner tubes is a general phenomenon of small diameter inner tubes.

8.2 Experimental

Catalyst preparation. The CVD catalyst was a modified version of the Fe/Mo/MgO system developed by Liu et al. [22] for SWCNT synthesis. $(NH_4)Mo_7O_{24}$ (Reanal) and $Fe(NO_3)_3 \cdot 9\ H_2O$ (Aldrich) were dissolved in distilled water and the solution was added to the aqueous suspension of MgO and sonicated for 30 minutes at room temperature. The resulting slurry was dried in two steps, under vacuum at 90 °C for 1 h and then at atmospheric pressure at 120 °C overnight. The catalyst possessed a molar Fe:Mo:MgO ratio of 1:0.1:110.

Nanotube synthesis. Nanotubes were synthesized in a fixed bed horizontal quartz tube reactor with a diameter of 60 mm and a length of 110 cm. 0.30 g catalyst was placed in a quartz boat and shoved to the middle of the reactor. After purging the system with Ar at room temperature, the gas stream was changed to the C_2H_2:Ar (10 cm^3/min:150 cm^3/min volumetric flow rate at ambient temperature and pressure) reaction mixture. The reactor was pushed into the furnace and kept there at 850 °C for 20 minutes. Then, the reactor was removed from the furnace and purged with a pure Ar stream until cooling down to room temperature. The catalyst was removed from the sample by dissolving in excess of concentrated HCl solution at room temperature. The remaining carbonaceous material was filtered and washed with distilled water and dried at 120 °C. Amorphous carbon content was diminished by oxidizing in flowing air at 300 °C for 1 hour.

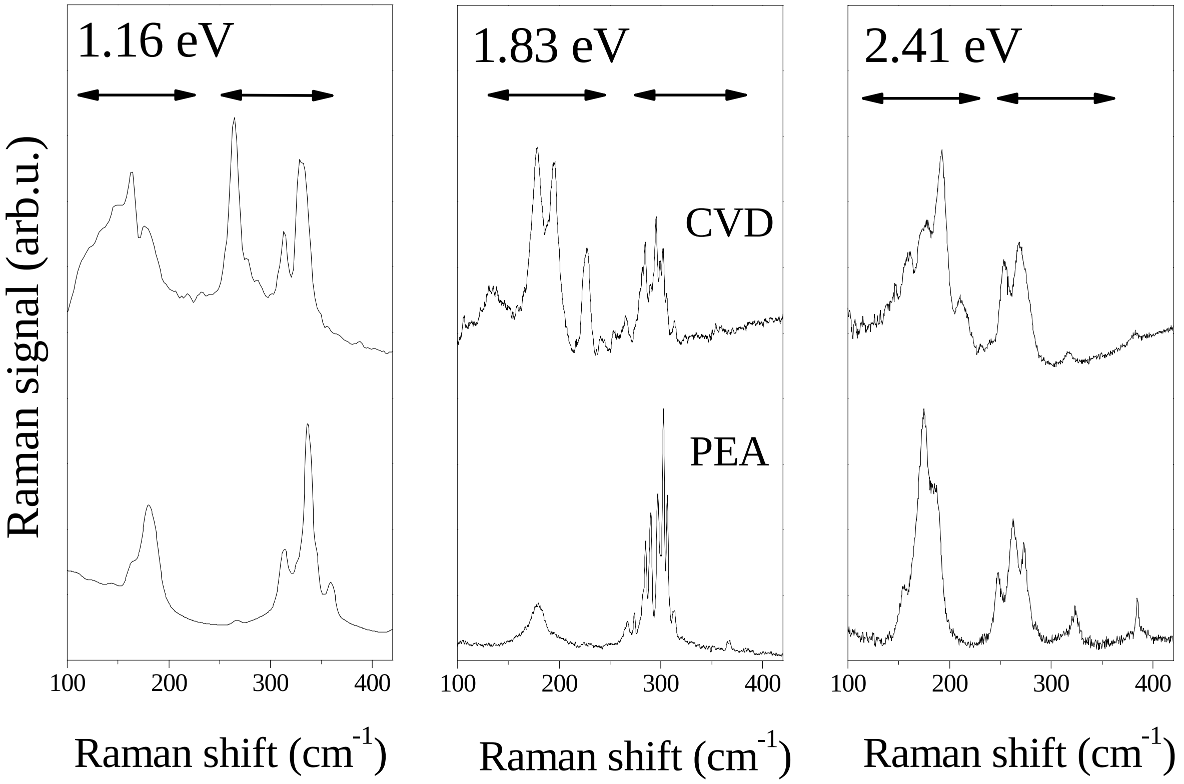

FIGURE 8.1. Comparison of CVD- (upper curves) and PEA-DWCNT (lower curves) samples at 1.16, 1.83, and 2.41 eV. The distinct lower and upper Raman shift ranges indicated by arrows correspond to the outer and inner tube RBM responses, respectively.

The HiPco samples used as reference were purchased from CNI (Carbon Nanotechnologies Inc., Houston, USA).

Raman spectroscopy. Multi frequency Raman spectroscopy was performed on a Dilor xy triple axis spectrometer in the 1.83-2.54 eV (676-488 nm) energy range and in a Bruker FT-Raman spectrometer for the 1.16 eV (1064 nm) excitation at room temperature and at 90 K. The triple axis spectrometer can be operated in subtractive and additive mode allowing to take normal and high resolution spectra. The high resolution mode has a spectral resolution of 0.4 cm^{-1} at 1.83 eV excitation as determined from the spectrometer response to the elastically scattered light.

8.3 Experimental results

In Fig. 8.1., we show the Raman spectra of the CVD grown material and the PEA-DWCNT samples for three laser excitations. Comparison of spectra taken with different laser excitation energies is required due to the strong photoselectivity of the nanotube Raman response. The radial breathing mode (RBM) of SWCNTs with $d \approx$2.1 to 0.6 nm dominates the Raman response for the displayed 120 to 400 cm^{-1} spectral range. The spectral ranges of 120-220 cm^{-1} and 240-400 cm^{-1} were previously identified with the outer and inner tube Raman responses for the PEA-DWCNTs, respectively [6]. Surprisingly, the CVD grown material shows a similar pattern with higher and lower Raman shifted ranges and a gap in between. We also observed similar spectra for the two materials at other excitation energies (not shown). It is tempting to assume that in the CVD grown material the same spectral regions come from inner and outer tubes, too. This means that the current CVD sample contains a sizeable amount of DWCNTs rather than a broad distribution of SWCNTs as it was originally found for tubes from a similar preparation [22]. Below, we present other spectroscopic evidence which further supports that the lower and higher spectral ranges originate from outer and inner tubes in the CVD-DWCNT samples, respectively.

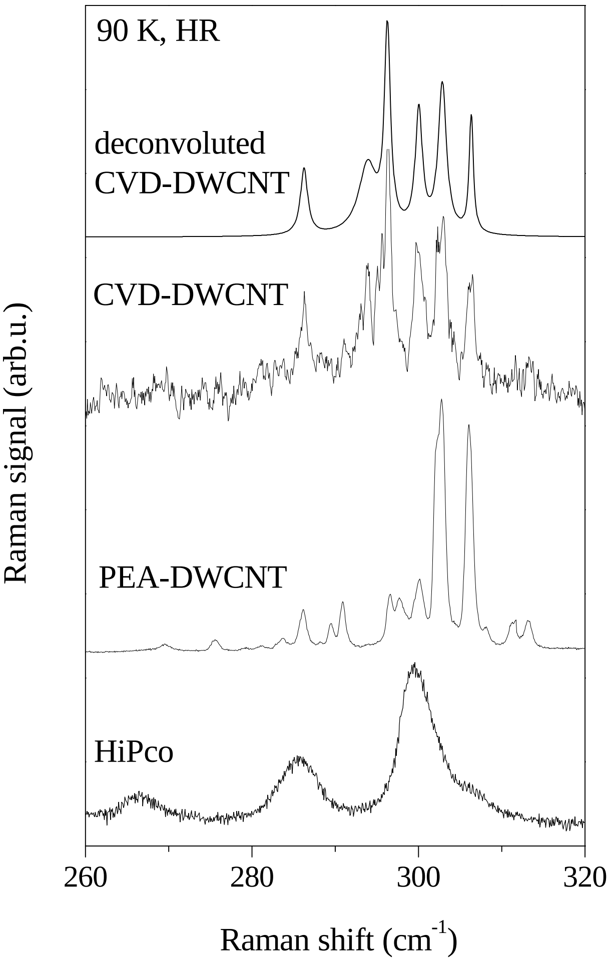

FIGURE 8.2. High resolution Raman spectra taken at 1.83 eV excitation and 90 K on the CVD- and PEA-DWCNT and an SWCNT reference (HiPco) sample. The deconvoluted spetrum is also shown for the CVD-DWCNT sample. The narrow linewidths indicate the long radial breathing mode phonon lifetimes of the inner tubes in both DWCNT materials.

Although the inner and outer tube diameter distribution is very similar in the two materials, the Raman intensities are different: the inner tube modes Raman intensities are on average a factor two smaller for the CVD-DWCNT than for the PEA-DWCNT sample. This indicates a smaller density of the corresponding DWCNTs in the earlier sample, however, an accurate determination based on the Raman intensities alone is not possible as it is affected by a number of sample dependent factors such as the surface morphology.

The determination of the phonon life-times in the inner tubes in CVD-DWCNTs is the important contribution of the current work. This parameter can be used to characterize the defect content on the tubes. Often, the intensity of the defect induced D-mode is used to estimate the defect concentration. However, it was shown recently that the D-modes of inner and outer tubes overlap, thus preventing a meaningful analysis unless ^{13}C labelling of the inner tubes is used to separate their response [8]. Long phonon life-times in the inner tubes can be measured in high-resolution (HR) Raman experiments at 90 K and the corresponding spectra is shown in Fig. 8.2. For comparison, we show a spectrum taken on an SWCNT sample prepared with the HiPco process (lowest curve in Fig. 8.2). The HiPco sample contains tubes with similar diameters as the inner tubes in the DWCNT samples. Remarkably, the inner tubes have a very narrow line-width for both DWCNT materials whereas the line-width of the HiPco sample is significantly larger.

The accurate Lorentzian line-widths, that measure the intrinsic phonon life-times, were determined by fitting the experimental spectra with Voigtian line-shapes whose Gaussian component is the spectrometer response for the elastically scattered light. The resulting deconvoluted spectrum is also shown for the CVD-DWCNTs in Fig. 8.2. Values for the FWHMs of the Lorentzian lines down to 0.8 cm^{-1} were found for the CVD-DWCNTs which is almost as narrow as the FWHMs observed for the PEA-DWCNTs, down to 0.4 cm^{-1} [6]. This is an order of magnitude smaller than the line-widths of 5-6 cm^{-1} found for the HiPco sample, for the outer tubes in the current

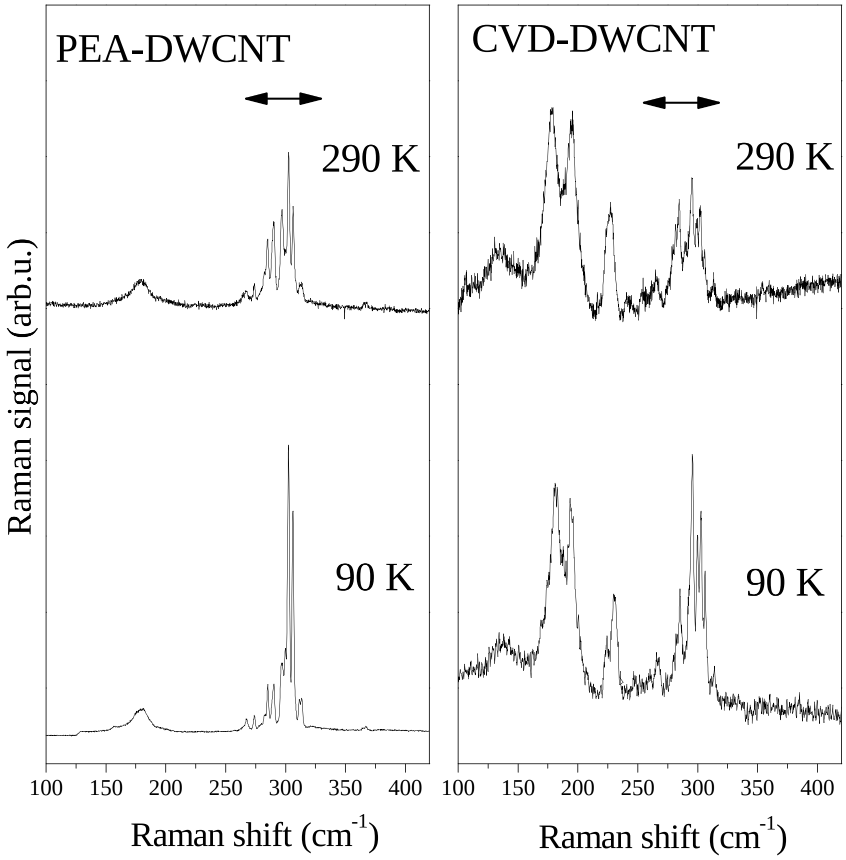

FIGURE 8.3. Temperature dependence of the CVD- and PEA-DWCNT spectra taken at 1.83 eV excitation. The inner tube RBM modes (arrows) increase at lower temperature compared to the outer tube RBMs.

samples, or for individual SWCNTs [23] indicating the highly unperturbed nature of the inner tubes in both materials.

The observable RBM modes agree in both materials within the 0.3 cm^{-1} experimental precision of the line position measurement of the HR experiment. The reason for the larger number of RBMs in the DWCNT samples as compared to the HiPco sample was explained previously by the number of possible inner and outer tube pairs. It was shown that an inner tube can be grown in several outer ones and the corresponding RBMs are modified due to the inner-outer tube interaction [6, 7]. The current result shows that the splitting is present irrespective of the DWCNT growth method. This confirms that the origin of the splitting is the inner-outer tube interaction as previously thought.

In Fig. 8.3, we show the temperature dependent Raman spectra for the two materials for the RBM ranges at the 1.83 eV excitation. The integrated intensity of the inner and outer tube RBMs follows a distinct temperature dependence for both compounds: it increases by a factor ~2 at lower temperatures for the inner and is constant for the outer tubes. Similar changes can be observed for the other laser excitations. The increase of integrated intensity proves that it is not caused by the lengthening of phonon life-times, i.e. narrowing of the modes, but it is due to an increasing life-time of the quasiparticle state which is excited during the Raman process. The details of this mechanism are studied and published separately [24]. In brief, the quasiparticle life-time is temperature independent and short for the outer tubes, whereas it is longer and further lengthens with decreasing temperatures for the inner tubes. In general, dirty and clean systems are characterized by temperature independent short and longer temperature dependent life-times, respectively. Analogous situations are encountered for the momentum relaxation time in dirty and clean conductors [25]. Therefore, the observed effect suggests that the outer and inner tubes behave as dirty and clean systems, respectively. The cleanliness of inner tubes is associated with the low concentration of lattice defects or impurities and that it is well protected from the environment.

8.4 Discussion

The similarity between the observed RBM patterns in the CVD- and PEA-DWCNT samples suggests that the 120-220 cm^{-1} and 240-400 cm^{-1} spectral ranges originate from outer and inner tubes in the two samples, respectively. The larger number of observed than geometrically allowed tubes for the latter range is a further evidence supporting the DWCNT nature of the CVD-DWCNT sample as it is characteristic for DWCNTs and originates from the interaction of inner and outer tubes [6, 7]. In addition, RBMs in the two spectral ranges have very different properties for both samples. Linewidths of the RBMs in the 240-400 cm^{-1} spectral range become narrower on lowering temperature, reaching an order of magnitude smaller line-widths than the temperature independent line-widths of the RBMs in the 120-220 cm^{-1} spectral range. Similarly, Raman intensities of the RBMs in the 240-400 cm^{-1} spectral range increase on decreasing temperature whereas the Raman intensity of the 120-220 cm^{-1} spectral range modes is temperature independent. This proves that the two spectral ranges come from tubes with distinct properties and further supports the above assignment. This also shows that inner tubes have long phonon and quasiparticle life-times indicating that they are highly defect free and are well protected from the environment.

The observation of long phonon- and quasiparticle life-times, and the concomitant high perfectness of inner tubes in non peapod-grown DWCNT is surprising. The high perfectness of inner tubes in PEA-DWCNT sample was associated with the catalyst-free growth conditions and the perfectness of the growth conditions as the inside of the host tubes can be considered as a nano clean-room [6, 26]. As a result, only inner tubes in PEA-DWCNTs were thought to be highly perfect. This paradigm appears to be violated by the current CVD-DWCNTs. Previous results have considered large diameter inner tubes with $d \approx 1.52$ nm where the inner tubes had a large linewidth [15]. Interestingly, the inner and outer tube diameters in the currently described CVD-DWCNTs are very similar to the PEA-DWCNTs. Similar diameter inner tubes as those used here were reported, however the temperature dependent effects were not studied [14, 18–21]. Therefore, it cannot be ruled out that perfectness of small diameter inner tubes is a general feature.

Unfortunately, the dominant contribution to the SWCNT RBM phonon and quasiparticle life-times is not fully understood. It has been speculated that SWCNTs strongly interact with attached impurities as well as contain a number of defects, partly produced during synthesis or during purification. Inner tubes are well protected from attached impurities. The effect of attached impurities can also give rise to an inhomogeneous broadening. This would explain why the similarly small diameter tubes in the HiPco samples show significantly broader RBMs. Concerning lattice defects during growth, it can only be speculated that the ensemble of the two shells of a growing DWCNT energetically prefers the formation of a highly perfect inner tube. Alternatively, it is also possible that the inner tubes are grown in the CVD-DWCNT material only when the outer tube has been pre-formed. Then, the outer tube provides a host template similarly as in the case of PEA-DWCNTs, which enable the growth of highly defect-free inner tubes. Clearly, more theoretical work is required to understand the growth processes of both peapod based and CVD grown DWCNTs.

8.5 Conclusion

In conclusion, we reported the CCVD synthesis of DWCNTs with highly unperturbed inner tubes similar to the inner tubes in peapod based DWCNTs. This is a surprising result as for the latter material the inner tubes are grown in a catalyst free nano clean-room environment. The diameter distributions of the inner tubes are similar for both kinds of materials and we suggested that the diameter of the inner tubes plays an important role for their defect-free nature. The currently synthesized material is expected to have improved properties compared to other DWCNTs and is a potential candidate for applications such as conducting wires with increased ballistic transport length or reinforcing element with improved mechanical properties.

We thank Dóra Méhn for her assistance in the nanotube synthesis. This work was supported by FWF project P17345, by EU projects BIN2-2001-00580, MEIF-CT-2003-501099 and by OTKA T046491 and F046361. Á. K. and F. S. acknowledge support from a Zoltán Magyary and Z. K. acknowledge support from a János Bolyai fellowship.

References

[1] Z. K. Tang, L. Y. Zhang, N. Wang, X. X. Zhang, G. H. Wen, G. D. Li, J. N. Wang, C. T. Chan, and P. Sheng, Science **292**, 2462 (2001).

[2] H. Ishii, H. Kataura, H. Shiozawa, H. Yoshioka, H. Otsubo, Y. Takayama, T. Miyahara, S. Suzuki, Y. Achiba, M. Nakatake, et al., Nature **426**, 540 (2003).

[3] H. Rauf, T. Pichler, M. Knupfer, J. Fink, and H. Kataura, Phys. Rev. Lett. **93**, 096805 (2004).

[4] K. P. Bohnen, R. Heid, H. J. Liu, and C. T. Chan, Phys. Rev. Lett. **93**, 245501 (2004).

[5] D. Connétable, G.-M. Rignanese, J.-C. Charlier, and X. Blase, Phys. Rev. Lett. **94**, 015503 (2005).

[6] R. Pfeiffer, H. Kuzmany, C. Kramberger, C. Schaman, T. Pichler, H. Kataura, Y. Achiba, J. Kürti, and V. Zólyomi, Phys. Rev. Lett. **90**, 225501 (2003).

[7] R. Pfeiffer, C. Kramberger, F. Simon, H. Kuzmany, V. N. Popov, and H. Kataura, Eur. Phys. J. B **42**, 345 (2004).

[8] F. Simon, C. Kramberger, R. Pfeiffer, H. Kuzmany, J. Zólyomi, V. Kürti, P. M. Singer, and H. Alloul, Phys. Rev. Lett. **95**, 017401 (2005).

[9] J. Kürti, V. Zólyomi, M. Kertész, and S. Guangyu, New. J. Phys. **5**, 125.1125.21 (2003).

[10] B. W. Smith, M. Monthioux, and D. E. Luzzi, Nature **396**, 323 (1998).

[11] B. W. Smith and D. Luzzi, Chem. Phys. Lett. **321**, 169 (2000).

[12] S. Bandow, M. Takizawa, K. Hirahara, M. Yudasaka, and S. Iijima, Chem. Phys. Lett. **337**, 48 (2001).

[13] J. L. Hutchison, N. A. Kiselev, E. P. Krinichnaya, A. V. Krestinin, R. O. Loutfy, A. P. Morawsky, V. E. Muradyan, E. D. Obraztsova, J. Sloan, S. V. Terekhov, et al., Carbon **39**, 761 (2001).

[14] M. Endo, H. Muramatsu, T. Hayashi, Y. A. Kim, M. Terrones, and N. S. Dresselhaus, Nature **433**, 476 (2005).

[15] W. Ren, F. Li, J. Chen, S. Bai, and H.-M. Cheng, Chem. Phys. Lett. **359**, 196 (2002).

[16] S. C. Lyu, T. J. Lee, C. W. Yang, and C. J. Lee, Chem. Phys. Lett. **12**, 1404 (2003).

[17] E. Flahaut, R. Bacsa, A. Peigney, and C. Laurent, Chem. Commun. **12**, 1442 (2003).

[18] J. Wei, B. Jiang, X. Zhang, H. Zhu, and D. Wu, Chem. Phys. Lett. **376**, 753 (2003).

[19] L. Ci, Z. Zhou, X. Yan, D. Liu, H. Yuan, L. Song, Y. Gao, J. Wang, L. Liu, W. Zhou, et al., J. Appl. Phys. **94**, 5715 (2003).

[20] L. Ci, Z. Zhou, X. Yan, D. Liu, H. Yuan, L. Song, J. Wang, Y. Gao, J. Zhou, W. Zhou, et al., J. Phys. Chem. B **107**, 8760 (2003).

[21] R. R. Bacsa, A. Peigney, C. Laurent, P. Puech, and W. S. Bacsa, Phys. Rev. B **65**, 161404 (2002).

[22] B. C. Liu, S. C. Lyu, S. I. Jung, H. K. Kang, C.-W. Yang, J. W. Park, P. C.Y., and C. J. Lee, Chem. Phys. Lett. **383**, 104 (2004).

[23] A. Jorio, R. Saito, J. H. Hafner, C. M. Lieber, M. Hunter, T. McClure, G. Dresselhaus, and M. S. Dresselhaus, Phys. Rev. Lett. **86**, 1118 (2001).

[24] F. Hasi, F. Simon, and H. Kuzmany, J. Nanosci. Nanotechn. **5**, 1785 (2005).

[25] N. W. Ashcroft and N. D. Mermin, *Solid State Physics* (Saunders College Publishing, Philadelphia, 1976).

[26] F. Simon, R. Pfeiffer, C. Kramberger, M. Holzweber, and H. Kuzmany, *The Raman response of double wall carbon nanotubes* (Springer New York, 2005), pp. 203–224.

9

Interaction between concentric Tubes in DWCNTs

R. Pfeiffer, Ch. Kramberger, F. Simon, H. Kuzmany, V. N. Popov, and H. Kataura

European Physical Journal B **42**, *345 (2004).*

ABSTRACT A detailed investigation of the Raman response of the inner tube radial breathing modes (RBMs) in double-wall carbon nanotubes is reported. It revealed that the number of observed RBMs is two to three times larger than the number of possible tubes in the studied frequency range. This unexpected increase in Raman lines is attributed to a splitting of the inner tube response. It originates from the possibility that one type of inner tubes may form in different types of outer tubes. In this case, a splitting of lines results since the inner tube RBM frequency depends on the diameter of the outer tube. Finally, a comparison of the inner tube RBMs and the RBMs of tubes in bundles gave clear evidence for a stronger interaction between tubes in a bundle as compared to the interaction between inner and outer tubes.

9.1 Introduction

Single-wall carbon nanotubes (SWCNTs) [1, 2] have attracted a lot of scientific interest over the last decade due to their unique structural and electronic properties. In 1998, Smith et al. [3] discovered that fullerenes can be encapsulated in SWCNTs, forming so-called peapods [4–6]. By annealing the peapods at high temperatures in a dynamic vacuum the enclosed C_{60} peas transform into SWCNTs within the outer tubes, thus producing double-wall carbon nanotubes (DWCNTs) [7, 8]. The growth process of the inner tubes is a new route for the formation of SWCNTs under shielded conditions in the absence of any additional catalyst.

A detailed Raman study of the radial breathing modes (RBMs) of the inner tubes revealed intrinsic linewidths down to $0.4\,\mathrm{cm}^{-1}$ [9]. These small linewidths indicate long phonon lifetimes and therefore highly defect free inner tubes. Thus, they are a direct experimental evidence for a nano-cleanroom reactor on the inside of SWCNTs.

Peapod grown DWCNTs are also interesting from another point of view. Usually, they are produced from standard SWCNTs with diameters around 1.4 nm. Taking into account the van der Waals interaction between the walls this means that the diameters of the inner shell tubes are around 0.7 nm. For these tubes the possible diameters can no longer be assumed to form a quasi-continuum. Additionally, due to the inverse relation between RBM frequency and diameter, the spectral distance between the RBMs of different inner tube types is (with few exceptions) much larger than between different outer tube RBMs. This opens the possibility to study the properties of individual SWCNTs in a bulk sample. A first application of this was the assignment of the chiral vectors to all inner tubes [10].

Studying the Raman response of the inner tube RBMs in high resolution at 20 K revealed that the number of observed lines is about two to three times larger than the number of geometrically allowed inner tubes. In the following, we show that this unexpected increase of Raman lines can be attributed to a splitting of the response from the inner tubes. This splitting originates from the possibility for one inner tube type to form in several outer tube types (with different diameters) and the fact that the RBM frequency of the inner tube depends on the diameter of the encapsulating parent tube. A quantitative explanation for the splitting was obtained by calculating the RBM frequencies of the inner tubes as a function of the outer tube diameter within a continuum model. Using two different scenarios regarding the possible inner-outer shell pairs, we compared the splitting obtained from the simulation with the experimentally obtained splitting. From this we conclude that not only the best fitting inner tubes are formed.

9.2 Experimental

The starting material for the DWCNTs were C_{60} peapods (in the form of bucky paper), produced by a previously described method [5]. The mean diameter of the assumed Gaussian diameter distribution of the outer tubes was 1.39(2) nm with a variance of 0.1 nm, as determined from the RBM Raman response [11]. The filling of the tubes large enough for C_{60} to enter was close to 100 % as evaluated from a Raman [12] and EELS analysis [13]. These peapods were slowly heated up to 1280 °C in a dynamic vacuum, annealed for 2 h, and were then slowly cooled down to room temperature.

To compare the RBM positions of the inner tubes with that of the same tube types in a bundle, we recorded also the Raman response of a bulk SWCNT sample produced with the high-pressure carbon monoxide (HiPco) scheme [14]. HiPco tubes have a broad diameter distribution from 0.8 to 1.4 nm, centered around 1.0 nm [15].

The Raman spectra were measured with a Dilor xy triple spectrometer using various lines of an Ar/Kr laser, a He/Ne laser and a Ti:sapphire laser. The spectra were recorded at 90 and 20 K in normal (NR) and high resolution (HR) mode, respectively ($\Delta\bar{\nu}_{\mathrm{NR}} = 1.3\,\mathrm{cm}^{-1}$ and $\Delta\bar{\nu}_{\mathrm{HR}} = 0.4\,\mathrm{cm}^{-1}$ in the red). In these measurements the samples were glued on a copper cold finger with silver paste.

9.3 Theory

The RBM frequencies of a given DWCNT were calculated using a continuum model (model 2 in Ref. 16). In this model, the DWCNT is represented by two nested hollow cylinders with diameters d_i and d_o of the inner and outer shells, respectively. The interaction between two points at a distance r on different shells was described by a Lennard-Jones (LJ) potential

$$V(r) = 4\epsilon[(\sigma/r)^{12} - (\sigma/r)^6]\,, \tag{9.1}$$

where $\epsilon = 2.964\,\mathrm{meV}$ and $\sigma = 0.3407\,\mathrm{nm}$ [17].

The total interaction energy Φ between the two shells was calculated by a numerical integration over a unit length of the shells. For this, the two shells were approximated by quadratic meshes. The mass of the carbon atoms was equally distributed over the meshes and located in their centers. The interaction energy was then calculated by summing the LJ potential over all mesh centers. The size of the meshes was reduced until the interaction energy had converged.

The interaction part of the dynamical matrix was then obtained by a numerical differentiation of Φ with respect to d_i and d_o. It was also assumed that the separate shells are elastic and are characterized with force constants k_i and k_o for the radial breathing motion. The k's were determined from the RBM frequency $\bar{\nu}_\mathrm{RBM}$ of a tube which is related to the tube diameter d by [18–20]

$$\bar{\nu}_\mathrm{RBM} = C_1/d + C_2\,, \tag{9.2}$$

where C_1 and C_2 are constants. The role of C_2 is to account for all frequency shifts due to the interaction with the environment. Since this interaction was explicitly modeled in our simulations, C_2 was set zero in the calculations. The shell diameters were taken from a DFT study [10], giving

$$d = \left(\frac{1}{d_\mathrm{G}} - \frac{0.0050}{d_\mathrm{G}^2} - \frac{0.0013}{d_\mathrm{G}^4}\right)^{-1}\,, \tag{9.3}$$

where

$$d_\mathrm{G} = \frac{\sqrt{3}\,a_\mathrm{CC}}{\pi}\sqrt{m^2 + mn + n^2} \tag{9.4}$$

is the graphene folding diameter, $a_\mathrm{CC} = 0.141\,\mathrm{nm}$ is the C$-$C distance in graphene and (m, n) is the chiral vector of the tube. Especially for small diameter tubes ($d \lessapprox 1\,\mathrm{nm}$) the DFT derived diameter has to be used instead of the graphene folding diameter.

The dynamical matrix D of the DWCNT can then be written in the form

$$D = -\frac{1}{\sqrt{m_\mathrm{i} m_\mathrm{o}}}\begin{pmatrix} k_\mathrm{i} + \partial^2\Phi/\partial d_\mathrm{i}^2 & \partial^2\Phi/\partial d_\mathrm{i}\partial d_\mathrm{o} \\ \partial^2\Phi/\partial d_\mathrm{o}\partial d_\mathrm{i} & k_\mathrm{o} + \partial^2\Phi/\partial d_\mathrm{o}^2 \end{pmatrix}\,, \tag{9.5}$$

where m_i and m_o are the masses (per unit length) of the inner and outer shells, respectively. We note in passing that this form of D differs from that in Ref. 21, where the partial derivatives were assumed to be equal. The RBM frequencies are finally obtained as solutions of the vibrational eigenvalue problem for the DWCNT.

The results of the relaxation of the DWCNTs with respect to a displacement of the shell axis from the coaxial position revealed that the two shells remain concentric for $\Delta d = d_\mathrm{o} - d_\mathrm{i} < 0.78\,\mathrm{nm}$. For diameter differences $\Delta d > 0.78\,\mathrm{nm}$ the inner tube moved away from the coaxial position. For coaxial shells, the relaxation of the DWCNT with respect to d_i (for fixed d_o) or vise versa yielded an equilibrium value for Δd of about $0.68\,\mathrm{nm}$.

For the following analysis, we calculated the RBM frequencies for all inner-outer tube pairs with inner tubes between $(5, 3)$ ($d_\mathrm{i} = 0.55\,\mathrm{nm}$) and $(14, 0)$ ($d_\mathrm{i} = 1.09\,\mathrm{nm}$) and possible diameter differences in the range 0.66–0.74 nm.

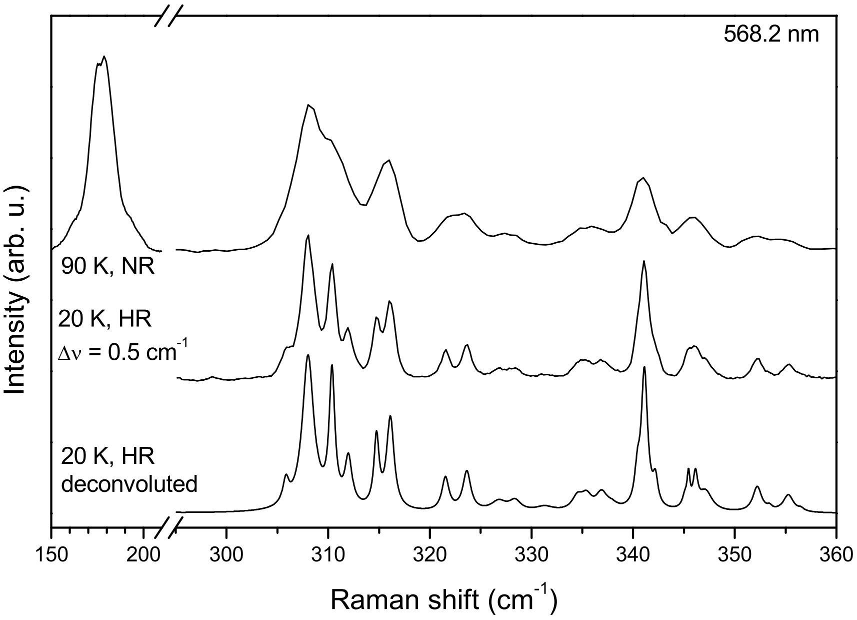

FIGURE 9.1. RBM Raman response of the inner tubes at 90 K and normal resolution, 20 K and high resolution, and Lorentzian components of the 20 K and high resolution spectrum (top to bottom).

9.4 Experimental Results

Figure 9.1 depicts the Raman response of the inner tube RBMs. While the NR spectrum shows only very broad lines, the HR spectrum reveals much richer details with rather small linewidths. This becomes even more obvious when the as measured spectrum was fitted with Voigtian lines (Lorentzians convoluted with a Gaussian spectrometer response) where the spectrometer response was taken from a fit to the elastically scattered light. The resulting Lorentzian components are equivalent to a deconvoluted spectrum [9].

Using the diameter-frequency relationship from Eq. (9.2) it is possible to determine the number of inner tubes for a given frequency range. There is some ongoing discussion on the value of C_1, where reported numbers range from 224 to 250 cm^{-1} nm [10, 22, 23]. In the following, we use the value of 233 cm^{-1} nm as derived from a systematic analysis of the inner shell tubes in DWCNTs [10].

Regardless of the exact value of C_1, between 300 and 350 cm^{-1} one should only see the response of eight different tubes. By looking at the HR spectrum in figure 9.1, one can easily identify about 18 peaks and shoulders in this range. Hence, one can observe about two to three times more RBMs as there are geometrically allowed tubes.

Figure 9.2 depicts selected high resolution Raman spectra of the inner RBMs. Using the refined frequency-diameter relation from Ref. 10, one should find the RBMs of 28 distinct inner tubes between 270 and 400 cm^{-1}. Again the observed number of lines in this region is about three times larger. For some chiralities the split widths are indicated by lines under the folding vector components.

In order to determine the number of the split components and the width of the splitting, we fitted the spectra from figure 9.2 with a number of Voigtian lines. Using the chirality assignment of Ref. 10, sets of RBM frequencies were assigned to selected inner tube types. The tubes were selected such that the assignment was unambiguous. If the frequency sets of two inner tubes overlapped the tubes were not considered in the following analysis.

For the selected inner tubes, we subtracted the mean value from the assigned frequencies and plotted the split components vs. inner tube diameter in figure 9.3. It shows that the number of split components ranges between two and four with no obvious influence of the tube chirality. Additionally, the width of the splitting is about 4 cm^{-1}. Since not all inner tubes were considered

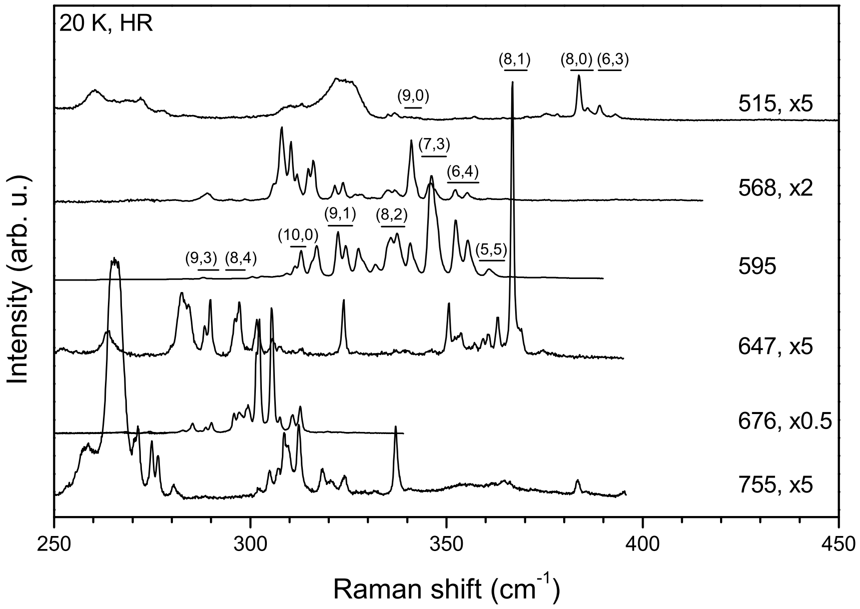

FIGURE 9.2. High resolution Raman response of the inner tube RBMs for several excitation wavelengths at 20 K. Selected chiralities after Ref. [10]. Split widths are indicated by lines under the chirality vectors.

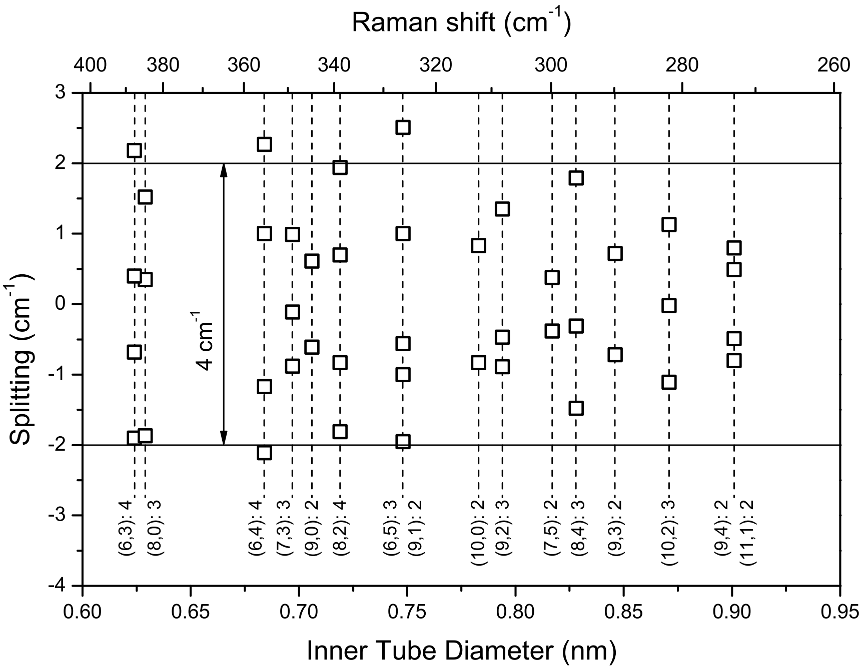

FIGURE 9.3. Number of split components and width of splitting for selected individual inner tubes from the spectra in figure 9.2 after subtracting the mean value of the RBM frequencies. The dashed lines connect split components assigned to the same inner tube. Additionally, the tube chiralities and the number of split components is included.

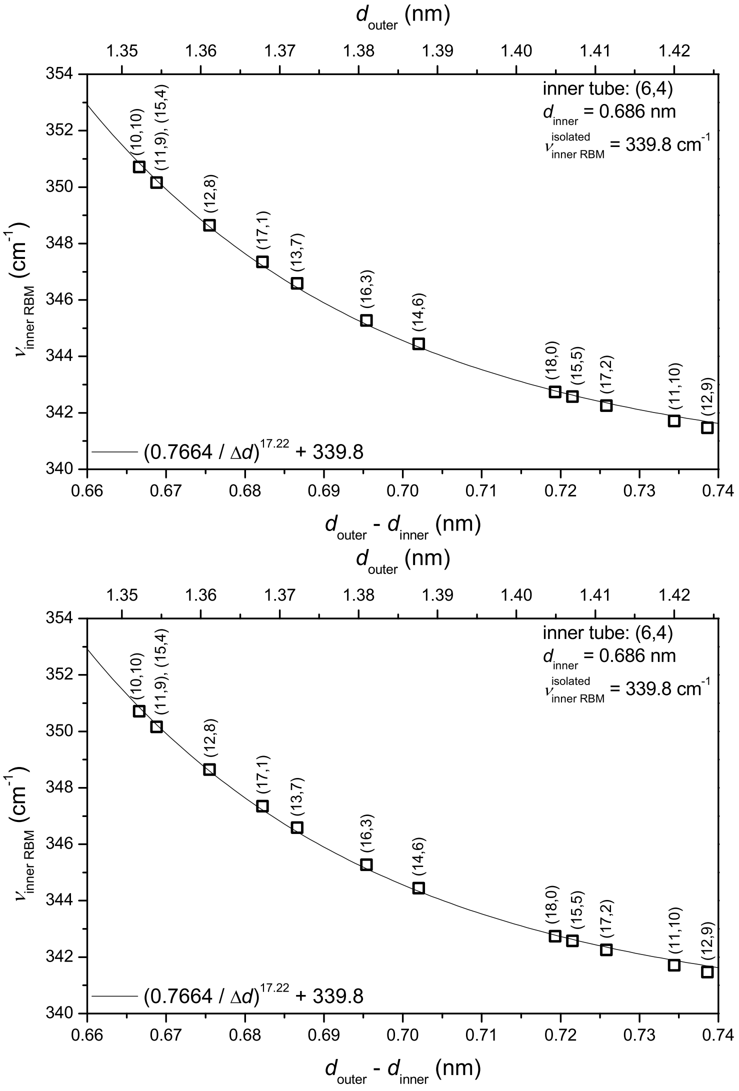

FIGURE 9.4. Top: Calculated RBM frequency of a $(6,4)$ inner tube as a function of the encapsulating tube diameter d_o. Bottom: Calculated RBM frequency of a $(10,10)$ outer tube as a function of the encapsulated tube diameter d_i. The diameters were calculated from Eq. (9.3). The lines are fits with the given parameters as indicated in the lower left corners.

in the analysis, this splitting value is a lower limit.

9.5 Simulation Results

Figure 9.4 (top) demonstrates the dependence of the calculated RBM frequency of a $(6,4)$ inner tube on the diameter of the outer tube. The isolated $(6,4)$ tube has a diameter of $d_\mathrm{i} = 0.686\,\mathrm{nm}$ and a frequency of $\bar{\nu}^{\mathrm{isolated}}_{\mathrm{inner\ RBM}} = 339.8\,\mathrm{cm}^{-1}$ (excluding C_2) [10]. Due to the interaction between the two shells, the inner RBM frequency increases by up to $12\,\mathrm{cm}^{-1}$ with decreasing outer tube diameter. In the diameter difference range studied, the RBM frequencies can be fitted with $(a/\Delta d)^b + \bar{\nu}^{\mathrm{isolated}}_{\mathrm{RBM}}$ (see figure 9.4, lower left corners).

Similarly, figure 9.4 (bottom) depicts the RBM frequency of a $(10,10)$ outer tube as a function of the inner tube diameter. Again, the larger the inner tube diameter the larger the shift of the outer tube RBM. Indeed, slight upshifts of a few cm^{-1} of the outer tube RBMs of DWCNTs were observed when directly compared with the empty reference SWCNTs. However, due to the quasi-continuous diameter distribution of the outer tubes, exact measurements are difficult.

In a first step, we assumed that in all outer tubes in our sample only the best fitting inner tubes are formed. Best fitting means that for every outer tube the inner tube was selected such that $|d_\mathrm{o} - d_\mathrm{i} - 0.68\,\mathrm{nm}|$ becomes a minimum. The splitting calculated for this assumption is depicted in figure 9.5 (top). The number of split components and the width of the splitting are smaller than the experimentally observed values. Therefore, in a second step, we assumed also the second best

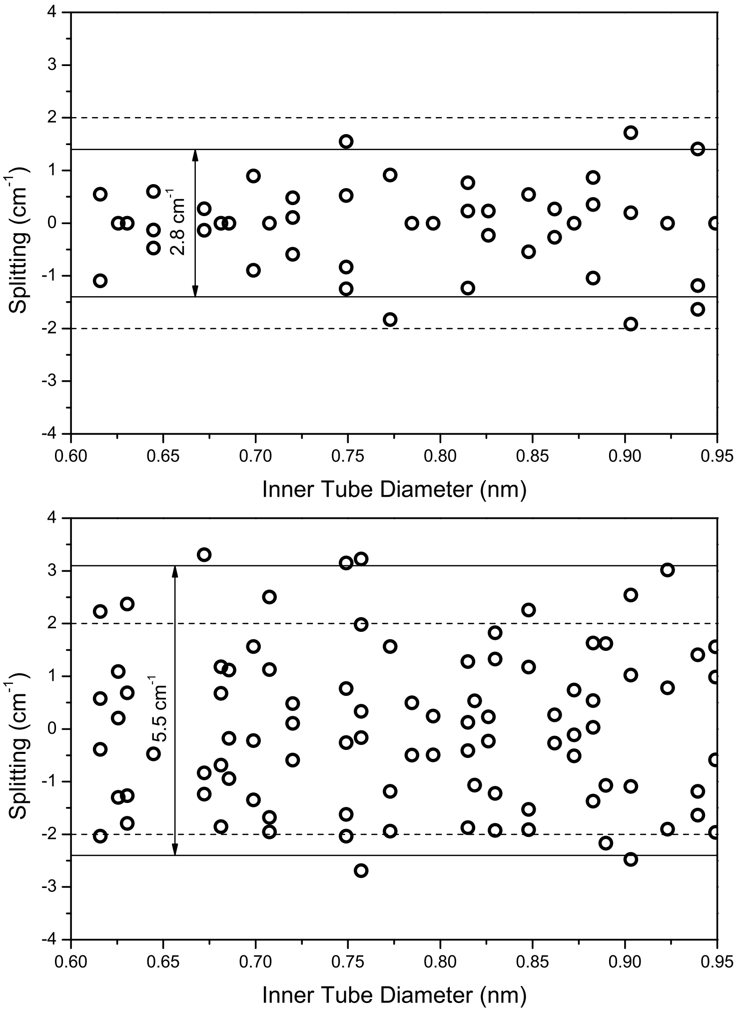

FIGURE 9.5. Number of split components and width of splitting for individual inner tubes from the theory after subtracting the mean value of the calculated RBM frequencies. Top: Only the best fitting inner tubes are formed. Bottom: The best and second best fitting inner tubes are formed. The dashed lines mark the width of splitting obtained from the experiment.

fitting inner tubes to form. As figure 9.5 (bottom) shows, this assumption results in a splitting of 5.5 cm^{-1} which is larger than observed. This suggests that also second best fitting inner tubes form in cases where the energy balance is in favor for it.

Figure 9.6 compares the percentages of the number of inner tube split components obtained from the experiment with the two theoretical models discussed above. If only best fitting inner tubes form, mainly 1, 2, and 3 split components should be observed. If best and second best fitting inner tubes form, mainly 3 and 4 split components are to be expected. The experimental curve lies between the two model curves peaking around 2–3 split components.

9.6 Comparison with Tubes in Bundles

Our calculations have shown that the upshift of the inner tube RBMs can be as high as 12 cm^{-1}. Such an upshift of the RBM frequency does not only occur for inner tubes in DWCNTs but also for SWCNTs in bundles [20, 24]. In both cases this shift is due to the van der Waals interaction with the surrounding tubes. However, in the case of the concentric tubes the interaction is between a tube outside and a tube inside whereas in the case of the bundles it is between two tube outsides. Therefore, it was interesting to compare the upshift of encaged and bundled tubes. For this comparison we used a typical HiPco sample with a broad diameter distribution such that similar tube diameters could be compared.

Figure 9.7 depicts the RBM Raman response of the inner tubes and the HiPco tubes. The two samples were measured simultaneously in the same experiment. This means, the spectra were recorded without changing the spectrometer position which guarantees a high precision of the

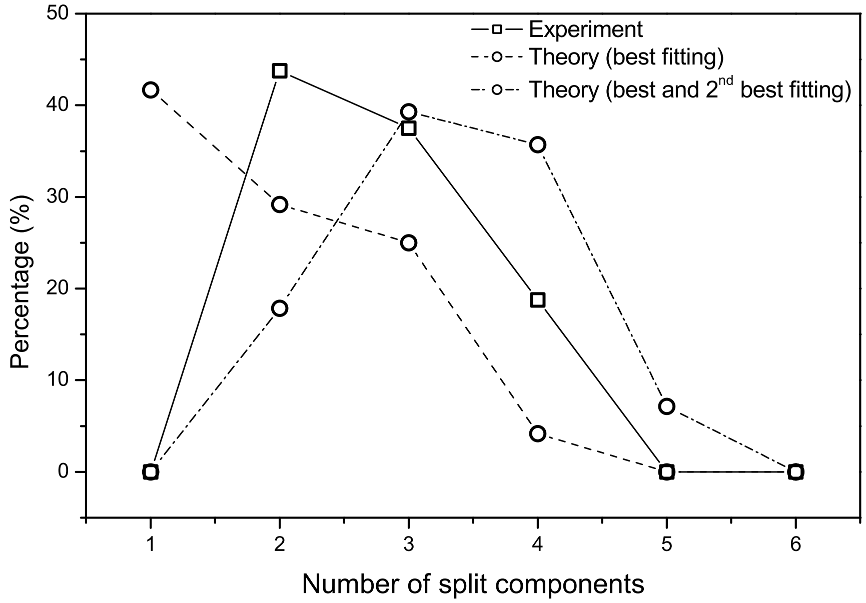

FIGURE 9.6. Percentages of the number of split components from the experiment and the two theoretical models.

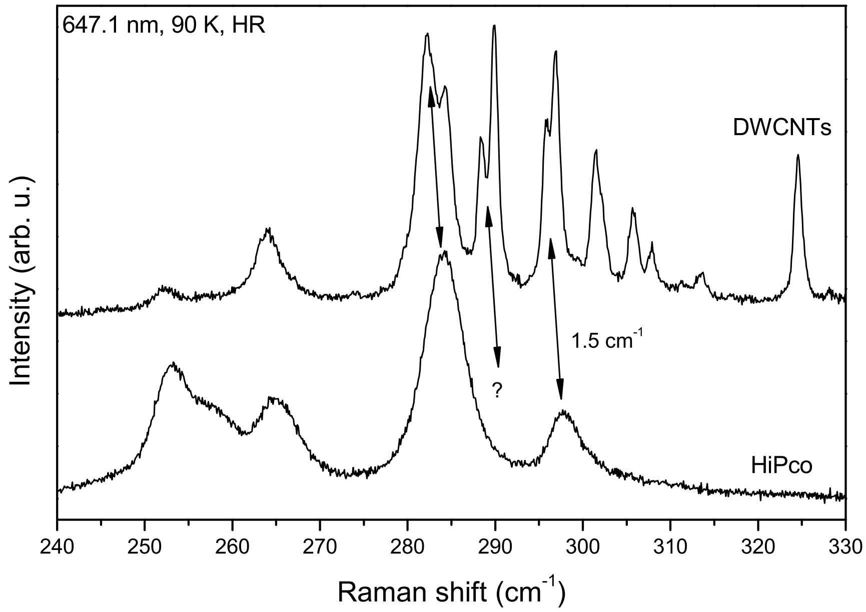

FIGURE 9.7. RBM Raman response of small diameter tubes as inner tubes of DWCNTs (top) and in a typical HiPco sample (bottom). The HiPco RBMs are 1.5 cm^{-1} more upshifted than the inner tube RBMs. Additionally, the resonances of some bundled tubes are different to the corresponding encaged tubes.

measured frequency differences. Several observations can be made in this figure. First, compared to the inner tube RBMs the HiPco RBMs are broader and do not get narrower in the HR mode. This is an important detail of the results, since it demonstrates that the narrow linewidth is not a mere consequence of the small tube diameter. It rather underlines the high quality of the inner tubes. Additionally, the HiPco RBMs may be broadened due to the inhomogeneous environment within the bundles [24].

Second, the HiPco RBMs are about $1.5\,\mathrm{cm}^{-1}$ more upshifted than the inner tube RBMs. The stronger upshift of the RBMs of the HiPco sample suggests a stronger interaction between the tubes in the bundles as compared to the interaction between the inner and outer shells of a DWCNT. This experimental evidence is rather surprising, since the interaction area for one tube in a bundle is certainly smaller than for inner-outer tube pairs. Thus, the reason for the upshift is not yet fully understood. It may be related to a larger equilibrium diameter difference in the concentric tubes as compared to the distance between tubes in the bundles. This increased distance would reduce the interaction between inner and outer tubes. There is some support for this idea from the fact that the experimentally observed wall to wall distance in the concentric tubes is slightly larger than the value expected from graphite (0.72 compared to 0.68 nm) [25]. Since the wall to wall distance enters with a high power into the interaction potential a reduced interaction is reasonable. Additionally, the inhomogenous and non-radially symmetric environment in the bundles may also play a role.

Third, some RBMs are missing in the HiPco spectrum (in this case the $(9,3)$ tube). Since the RBM response of even thinner tubes than the missing species is present in the HiPco spectrum the observed absence cannot be explained by the diameter distribution of the HiPco material. In fact, the missing lines show up for other excitation energies [26]. This means, the resonances of the encaged tubes are slightly different to the resonances in the bundled tubes. This change in resonance energy can depend on the tube chirality. In fact, a chirality dependence of the electron-lattice interaction was recently reported from *ab-initio* calculations [27].

9.7 Discussion

The continuum model we are using was parameterized for graphite [17] and subsequently used for simulations of multi-shell fullerenes [28] and multi-wall carbon nanotubes [16]. As mentioned above, it resulted in an equilibrium diameter difference of about 0.68 nm. Abe et al. [25] reported X-ray measurements that suggest a more likely diameter difference of 0.72 nm. Even though a recent Raman analysis supports this value [29], we think our main results are not affected by this difference. For larger equilibrium diameters the interaction will be weaker in general and therefore more likely reduce the calculated splitting.

In the simulations we were using, only the diameter dependence of the RBM frequency shift can be evaluated but not the influence of differing chiralities of the inner and outer tubes in one DWCNT. Due to the large unit cells of the DWCNTs such microscopic calculations would be very difficult. Only special geometries such as $(5,5)@(10,10)$ can be evaluated. Additionally, the LJ simulations are based on the approximation of the atoms with point charges. In practice, the interaction between the two layers arises from a quantum mechanical interaction between the delocalized electron density of these layers thus making the stacking less important. Furthermore, our simplification is justified by the experimental results depicted in figure 9.3 which show no obvious dependence of the number of split components on the chiral angle of the inner tube. Therefore, we conclude that the chirality plays only a minor role. On the other hand, an influence of the chirality on the interaction energy may not be completely negligible. It can be the reason for the observed best and second best fitting tube grown inside the outer tube.

The good consistency between the calculated splitting and the observed results further supports the given interpretation. With these results each component of the split lines can be assigned to a distinct double-wall pair.

Accepting the radial tube-tube interaction as the reason for the extended splitting has also important consequences for the growth dynamics. Always those tubes will grow which are energetically most favorable at the high transformation temperatures. This holds even if nucleation of inner tube growth starts at different positions in the outer tube. In our understanding, the energetically more favorable tubes will eventually "eat up" the less favorable ones. Interesting configurations occur for the growth of a chiral tube inside an achiral tube. There, the two possible stereo-isomers are equal in energy but cannot match. The proven low concentration of defects on the inner tubes evidences that always one of the equienergetic tubes will win.

9.8 Summary

We have shown that the RBMs of the inner tubes of DWCNTs are split into several components and provided a quantitative understanding from calculations. The splitting is attributed to the interaction between inner and outer tubes that causes a change of the inner tube RBM frequency. Since it is possible that one type of inner tube forms in several types of outer tubes (with slightly different diameters) every inner tube gives rise to more than one RBM in the Raman spectrum. We have further demonstrated that not only the best fitting structure is established. Finally, we have compared the RBM Raman response of inner tubes with that of similar diameter tubes in bundles. Surprisingly, the bundled tube RBMs are more upshifted than the encaged tube RBMs and some Raman lines are missing in the HiPco spectra. The latter effect is considered as a consequence of a chirality dependent shift of resonance levels.

The authors acknowledge financial support from the FWF in Austria, project P14893, and from the EU Marie-Curie project MEIF-CT-2003-501099 (PATONN). VNP was supported by a fellowship from the Federal Science Policy Office for promoting the S&T cooperation with Central and Eastern Europe, by a NATO CLG, and from the EU Marie-Curie project MEIF-CT-2003-501080.

References

[1] S. Iijima and T. Ichihashi, Nature **363**, 603 (1993).
[2] A. Thess, R. Lee, P. Nikolaev, H. Dai, P. Petit, J. Robert, C. Xu, Y. H. Lee, S. G. Kim, A. G. Rinzler, et al., Science **273**, 483 (1996).
[3] B. W. Smith, M. Monthioux, and D. E. Luzzi, Nature **396**, 323 (1998).
[4] B. W. Smith and D. E. Luzzi, Chem. Phys. Lett. **321**, 169 (2000).
[5] H. Kataura, Y. Maniwa, T. Kodama, K. Kikuchi, K. Hirahara, K. Suenaga, S. Iijima, S. Suzuki, Y. Achiba, and W. Krätschmer, Synthetic Met. **121**, 1195 (2001).
[6] F. Simon, H. Kuzmany, H. Rauf, T. Pichler, J. Bernardi, H. Peterlik, L. Korecz, F. Fülöp, and A. Jánossy, Chem. Phys. Lett. **383**, 362 (2003).
[7] S. Bandow, M. Takizawa, K. Hirahara, M. Yudasaka, and S. Iijima, Chem. Phys. Lett. **337**, 48 (2001).
[8] S. Bandow, G. Chen, G. U. Sumanasekera, R. Gupta, M. Yudasaka, S. Iijima, and P. C. Eklund, Phys. Rev. B **66**, 075416 (2002).
[9] R. Pfeiffer, H. Kuzmany, C. Kramberger, C. Schaman, T. Pichler, H. Kataura, Y. Achiba, J. Kürti, and V. Zólyomi, Phys. Rev. Lett. **90**, 225501 (2003).
[10] C. Kramberger, R. Pfeiffer, H. Kuzmany, V. Zólyomi, and J. Kürti, Phys. Rev. B **68**, 235404 (2003).
[11] H. Kuzmany, W. Plank, M. Hulman, C. Kramberger, A. Grüneis, T. Pichler, H. Peterlik, H. Kataura, and Y. Achiba, Eur. Phys. J. B **22**, 307 (2001).
[12] H. Kuzmany, R. Pfeiffer, C. Kramberger, T. Pichler, X. Liu, M. Knupfer, J. Fink, H. Kataura, Y. Achiba, B. W. Smith, et al., Appl. Phys. A **76**, 449 (2003).
[13] X. Liu, T. Pichler, M. Knupfer, M. S. Golden, J. Fink, H. Kataura, Y. Achiba, K. Hirahara, and S. Iijima, Phys. Rev. B **65**, 045419 (2002).
[14] J. H. Hafner, M. J. Bronikowski, B. R. Azamian, P. Nikolaev, A. G. Rinzler, D. T. Colbert, K. A. Smith, and R. E. Smalley, Chem. Phys. Lett. **296**, 195 (1998).
[15] P. Nikolaev, M. J. Bronikowski, R. K. Bradley, F. Rohmund, D. T. Colbert, K. A. Smith, and R. E. Smalley, Chem. Phys. Lett. **313**, 91 (1999).
[16] V. N. Popov and L. Henrard, Phys. Rev. B **65**, 235415 (2002).

[17] J. P. Lu, X.-P. Li, and R. M. Martin, Phys. Rev. Lett. **68**, 1551 (1992).

[18] R. A. Jishi, L. Venkataraman, M. S. Dresselhaus, and G. Dresselhaus, Chem. Phys. Lett. **209**, 77 (1993).

[19] J. Kürti, G. Kresse, and H. Kuzmany, Phys. Rev. B **58**, R8869 (1998).

[20] L. Henrard, E. Hernández, P. Bernier, and A. Rubio, Phys. Rev. B **60**, R8521 (1999).

[21] E. Dobardžić, J. Maultzsch, I. Milošević, C. Thomsen, and M. Damnjanović, phys. stat. sol. (b) **237**, R7 (2003).

[22] A. Jorio, R. Saito, J. H. Hafner, C. M. Lieber, M. Hunter, T. McClure, G. Dresselhaus, and M. S. Dresselhaus, Phys. Rev. Lett. **86**, 1118 (2001).

[23] S. M. Bachilo, M. S. Strano, C. Kittrell, R. H. Hauge, R. E. Smalley, and R. B. Weisman, Science **298**, 2361 (2002).

[24] L. Henrard, V. N. Popov, and A. Rubio, Phys. Rev. B **64**, 205403 (2001).

[25] M. Abe, H. Kataura, H. Kira, T. Kodama, S. Suzuki, Y. Achiba, K.-i. Kato, M. Takata, A. Fujiwara, K. Matsuda, et al., Phys. Rev. B **68**, 041405(R) (2003).

[26] F. Simon, R. Pfeiffer, C. Kramberger, M. Holzweber, and H. Kuzmany, *The Raman response of double wall carbon nanotubes* (Springer New York, 2005), pp. 203–224.

[27] M. Machón, S. Reich, J. Maultzsch, P. Ordejón, and C. Thomsen, in *Proceedings of the IWEPNM* (2004), in print.

[28] J. P. Lu and W. Yang, Phys. Rev. B **49**, 11421 (1994).

[29] F. Simon, A. Kukovecz, C. Kramberger, R. Pfeiffer, F. Hasi, H. Kuzmany, and H. Kataura, Phys. Rev. B **71**, 165439 (2005).

10

Resonance Raman scattering from phonon overtones in double-wall carbon nanotubes

R. Pfeiffer, H. Kuzmany, F. Simon, S. N. Bokova, and E. Obraztsova

Physical Review B **71**, *155409 (2005).*

ABSTRACT The resonance behavior and the dispersion of the G′ line in double-wall carbon nanotubes were investigated by multi-frequency Raman scattering. Using a large number of laser lines for excitation, the dispersion for the response from the inner tubes and from the outer tubes was found to be 85 and 99 cm^{-1}/eV, respectively. The reduction of the dispersion for the inner tubes is a consequence of their high curvature and suggests a flattening of the phonon dispersion at the K point in the Brillouin zone. The frequency position for the G′ line of the inner tubes for a given laser energy was likewise strongly reduced as compared to values expected from tubes with standard diameter. This was again assigned to the strong curvature of the small diameter inner tubes. Finally, the G′ line scattering cross-sections for the outer tubes and for the inner tubes revealed resonances according to the transitions between the corresponding Van Hove singularities. The response from the inner tubes was particular strong in good agreement with the expected resonance enhancement resulting from their high curvature.

10.1 Introduction

Single-wall carbon nanotubes (SWCNTs) have been attracting considerable interest for a number of years as they are very good examples for one-dimensional systems on the one hand and exhibit a high application potential on the other hand. [1–3] Recently, particular attention has been dedicated to double-wall carbon nanotubes (DWCNTs). Such systems are of special interest if the inner shell tubes are grown from fullerenes encapsulated into the primary outer shell tubes (so-called peapods [4]). [5] On heating to temperatures as high as 1250 °C the fullerenes in the peapods transform into inner shell tubes with a high degree of perfectness. [6]

Peapod grown DWCNTs are exceptional for several reasons. Normally, peapods are obtained from SWCNTs with mean tube diameters between 1.3 and 1.5 nm. Since the intertube distance in the DWCNTs is about 0.35 nm (the interlayer distance in graphite), the diameters of the inner shell tubes are around 0.7 nm, coming close to SWCNTs grown in zeolites. [7, 8] The diameter distribution of the inner tubes is expected to follow roughly the distribution of the outer ones, except for a cut off below 0.5 nm. [9] This cut off is a consequence of the rather large size of the fullerenes which cannot enter tubes with diameters smaller than about 1.2 nm.

Referring to applications, DWCNTs share the advantages of multi-wall tubes in a sense that they are rather stiff and properties from the two shells average out. Conversely, they still have some advantages of SWCNTs, e.g., small diameters and low weight. For fundamental research, the very small radii of the inner tubes are of particular interest. Additionally, the unit cells become small enough to allow for application of density functional calculations. Such calculations are indeed necessary to describe the physical properties as a consequence of the high curvature of the narrow tubes.

One of the famous and important properties of the SWCNTs is their electronic structure. Due to the one-dimensional nature of the tubes the electronic density of states is jammed into Van Hove singularities (VHSs). Within a simple tight-binding approximation, optical transitions are between VHSs symmetric to the Fermi level. The transition energies for semiconducting and metallic tubes are assigned as E_{ii}^{S} and E_{ii}^{M}, respectively. In a linear approximation, these energies scale with $1/D$, where D is the tube diameter. [10] In a refined description, the trigonal warping of constant energy contours and the influence of the chirality must be considered. [10] Symmetry-adapted non-orthogonal tight-binding calculations yield more precise results with lower transition energies and a stronger deviation from a $1/D$ law since tube curvature is included. [11] In addition, the exact values for the electronic energies are modulated by excitonic effects, particularly for the low i transitions [12] and by the effect of bundling or dressing with surfactants. Finally, and certainly of particular importance for very small inner shell tubes, the influence of the curvature must be considered explicitly. If the tube diameters become significantly lower than 1 nm, characteristic differences in the electronic structure as compared to tight-binding results were reported from *ab initio* calculations. [13]

A plot of the transition energies vs. tube diameter for all geometrically allowed tubes, known as Kataura plot [16], is very helpful and important to understand optical and resonance Raman effects. The plot depicted in Fig. 10.1, with the inverse tube diameter used on the abscissa, is based on calculations by Popov [11]. The calculated energies from this work were subsequently scaled to match the experimental ones of Fantini et al. [14] and Weisman and Bachilo [15] (obtained from HiPco tubes dispersed in aqueous solution and wrapped in SDS). The scaling factors for each transition and SWCNT type (metallic as well as semiconducting type I and II) depended linearly on the inverse tube diameter. The horizontally hatched area marks the range of laser energies used in our experiments. The vertically hatched areas mark the diameter distribution of the outer (left) and inner tubes (right), respectively.

Raman spectroscopy has been demonstrated in numerous experiments to be a key analytical technique for the investigation of SWCNTs. The resonance enhancement for transitions between VHSs makes the technique particularly appealing. Four characteristic Raman modes are known: The radial breathing mode (RBM) around 180 cm^{-1}, the defect line (D mode) around 1350 cm^{-1},

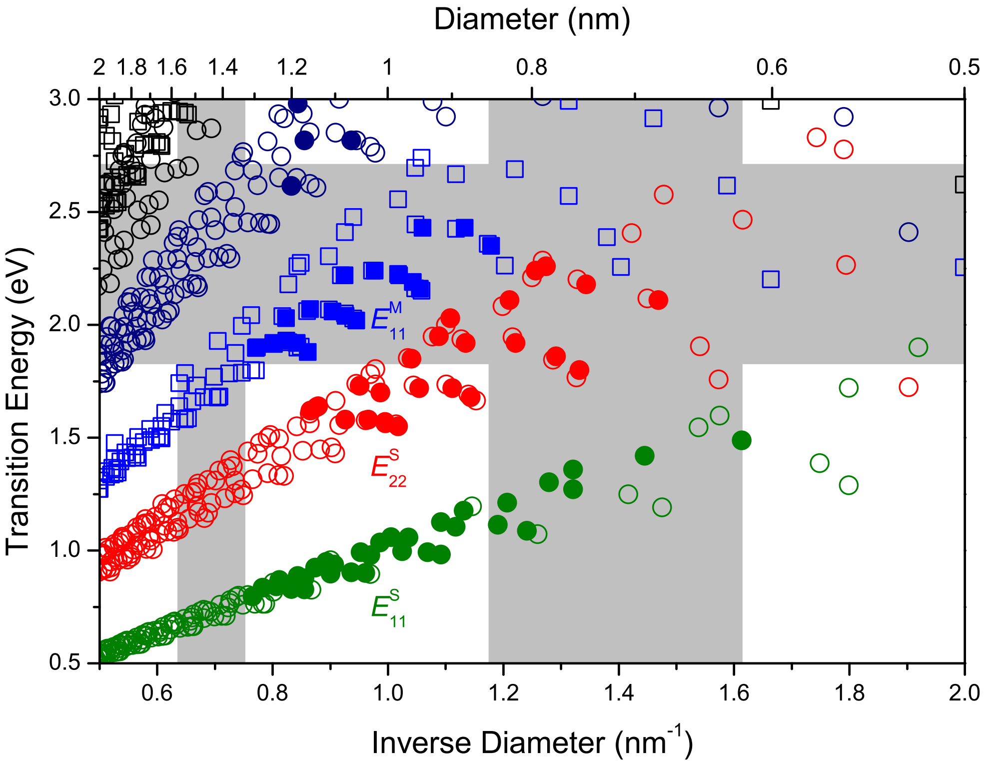

FIGURE 10.1. Transition energies vs. inverse diameter of SWCNTs (Kataura plot), based on calculations by Popov [11] (open symbols). The calculated energies were scaled to fit the experimental results of Fantini et al. [14] (filled symbols for E_{22}^{S} and E_{11}^{M}). The E_{11}^{S} branch was taken from Weisman and Bachilo [15]. The hatched areas assign the energy range used for excitation of Raman spectra (horizontally) and the tube diameter ranges for outer (left) and inner tubes (right). The widths of the vertical bars are the FWHMs of the assumed Gaussian distributions.

the graphitic mode around 1590 cm^{-1} (G mode) and the overtone of the D mode around 2700 cm^{-1} (G′ or D* mode).

For all lines the frequency depends on the tube diameter. This dependence is rather strong and scales as the inverse tube diameter for the RBM whose frequency increases with decreasing diameter. [17, 18] The frequencies for the other Raman lines also depend on the inverse diameter, however, they decrease with decreasing tube diameter.[19, 20]

Additionally, the line position depends also on the energy of the exciting laser. This holds at least for the RBM, the D line, and the G′ line and is known as dispersion of the Raman modes. The origin of the dispersion is characteristically different for the RBM response on the one side and for the D and the G′ lines on the other side. In the former case it is related to a photoselective resonance scattering which requires a distribution of tube diameters in the sample. In contrast, in the case of the D line and the G′ line the response comes from phonons related to the K point in graphene, or from phonons close to this point.[21, 22] A double resonance scattering process was found to be the origin of the dispersion [22], similarly as it has been reported for graphene [21] and the magnitude of the effect (shift in line position versus change in excitation energy) is determined by the slope of the phonon dispersion near the K point in graphite.[23]

Double resonance Raman scattering is well known in resonance Raman theory. It was recently applied to understand the D line in SWCNTs in a quantitative manner [22–24]. To satisfy energy and momentum conservation scattering by an impurity must be included into the overall Raman process for the D line. For the double resonance leading to the G′ line the process is similar but no contribution from a defect is required, rather a second phonon takes care for momentum conservation. The principle of this mechanism as it is operating for the two phonon process is depicted in Fig. 10.2.

The figure depicts contours of equal energy at two neighboring K points of the graphene band

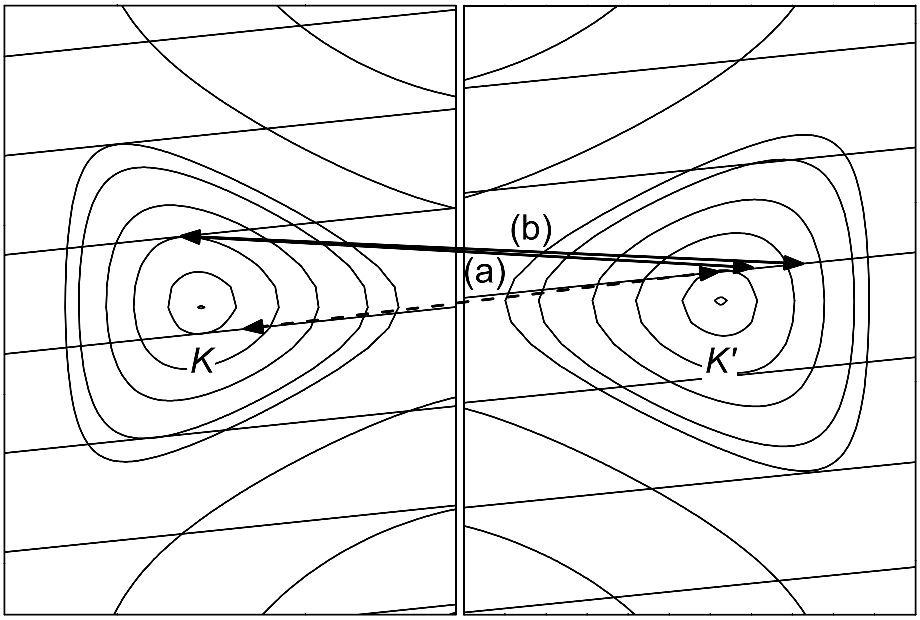

FIGURE 10.2. Double resonance scattering for the Raman response of the G$'$ line in SWCNTs. Closed curves: equal energy contours of the graphene band structure, parallel lines: allowed k-states for a $(8,4)$ tube. Full drawn arrows represent double resonance scattering processes for the incoming (a) and for the outgoing (b) light where Van Hove singularities are involved (triple resonance). The dashed arrow represents also a triple resonance but with less efficiency.

structure. The parallel lines are the allowed k states for a $(8,4)$ tube. The two full drawn arrows depict two examples for particular strong resonance enhancements (triple resonance).[23] For the arrow (a) the primary electron-hole excitation meets a transition between two VHSs (ingoing resonance). The scattering from K to K' by the phonon $(\hbar\Omega_q, q)$ ends on an eigenstate of the tube which is in general not a VHS. Backscattering by the phonon $(\hbar\Omega_q, -q)$ takes the electron back to its original k value but at an energy $2\hbar\Omega_q$ below the eigenstate (for Stokes scattering). The final recombination is therefore non resonant. For the outgoing resonance (vector (b)) the primary electron-hole excitation is non resonant, scattering is to a SWCNT state on the K' position and back scattering is into the VHS on the K position. As far as the incoming light is concerned the difference in energy between the two resonances is as large as $2\hbar\Omega_q = 0.33\,\text{eV}$ where q is (almost) the wave vector of the K point phonon. An alternative but less efficient triple resonance occurs if the electron is scattered to the VHS on the K' side and either the primary excitation or the final recombination is non resonant. In all cases two transitions are in resonance whereas the third transition is off resonance. In addition, for the triple resonance of the ingoing and outgoing resonance two VHSs are involved. Double resonance may as well occur between any two appropriate states on the two K points. It does not need the VHSs. This means the expected resonance profiles may be rather broad. The theory for double resonance scattering for the G$'$ line is more complicated than the theory for the D line, since the two phonon density of states for the K point derived phonons has to be considered. As a consequence of the zone folding many branches can contribute.

Whereas considerable investigations have been dedicated to the RBM analysis in the DWCNTs [6, 25] very little has been reported on the G line response [26] and almost nothing is known about the D and G$'$ lines. The D line response is important since its intensity is related to the number of defects in the tubes. Since the RBM response from the inner shell tubes exhibits unusual narrow lines [6] the relative concentration of the defects must be small and only a weak D line response is expected. On the other hand, small tube diameters enhance the electron-phonon (e-ph) coupling [27] which raises Raman intensities. Unfortunately, the D line of SWCNTs exhibits a structured profile [24] as a consequence of the resonance from the VHSs and the warped energy contours. Since the diameter dependence of the D mode frequency is rather small [19], the contributions from inner and outer shell tubes overlap in general and are not easy to separate. Therefore, in this contribution we concentrate on the behavior of the G′ line where the separation between response from the inner tubes and outer tubes is twice as high as for the D line. Since the G′ line response is independent of any defect concentration and the inner tube response still gains from enhanced e-ph coupling, a strong signal from the inner tubes is expected.

The response from the outer and from the inner tubes was indeed found to be well separated. In fact, the separation was more than twice as strong as expected from results reported previously for the diameter dependence of this mode as analyzed from individual SWCNTs [19]. Peak resonances were different for the two tube species but could be correlated to ingoing and outgoing resonances of the light with respect to VHSs. The resonance cross-section was strongly enhanced for the inner shell tubes but explicit evaluation of the enhancement was difficult due to secondary effects such as a shielding of the inner tubes by the outer ones (antenna effect).

10.2 Experimental

Nanotubes were purchased from Nanocarblab and filled with C_{60} fullerenes as reported previously [28]. The diameter distribution of the starting material was determined from Raman analysis and revealed for the peak and for the variance of a Gaussian distribution the values $\overline{D} = 1.45\,\mathrm{nm}$ and $\sigma = 0.1\,\mathrm{nm}$, respectively. The resulting mats of bundled peapods were vacuum annealed at 800 K to get rid of any non encapsulated C_{60}. Measurements of the filling ratio using bulk sensitive electron energy loss spectroscopy [29] and Raman spectroscopy [30] revealed a maximum C_{60} occupancy of about 80 %. This is very close to the theoretical limit of 95 % expected for the tubes used. Under theses conditions the absolute filling of the outer tubes with inner shell tubes which means the ratio of carbon atoms in the outer tubes to the carbon atoms in the peas is 0.28. Of course this ratio remains after the transformation to the DWCNTs. After the 800 K annealing the peapods were subjected to a high temperature annealing at 1250 °C and subsequently slowly cooled to room temperature. The resulting DWCNTs exhibited very narrow Raman lines for the RBM down to $0.4\,\mathrm{cm}^{-1}$. [6] Control experiments were performed with slightly smaller tubes grown by laser ablation and purchased from Tubes at Rice. Diameter distribution, again as determined from first and second moments of the RBM response in Raman experiments was given by $\overline{D} = 1.35\,\mathrm{nm}$, $\sigma = 0.1\,\mathrm{nm}$. Preparation of the DWCNTs was performed as described above. The smaller tube diameter certainly leads to a smaller fraction of DWCNTs relative to the unfilled tubes in these sample as compared to the fraction in the Nanocarblab material but otherwise the results were the same.

Raman spectra were recorded for laser lines extending from 1.83 to 2.71 eV at ambient conditions using a Dilor xy triple spectrometer with a back thinned and blue enhanced CCD detector. Since the lines of interest here were rather broad, normal resolution was used. The system was calibrated for intensities with Si powder ($\lessapprox 250\,\mu\mathrm{m}$). The integrated intensity of the Si first-order phonon mode was divided by the incident laser power and then scaled to the Si Raman cross-section reported by Renucci et al. [31] with a factor f. To obtain the Raman cross-section of the G′ mode its integrated intensity was divided by the incident laser power and then scaled with the same factor f. This procedure corrects for the spectrometer/detector sensitivity and the ω^4 dependence of the Raman process.

10.3 Results

Figure 10.3 depicts the response of the G′ mode for the three basic materials under investigation: pristine SWCNTs, peapods, and the resulting DWCNTs, all recorded for the same starting material and the same laser excitation. The response from the pristine material and from the peapods exhibits a smooth line profile with a quasi Voigtian shape. Looking into details, flat structures and a weak asymmetry can be observed. Such structures could originate from the $A_1(\mathrm{L})$ branch

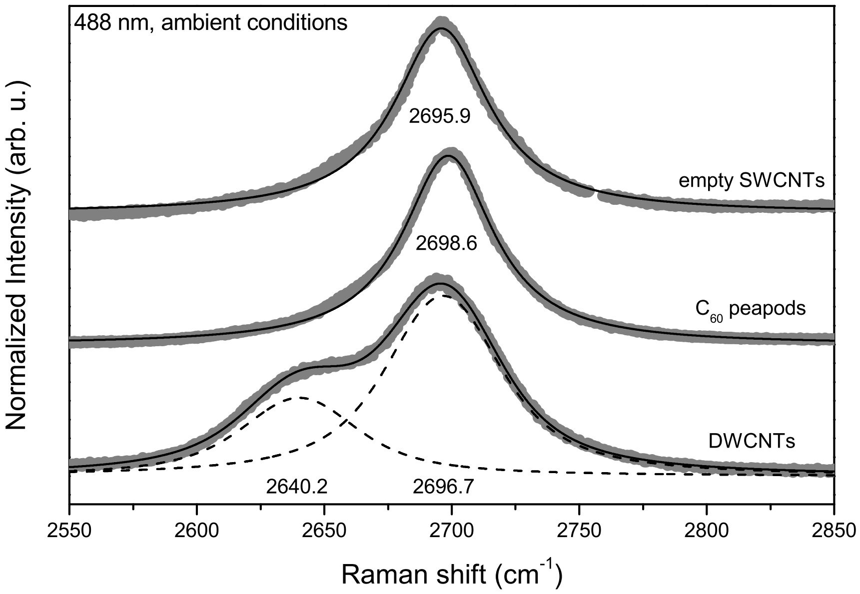

FIGURE 10.3. Raman response of the G′ line in various carbon nanotube materials as exited with a 488 nm laser. Top: pristine nanotubes, center: peapods, bottom: DWCNTs. Dashed lines are Voigtian fits. All spectra are normalized to equal height.

for metallic tubes which is known to be dramatically downshifted due to e-ph coupling [20]. Also, the peak position of the lines are modulated and located at 2696 and 2699 cm^{-1} for the pristine material and the peapods, respectively. The line widths are about 45 (pristine tubes) and 43 cm^{-1} (peapods). In the case of the DWCNTs a clear shoulder has developed at the low frequency side of the G′ response from the outer tubes.

This shoulder is assumed to originate from the G′ line of the inner shell tubes. From the Voigtian fits the line positions for the lower and higher frequency peak are at 2640 and 2697 cm^{-1}, respectively, with widths of 55 and 54 cm^{-1}. Since the G′ line is known to exhibit a characteristic resonance profile it was certainly interesting to check for such profiles in the peapods and in the DWCNTs.

Results for excitation with various lasers are depicted in Fig. 10.4 for the peapods. The response exhibits the expected result. The G′ line shifts continuously downwards without any dramatic change of its shape. Even though intensities are not yet calibrated a noticeable drop in the cross-section can be expected from the noisy spectra for red laser excitation.

Details of the dispersion and of the resonance excitation can be obtained from a fit of all spectra to Voigtian lines and making use of the calibration of the spectrometer. Results for both, the dispersion and the resonance cross-section are depicted in Fig. 10.5. The dispersion exhibits on the average a straight line with a slope of 96.2 cm^{-1}/eV. On top of this line an oscillatory behavior of the response can be seen as it is well known for the pristine tubes. [23] The slope of the line is slightly smaller than the slope obtained for pristine tubes reported to be 110(3) cm^{-1}/eV.[23]

To obtain the cross-section for second order scattering $|d\chi(\omega)/dQ|^2$ the spectra were calibrated as described above. No additional correction for absorption was included, since it is not well enough known. The cross-section obtained in this way is continuously increasing with increasing laser energy with a very broad hump around 2.1 eV, a shoulder around 2.5 eV and an onset of a peak value at 2.7 eV. Any correction for absorption would only lead to a further increase of the cross-section with increasing light energy, since the absorption of bucky paper is continuously increasing with the latter. Thus, the scattering volume is decreasing with increasing energy. The pattern obtained is very similar to the response from the outer shell tubes in the DWCNTs and will therefore be described in more detail in the discussion of the latter results.

The response of the G′ lines in the DWCNTs is depicted in Fig. 10.6 as excited for various lasers. Again clear evidence can be seen for the dispersion effect of both lines and for a resonance

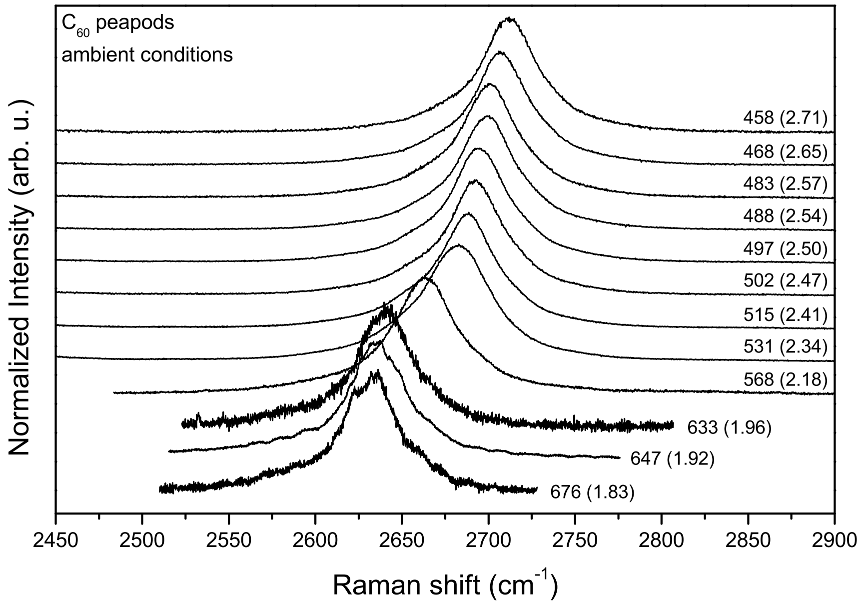

FIGURE 10.4. Raman response of the G′ line in peapods as recorded with various lasers indicated in the figure in nm (eV). All spectra are normalized to equal height.

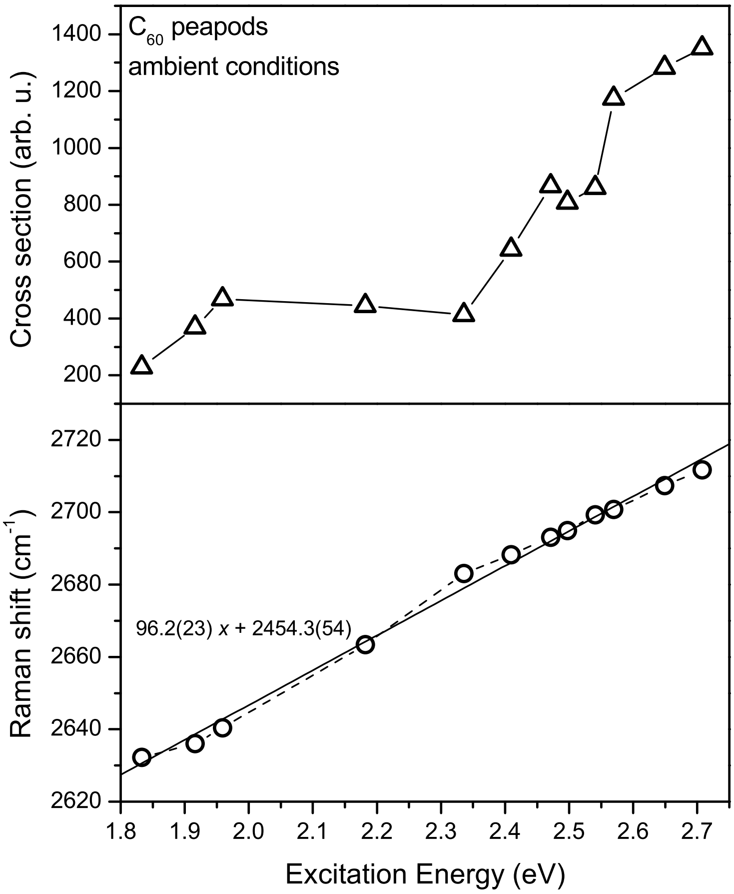

FIGURE 10.5. Dispersion (circles) and Raman cross-section (triangles) of the G′ line in peapods. The straight line indicates the linearized response. The dashed line along the experimental points is a guide for the eye and demonstrates the oscillatory behavior.

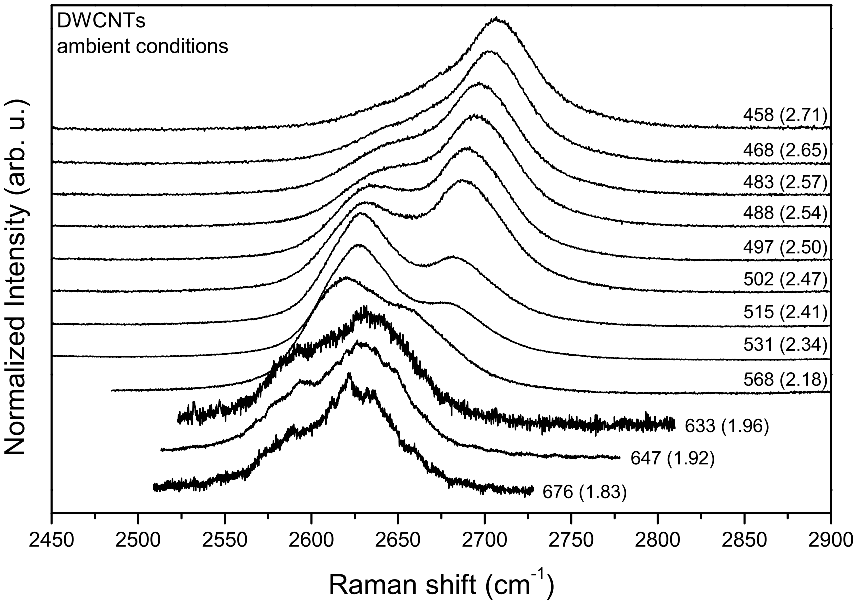

FIGURE 10.6. Raman response of the G′ lines in DWCNTs as recorded with various lasers indicated in the figure in nm (eV). All spectra are normalized to equal height.

behavior which differs for the response from the two concentric shells. In the case of green and yellow laser excitation the response from the inner tubes is stronger than the response from the outer tubes, even though the concentration of carbons in the inner tubes per volume is only about 28 % of the concentration of carbons in the outer tubes. Eventually, for excitation with deep red light the spectra become very weak and the intensity from the inner tubes G′ line drops again to below the response from the outer tubes G′ line. This indicates a rather sharp resonance profile for the inner tubes as compared to the outer tubes.

Like in the case of the peapods a fit of Voigtian lines to the spectra reveals the dispersion. Figure 10.7 shows the result for the peak positions as a function of laser energy for both shells. As expected, the relations are quasi linear in both cases with a superimposed oscillation. This oscillation is out of phase for the two shells. In addition, there is a noticeable difference in the slope of the lines. For the outer tubes we find 99.1 cm^{-1}/eV whereas the G′ line for the inner tubes yields 85.4 cm^{-1}/eV. This difference is significant as the RMS error as depicted from the figure is much smaller than this difference. In fact the real error is still considerably lower, since the oscillatory behavior has not been considered in the evaluation of the error.

Figure 10.7 also depicts the difference in mode frequency for the two G′ lines as evaluated from the straight line to straight line distance at 2.41 eV excitation energy. The obtained distance is much larger than the distance evaluated from the relation

$$\bar{\nu} = 2708.1 - 35.4/D\,. \tag{10.1}$$

This relation was derived from a diameter dependent evaluation of line shifts in individual tube experiments [19] for tubes with diameters between 1.25 and 2.5 nm at 2.41 eV. The above equation yields 2684 cm^{-1} for the outer tube G′ frequency in very good agreement with the result of 2684 cm^{-1} from the DWCNT experiments reported here but much too high values (2658 cm^{-1} as compared to 2628 cm^{-1} observed here) for the inner tubes. The dash-dotted line in the figure indicates the position of the G′ mode for the inner tubes as predicted from Eq. (10.1) if the same slope is assumed as it was observed for the inner shell tubes.

Evaluation of Raman intensities is not a trivial task and needs a careful calibration and alignment of the experiments. Even then, results may be dressed with a substantial error. If two lines from the same spectrum are compared these problems are almost excluded and results almost free of error can be expected. The results of Fig. 10.6 are very suggestive to proceed with the analysis in this form. Peak intensities were obtained from the line fit analysis and the results are shown in

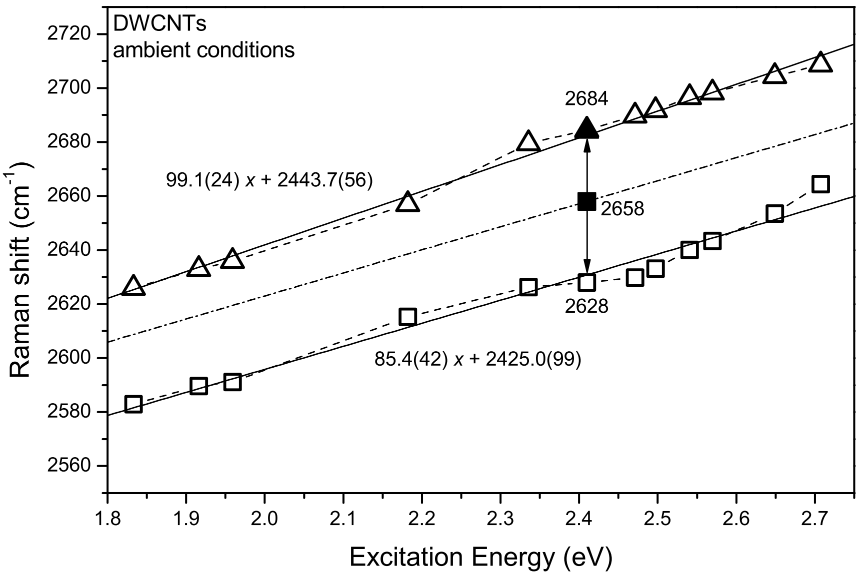

FIGURE 10.7. Dispersion of peak positions for the G′ mode of the outer (upper graph) and inner (lower graph) tubes in a DWCNT system. The dashed lines are guides for the eye to demonstrate the oscillatory behavior. The arrow assigns the distance between outer and inner tube frequency at 2.41 eV. The dash–dotted line is the linearized dispersion expected from individual tube experiments [19] if the same slope is assumed as it was observed for the inner shell tubes.

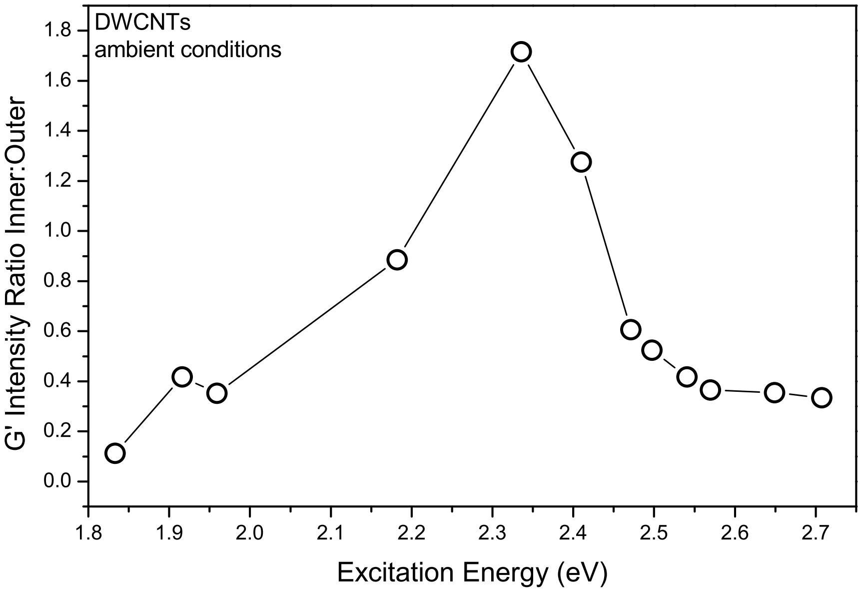

FIGURE 10.8. Peak intensity ratio of inner tube response divided by outer tube response as a function of laser excitation for the G′ modes of DWCNTs.

Fig. 10.8.

The graph shows a clear maximum at 2.34 eV with an asymmetric energy distribution on the left and on the right side of the peak. No correction for the different amounts of carbon in the two shells was performed since this would only yield a different scale on the ordinate. The peak is expected to be close to the energy where the resonance cross-section for the inner tubes has a maximum. At low energies the response from the inner tubes drops much faster than the response from the outer tubes. In contrast at high energies the ratio between scattering from inner and outer tubes approaches a constant value.

More detailed information can be drawn from an evaluation of the scattering cross-section for the two shells explicitly.

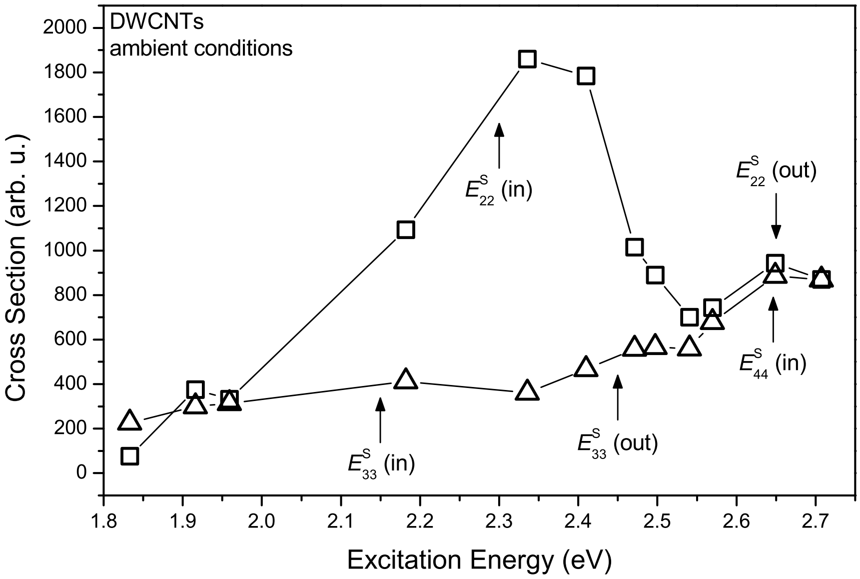

FIGURE 10.9. Raman cross-section for the G' line of the inner (squares) and outer tubes (triangles). The measured response was corrected for the different amounts of carbon in the two shells. Arrows mark the mean transition energies as depicted from Fig. 10.1.

Looking at the cross-section of the inner tubes in Fig. 10.9, we recognize immediately the dramatic enhancement as compared to the outer tubes. This enhancement is up to a factor five for the corresponding peak positions around 2.3 eV. Also, the resonance is rather narrow and peaks at 2.35 eV as expected from Fig. 10.8. At the high energy end of the profile a second peak appears around 2.65 eV. At the low energy side the cross-section approaches zero. The overall recorded enhancement of the resonance is about 25. The scattering cross-section of the outer tubes is different to the cross-section of the inner tubes but very similar to the result obtained for the peapods in Fig. 10.5. It is continuously increasing with increasing laser energy and exhibits several broad humps or shoulders around 2.15, 2.5, and 2.65 eV. These humps as well as the peak and the shoulder observed for the inner tubes are expected to be correlated to the resonance transitions between the VHSs. The overall enhancement of the cross-section for the outer tubes is about 4.

10.4 Discussion

The above findings are interesting on mainly three points: The strongly enhanced e-ph coupling for the inner shell tubes, the resonance profiles for the two concentric shells, and the deviation of the dispersion for the inner tubes from results known so far.

10.4.1 Enhanced electron-phonon coupling

Enhancement of e-ph coupling with increasing curvature in carbon cages was already observed from *ab initio* calculations in fullerenes. [32, 33] The increasing contribution of the σ bonding to the interaction between the carbon atoms is the reason. Results in the same direction were obtained for the nanotubes. Even though such results were evaluated for the e-ph coupling in the conduction band [27] or exhibit a strong dependence on chirality [34, 35] they can be expected to provide a qualitative information on the relation between coupling and tube diameter. From an extrapolation of the e-ph coupling constants evaluated in Ref.[27] the latter are about 1.6 times higher for the tubes with diameter 0.7 nm as compared to the tubes with 1.45 nm. Since the e-ph coupling enters to the 4th power into the Raman intensity for a two phonon process, intensities from the inner shell tubes can be expected to be 8 times higher as compared to the intensities from the outer shell tubes. The enhancement of the cross section observed experimentally is not quite as high. This may be due to a partial shielding of the inner tubes by the outer tubes or by field induced charges which generate a depolarization field [36] (antenna effect). A first experimental evidence for the enhanced e-ph coupling was already obtained from the strongly enhanced Raman response reported for the RBM modes [6]. The experimental demonstration of the enhancement of the e-ph coupling is important for the characterization of the inner shell nanotubes. Since these tubes are highly defect free any response from the D line should be very weak unless enhanced e-ph coupling raises the scattering cross section.

10.4.2 Resonance profiles for the two concentric shells

The resonance profile for Raman excitation in SWCNTs is determined by transitions between VHSs as they are plotted in Fig. 10.1. Since Fig. 10.1 is based on dispersed HiPco tubes wrapped with SDS, it is not straightforward to apply it to DWCNTs. In fact, Fantini et al. [14] reported that the transition energies of HiPco tubes in bundles are about 75 meV below the corresponding energies of the SDS wrapped tubes. Fortunately, the resonances we are discussing for the G′ lines are rather broad. This means the results of Fig. 10.1 provide still a valuable information for the interpretation of the data. This holds in particular since curvature effects, which are relevant for the small diameter inner tubes, are included in the calculation. Also, it must be kept in mind that the cross sections we are discussing here refer to the overall material consisting of many different tubes. It is not the cross section of a single nanotube itself. For the assignment of the observed resonances ingoing as well as outgoing light must be considered, since for the high frequencies under consideration the difference in transition energy can be as high as 0.33 eV.

Starting with the analysis of the inner shell tubes and comparing the resonance positions with the data of Fig. 10.1, we can assign the resonance at 2.3 eV to the transitions E_{22}^{S}. In addition, ingoing resonances for E_{11}^{M} transitions contribute. According to Fig. 10.1, the resonance can be rather broad, up to 1 eV which is indeed the case. Thus, according to the condition of the experiment, the resonance is determined by the distribution of tube diameters rather than by the widths of the transitions between VHSs. The resonance at 2.65 eV fits to the transition E_{22}^{S} for the outgoing photons. In this case the excitation energy has to be about 0.33 eV higher than the resonance transition. This is exactly the case for the shoulder in the cross section. The overall background in the cross section comes from the conventional double resonance and from the less efficient triple resonance which does not involve two VHSs.

For the outer tubes we can correlate the broad low energy hump around 2.15 eV with the resonance at the E_{33}^{S} transition for the incoming photons. The shoulder at 2.5 eV fits well to the E_{33}^{S} transition for the outgoing photons, whereas the structure at highest energy (2.65 eV) matches well with the ingoing E_{44}^{S} transition. The broadening and smearing out of the resonances is not surprising. Particularly for the outer tubes it originates not only from conventional double resonances but also from the increasing influence of the chiral angle on the transition energies with increasing folding index, as it can be seen from Fig. 10.1.

10.4.3 Dispersion of the G′ line for the high curvature inner tubes

The difference in the G′ line dispersion between inner shell and outer shell tubes is of particular interest. This difference refers to the slope of the dispersion as well as to the absolute line positions. Since the former is a replica of the phonon dispersion around the K point a flattening of this dispersion with increasing curvature must be concluded from the smaller value of the inner tubes dispersion.

Concerning the absolute value of the downshift observed for the inner tubes G′ lines as compared to the outer shell positions, we must keep in mind that Eq. (10.1) was derived from single tube experiments with diameters between 1.25 and 2.5 nm. The leading constant of 2708 cm^{-1} is the frequency for the G′ mode in graphite. As the experiments in Ref.[19] demonstrate, curvature decreases all high frequency optical modes. This is consistent with *ab initio* calculations for the

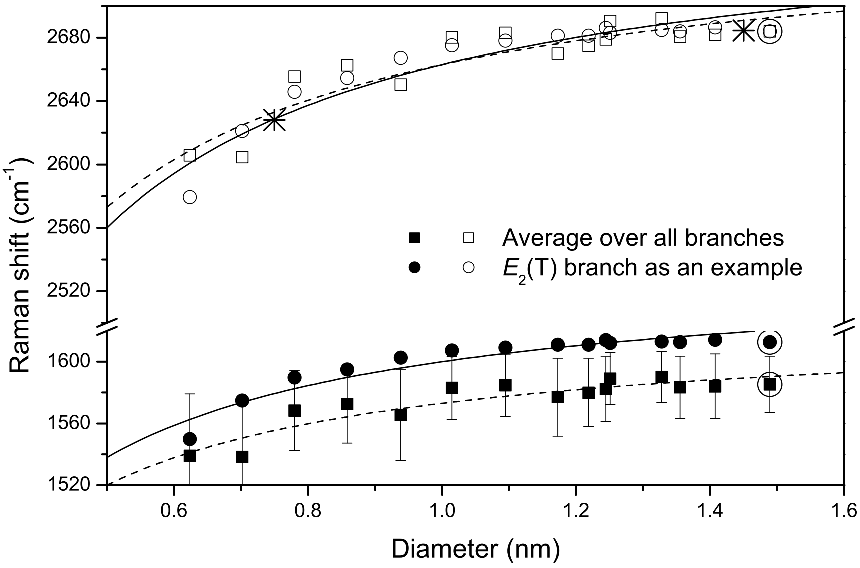

FIGURE 10.10. Comparison of calculated and observed G′ line frequencies. Bullets and full squares are G line frequencies as calculated from Dubay et al. [20] for the $E_2(T)$ branch and as averaged for all branches (the error bars depict the standard deviation). The circled points were used for the scaling. The open symbols are the scaled frequencies for the G′ line. The two asterisks represent the experimental results for the outer and inner tubes at 2.41 eV. The lines are fits as described in the text.

G mode as a function of diameter [20] where a dramatic and nonlinear decrease of the mode frequency was found for tubes with diameters < 1 nm. Thus, the discrepancy between the results from the linearized decrease given by Eq. (10.1) and from the inner shell tubes is understandable from the small tube diameter. The influence of high curvature has been reported also for the RBMs but due to the low frequency of the latter it is only a few wave numbers and difficult to observe.[25] In the case of the G′ mode the relative deviation from linearity is about the same but due to the high frequency it comes out between 20 and 30 cm^{-1} (depending on the exciting laser used) and is therefore easily detectable. Calculation of the downshift is unfortunately difficult since the K point phonons of all branches and of all tubes contribute.

Because of the folding of the graphite Brillouin zone into the nanotube zone and because of the nanotube curvature, the G band in nanotubes contains several modes with different symmetries. The tangential modes that are Raman active exhibit A, E_1, and E_2 (A_{1g}, E_{1g}, and E_{2g} for symmorphic groups) symmetries. [37] Assuming that the whole optical branch is modulated by curvature in the same way we can scale the K point frequencies to the Γ point modes for large tube diameters and thus reveal a mapping of the former on the tube diameters. The mapping was performed in two ways. In the first attempt only the transversal E_2 modes were considered as the main contributors to the G′ line. In a second attempt, the average frequency at the Γ point of all branches was considered and used to map the position of the G′ line as a function of tube diameter. The mapping was done such that the calculated E_2(T) frequency at $D = 1.5$ nm was scaled to the experimental G′ position of the outer tubes for 2.41 eV excitation. The averaged values were scaled the same way.

The diameter dependences of the Raman frequencies in Fig. 10.10 were fitted with $\bar{\nu} = A + B/D$. For the E_2(T) and averaged G mode branches we get $\bar{\nu}_{\mathrm{G}} = 1662(6) - 62(6)/D$ and $\bar{\nu}_{\mathrm{G}} = 1626(7) - 53(6)/D$, respectively. For the scaled G′ frequencies we get $\bar{\nu}_{\mathrm{G}'} = 2766(9) - 103(9)/D$ and $\bar{\nu}_{\mathrm{G}'} = 2753(11) - 90(11)/D$. A mapping for the other excitation energies gave similar results.

The good agreement between observed (asterisks) and calculated (open symbols) results justifies the interpretation of the discrepancy between single tube experiments and the results reported here as due to curvature effects as well as the down mapping procedure. Interestingly, a simple diameter scaling in Eq. (10.1) with diameters as calculated from *ab initio* DFT [25] does not give the correct behavior. In contrast, since DFT yields higher tube diameters as compared to the tight-binding values, the G′ line frequencies would upshift toward the line from the outer tubes as compared to the results from Ref. 19.

10.5 Summary

In summary, we have reported detailed experimental results for the Raman line position and intensity for the G′ line in DWCNTs. The response appears as a double peaked band with a characteristically different resonance cross section profile. Both components of the band exhibit the expected dispersion but the value of the inner shell tubes is lower ($85.4\,\mathrm{cm}^{-1}$) as compared to the value of the outer shell tubes ($99.1\,\mathrm{cm}^{-1}$). The superimposed oscillatory behavior have opposite phase for the two tube systems. The downshift in frequency between the G′ line from the inner tubs and from the outer tubes is significantly larger than expected from measurement on conventional diameter tubes. This is demonstrated to be a consequence of the strong curvature of the inner shell tubes. Finally, the scattering cross section reveals the nature of the triple resonance from the VHSs.

Acknowledgments: Work supported by the FWF in Austria (P 14893) and by the EU projects NANOTEMP (BIN2-2001-00580) and PATONN (MEIF-CT-2003-501099). E.O. acknowledges funding from the RAS program "Low-dimensional quantum structures". Valuable discussions with J. Kürti, V. Zólyomi and G. Kresse are greatly acknowledged. We thank V. N. Popov for supplying his calculated transition energies.

References

[1] R. Saito, G. Dresselhaus, and M. Dresselhaus, *Physical Properties of Carbon Nanotubes* (Imperial College Press, 1998).
[2] M. S. Dresselhaus, G. Dresselhaus, and P. Avouris, *Carbon Nanotubes: Synthesis, Structure, Properties, and Applications* (Springer, Berlin, Heidelberg, New York, 2001).
[3] S. Reich, C. Thomsen, and J. Maultzsch, *Carbon Nanotubes* (Wiley-VCH, Weinheim, 2004).
[4] B. W. Smith, M. Monthioux, and D. E. Luzzi, Nature **396**, 323 (1998).
[5] S. Bandow, M. Takizawa, K. Hirahara, M. Yudasaka, and S. Iijima, Chem. Phys. Lett. **337**, 48 (2001).
[6] R. Pfeiffer, H. Kuzmany, C. Kramberger, C. Schaman, T. Pichler, H. Kataura, Y. Achiba, J. Kürti, and V. Zólyomi, Phys. Rev. Lett. **90**, 225501 (2003).
[7] Z. K. Tang, H. D. Sun, J. Wang, J. Chen, and G. Li, Appl. Phys. Lett. **73**, 2287 (1998).
[8] Z. K. Tang, L. Y. Zhang, N. Wang, X. X. Zhang, G. H. Wen, G. D. Li, J. N. Wang, C. T. Chan, and P. Sheng, Science **292**, 2462 (2001).
[9] F. Simon, A. Kukovecz, C. Kramberger, R. Pfeiffer, F. Hasi, H. Kuzmany, and H. Kataura, Phys. Rev. B **71**, 165439 (2005).
[10] R. Saito, G. Dresselhaus, and M. S. Dresselhaus, Phys. Rev. B **61**, 2981 (2000).
[11] V. N. Popov, New J. Phys. **6**, 17 (2004).
[12] C. L. Kane and E. J. Mele, Phys. Rev. Lett. **93**, 197402 (2004).
[13] J. Kürti, V. Zólyomi, M. Kertész, and S. Guangyu, New. J. Phys. **5**, 125.1125.21 (2003).
[14] C. Fantini, A. Jorio, M. Souza, M. S. Strano, M. S. Dresselhaus, and M. A. Pimenta, Phys. Rev. Lett. **93**, 147406 (2004).
[15] R. B. Weisman and S. M. Bachilo, Nano Lett. **3**, 1235 (2003).
[16] H. Kataura, Y. Kumazawa, Y. Maniwa, I. Umezu, S. Suzuki, Y. Ohtsuka, and Y. Achiba, Synthetic Met. **103**, 2555 (1999).
[17] R. A. Jishi, L. Venkataraman, M. S. Dresselhaus, and G. Dresselhaus, Chem. Phys. Lett. **209**, 77 (1993).
[18] J. Kürti, G. Kresse, and H. Kuzmany, Phys. Rev. B **58**, R8869 (1998).
[19] A. G. Souza Filho, A. Jorio, G. G. Samsonidze, G. Dresselhaus, M. A. Pimenta, M. S. Dresselhaus, A. K. Swan, M. S. Ünlü, B. B. Goldberg, and R. Saito, Phys. Rev. B **67**, 035427 (2003).
[20] O. Dubay, G. Kresse, and H. Kuzmany, Phys. Rev. Lett. **88**, 235506 (2002).
[21] C. Thomsen and S. Reich, Phys. Rev. Lett. **85**, 5214 (2000).
[22] J. Maultzsch, S. Reich, and C. Thomsen, Phys. Rev. B **64**, 121407(R) (2001).
[23] J. Kürti, V. Zólyomi, A. Grüneis, and H. Kuzmany, Phys. Rev. B **65**, 165433 (2002).

[24] V. Zólyomi, J. Kürti, A. Grüneis, and H. Kuzmany, Phys. Rev. Lett. **90**, 157401 (2003).

[25] C. Kramberger, R. Pfeiffer, H. Kuzmany, V. Zólyomi, and J. Kürti, Phys. Rev. B **68**, 235404 (2003).

[26] S. Bandow, G. Chen, G. U. Sumanasekera, R. Gupta, M. Yudasaka, S. Iijima, and P. C. Eklund, Phys. Rev. B **66**, 075416 (2002).

[27] L. X. Benedict, V. H. Crespi, S. G. Louie, and M. L. Cohen, Phys. Rev. B **52**, 14935 (1995).

[28] H. Kataura, Y. Maniwa, T. Kodama, K. Kikuchi, K. Hirahara, K. Suenaga, S. Iijima, S. Suzuki, Y. Achiba, and W. Krätschmer, Synthetic Met. **121**, 1195 (2001).

[29] X. Liu, T. Pichler, M. Knupfer, M. S. Golden, J. Fink, H. Kataura, Y. Achiba, K. Hirahara, and S. Iijima, Phys. Rev. B **65**, 045419 (2002).

[30] H. Kuzmany, R. Pfeiffer, C. Kramberger, T. Pichler, X. Liu, M. Knupfer, J. Fink, H. Kataura, Y. Achiba, B. W. Smith, et al., Appl. Phys. A **76**, 449 (2003).

[31] J. B. Renucci, R. N. Tyte, and M. Cardona, Phys. Rev. B **11**, 3885 (1975).

[32] O. Gunnarsson, Rev. Mod. Phys. **69**, 575 (1997).

[33] M. Schluter, M. Lannoo, M. Needels, G. A. Baraff, and D. Tománek, Phys. Rev. Lett. **68**, 526 (1992).

[34] M. Machón, S. Reich, J. M. Pruneda, C. Thomsen, and P. Ordejón, in *Proceedings of the IWEPNM* (2003), pp. 427–430.

[35] M. Machón, S. Reich, J. Maultzsch, P. Ordejón, and C. Thomsen, in *Proceedings of the IWEPNM* (2004), in print.

[36] L. X. Benedict, S. G. Louie, and M. L. Cohen, Phys. Rev. B **52**, 8541 (1995).

[37] A. Jorio, G. Dresselhaus, M. S. Dresselhaus, M. Souza, M. S. S. Dantas, M. A. Pimenta, A. M. Rao, R. Saito, C. Liu, and H. M. Cheng, Phys. Rev. Lett. **85**, 2617 (2000).

11

Fine Structure of the Radial Breathing Mode in Double-Wall Carbon Nanotubes

R. Pfeiffer, F. Simon, H. Kuzmany, and V. N. Popov

Physical Review B **72**, *161404 (2005).*

ABSTRACT The analysis of the Raman scattering cross section of the radial breathing modes of double-wall carbon nanotubes allowed to determine the optical transitions of the inner tubes. The Raman lines are found to cluster into species with similar resonance behavior. The lowest components of the clusters correspond well to SDS wrapped HiPco tubes. Each cluster represents one particular inner tube inside different outer tubes and each member of the clusters represents one well defined pair of inner and outer tubes. The number of components in one cluster increases with decreasing of the inner tube diameter and can be as high as 14 spread over 30 cm^{-1}. This suggests a lot of variation in the diameter difference of inner/outer tube pairs.

Double-wall carbon nanotubes (DWCNTs) are new and interesting structures in the family of carbon nanophases, especially when they are grown by annealing of so-called peapods, i. e. single-wall carbon nanotubes (SWCNTs) filled with fullerenes.[1] The outer tubes diameters of such DWCNTs are of the same small size (around 1.4 nm) as it is typical for SWCNTs. This means, they provide the same spatial resolution for sensors or the same field enhancement for electron emitters as the latter but exhibit higher stiffness. The inner tubes, with typical diameters of 0.7 nm, have a rather high curvature and are thus expected to exhibit significant deviations from graphene with respect to their mechanical and electronic properties. Amongst others, the electron-phonon coupling is expected to be considerably increased as compared to graphene, which might result in superconductivity or a Peierls transition. Also, the concentric layers in the DWCNTs represent curved graphite sheets with an interesting van der Waals type interaction and DWCNTs are well defined model materials for multi-wall CNTs. Finally, by filling SWCNTs with isotope labeled fullerenes it is possible to produce DWCNTs with ^{13}C enriched inner and normal ^{12}C outer tubes.[2]

The peapod-grown DWCNTs attracted additional interest as the inner tubes are grown in an highly unperturbed environment and thus exhibit unusual narrow lines for the radial breathing mode (RBM) Raman response.[3] In this sense, the inside of the outer tubes has been termed a “nano clean-room”. Moreover, the Raman signal from the RBMs of the inner tubes exhibits strong resonance enhancement and the observed number of lines is larger than the number of geometrically allowed species.[4]

Similarly to the outer tubes, the geometric and electronic properties of the inner tubes are uniquely determined by their chiral vectors (m, n), along which the graphene layers are rolled up into tubes.[5] Due to the quasi one-dimensionality of the tubes, the electronic states are jammed into Van Hove singularities (VHSs). Recent experiments suggest that the optical transitions of semiconducting (E_{ii}^{S}) and metallic (E_{ii}^{M}) tubes arise from excitonic states close to the VHSs instead from the VHSs as such.[6] These transition energies scatter around lines with slopes proportional to the inverse tube diameter $1/D$. Refined calculations revealed considerable curvature corrections to the transition energies, especially for small diameter tubes.[7–9] Experimental information on these effects has recently been obtained from the Raman and luminescence measurements of HiPco (high pressure carbon monoxide grown) tubes with a mean diameter of about 1 nm.[10–12] The pattern of the deviation from the linear relation between E_{ii} and $1/D$ can be categorized into tube families with respect to $2m + n = \text{const}$. There are the metallic tubes with $2m + n \equiv 0 \pmod 3$ and two types of semiconducting tubes with $2m + n \equiv 1 \pmod 3$ (SI) and $2m + n \equiv 2 \pmod 3$ (SII). For the E_{22}^{S} transition, the SI tubes deviate strongly from the linear relation towards lower transition energies whereas the SII tubes exhibit a smaller deviation towards higher transition energies. In all cases zigzag-like tubes close to $(m, 0)$ show the largest deviation from the linear relationship.

The RBM frequencies also scale roughly as $1/D$ and have therefore been used repeatedly for the structural analysis of SWCNTs, particularly with respect to the diameter distribution. By analyzing the Raman cross section of the RBMs it is possible to determine chiralities and electronic transition energies of CNTs.[11, 12]

Here, we present the results of resonance Raman measurements in the RBM range of DWCNTs. These measurements unraveled the optical transitions of the inner tubes which cannot be accessed by optical and scanning probe experiments. Using a contour-plot where the Raman cross-section is plotted over a 2D grid of RBM frequency and laser excitation energy, we found a well expressed fine structure in the resonance pattern. An analysis of this pattern showed a clustering of the inner tubes RBMs near the HiPco transition energies and frequencies. The clusters start around the HiPco frequencies and extend up to 30 cm^{-1} to higher frequencies. They consist of up to 14 well expressed components. Each cluster represents one particular inner tube inside different outer tubes and each member of the clusters represents a well defined pair of one inner in one outer tube. Within one cluster, the transition energies show a red-shift of about 2 meV/cm^{-1}. We explain the existence of such “pair-spectra” and the red-shift of the transition energies by the interactions

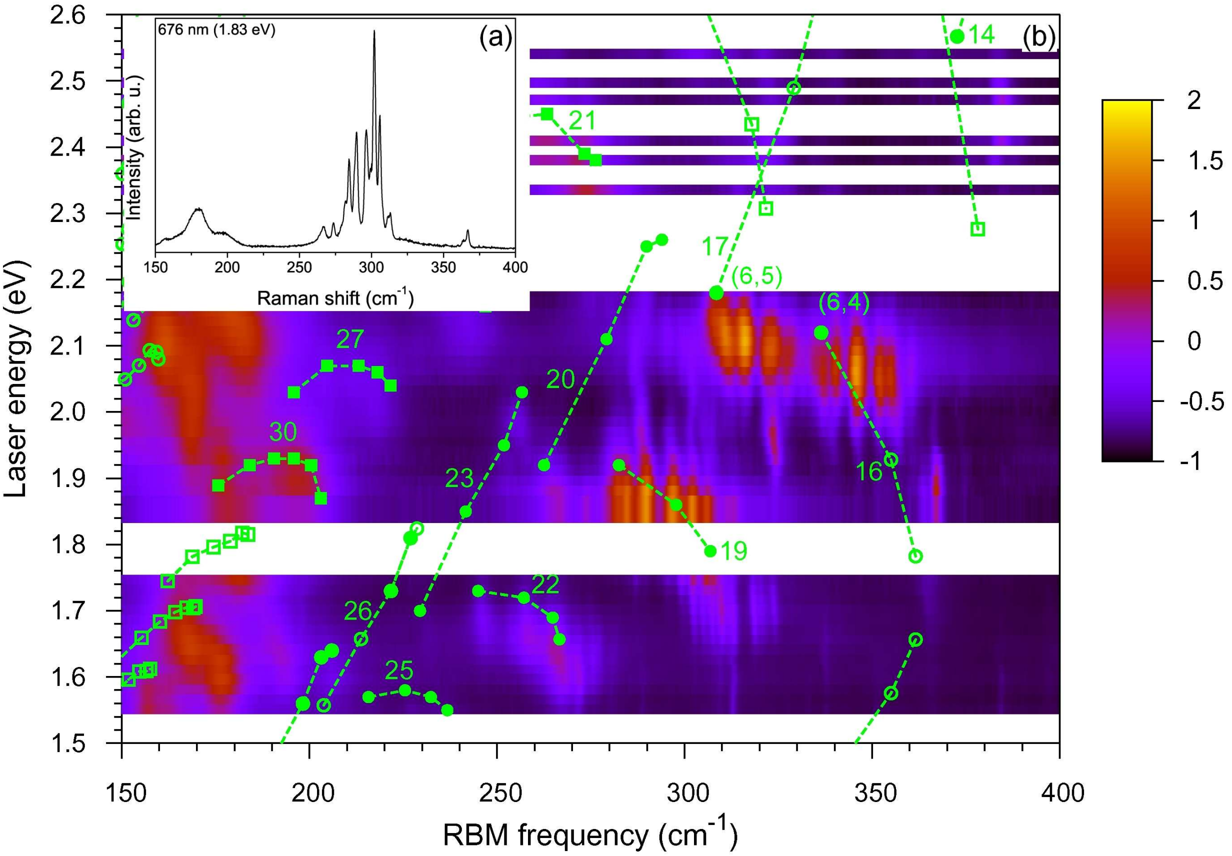

FIGURE 11.1. (a) Raman response of the RBM region of DWCNTs sample B. (b) Logarithm of the Raman cross-section of the tubes as a function of laser energy and RBM frequency. Filled symbols are measured RBM frequencies and transition energies of SDS wrapped HiPco tubes averaged from Refs. [10–12] (circles and squares denote semiconducting and metallic tubes, respectively). Open symbols are extended tight-binding calculations [9] corrected for many body effects[13]. Tube families are connected with dashed lines and assigned by family numbers $2m + n = \text{const}$.

between the inner and outer tubes. This explanation is supported by model calculations.

The DWCNTs studied here were obtained by annealing C_{60} peapods at 1250 °C in a dynamic vacuum for 2 h.[1] Two samples with mean outer diameters of 1.39 nm (sample A) and 1.45 nm (sample B) were studied here. The Raman spectra for the measurement of the resonance cross section were recorded in backscattering geometry at ambient conditions using a Dilor XY triple spectrometer operated in normal resolution and a LN_2 cooled CCD detector. Selected spectra were measured in high resolution (HR) at 90 K. In this case, the resolution of the spectrometer was 0.5 cm^{-1} for red laser excitation. The spectra were obtained with different lasers such as an Ar/Kr, a Ti:Sapphire, and a dye laser with Rhodamine 6G and Rhodamine 101. Excitation was between 1.54 and 2.54 eV (488 to 803 nm) with a spacing of about 15 meV in the red to yellow spectral region. The frequencies were corrected using calibration lamps. In order to determine Raman cross-sections and to correct for the spectrometer/detector sensitivity, all spectra were normalized to the well known cross-section for the Si F_{1g} mode around 520 cm^{-1}.

Figure 11.1(a) depicts a typical Raman spectrum of DWCNTs in the frequency range of the RBM. The broad and structured line pattern around 180 cm^{-1} and the set of strong and narrow lines in the spectral range from 230 to 400 cm^{-1} originate from the outer and from the inner tubes, respectively. Figure 11.1(b) shows the color coded logarithm of the RBM Raman cross-section of DWCNTs sample B as a function of laser energy and RBM frequency for normal spectrometer resolution. The broad band between 150 and 210 cm^{-1} is the response from the outer tubes. Between about 230 and 400 cm^{-1} one can observe the RBM response of the inner tubes. For this energy range, mainly the E_{22}^{S} (circles) and parts of the E_{11}^{M} transitions (squares) can be seen.

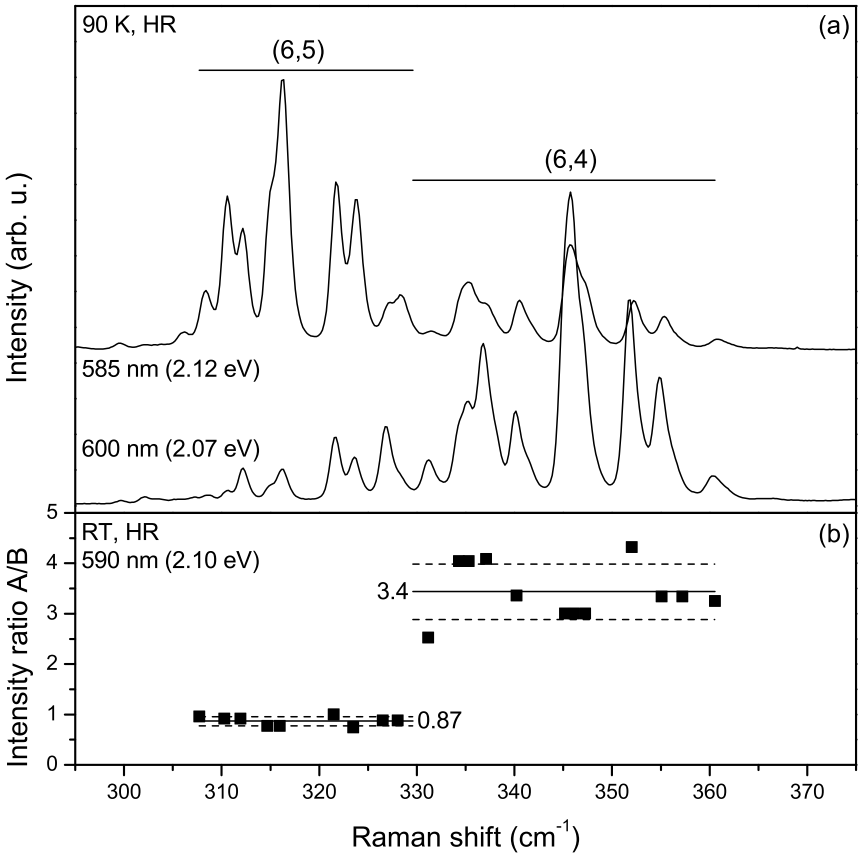

FIGURE 11.2. (a) High resolution Raman response for the $(6,5)$ and $(6,4)$ inner tubes for sample A as excited with two different lasers. The horizontal lines cover the widths of the clusters. (b) Intensity ratio of the RBM components for the $(6,5)$ and $(6,4)$ tubes of samples A and B with small and large mean outer tubes diameters, respectively. The dashed lines indicate the standard deviation.

From the comparison with results for HiPco tubes one can easily identify the families 22, 19, and 16 in the SI branch of the E_{22}^{S} transition. Resonances from the SII tubes (families 23, 20, and 17) are in general weaker but can still be observed, especially the $(6,5)$ tube in family 17. The metallic transitions are also close to the HiPco results.

The RBMs of the inner tubes clearly show a clustering of components close to the HiPco transitions. The low frequency end of the clusters coincides well with the results from the HiPco tubes except for a downshift in energy of about 50 meV. For the $(6,4)$ inner tube in family 16 the total width of the cluster is about $30\,\mathrm{cm}^{-1}$. The width of the clustered lines clearly decreases with increasing inner tube diameter. For the largest diameter inner tubes (family 22) almost no clustering is observed and results are in very good agreement with the response from the HiPco tubes.

A number of very intensive Raman lines are located close to the transitions of the isolated $(6,5)$ and $(6,4)$ tubes in families 17 and 16, respectively. The two tubes are well separated in frequency and the clusters can be well assigned to those tubes. In the following discussion we will therefore mainly refer to these tubes, although all results hold correspondingly for the other inner tubes. Within one cluster the peak resonances of the components are clearly shifted to lower energies with increasing frequency. For the $(6,5)$ and $(6,4)$ cluster we get $-2.7(6)\,\mathrm{meV/cm}^{-1}$ and $-0.9(4)\,\mathrm{meV/cm}^{-1}$, respectively. On the average, the shift is about $-2\,\mathrm{meV/cm}^{-1}$.

Two strong resonances at $(322\,\mathrm{cm}^{-1}, 1.92\,\mathrm{eV})$ and at $(368\,\mathrm{cm}^{-1}, 1.86\,\mathrm{eV})$ could not be assigned, although they were observed in all samples studied. The lower energy resonance may be related to the $(7,2)$ tube of family 16. The higher energy resonance could originate from $(6,5)$ with a non symmetric resonance transition.[14]

In order to demonstrate the clustering effect more clearly and to get some information on the

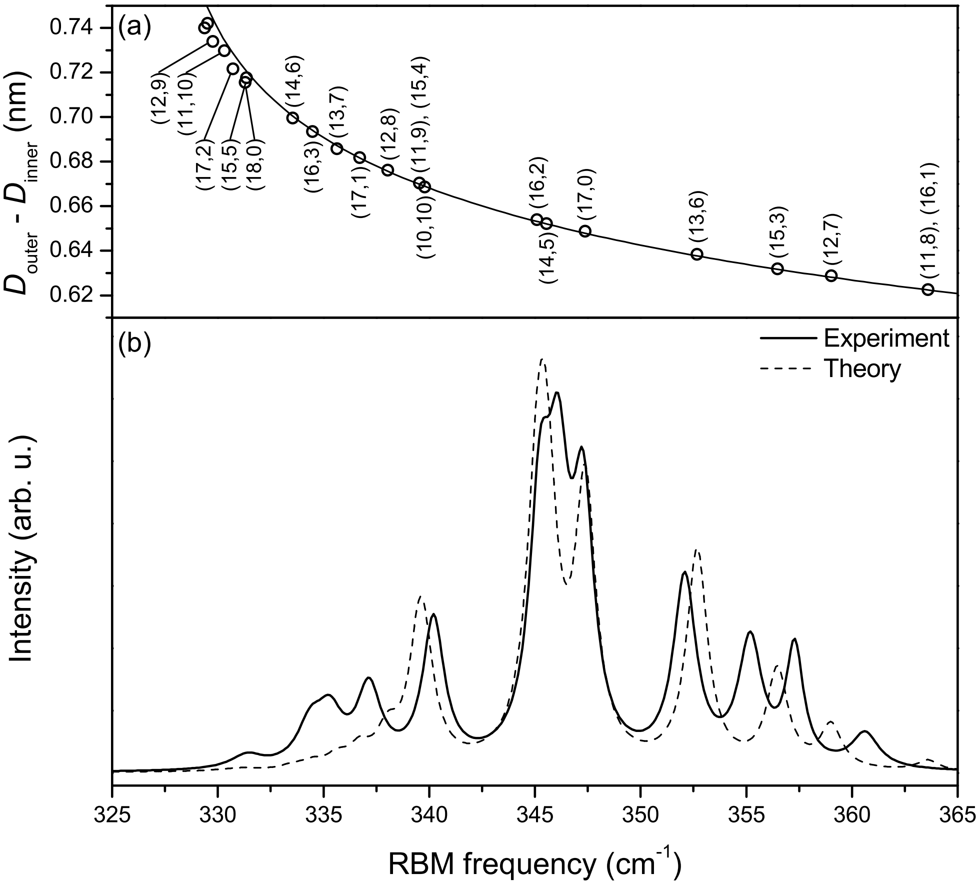

FIGURE 11.3. (a) RBM frequency of a $(6,4)$ inner tube as a function of the diameter difference to various outer tubes (indicated by their chiral vectors). (b) Raman line pattern for the RBM of the $(6,4)$ inner tube as obtained from experiment (solid line) and from theory (dashed line) as described in the text.

number of components in the clusters, we measured the spectral range of the RBM for the $(6,5)$ and for the $(6,4)$ tubes in high resolution at low temperature (see Fig. 11.2(a)).

While for the lower energy laser all components of the $(6,4)$ species are in resonance the components of the $(6,5)$ tubes remain weak. For the higher energy laser the result is just opposite. From a fit to the observed structures a total number of 9 and 14 components were found for the $(6,5)$ and the $(6,4)$ clusters, respectively.

To check the stability of the clustered components in the spectra we compared the patterns for two samples with different outer tube diameters. As Fig. 11.2(b) shows, the $(6,4)$ cluster is about a factor 3.4 stronger in intensity in sample A (1.39 nm) than in sample B (1.45 nm). The intensity of the $(6,5)$ components in sample A is only about 87 % of that in sample B. This is as expected, since for the smaller diameter outer tubes proportionally more smaller inner tubes grow.[15]

The crucial result that a rather large number of peaks in the RBM range of the Raman spectra have the same resonance behavior is surprising. It strongly suggests that all components of one cluster originate from the same inner tube. This means, the inner tubes can be accommodated in a rather large number of different outer tubes and the wall to wall distance can be quite different from its optimum value.[16] Thus, the clustered lines represent pair spectra of one inner tube inside several well defined outer tubes.

Figure 11.3(a) depicts the calculated upshift of the RBM frequency of a $(6,4)$ inner tube as a function of the diameter difference to various outer tubes. In the calculations we considered the tubes as elastic continuum cylinders interacting with each other with a Lennard-Jones (LJ) potential parameterized for graphite.[17] The relaxed structure of the DWCNTs was found by minimization of the total energy E equal to the sum of the elastic energies of both tubes and the inter tube interaction energy E_{LJ}, $E = Y_1\pi[R_{\mathrm{i}}(\Delta R_{\mathrm{i}}/R_{\mathrm{i}})^2 + R_{\mathrm{o}}(\Delta R_{\mathrm{o}}/R_{\mathrm{o}})^2] + E_{\mathrm{LJ}}$. Here R_{i} and R_{o}

are the inner and outer tube radii, ΔR_i and ΔR_o are their changes, $Y_1 = Yd$, $Y = 1.06\,\mathrm{TPa}$ is the graphene in-plane Young's modulus, and $d = 0.335\,\mathrm{nm}$ is the tube wall thickness. Compared with the continuum model results[4], the frequency upshift for small diameter differences became slightly smaller.

In Fig. 11.3(b) the solid line is the experimental spectrum of sample A obtained in HR at 90 K where the intensity of each component was normalized to its measured maximum cross section. The spectrum thus shows the population distribution of the inner/outer tube pairs. The calculated spectrum (dotted line in Fig. 11.3(b)) was obtained by assigning a Lorentzian to each calculated frequency whose intensity was for simplicity assumed to be determined by a Gaussian distribution. This procedure anticipates equal resonance matrix elements for all members of a cluster which is certainly well justified. The calculated frequencies were scaled with a factor 0.98. To get the best agreement between theory and experiment, the parameters of the Gaussian were $\omega_0 = 348.9\,\mathrm{cm}^{-1}$ and $\sigma = 5.2\,\mathrm{cm}^{-1}$. For the intermediate frequencies, experiment and theory are in good agreement. For lower and higher frequencies, the components deviate from the experiment. The maximum of the simulated spectrum is found for a diameter difference of about 0.66 nm, which is smaller than the experimental value of 0.72 nm reported in Ref. [18]. This shows, that the LJ potential must be reparameterized for the curved sp^2 networks of DWCNTs.

The frequency upshift and the transition energy downshift within one cluster can be understood from an increasing interaction between the two shells for decreasing diameter difference. This interaction acts on the inner shell like a radial pressure. The pressure dependence of E_{22} for the $(6,4)$ and the $(6,5)$ inner tubes was calculated in the extended tight-binding framework.[9] The corresponding values are $-7.8\,\mathrm{meV/GPa}$ and $-2.5\,\mathrm{meV/GPa}$. After Ref. [19] the frequencies shift with about $1.1\,\mathrm{cm}^{-1}/\mathrm{GPa}$. Thus one gets $-7.1\,\mathrm{meV/cm}^{-1}$ and $-2.3\,\mathrm{meV/cm}^{-1}$, respectively. The signs and the order of magnitude compare well with the experiment. Additionally, from the measured pressure induced shift of the E_{22}^S transition[20] for a $(6,5)$ tube of $-4\,\mathrm{meV/GPa}$ one gets $-3.6\,\mathrm{meV/cm}^{-1}$, which is very close the experimental value of $-2.7\,\mathrm{meV/cm}^{-1}$.

In summary, we report on the optical transitions of very high curvature SWCNTs accommodated inside host outer tubes as derived from their resonance Raman cross section. The observed Raman lines are clustered and represent pair spectra between one inner tube and several well defined outer tubes. The number of components in the cluster increases with decreasing tube diameter. The leading edges of the clusters correspond to the HiPco tubes with respect to frequency and transition energy except for a red-shift of 50 meV. Additional red-shifts of about $2\,\mathrm{meV/cm}^{-1}$ within a cluster are understood from a radial pressure generated by different outer tubes. These results provide now a unified picture for the high curvature nanotubes from the HiPco process and from the DWCNTs species.

Acknowledgments: Valuable discussions with A. Jorio, A. Rubio and L. Wirtz are gratefully acknowledged. Work supported by FWF project P17345, Marie-Curie projects MEIF-CT-2003-501099 and MEIF-CT-2003-501080, and by NATO CLG 980422.

References

[1] S. Bandow, M. Takizawa, K. Hirahara, M. Yudasaka, and S. Iijima, Chem. Phys. Lett. **337**, 48 (2001).

[2] F. Simon, C. Kramberger, R. Pfeiffer, H. Kuzmany, J. Zólyomi, V. Kürti, P. M. Singer, and H. Alloul, Phys. Rev. Lett. **95**, 017401 (2005).

[3] R. Pfeiffer, H. Kuzmany, C. Kramberger, C. Schaman, T. Pichler, H. Kataura, Y. Achiba, J. Kürti, and V. Zólyomi, Phys. Rev. Lett. **90**, 225501 (2003).

[4] R. Pfeiffer, C. Kramberger, F. Simon, H. Kuzmany, V. N. Popov, and H. Kataura, Eur. Phys. J. B **42**, 345 (2004).

[5] S. Reich, C. Thomsen, and J. Maultzsch, *Carbon Nanotubes* (Wiley-VCH, Weinheim, 2004).

[6] F. Wang, G. Dukovic, , L. E. Brus, and T. F. Heinz, Science **308**, 838 (2005).

[7] V. N. Popov and L. Henrard, Phys. Rev. B **65**, 235415 (2002).

[8] G. G. Samsonidze, R. Saito, N. Kobayashi, A. Grüneis, J. Jiang, A. Jorio, S. G. Chou, G. Dresselhaus, and M. S. Dresselhaus, Appl. Phys. Lett. **85**, 5703 (2004).

[9] V. N. Popov, New J. Phys. **6**, 17 (2004).

[10] S. M. Bachilo, M. S. Strano, C. Kittrell, R. H. Hauge, R. E. Smalley, and R. B. Weisman, Science **298**, 2361 (2002).

[11] C. Fantini, A. Jorio, M. Souza, M. S. Strano, M. S. Dresselhaus, and M. A. Pimenta, Phys. Rev. Lett. **93**, 147406 (2004).

[12] H. Telg, J. Maultzsch, S. Reich, F. Hennrich, and C. Thomsen, Phys. Rev. Lett. **93**, 177401 (2004).

[13] A. Jorio, C. Fantini, M. A. Pimenta, R. B. Capaz, G. G. Samsonidze, G. Dresselhaus, M. S. Dresselhaus, J. Jiang, N. Kobayashi, A. Grüneis, et al., Phys. Rev. B **71**, 075401 (2005).

[14] A. Grüneis, R. Saito, J. Jiang, G. G. Samsonidze, M. A. Pimenta, A. Jorio, A. G. Souza Filho, G. Dresselhaus, and M. S. Dresselhaus, Chem. Phys. Lett. **387**, 301 (2004).

[15] F. Simon, A. Kukovecz, C. Kramberger, R. Pfeiffer, F. Hasi, H. Kuzmany, and H. Kataura, Phys. Rev. B **71**, 165439 (2005).

[16] A. Hashimoto, K. Suenaga, K. Urita, T. Shimada, T. Sugai, S. Bandow, H. Shinohara, and S. Iijima, Phys. Rev. Lett. **94**, 045504 (2005).

[17] J. P. Lu, X.-P. Li, and R. M. Martin, Phys. Rev. Lett. **68**, 1551 (1992).

[18] M. Abe, H. Kataura, H. Kira, T. Kodama, S. Suzuki, Y. Achiba, K.-i. Kato, M. Takata, A. Fujiwara, K. Matsuda, et al., Phys. Rev. B **68**, 041405(R) (2003).

[19] U. D. Venkateswaran, D. L. Masica, G. U. Sumanasekera, C. A. Furtado, U. J. Kim, and P. C. Eklund, Phys. Rev. B **68**, 241406(R) (2003).

[20] J. Wu, W. Walukiewicz, W. Shan, E. Bourret-Courchesne, J. W. Ager III, K. M. Yu, E. E. Haller, K. Kissell, S. M. Bachilo, R. B. Weisman, et al., Phys. Rev. Lett. **93**, 017404 (2004).

12

Isotope engineering in carbon nanotube systems

F. Simon, Ch. Kramberger, R. Pfeiffer, H. Kuzmany, V. Zólyomi, J. Kürti, P. M. Singer, and H. Alloul

Physical Review Letters **95**, *017401 (2005).*

ABSTRACT The synthesis of a unique isotope engineered system, double-wall carbon nanotubes with natural carbon outer and highly ^{13}C enriched inner walls, is reported from isotope enriched fullerenes encapsulated in single-wall carbon nanotubes (SWCNTs). The material allows to observe the D-line of the highly defect free inner tubes that can be related to a curvature induced enhancement of the electron-phonon coupling. *Ab-initio* calculations explain the inhomogeneous broadening of inner tube Raman modes due to the distribution of different isotopes. Nuclear magnetic resonance shows a significant contrast of the isotope enriched inner SWCNTs compared to other carbon phases and provides a macroscopic measure of the inner tube mass content. The high curvature of the small diameter inner tubes manifests in an increased distribution of the chemical shift tensor components.

Isotope engineering (IE) of materials provides an important degree of freedom for both fundamental studies and applications. The change in phonon energies upon isotope substitution, while leaving the electronic properties unaffected, has been used repeatedly to identify vibrational modes [1–3] and gave insight into underlying fundamental mechanisms, such as phonon-mediated superconductivity [4]. Applications of IE involve for instance the controlled doping of isotope engineered ready-prepared Si heterostructures by means of neutron irradiation [5], fabrication of mononuclear devices with controlled heat conducting properties [6], and the basic architecture for spintronics and quantum computing [7]. Recently, single-wall carbon nanotubes (SWCNTs) have been intensively studied as a result of the envisaged broad range of applicability and the unique physical properties related to their quasi one-dimensional electronic structure. Examples include the presence of Van Hove singularities in the electronic density of states [8], and the Tomonaga-Luttinger liquid behavior [9]. IE of carbon nanotubes using isotope enriched graphite as the starting material was attempted in order to allow NMR spectroscopy [10, 11]. However, the NMR studies have been hampered by the fact that the ^{13}C NMR active nuclei can be found in all species of carbons, e.g. amorphous or graphitic carbon, inevitably present even in the purified SWCNT materials, and no nanotube selective enrichment or purification could be achieved until now. Vibrational spectroscopic methods are appropriate choices to study the effect of IE. For SWCNTs, Raman spectroscopy has proven to be most convenient to characterize their electronic and structural properties. In addition, Raman studies on double-wall carbon nanotubes (DWCNTs) [12], synthesized from fullerenes encapsulated inside the tubes (fullerene peapods) [13], provide a unique opportunity to study the small diameter inner tubes, while the outer ones are left intact during the synthesis.

In this Letter, we report the preparation and properties of a new and unique hybrid carbon nanotube material. It consists of DWCNTs where the highly defect free inner tube [14] is isotope engineered and contains ^{13}C with controlled level of enrichment, whereas the outer tube remains natural carbon. This material is obtained by filling a host SWCNT with isotope labelled C_{60} or C_{70} fullerenes and transforming the resulting peapods to an inner tube by high temperature annealing. Raman scattering is demonstrated to reveal for the first time an unexpected strong response from the D-line of the inner tubes, even though the latter are highly defect free. It demonstrates the strong and curvature induced enhancement of the electron-phonon coupling. Even at the high temperature of the peapod transformation, no exchange of carbon between inner and outer shell is observed. The random distribution of ^{13}C atoms in the wall of the inner tube leads to a line broadening which was quantitatively explained by first principle calculations. In significant contrast to non isotope enriched tubes, the present material provides an excellent object for NMR spectroscopy. This technique allows the measurement of the mass fraction of a material encapsulated in carbon nanotubes for the first time. The effect of high curvature is demonstrated for the small diameter inner tubes from unusual line-shapes of the static and dynamic NMR response.

Commercial SWCNT material (Nanocarblab, Moscow, Russia), ^{13}C isotope enriched fullerenes (MER Corp., Tucson, USA), and fullerenes of natural carbon (Hoechst AG, Frankfurt, Germany) were used to prepare fullerene peapods C_{60},C_{70}@SWCNT. The SWCNTs were purified by the supplier to 50 weight %. The tube diameter distribution was determined from Raman spectroscopy [15] and revealed $d = 1.40$ nm and $\sigma = 0.10$ nm for the mean diameter and the variance of the Gaussian distribution, respectively. We used two grades of ^{13}C enriched fullerene mixtures: 25 and 89 %, whose values are slightly refined in our study. The 25 % grade was nominally C_{60}, and the 89 % grade was nominally C_{70}. The natural carbon C_{60} had a purity of ¿ 99 %. For the fullerene encapsulation, the SWCNTs and the fullerenes were sealed under vacuum in a quartz ampoule and annealed at 650 °C for 2 hours [16]. Fullerenes enter the inside of the SWCNTs at this temperature due to their high vapor pressure that is maintained in the sealed environment. Non-encapsulated fullerenes were removed by dynamic vacuum annealing at the same temperature for 1 hour. The filling of SWCNTs with the fullerenes was characterized by observing the peapod structure in high-resolution transmission electron microscopy (HR-TEM), by X-ray studies of

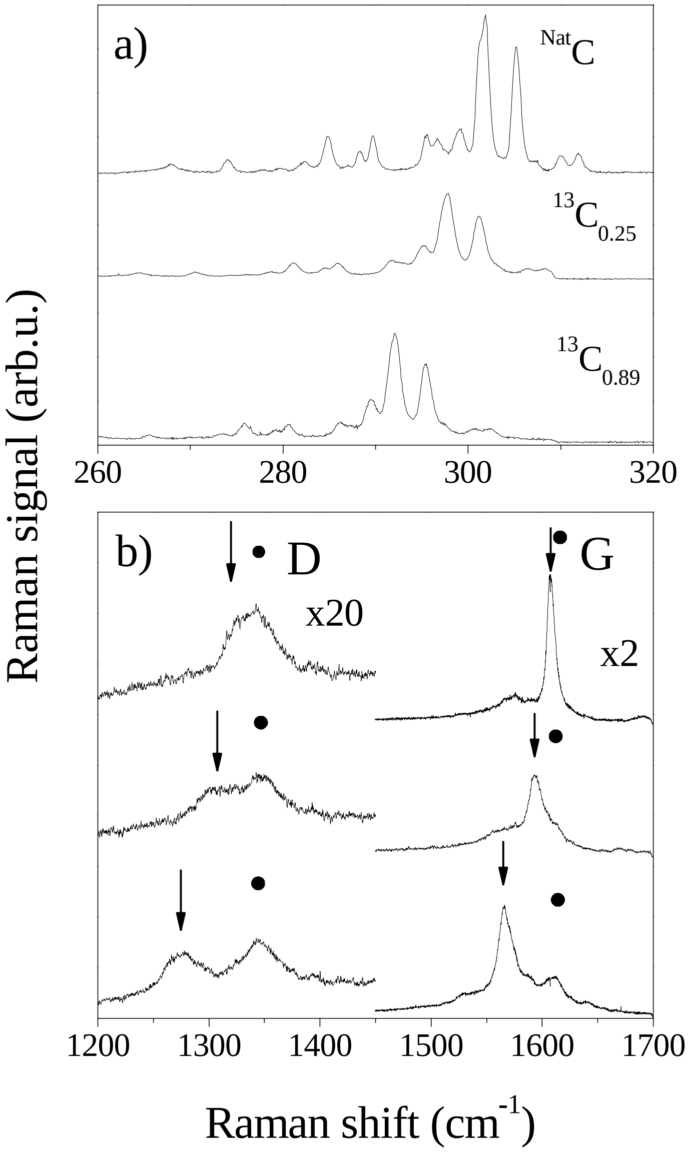

FIGURE 12.1. Raman spectra of DWCNTs with ^{Nat}C and ^{13}C enriched inner tubes at λ=676 nm laser excitation and 90 K. (a) RBM Raman response (b) D and G mode Raman response. Arrows and filled circles indicate the D (left) and G (right) modes corresponding to the inner and outer tubes, respectively.

the one-dimensional array of fullerenes inside the SWCNTs and by the detection of the fullerene modes from the cages encapsulated inside the SWCNTs using Raman spectroscopy [16, 17]. The peapods were transformed to DWCNTs by a dynamic vacuum treatment at 1250 °C for 2 hours following Ref. [12]. Again, the DWCNT transformation was followed by HR-TEM and by the observation of the DWCNT structure factors using X-ray studies. In addition, new Raman modes emerge after the 1250 °C heat treatment particularly in a frequency range that is clearly upshifted from the outer tube radial breathing modes (RBMs). According to the $1/d$, scaling of the RBM modes, where d is the tube diameter, these lines are an additional proof for the growth of the small diameter inner shell tubes [12, 14]. The Raman spectra of the samples are discussed in detail in the following. DWCNTs based on the fullerenes with different ^{13}C enrichment grades are denoted as ^{Nat}C-, ^{13}C$_{0.25}$- and ^{13}C$_{0.89}$-DWCNT. Vibrational analysis was performed on a Dilor xy triple Raman spectrometer in the 1.64-2.54 eV (676-488 nm) energy range at 90 K. The spectral resolution was 0.5-2 cm^{-1} depending on the laser wavelength and the resolution mode used. First principles calculations were performed with the Vienna ab initio Simulation Package (VASP) [18]. Magic angle spinning (MAS) and static ^{13}C-NMR spectra were measured at ambient conditions using a Chemagnets (Varian Inc.) MAS probe at 7.5 Tesla. The ^{13}C-NMR spectra were obtained by a Fourier transformation of the free induction decay following the excitation pulse.

In Fig. 12.1, we show the Raman spectra of ^{Nat}C-, ^{13}C$_{0.25}$- and ^{13}C$_{0.89}$-DWCNTs for the RBMs

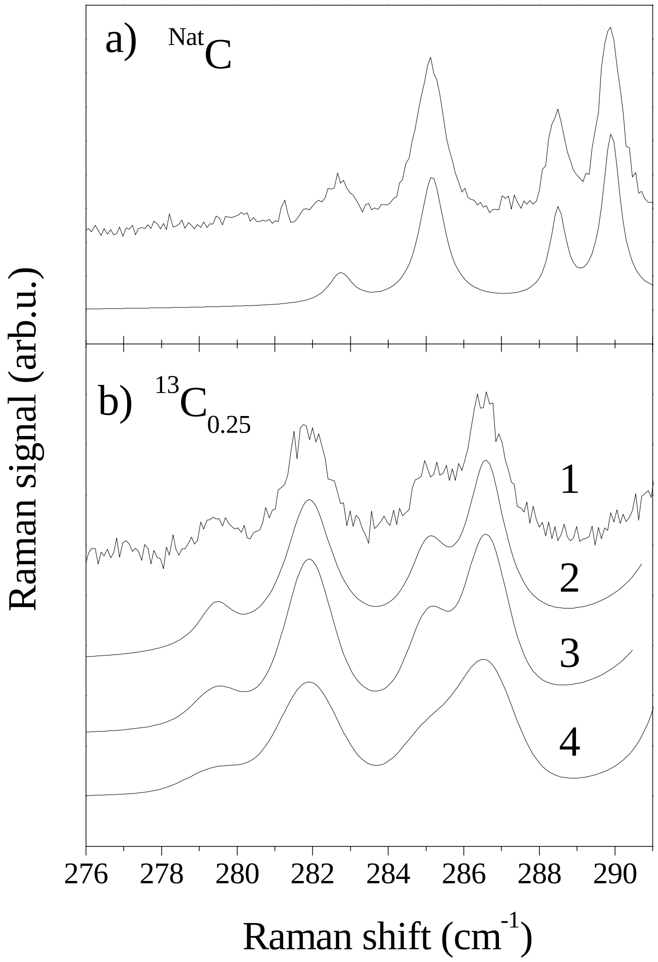

FIGURE 12.2. RBMs of some inner tubes at λ=676 nm laser excitation with 0.5 cm^{-1} spectral resolution. a) $^{\mathrm{Nat}}$C, b) ^{13}C$_{0.25}$. Smooth solid curves are the line-shapes after deconvolution by the spectrometer response. The dashed curve is a simulated line-shape with an extra Gaussian broadening to the intrinsic lines of the $^{\mathrm{Nat}}$C material. The dotted curve is calculated line-shape (see text).

(Fig. 12.1a), and the D and G mode spectral ranges (Fig. 12.1b) at 676 nm excitation. The narrow lines in Fig. 12.1a were previously identified as the RBMs of the inner tubes [14]. An overall downshift of the inner tube RBMs is observed for the ^{13}C enriched materials accompanied by a broadening of the lines. The downshift is clear evidence for the effective ^{13}C enrichment of inner tubes. The magnitude of the enrichment and the origin of the broadening are discussed below.

The RBM lines are well separated for inner and outer tubes due to the $\nu_{\mathrm{RBM}} \propto 1/d$ relation and a mean inner tube diameter of $\sim$ 0.7 nm [19, 20]. However, other vibrational modes such as the defect induced D and the tangential G modes strongly overlap for inner and outer tubes. Arrows in Fig. 12.1b indicate a gradually downshifting component of the observed D and G modes. This component is assigned to the D and G modes of the inner tubes. The sharper appearance of the inner tube G mode, as compared to the response from the outer tubes, is related to the excitation of semiconducting inner tubes and metallic outer tubes [14, 21].

The relative magnitude of the inner to outer tube D modes are comparable, as best seen for the highest enriched sample. The D mode originates from a double resonance process, which is induced by the defects in the sample [22–24]. The inner tubes were shown to contain significantly less defects than the outer ones, as proven by the narrow RBM phonon line-widths [14]. Thus, the experimentally observed D band intensity ratio suggests a competitive effect, in which the enhanced electron-phonon coupling in small diameter SWCNTs [25] compensates for the smaller number of defects.

The shift of the RBM, D and G modes were analyzed for the two grades of enrichment. The average value of the relative shift for these modes was found to be $(\nu_0 - \nu)/\nu_0 = 0.0109(3)$ and 0.0322(3) for the ^{13}C$_{0.25}$- and ^{13}C$_{0.89}$-DWCNT samples, respectively. Here, ν_0 and ν are the Raman shifts of the same inner tube mode in the natural carbon and enriched materials, respectively.

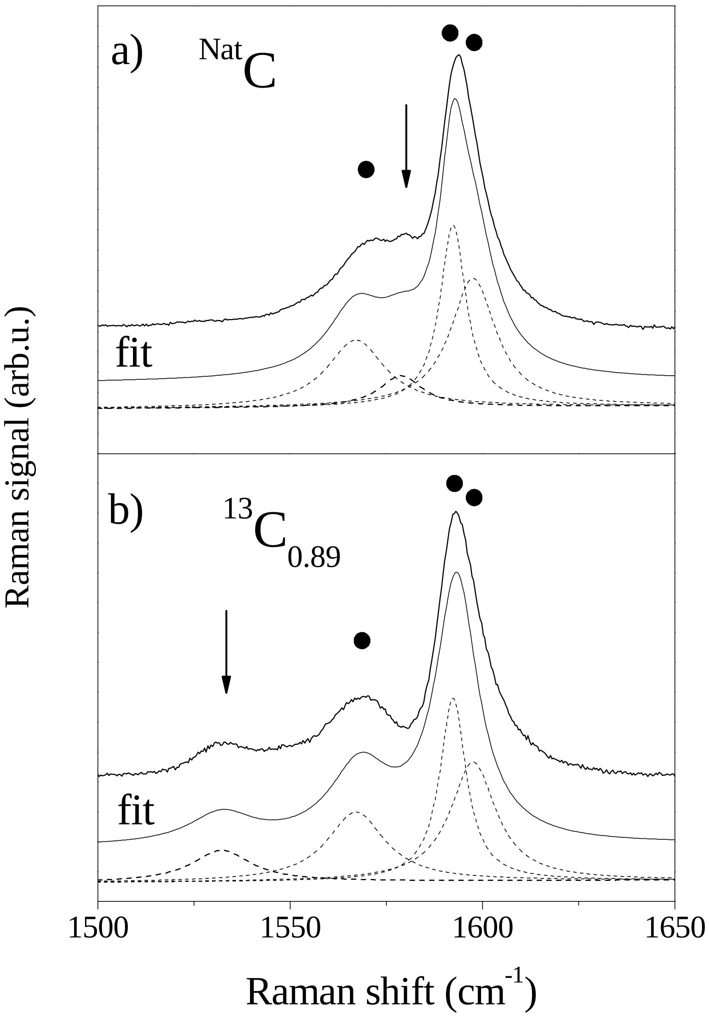

FIGURE 12.3. G modes of DWCNT with $^{\mathrm{Nat}}$C (a) and 89 % ^{13}C (b) enriched inner walls at λ=488 nm laser excitation and 90 K. Filled circles indicate the non-shifting components of the outer tube G modes. Arrows show the only shifting componenent, identified as the inner tube G mode. Dashed curves show the deconvolution of the observed spectra.

In the simplest continuum model, the shift originates from the increased mass of the inner tube walls. This gives $(\nu_0 - \nu)/\nu_0 = 1 - \sqrt{\frac{12+c_0}{12+c}}$, where c is the concentration of the ^{13}C enrichment on the inner tube, and $c_0 = 0.011$ is the natural abundance of ^{13}C in carbon. The resulting values of c are 0.277(7) and 0.824(8) for the 25 and 89 % samples, respectively.

The validity of the continuum approximation for the RBM was verified by performing first principles calculations on the (n,m)=(5,5) tube as an example. Here, the (n,m) defines the direction along which the graphene sheet is rolled-up into a tube. In the calculation, the Hessian was determined by DFT. Then, a large number of random ^{13}C distributions were generated and the RBM vibrational frequencies were determined from the diagonalization of the corresponding dynamical matrix for each individual distribution. We observed that the distribution of the resulting RBM frequencies can be approximated by a Gaussian where center and variance determine the isotope shifted RBM frequency and the spread in these frequencies. The difference between the shift determined from the continuum model and from the ab-initio calculations is below 1 %.

The broadening for the ^{13}C enriched inner tubes is best observed for the narrow RBMs. In Fig. 12.2a-b we show the RBMs of some inner tubes for the $^{\mathrm{Nat}}$C and ^{13}C$_{0.25}$ samples. Smooth solid curves are the line-shapes after deconvolution with the Gaussian response of our spectrometer. In Fig. 12.2a, this is a Lorentzian, but in Fig. 12.2b, the line-shape still contains a Gaussian component, as discussed below. The FWHMs of the resulting line-shapes are 0.76(4), 0.76(4), 0.44(4), 0.54(4) and 1.28(6), 1.30(6), 1.12(6), 1.16(6) for the inner tube RBMs shown in Fig. 12.2 of the $^{\mathrm{Nat}}$C and ^{13}C$_{0.25}$ materials, respectively. The origin of the extra broadening is due to the random distribution of ^{12}C and ^{13}C nuclei. We found that the ratio between the half width of extra broadening and the shift, $\Delta\nu/(\nu_0 - \nu)$, is approximately 0.19 for a 30 % ^{13}C enriched

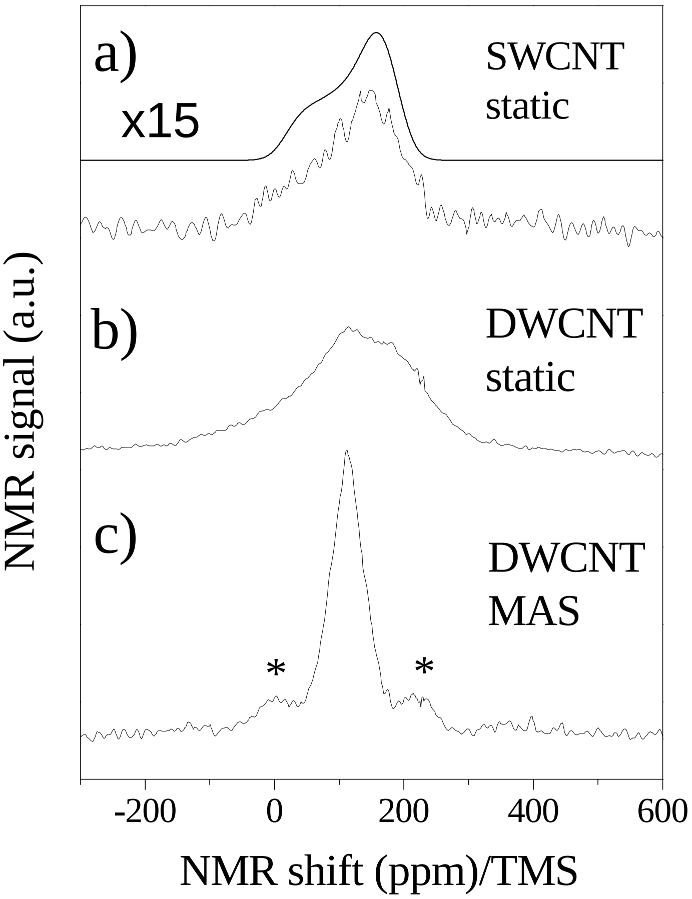

FIGURE 12.4. NMR spectra normalized by the total sample mass, taken with respect to the tetramethylsilane (TMS) shift. (a) Static spectrum for non-enriched SWNT enlarged by a factor 15. Smooth solid line is a CSA powder pattern simulation with parameters published in the literature [10]. (b) Static and (c) MAS spectra of $^{13}C_{0.89}$-DWCNT, respectively. Asterisks show the sidebands at the 8 kHz spinning frequency.

sample. The corresponding broadened line-shapes are shown by dotted curves in Fig. 12.2b. When the magnitude of the Gaussian randomness related broadening was fit (shown as dashed curve in Fig.12.2b), we found that $\Delta\nu/\left(\nu_0-\nu\right)=0.15$. Similar broadening was observed for the 89 % sample which can also be reproduced by the calculation.

Identification of the different signals also allowed to address whether carbon exchange between the inner and outer tubes occurs during the DWCNT synthesis. In Fig. 12.3 we compare the G mode spectra of $^{\mathrm{Nat}}$C- and $^{13}C_{0.89}$-DWCNTs at 488 nm excitation. For this excitation, the G mode of the outer tubes dominates the spectrum since semiconducting outer tubes and conducting inner tubes are in resonance [21]. Indeed, the only shifting component observed is small (arrows in Fig. 12.3) compared to the non-shifting components (filled circles in Fig. 12.3). Even though it is known that the SWCNT G mode consists of several components [26, 27], we deconvoluted the spectra with one Lorentzian line for the shifted component and three Lorentzians for the non-shifted components for convenience. The non-shifting components correspond to the outer tube G modes and are unaffected by the ^{13}C enrichment within the 1 cm^{-1} experimental accuracy. This gives an upper limit to the extra ^{13}C in the outer wall of 1.7 %.

Macroscopic information about the ^{13}C enrichment of the current material can be obtained from NMR spectroscopy as it is sensitive to the number of ^{13}C nuclei in the sample. In Fig. 12.4, we show the static and magic angle spinning spectra of ^{13}C enriched DWCNTs, and the static spectrum for the SWCNT starting material. The mass fraction belonging to the highly enriched phase can be calculated from the integrated signal intensity by comparing it to the signal intensity of the 89 % ^{13}C enriched fullerene starting material. We found the mass fraction of the highly enriched phase relative to the total sample mass to be 13(4) %. The expected mass ratio of inner tubes as compared to the total sample mass is 15 %, which is obtained from the SWCNT purity (50 %), ~70 % volume filling in highly filled peapod samples [28], and the mass ratio of encapsulated fullerenes to the mass of the SWCNTs. Thus, the measured mass fraction of the highly enriched phase is very similar to that of the calculated mass fraction of inner tubes. This suggests that the NMR signal comes nominally from the inner tubes, and other carbon phases such as amorphous or graphitic carbon are non ^{13}C enriched.

The typical chemical shift anisotropy (CSA) powder pattern is observed for the SWCNT sample in agreement with previous reports [10, 11]. However, the static DWCNT spectrum cannot be explained with a simple CSA powder pattern even though the spectrum is dominated by the inner tube signal. The complicated structure of the spectrum suggests that the chemical shift tensor parameters are distributed for the inner tubes. It is the result of the higher curvature of inner tubes as compared to the outer ones: the variance of the diameter distribution is the same for the inner and outer tubes [21] but the corresponding bonding angles show a larger variation [29]. In addition, the residual line-width in the MAS experiment, which is a measure of the sample inhomogeneity, is 60(3) ppm, i.e. about twice as large as the ~35 ppm found previously for SWCNT samples [10, 11]. The isotropic line position, determined from the MAS measurement, is 111(2) ppm. This value is significantly smaller than the isotropic shift of the SWCNT samples of 125 ppm [10, 11]. This difference might originate from i) the different C-C bonding angle of the small inner tubes, ii) diamagnetic shielding due to the outer tubes. Currently, experiments with inner tubes grown in different diameter outer tubes are underway to clarify this point.

In conclusion, we report on the synthesis of ^{13}C enriched inner tubes embedded inside a host outer tube. ^{13}C only resides in the inner shell of the DWCNTs, without enriching other carbon phases such as the inevitable amorphous carbon or graphite, or the outer shell tubes. The method is based on the transformation of SWCNTs encapsulating ^{13}C enriched fullerenes into DWCNTs. The ^{13}C enriched inner tubes facilitate the identification of the vibrational modes of inner and outer tube components even if they exhibit only a weak diameter dependence. The inner tube selective enrichment significantly simplifies the analysis of NMR experiments where only nanotube sensitive information is desired. The synthesis method opens the way for the controllable isotope labeling of nanotubes without labeling the unwanted side-products. The described isotope engineering may eventually find application for the controllable doping of SWCNTs, similar to the isotope engineering applied in the Si semiconducting industry.

Acknowledgement: We gratefully acknowledge H. Peterlik for the X-ray studies. Support from the FWF project Nr. 14893, the OTKA T038014 and the EU projects BIN2-2001-00580, MEIF-CT-2003-501099, and HPMF-CT-2002-02124 are acknowledged. Calculations were performed on the Schrödinger II cluster at the University of Vienna.

References

[1] M. C. Martin, J. Fabian, J. Godard, P. Bernier, J. M. Lambert, and L. Mihály, Phys. Rev. B **51**, 2844 (1995).

[2] A. Rosenberg and C. Kendziora, Phys. Rev. B **51**, 9321 (1995).

[3] P. J. Horoyski, M. L. W. Thewalt, and T. R. Anthony, Phys. Rev. B **54**, 920 (1996).

[4] J. Bardeen, L. N. Cooper, and J. R. Schrieffer, Phys. Rev. **108**, 1175 (1957).

[5] J. Meese, *Neutron Transmutation Doping of Semiconductors* (Plenum Press, NY, 1979).

[6] W. S. Capinski, H. J. Maris, E. Bauser, I. Silier, M. Asen-Palmer, T. Ruf, M. Cardona, and E. Gmelin, Appl. Phys. Lett. **71**, 2109 (1997).

[7] I. Shlimak, HAIT J. Sci. Eng. **1**, 196 (2004).

[8] R. Saito, G. Dresselhaus, and M. Dresselhaus, *Physical Properties of Carbon Nanotubes* (Imperial College Press, 1998).

[9] H. Ishii, H. Kataura, H. Shiozawa, H. Yoshioka, H. Otsubo, Y. Takayama, T. Miyahara, S. Suzuki, Y. Achiba, M. Nakatake, et al., Nature **426**, 540 (2003).

[10] X.-P. Tang, A. Kleinhammes, H. Shimoda, L. Fleming, K. Y. Bennoune, S. Sinha, C. Bower, O. Zhou, and Y. Wu, Science **288**, 492 (2000).

[11] C. Goze-Bac, S. Latil, P. Lauginie, V. Jourdain, J. Conard, L. Duclaux, A. Rubio, and P. Bernier, Carbon **40**, 1825 (2002).

[12] S. Bandow, M. Takizawa, K. Hirahara, M. Yudasaka, and S. Iijima, Chem. Phys. Lett. **337**, 48 (2001).

[13] B. W. Smith, M. Monthioux, and D. E. Luzzi, Nature **396**, 323 (1998).

[14] R. Pfeiffer, H. Kuzmany, C. Kramberger, C. Schaman, T. Pichler, H. Kataura, Y. Achiba, J. Kürti, and V. Zólyomi, Phys. Rev. Lett. **90**, 225501 (2003).

[15] H. Kuzmany, W. Plank, M. Hulman, C. Kramberger, A. Grüneis, T. Pichler, H. Peterlik, H. Kataura, and Y. Achiba, Eur. Phys. J. B **22**, 307 (2001).

[16] H. Kataura, Y. Maniwa, T. Kodama, K. Kikuchi, K. Hirahara, K. Suenaga, S. Iijima, S. Suzuki, Y. Achiba, and W. Krätschmer, Synthetic Met. **121**, 1195 (2001).

[17] T. Pichler, H. Kuzmany, H. Kataura, and Y. Achiba, Phys. Rev. Lett. **87**, 267401 (2001).

[18] G. Kresse and D. Joubert, Phys. Rev. B **59**, 17581775 (1999).

[19] M. Abe, H. Kataura, H. Kira, T. Kodama, S. Suzuki, Y. Achiba, K.-i. Kato, M. Takata, A. Fujiwara, K. Matsuda, et al., Phys. Rev. B **68**, 041405(R) (2003).

[20] F. Simon, A. Kukovecz, C. Kramberger, R. Pfeiffer, F. Hasi, H. Kuzmany, and H. Kataura, Phys. Rev. B **71**, 165439 (2005).

[21] F. Simon, R. Pfeiffer, C. Kramberger, M. Holzweber, and H. Kuzmany, *The Raman response of double wall carbon nanotubes* (Springer New York, 2005), pp. 203–224.

[22] C. Thomsen and S. Reich, Phys. Rev. Lett. **85**, 5214 (2000).

[23] J. Kürti, V. Zólyomi, A. Grüneis, and H. Kuzmany, Phys. Rev. B **65**, 165433 (2002).

[24] V. Zólyomi, J. Kürti, A. Grüneis, and H. Kuzmany, Phys. Rev. Lett. **90**, 157401 (2003).

[25] L. X. Benedict, V. H. Crespi, S. G. Louie, and M. L. Cohen, Phys. Rev. B **52**, 14935 (1995).

[26] M. A. Pimenta, A. Marucci, S. A. Empedocles, M. G. Bawendi, E. B. Hanlon, A. M. Rao, P. C. Eklund, R. E. Smalley, G. Dresselhaus, and M. S. Dresselhaus, Phys. Rev. B **58**, 16016 (1998).

[27] O. Dubay, G. Kresse, and H. Kuzmany, Phys. Rev. Lett. **88**, 235506 (2002).

[28] X. Liu, T. Pichler, M. Knupfer, M. S. Golden, J. Fink, H. Kataura, Y. Achiba, K. Hirahara, and S. Iijima, Phys. Rev. B **65**, 045419 (2002).

[29] J. Kürti, V. Zólyomi, M. Kertész, and S. Guangyu, New. J. Phys. **5**, 125.1125.21 (2003).

13

NMR Evidence for Gapped Spin Excitations in Metallic Carbon Nanotubes

P. M. Singer, P. Wzietek, H. Alloul, F. Simon, and H. Kuzmany

Physical Review Letters **95**, *236403 (2005).*

ABSTRACT We report on the spin dynamics of ^{13}C isotope enriched inner-walls in double-wall carbon nanotubes (DWCNT) using ^{13}C nuclear magnetic resonance (NMR). Contrary to expectations, we find that our data set implies that the spin-lattice relaxation time (T_1) has the same temperature (T) and magnetic field (H) dependence for most of the innerwall nanotubes detected by NMR. In the high temperature regime ($T \gtrsim 150$ K), we find that the T and H dependence of $1/T_1T$ is consistent with a 1D metallic chain. For $T \lesssim 150$ K we find a significant increase in $1/T_1T$ with decreasing T, followed by a sharp drop below $\simeq 20$ K. The data clearly indicates the formation of a gap in the spin excitation spectrum, where the gap value $2\Delta \simeq 40$ K ($\equiv 3.7$ meV) is H independent.

The electronic properties of carbon nanotubes have been of a topic of intense investigation ever since their discovery in early 1990's. According to band-structure calculations the basic electronic structure of single-wall carbon nanotubes (SWCNT) is expected to depend on the chiral wrapping vector (n, m) across the graphene plane, where tubes for which $(2n+m)/3 = integer$ are metallic, while all other tubes are semiconducting [1–4] with a large ∼1 eV gap [5]. While STM and transport measurements on *isolated* tubes demonstrate the diversity of tube properties, significant measurements on *macroscopic* amounts of tubes are only possible in selected cases. Photoemission spectroscopy (PES) measurements on metallic tubes in bundles [6, 7] suggest that strong electron-electron correlations can lead to a Tomonaga-Luttinger-liquid (TLL) state. Recently, double wall carbon nanotubes (DWCNT) have been synthesized by filling SWCNT with fullerenes (so called "peapods" [8]) followed by a high temperature reaction which merges the fullerenes into inner tubes [9, 10]. These DWCNT have some exceptional properties since the inner tubes are accommodated in a highly shielded environment under clean room conditions [11]. Raman experiments performed even on bucky paper material allows one to detect some significant properties of these inner tubes due to their small diameter (high curvature).

Nuclear magnetic resonance (NMR) is usually an excellent technique for probing the electronic properties at the Fermi level of metallic systems, take for instance conducting polymers, fullerenes, and high temperature superconductors to mention a few. However the 1.1% natural abundance of ^{13}C with nuclear spin I=1/2 limits the sensitivity of such experiments. Data taken on SWCNT essentially evidence a large distribution of properties since samples of identical tubes are presently out of reach. In this report, selective enrichment of the inner shells using ^{13}C isotope enriched fullerenes [12, 13] in the "peapod" synthesis route is used to probe the specific properties of the inner tubes. The ^{13}C enrichment allows us to increase the ^{13}C NMR sensitivity by two orders of magnitude, and furthermore achieve *selective* ^{13}C enrichment of the inner shells alone. This provides us with the possibility of singling out the electronic properties of these inner tubes for the first time. We show that, although these tubes are distributed in diameter and chirality, their electronic properties display a strikingly homogeneous behaviour. The magnetic properties of these inner wall nanotubes behave as for a 1D metal at room T, but exhibits a pronounced gap below ≃20 K. This unexpected result reveals that this specific macroscopic collection of carbon nanotubes is an object displaying original physical properties worth studying in more detail with macroscopic experimental techniques.

All ^{13}C NMR data in this report were taken with the sample sealed in a 6 mm diameter glass tube filled with 200 mbar of high purity Helium gas. Details of the synthesis techniques and various independent experimental evidences for the formation of 89% ^{13}C isotope enriched inner-walls inside natural 1.1% ^{13}C enriched outer walls are reported elsewhere [12]. We probed the low frequency spin dynamics (or low energy spin excitations, equivalently) of the inner-tubes using the spin lattice relaxation time, T_1, defined as the characteristic time it takes the ^{13}C nuclear magnetization to recover after saturation. The signal intensity after saturation, $S(t)$, was deduced by integrating the fast Fourier transform of half the spin-echo for different delay times t. All data were taken with excitation pulse lengths $\pi/2 = 3.0\mu$s and short pulse separation times of $\tau = 15\mu$s [14]. We obtained the value of T_1 by fitting the t dependence of $S(t)$ to the form $S(t) = S_a - S_b \cdot M(t)$, where $S_a \simeq S_b$ (> 0) are arbitrary signal amplitudes, and

$$M(t) = \exp\left[-\left(t/T_1^e\right)^{\beta}\right] \tag{13.1}$$

is the reduced magnetization recovery of the ^{13}C nuclear spins.

Fig. 13.1 shows the results of $M(t)$ for the inner-tubes as a function of the scaled delay time t/T_1^e, under various experimental conditions listed in the Figure. We find that $M(t)$ does not follow the single exponential form with $\beta = 1$ (dashed line), but instead fits well to the stretched exponential form with $\beta \simeq 0.65(5)$ which implies a distribution in underlying relaxation times T_1 across the sample. In such cases, T_1^e in Eq. (13.1) is directly proportional to the mean value $\overline{T_1}$ of the T_1 distribution as such $T_1^e = \overline{T_1} \cdot \beta/\Gamma(1/\beta)$, where Γ is the gamma function. We display the data in Fig. 13.1 on a semi-log scale for the *time* axis in order to accentuate the data for

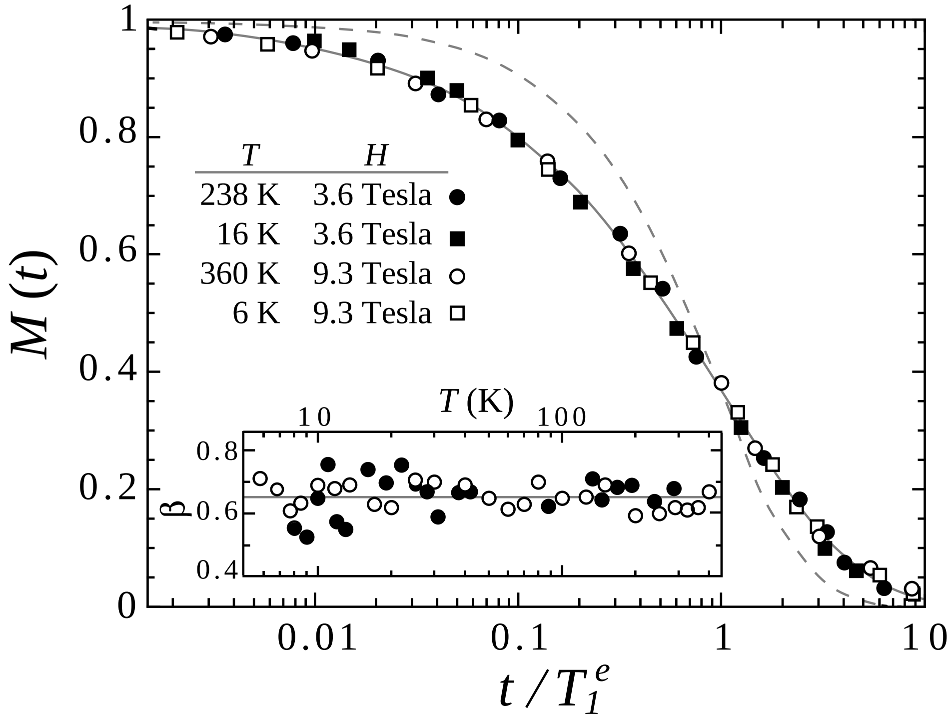

FIGURE 13.1. Reduced nuclear magnetization recovery, $M(t)$, as a function of the scaled delay time t/T_1^e (see Eq. (13.1), for various experimental conditions. Both axes are dimensionless. Solid grey curve shows stretched exponential fit with $\beta = 0.65$, while grey dashed curve shows single exponential with $\beta = 1$. Inset shows temperature dependence of the best fit values of β at 3.6 Tesla (●) and 9.3 Tesla (○), and average value of the data set $\beta = 0.65$ (solid line).

earlier decay times and to illustrate the collapse of the data set for the upper 90% of the NMR signal. We find that the upper 90% of the $M(t)$ data is consistent with constant $\beta \simeq 0.65(5)$ (see inset), implying a constant underlying distribution in T_1 for a large range of experimental conditions. The lower 10% of the $M(t)$ data (corresponding to longer delay times) comes from the non-enriched outer-walls which, as a result of their larger diameters, have much longer relaxation times under similar experimental conditions [15–18].

Two distinct origins for the multi-exponential magnetization recovery can be considered. The first is due to the powder average over the spatial anisotropy in T_1. The distribution is independent of the tube properties, and can also be found in the ^{13}C NMR data for alkali doped fullerenes A_nC_{60} [19, 20]. Given the similar diameter of C_{60} ($d = 0.71$ nm) to the average inner-wall diameter ($\overline{d} = 0.7$ nm [12, 13]) in this report, we can expect comparable bonding effects for the electron orbitals. It has been shown that in A_nC_{60} the T_1 for ^{13}C is dominated by dipole-dipole interactions between the electron spin in the $pp\pi$ bond and the ^{13}C nuclear spin [21]. In this case, the relaxation depends on the orientation of the p_π orbital (which is perpendicular to the tube surface) and the external magnetic field, and therefore contributes to the multi-exponential form of magnetization recovery for a powder average. This resultant T_1 distribution is independent of T and H.

Another source of multi-exponential recovery is from a distribution of the inner tube properties themselves, such as their diameter. According to Raman scattering, the inner tubes have a mean diameter of $\overline{d} \simeq 0.7$ nm with a standard deviation of $\sigma \simeq 0.1$ nm [12, 13]. Within this distribution lies a variety of tubes with different chirality and one can *a priori* expect to find metallic as well as semiconducting tubes [3]. If both semiconducting and metallic inner-tubes existed in our sample, one would expect the ratio of the T_1's between the different tubes to increase exponentially with decreasing T below the semiconducting gap ($\sim$ 5000 K [5]), which would drastically change the underlying T_1 distribution with decreasing T. This change would manifest itself as a large change in the shape of the recovery $M(t)$, however, as shown in Fig. 13.1 this is *not* the case.

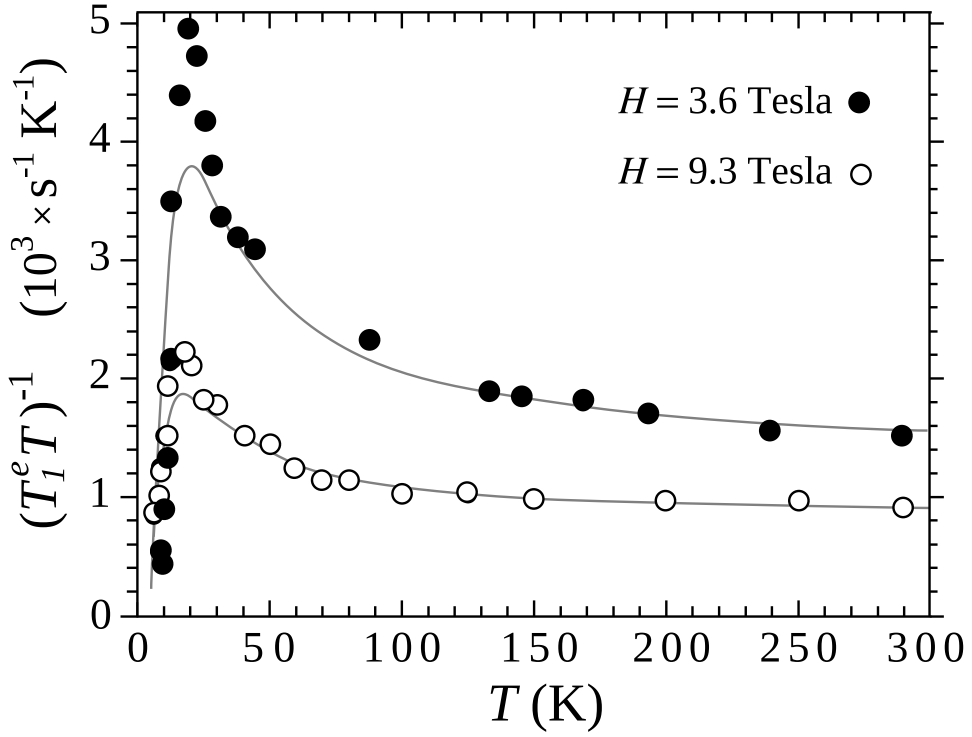

FIGURE 13.2. Temperature dependence of spin-lattice relaxation rate divided by temperature, $1/T_1^e T$, in units of ($10^3\times$ s^{-1} K $^{-1}$). Grey curves are best fits to Eq. (13.4) with $2\Delta = 46.8(40.2)$ K for $H = 3.6(9.3)$ Tesla, respectively.

We can therefore rule out the possibility of two components in T_1 with different T dependences, and instead we conclude *that all* T_1 *components exhibit the same* T *and* H *dependence within experimental scattering.*

The T_1 distribution in the sample, whether it arises from anisotropy or diameter variations (or both), shows a uniform T and H dependence. It is therefore appropriate to follow the T and H dependence of the mean value of the distribution (T_1^e in Eq. (13.1)), and thereby get insight into the homogenous electronic state of the inner tubes. In order to avoid unnecessary experimental scattering in T_1^e, we then go back and fit all the $M(t)$ data to Eq. (13.1) with a *fixed* value of $\beta = 0.65$. We plot the resulting temperature dependence of $1/T_1^e T$ in Fig. 13.2 for two different values of the magnetic field H. We can immediately separate the data into two temperature regimes; the high temperature regime $\gtrsim$ 150 K, and the low T regime $\lesssim$ 150 K. At high temperatures we find that $1/T_1^e T$ is independent of T which indicates a metallic state [14], which given the arguments above implies that all of the inner tubes are metallic. We also find a strong field dependence for T_1 which is best illustrated by plotting the high temperature value of $1/T_1^e T$ against $1/\sqrt{H}$ for H values ranging from 1.2 Tesla to 9.3 Tesla, as shown in Fig. 13.3.

We find that the data fit well to the form

$$\frac{1}{T_1^e T} \;=\; A + B\frac{1}{\sqrt{H}}, \tag{13.2}$$

where A and B are constants, which is very suggestive of a 1D spin diffusion mechanism for T_1 [22–24]. $B/\sqrt{H}$ corresponds to the diffusive contribution to the relaxation originating from the long wavelength (i.e. $q \simeq 0$) modes, while A corresponds to the non-diffusive contributions from $q > 0$ modes. A cutoff to the divergence in Eq. (13.2) as $H \to 0$ is often encountered in 1D spin chain systems [22–24] due to inter-chain coupling. In the present case, we can postulate that electron tunneling between inner to outer walls could cause similar cutoff effects, however the data down to the lowest field of H=1.2 Tesla indicates that the cutoff has not been reached yet. We therefore conclude that the high-temperature regime is consistent with a 1D metallic chain.

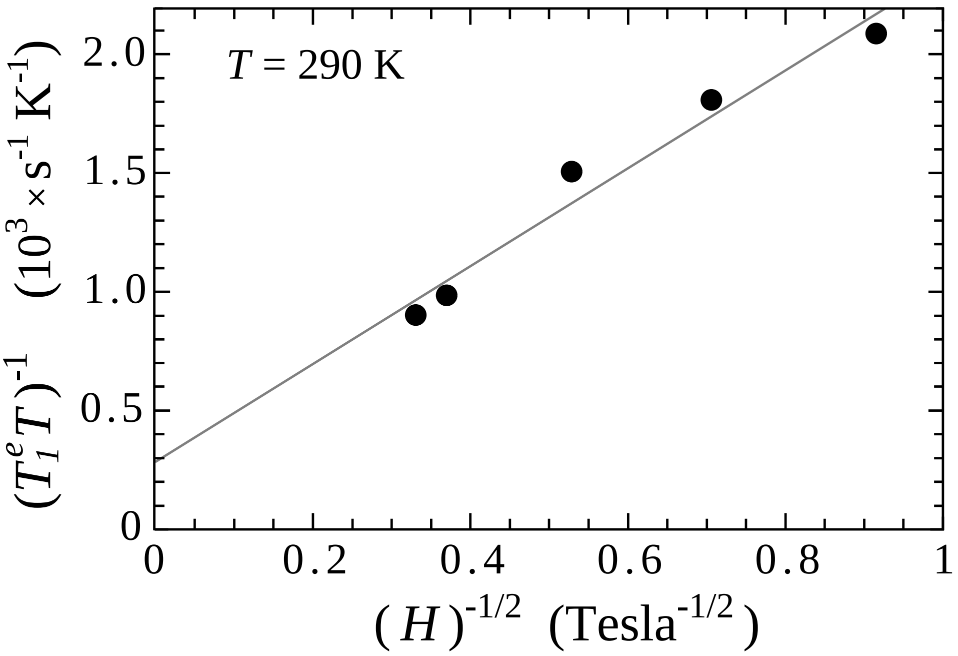

FIGURE 13.3. $1/T_1^eT$, in units of ($10^3\times$ s^{-1} K $^{-1}$), at fixed $T = 290$ K, plotted as a function of $1/\sqrt{H}$, in units of (Tesla$^{-1/2}$). Linear fit corresponds to $1/T_1^eT = A + B/\sqrt{H}$ with B = 0.00206 (Tesla$^{1/2}$ s^{-1} K^{-1}) and A = 0.00028 (s^{-1} K^{-1}).

The origin of the unusual T dependence of $1/T_1^eT$ in the low temperature regime ($\lesssim$ 150 K) is not immediately obvious. We can however rule out certain possibilities. Firstly, we can rule out the possibility of an activation type mechanism where T_1 is dominated by fluctuating hyperfine fields which are slowing down with decreasing T. If this were the case the temperature where $1/T_1^eT$ reached its maximum would shift with the resonance frequency ω [14], or the applied magnetic field $\omega = \gamma_n H$ ($\gamma_n/2\pi = 10.71$ MHz/Tesla is the gyromagnetic ratio for ^{13}C), equivalently. As shown in Fig. 13.2, however, we find no evidence of a shift in the peak temperature with H. Furthermore, at low temperatures $1/T_1^eT$ is found to drop below its high temperature value which rules out the possibility of an activation contribution *plus* a T independent contribution. Secondly, we also rule out the possibility that the T dependence of $1/T_1^eT$ is a result of paramagnetic centers which can arise from wall defects or impurity spins. The fact that a pronounced *gap* exists in $1/T_1^eT$ implies a pronounced gap in the low energy spin excitation spectrum, which cannot be explained by the presence of paramagnetic centers. We note that at the lowest temperatures < 5 K (not shown), T_1^e becomes so long (> 300 s) that the low energy spin excitations specific to the homogeneous properties of the inner-tubes become inefficient, and other excitations take over, possibly defect related. In such cases we find that the shape of $M(t)$ is no longer universal and that the underlying distribution in T_1 is smoothed out, possibly as a result of nuclear spin-diffusion.

Having ruled out the above possibilities, we are then lead to consider the simplest explanation for the experimental data using a non-interacting electron model of a 1D semiconductor with a small secondary gap (SG). The SG may be a result of the finite inner-wall curvature [4, 5, 25, 26], or perhaps the applied magnetic field itself [27]. We can fit the $1/T_1^eT$ data using this non-interacting model with only one free parameter, the homogeneous SG, 2Δ. We start by taking the normalized form of the gapped 1D density-of-states $n(E)$

$$n(E) \;=\; \begin{cases} \frac{E}{\sqrt{E^2-\Delta^2}} & \text{for } |E| > \Delta \\ 0 & \text{otherwise} \end{cases} \tag{13.3}$$

also known as the van-Hove singularity (E is taken with respect to the Fermi energy). We then use Eq. (13.3) to calculate $1/T_1^eT$ [28] as such

$$\frac{1}{T_1^eT} \;=\; \alpha(\omega)\int_{-\infty}^{\infty} n(E)n(E+\omega)\left(-\frac{\delta f}{\delta E}\right)dE, \tag{13.4}$$

where E and ω are in temperature units for clarity, f is the Fermi function $f = [\exp(E/T)+1]^{-1}$, and the amplitude factor $\alpha(\omega) = A + B'/\sqrt{\omega}$ is taken directly from Eq. (13.2) and Fig. 13.3 (where $B' = 4.53 \cdot 10^{-5}\mathrm{s}^{-1}\mathrm{K}^{-1/2}$ for $\omega \equiv H$ in temperature units). We note that factoring out the diffusion effects from the integral in Eq. (13.4) is an approximation valid only if A and B are T independent. Eq. (13.4) cannot be solved analytically, therefore we resort to numerical integration. The results of the best fit to Eq. (13.4) are presented in Fig. 13.2, where $2\Delta = 43(3)$ K ($\equiv 3.7$ meV) is found to be H independent (within experimental scattering) between 9.3 and 3.6 Tesla. We note that at the largest external field of 9.3 Tesla, $\omega = 4.5$ mK $\ll \Delta, T$, however, ω must be retained inside the integral. This is a consequence of the one dimensionality which yields a logarithmic divergence inside the integral of the form $\ln(T/\omega)$ for $T \lesssim \Delta$.

What could possibly be the origin of the observed gap? Tight binding calculations predict that applied magnetic fields can induce SG's of similar magnitude for metallic SWCNT [27]. However, such a scenario is excluded here from the absence of field dependence of the observed gap. Our data would be more consistent with a curvature induced SG for metallic tubes [4, 5, 25, 26], however for our typical inner-tubes the predicted values, $\sim$ 100 meV, are over an order of magnitude larger than our experimental data. Other scenarios, such as quantization of levels due to finite short lengths of the nanotubes could be considered as well, however, in all these cases a behaviour independent of tube size and chirality is certainly not expected.

This leads us to consider the effect of electron-electron interactions for the metallic inner tubes. It has been predicted that electron-electron correlations and a TLL state leads to an increase in $1/T_1T$ with decreasing T [29], which is a direct consequence of the 1D electronic state. The correlated 1D nature may also lead to a Peierls instability [3] with the opening of a small collective gap 2Δ and a sharp drop in $1/T_1T$ below $\Delta \sim 20$ K. Therefore, the presence of both a TLL state *and* a Peierls instability could possibly account for the data, although here again, the independence on tube geometry should be accounted for.

In conclusion, we have shown that the T_1 recovery data indicate that most of the inner-tubes have similar T and H dependences, with no indication of a metallic/semiconductor separation due to chirality distributions. At high temperatures ($T \gtrsim 150$ K) $1/T_1^eT$ of the inner tubes exhibit a metallic 1D spin diffusion state, with no low-field cutoff down to 1.2 Tesla. This metallicity could result from charge transfer from the outer to the inner tubes, however this speculation ought to be confirmed by independent experiments and theoretical calculations. Below $\sim$150 K, $1/T_1^eT$ increases dramatically with decreasing T, and a gap in the spin excitation spectrum is found below $\Delta \simeq 20$ K. We list various interpretations for this temperature dependence, ranging from a non-interacting secondary band-gap model to a 1D correlated electron model with a collective gap (possibly a Peierls instability). Firstly, these results should stimulate further experimental investigations on diversely synthesized DWCNT in order to check whether these observations are specific to the "peapod" synthesis route. Secondly, theoretical work on the incidence of 1D correlation effects for inner-wall nanotubes inside DWCNT should be helpful in sorting out the origin of our astonishing experimental evidence.

Support from the EU projects HPMF-CT-2002-02124, BIN2-2001-00580, and MEIF-CT-2003-501099, and the Austrian Science Funds (FWF) project Nr. 17345, are recognized. The authors also wish to thank V. Zólyomi and J. Kürti for valuable discussions.

References

[1] J. Mintmire, B. Dunlap, and C. T. White, Phys. Rev. Lett. **68**, 631 (1992).

[2] R. Saito, M. Fujita, G. Dresselhaus, and M. S. Dresselhaus, Phys. Rev. B **46**, 1804 (1992).

[3] R. Saito, G. Dresselhaus, and M. Dresselhaus, *Physical Properties of Carbon Nanotubes* (Imperial College Press, 1998).
[4] N. Hamada, S. Sawada, and A. Oshiyama, Phys. Rev. Lett. **68**, 1579.1581 (1992).
[5] J. Mintmire and C. White, Phys. Rev. Lett. **81**, 2506 (1998).
[6] H. Ishii, H. Kataura, H. Shiozawa, H. Yoshioka, H. Otsubo, Y. Takayama, T. Miyahara, S. Suzuki, Y. Achiba, M. Nakatake, et al., Nature **426**, 540 (2003).
[7] H. Rauf, T. Pichler, M. Knupfer, J. Fink, and H. Kataura, Phys. Rev. Lett. **93**, 096805 (2004).
[8] B. W. Smith, M. Monthioux, and D. E. Luzzi, Nature **396**, 323 (1998).
[9] B. W. Smith, M. Monthioux, and D. Luzzi, Chem. Phys. Lett. **315**, 31 (1999).
[10] S. Bandow, M. Takizawa, K. Hirahara, M. Yudasaka, and S. Iijima, Chem. Phys. Lett. **337**, 48 (2001).
[11] R. Pfeiffer, H. Kuzmany, C. Kramberger, C. Schaman, T. Pichler, H. Kataura, Y. Achiba, J. Kürti, and V. Zólyomi, Phys. Rev. Lett. **90**, 225501 (2003).
[12] F. Simon, C. Kramberger, R. Pfeiffer, H. Kuzmany, J. Zólyomi, V. Kürti, P. M. Singer, and H. Alloul, Phys. Rev. Lett. **95**, 017401 (2005).
[13] F. Simon, A. Kukovecz, C. Kramberger, R. Pfeiffer, F. Hasi, H. Kuzmany, and H. Kataura, Phys. Rev. B **71**, 165439 (2005).
[14] C. P. Slichter, *Principles of Magnetic Resonance* (Spinger-Verlag, New York, 1989), 3rd ed.
[15] X.-P. Tang, A. Kleinhammes, H. Shimoda, L. Fleming, K. Y. Bennoune, S. Sinha, C. Bower, O. Zhou, and Y. Wu, Science **288**, 492 (2000).
[16] C. Goze-Bac, S. Latil, P. Lauginie, V. Jourdain, J. Conard, L. Duclaux, A. Rubio, and P. Bernier, Carbon **40**, 1825 (2002).
[17] H. Shimoda, B. Gao, X. P. Tang, A. Kleinhammes, L. Fleming, Y. Wu, and O. Zhou, Phys. Rev. Lett. **88**, 15502 (2002).
[18] A. Kleinhammes, S.-H. Mao, X.-J. Yang, X.-P. Tang, H. Shimoda, J. P. Lu, O. Zhou, and Y. Wu, Phys. Rev. B **68**, 75418 (2003).
[19] R. Tycko, G. Dabbagh, M. Rosseinsky, D. Murphy, A. Ramirez, and R. Fleming, Phys. Rev. Lett. **68**, 1912 (1992).
[20] V. Brouet, H. Alloul, S. Garaj, and L. Forró, Phys. Rev. B **66**, 155122 (2002).
[21] V. Antropov, I. Mazin, O. Andersen, A. Liechtenstein, and O. Jespen, Phys. Rev. B **47**, R12373 (1993).
[22] J.-P. Boucher, M. A. Bakheit, M. Neichtshein, M. Villa, G. Bonera, and F. Borsa, Phys. Rev. B **13**, 4089 (1976).
[23] G. S. *et al.*, J. Phys. (Paris) **38**, 931 (1977).
[24] C. Bourbonnais, R. T. Henriques, P. Wzietek, D. Kngeter, J. Voiron, and D. Jrome, Phys. Rev. B **44**, 641 (1991).
[25] C. Kane and E. Mele, Phys. Rev. Lett. **78**, 1932 (1997).
[26] V. Zólyomi and J. Kürti, Phys. Rev. B **70**, 085403 (2004).
[27] J. P. Lu, Phys. Rev. B **74**, 1123 (1995).
[28] T. Moriya, J. Phys. Soc. Jpn. **18**, 516 (1963).
[29] H. Yoshioka, J. Phys. Chem. Solids. **63**, 1281 (2002).

14

The Raman Response of Double Wall Carbon Nanotubes

F. Simon, R. Pfeiffer, C. Kramberger, M. Holzweber, and H. Kuzmany

in Applied Physics of Carbon Nanotubes *, S. V. Rotkin and S. Subramoney eds., Springer New York 2005, p. 203.*

ABSTRACT Raman spectroscopy on carbon nanotubes (CNT) yields a rich variety of information owing to the close interplay between electronic and vibrational properties. In this paper, we review the properties of double wall carbon nanotubes (DWCNTs). In particular, it is shown that SWCNT encapsulating C_{60}, so-called peapods, are transformed into DWCNTs when subject to a high temperature treatment. The inner tubes are grown in a catalyst free environment and do not suffer from impurities or defects that are usually encountered for as-grown SWCNTs or DWCNTs. As a consequence, the inner tubes are grown with a high degree of perfection as deduced from the unusually narrow radial breathing mode (RBM) lines. This apostrophizes the interior of the SWCNTs as a nano-clean room. The mechanism of the inner nanotube production from C_{60} is discussed. We also report recent studies aimed at the simplification and industrial scaling up of the DWCNT production process utilizing a low temperature peapod synthesis method. A splitting of the RBMs of inner tubes is observed. This is related to the interaction between the two shells of the DWCNTs as the same inner tube type can be encapsulated in different outer ones. The sharp appearance of the inner tube RBMs allows a reliable assignment of the tube modes to (n,m) indexes and thus provides a precise determination of the relation between the tube diameter and the RBM frequencies.

14.1 Introduction

Carbon nanotubes have been in the forefront of the nanomaterial research since their discovery [1]. They are not only fundamentally interesting materials due to their appealing one-dimensional structure but several applications have been envisaged. Some of them have already been established such as scanning probe-heads [2] or field emission devices [3, 4]. There is an active ongoing work in these fields to exploit the properties of these materials better and to improve the device qualities. Furthermore, high expectations are related to their applications as building elements of electronics, composite reinforcing materials and many more.

Carbon nanotubes can be represented as rolled up graphene sheets, i.e. single layers of graphite. Depending on the number of coaxial carbon nanotubes, they are usually classified into multi-wall carbon nanotubes (MWCNTs) and single wall carbon nanotubes (SWCNTs). Some general considerations have been clarified in the last 13 years of nanomaterial research related to these structures. MWCNTs are more homogeneous in their physical properties as the large number of coaxial tubes smears out individual tube properties. This makes them suitable candidates for applications where their nanometer size and the conducting properties can be exploited. In contrast, SWCNT materials are grown as an ensemble of weakly interacting tubes with different diameters. The physical properties of similar diameter SWCNTs can change dramatically as the electronic structure is very sensitive on the rolling-up direction, the so-called chiral vector. Depending on the chiral vector, SWCNTs can be metallic or semiconducting [5]. This provides a richer range of physical phenomena as compared to the MWCNTs, however significantly limits the range of applications. To date, neither the directed growth nor the controlled selection of SWCNTs with a well defined chiral vector has been performed successfully. Thus, their broad applicability is still awaiting. Correspondingly, current research is focused on the post-synthesis separation of SWCNTs with a narrow range of chiralities [6–9] or on methods which yield information that are specific to SWCNTs with different chiralities. An example for the latter is the observation of chirality selective band-gap fluorescence in semiconducting SWCNTs [10].

A more recently discovered third class of CNTs are double-wall carbon nanotubes (DWCNTs). DWCNTs were first observed to form under intensive electron radiation [11] in a high resolution transmission electron microscope from C_{60} encapsulated in SWCNTs, so-called peapods [12]. Following the synthesis of C_{60} peapods in macroscopic amounts [13], bulk quantities of the DWCNT material are available using a high temperature annealing method [14]. Alternatively, DWCNTs can be produced with usual synthesis methods such as arc-discharge [15] or CVD [16] under special conditions. According to the number of shells, DWCNTs are between SWCNTs and MWCNTs. Thus, one expects that DWCNTs may provide a material where improved mechanical stability as compared to SWCNTs coexists with the rich variety of electronic properties of SWCNTs. There are, of course, a number of yet unanswered questions e.g. if the outer tube properties are unaffected by the presence of the inner tube or if the commensurability of the tube structures plays a role. These questions should be answered before the successful application of these materials.

In this contribution, we review Raman studies of DWCNTs. We show that the study of inner tubes, in particular those from C_{60} peapod based DWCNTs provides some unique insight into the physics of SWCNTs. Such studies enabled the observation of unprecedently sharp Raman modes, which evidence that the inside grown SWCNTs are highly perfect mainly due to the catalyst free nano-clean room interior of outer SWCNT reactor tubes. The sharp Raman features of inner tube Raman radial breathing modes (RBMs) enable the indexing of chiral vectors thus providing a simple alternative to the band-gap fluorescence method.

This review is organized as follows: we describe the experimental methods and the sample preparation that are used for the current study. We compare the properties of DWCNTs grown with different methods. We show that the C_{60} peapod based DWCNTs have unique properties which underline the nano-clean room conditions encountered in the inside of SWCNTs. We describe a novel method for the preparation of the C_{60} peapod precursor material that enables the large scale productions of DWCNTs. We present a detailed investigation of the electronic struc-

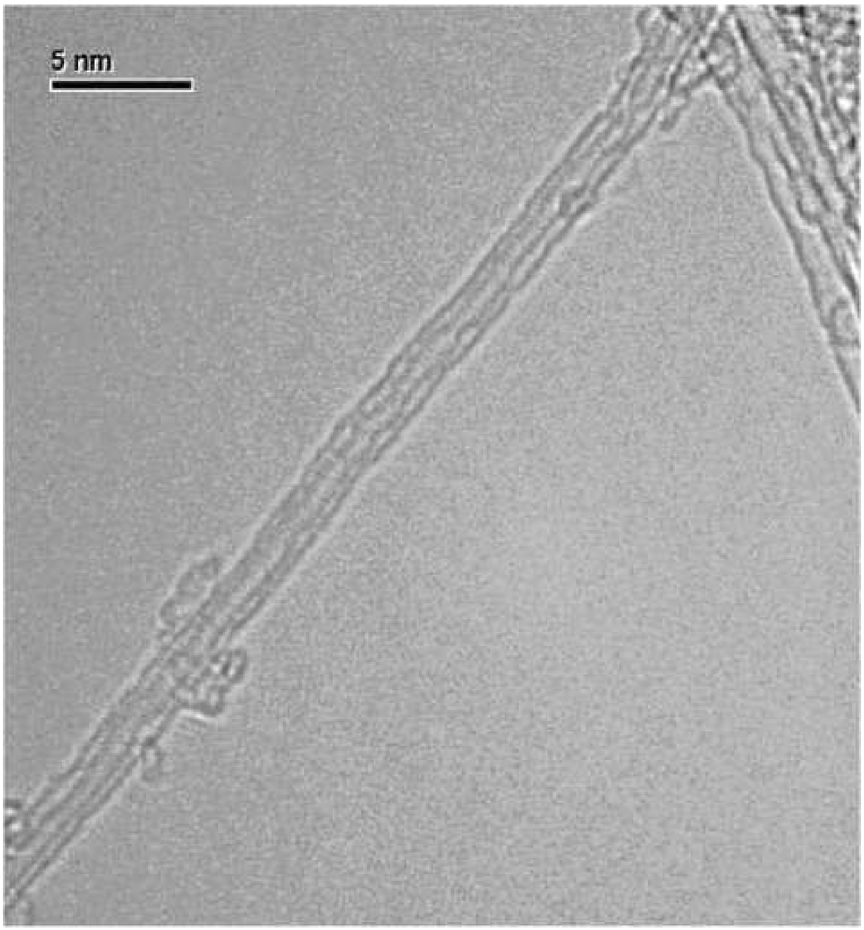

FIGURE 14.1. High-resolution TEM micrograph of a C_{60} peapod based DWCNT sample.

ture of the small diameter inner tubes. We also present the chiral vector assignment to such tubes thus refining the empirical parameters of the relation between the RBM frequencies and the tube diameters.

14.2 Experimental

SWCNT starting materials for the production of DWCNTs described herein were prepared by the laser ablation method. Their diameters were controlled in order to obtain efficient C_{60} encapsulation that results in high yield of inner nanotubes. The values of $d_{\mathrm{L}} = 1.39$ nm, $\sigma_{\mathrm{L}} = 0.1$ nm were obtained for the mean diameter and the variance of the distribution for the different samples using a large number of exciting laser energies following Ref. [17]. The SWCNT materials were purified following Ref. [13]. Peapod samples were prepared by annealing SWCNTs with C_{60} in a quartz ampoule following Ref. [13]. The peapod filling fraction was close to 100% as evidenced previously on similar samples using Electron Energy Loss Spectroscopy (EELS) [18]. The peapod materials were transformed to DWCNTs using the high temperature annealing method of Ref. [14]. The samples in the form of bucky-paper are kept in dynamic vacuum and on a copper tip attached to a cryostat, which allows temperature variation in the 20-600 K temperature range.

The Raman experiments were performed in a 180 degree backscattering geometry. A He/Ne, an Ar/Kr mixed gas, and a tunable Ti:sapphire laser pumped by an Ar laser were used for the excitation at 30 different laser lines. Multi frequency Raman spectroscopy was performed on a Dilor xy triple axis spectrometer in the 1.64-2.54 eV (755-488 nm) energy range and in a Bruker FT-Raman spectrometer for the 1.16 eV (1064 nm) excitation at 90 K. We operated the Dilor spectrometer in two modes, high and normal resolution. The high resolution uses the additive

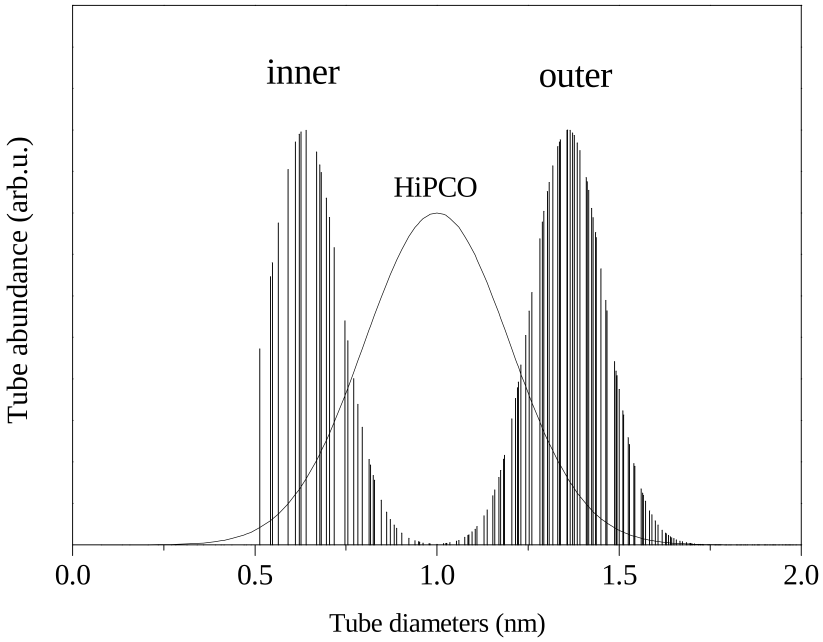

FIGURE 14.2. Schematic diameter distribution of geometrically allowed tubes in the DWCNTs of the current study. The envelope of the approximate diameter distibution in a HiPco sample is shown for comparison.

mode of the spectrometer and the spectral resolution as determined from the FWHM of the elastically scattered light was 0.4-0.7 cm^{-1} going from red to blue excitation. Similarly, spectral resolution in the normal mode was 1-2 cm^{-1} depending on the laser line. Measurements with the FT-Raman spectrometer were recorded with 1 cm^{-1} resolution. Raman shifts were accurately calibrated against a series of spectral calibration lamps. *Ab initio* calculations were performed with the Vienna Ab Initio Simulation Package (VASP) [19].

14.3 Results and discussion

14.3.1 Synthesis of double-wall carbon nanotubes

Double-wall carbon nanotubes can be classified into two groups depending on the method used for their production. DWCNT samples produced with usual preparation methods [15] have less controllable parameters such as their diameter distributions and, as shown below, their quality is inferior compared to the C_{60} peapod based DWCNTs. Following the discovery of DWCNTs from C_{60} peapods under intensive electron irradiation [11], it was demonstrated using HR-TEM that a 1200°C heat treatment can also efficiently produce the inner nanotubes based on the C_{60} peapods [20]. The first characterization of bulk amounts of DWCNTs produced by this synthesis method was performed using Raman spectroscopy by Bandow et al. [14].

In Fig. 14.1 we show a typical HR-TEM micrograph of C_{60} peapod based DWCNT. The difference in the outer and inner tube diameter is thought to be close to twice the van der Waals distance of graphite, 0.335 nm. Indeed, X-ray studies have indeed shown that the inner and outer tube diameter difference is only slightly larger, 0.72±0.02 nm [21]. The corresponding situation for a DWCNT sample with outer tube distribution centered at the (10,10) tube is depicted in Fig. 14.2. The cut-off observed at small diameter inner tubes is given by the smallest outer tube diameter of 1.2 nm which allows the precursor C_{60} to enter [22, 23].

The transformation from C_{60} peapods to DWCNTs can be conveniently followed by Raman spectroscopy. In Fig. 14.3 we compare the Raman spectra of pristine SWCNTs, C_{60}@SWCNT peapods, and DWCNTs based on the peapod material. The emergence of additional vibrational

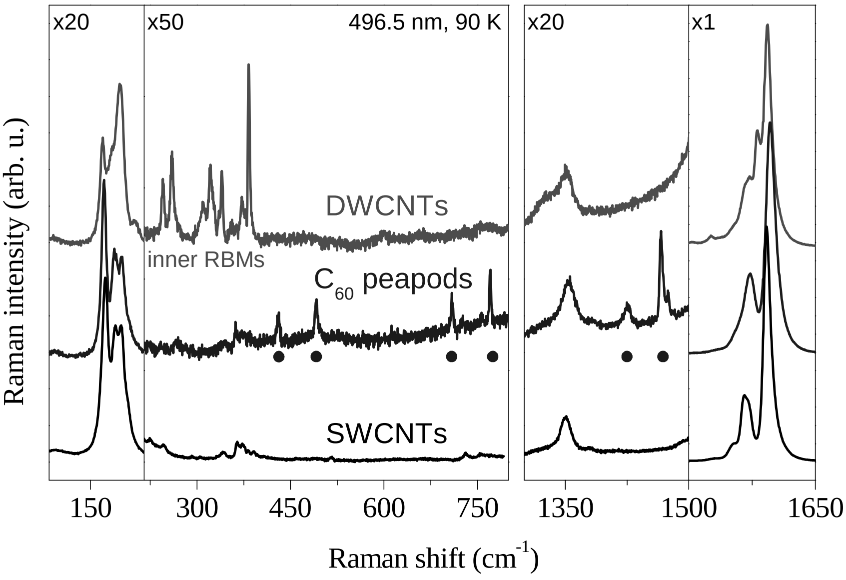

FIGURE 14.3. Raman spectra of pristine SWCNT, C_{60} peapod and C_{60} peapod based DWCNT samples for λ=497 nm laser excitation and 90 K. Bullets mark the positions of the modes of encapsulated C_{60}.

modes in the 200-450 cm^{-1} spectral range is evident in Fig. 14.3 for the DWCNT material as compared to the pristine and peapod materials. This emergence is accompanied by the disappearance of the modes of the encapsulated fullerene as denoted by circles in Fig. 14.3. The extra lines in the 200-450 cm^{-1} spectral range were identified as the radial breathing modes of the smaller diameter inner shell tubes. The disappearance of the fullerene peaks is evidence that the encapsulated C_{60} serves as carbon source for the internal tube formation [14, 24].

The inverse relationship between the RBM frequencies and tube diameters allows a tube diameter selective study of inner tube growth. In Fig. 14.4 we show the diameter selective growth of inner tubes. The topmost curve, A, shows the fully developed inner tube RBM spectrum after a 12 h annealing at 1280°C annealing, whereas B and C correspond to 0.5 and 1 hour annealing. The comparison reveals the more rapid development of small diameter inner tubes, followed by the slower development of larger diameter tubes. Similar diameter selective growth of inner tubes was found by Bandow et al. [25]. In the latter work, it was concluded from measurements at two laser excitations that small diameter inner tubes form first and are subsequently transformed to larger diameter inner tubes.

This observation is somewhat different from the one reported here. The difference might be related to the photoselective property of the Raman experiments, as the data reported here are based on measurements on a larger number of laser lines. The formation of smaller tubes in the beginning, followed by the development of larger diameter tubes later on provides useful input for the theories aimed at explaining the inner tube formation. From computer simulation it was demonstrated that C_{60} peapod based DWCNTs are formed by Stone-Wales transformations from C_{60} dimer precursors formed at high temperature by cyclo-addition [26, 27]. The free rotation of C_{60} molecules is a prerequisite for the dimer formation as it enables the molecules to have facing double bonds.

It has been found experimentally that the ellipsoidal shaped C_{70} are present as both "standing" or "lying" peapod configurations i.e. with the longer C_{70} axis perpendicular or parallel to the tube axis [28]. In small diameter tubes the lying C_{70} configuration is preferred and the molecules have facing pentagons and consequently no cyclo-additional double bond formation is possible in a linear chain. For such small diameter tubes, dimers may be formed in a canted C_{70} configuration. However this structure has not been observed experimentally. Experiments with C_{70} peapod based DWCNTs have shown that inner tubes can indeed be formed from lying C_{70} peapods,

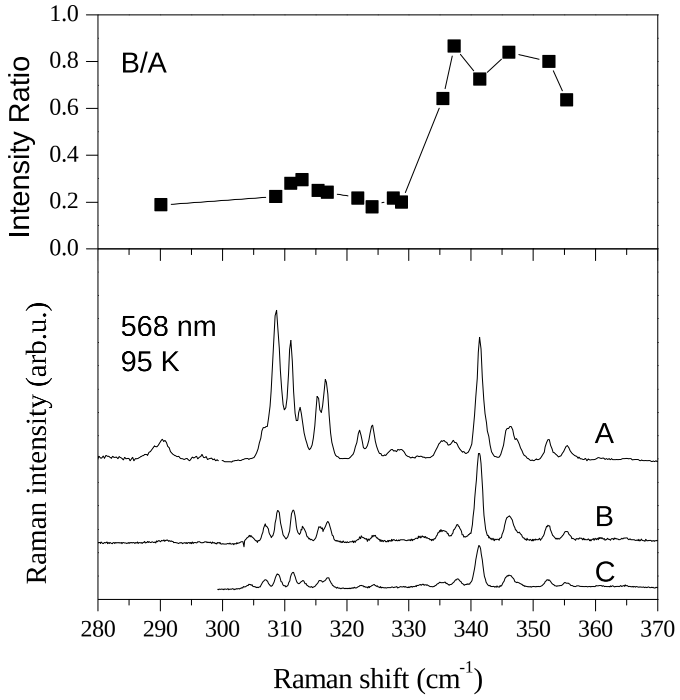

FIGURE 14.4. Diameter selective growth of inner tubes in C_{60} peapod based DWCNT measured at λ=568 nm laser excitation.

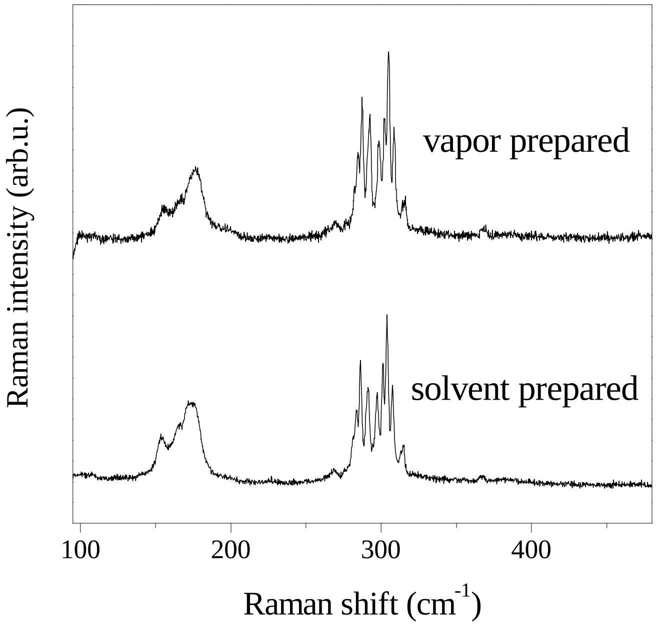

FIGURE 14.5. Comparison of DWCNTs formed from vapor prepared (upper curve) and solvent prepared (lower curve) peapod samples at λ=676 nm laser excitation and room temperature.

which presents a challenge to the current theories [29]. Clearly, more theoretical work is required on the formation process of inner tubes from fullerene peapod samples.

Apart from the lack of full understanding of the inner tube growth, the production process of the precursor fullerene peapods is relatively complicated and its scaling up to larger amounts is difficult. The usual, vapor filling, process involves the annealing of the fullerene together with the opened SWCNT material sealed together in a quartz ampoule. Recently, a new fullerene encapsulation technique involving the refluxing of the SWCNTs and the fullerenes in solvents was presented [30]. In Fig. 14.5 we show the comparison of DWCNT samples based on vapor and solvent filled C_{60} peapods. Clearly, the yield and diameter distribution of the inner tubes are identical in the two kinds of samples which proves that the solvent filling method is indeed a simple alternative to the vapor filling method. In contrast to the latter, it can be easily scaled up

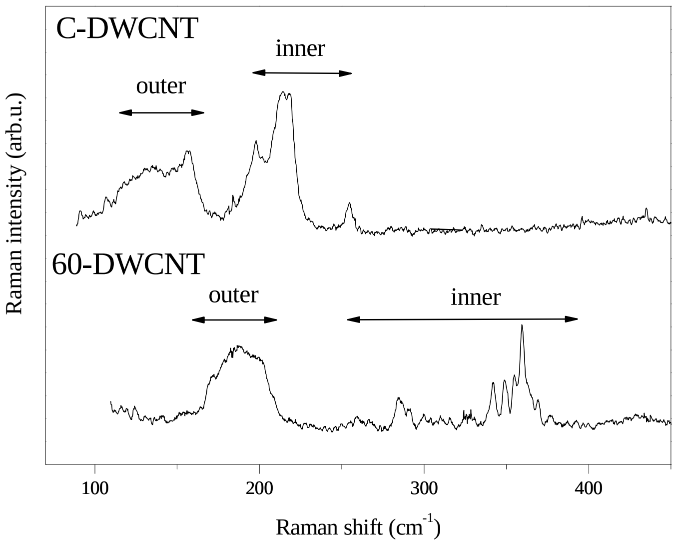

FIGURE 14.6. Comparison of CVD grown (C-DWCNT) and C_{60} peapod based DWCNT (60-DWCNT) materials at λ=633 nm laser excitation. Arrows indicate the Raman shift regions where RBMs of the outer and inner tubes are observed. The difference in inner and outer tube diameters in the two samples is apparent.

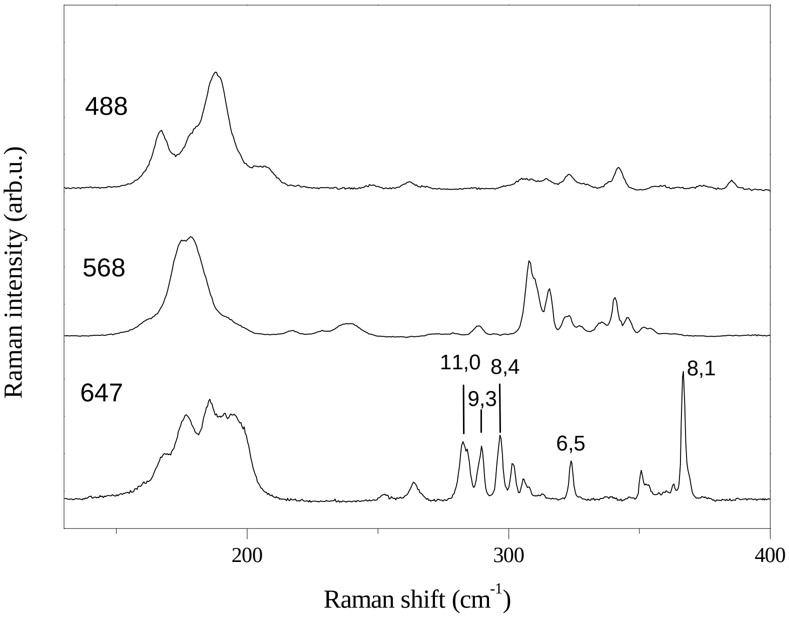

FIGURE 14.7. Raman response of the RBM of a DWCNT sample when excited with different lasers. The spectra were recorded at 90 K. The indexing for some inner tube RBMs is shown for the λ=647 nm laser energy.

to commercial quantities.

Production of DWCNTs has been reported by direct methods [15, 16]. Such DWCNTs are characteristically different from the tubes grown from the peapod precursors. In Fig. 14.6 we show the comparison of directly produced (C-DWCNT) and C_{60} peapod based DWCNT (60-DWCNT) materials. The C-DWCNTs were made from the catalytic decomposition of methane and was studied in detail previously [31]. There are clear similarities and differences in the comparison of the two kinds of DWCNT materials. Among the similarities, the Raman spectra of both compounds show two groups of bands. The lower frequency extending from 110-160 cm^{-1} for the C-DWCNT and from 165-200 cm^{-1} for the 60-DWCNT corresponds to the RBMs of the outer tubes. The modes seen at 190-250 for the C-DWCNT and at 250-370 cm^{-1} for the 60-DWCNT correspond to the RBMs of the inner tubes.

The difference in the observed RBM Raman shifts is related to the different diameters of the inner and outer tubes in the C-DWCNT and 60-DWCNT compounds. It was found that C-

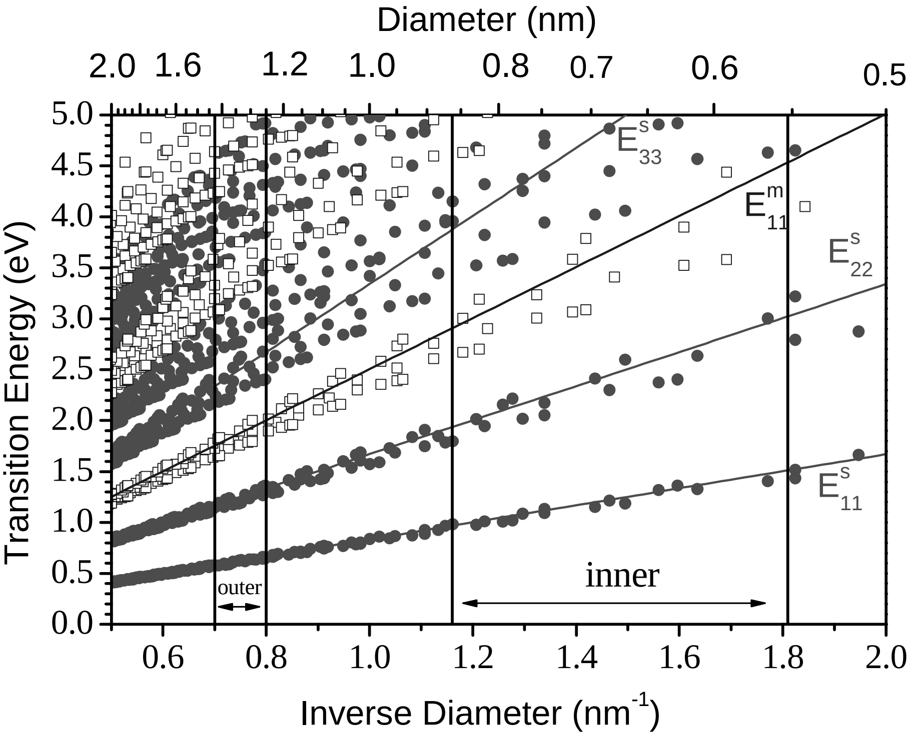

FIGURE 14.8. Kataura plot with vertical lines indicating the diameter regions of inner and outer nanotubes that are relevant for the current study.

DWCNT material shown in Fig. 14.6 has $d_{\text{inner}} = 1.52$ nm, $\sigma_{\text{inner}} = 0.6$ nm, and $d_{\text{outer}} = 2.26$ nm, $\sigma_{\text{outer}} = 0.4$ nm for the mean and the variance of the diameter distributions of the inner and outer tubes, respectively [16]. For the 60-DWCNT sample $d_{\text{inner}} = 0.67$ nm, $\sigma_{\text{inner}} = 0.1$ nm, and $d_{\text{outer}} = 1.39$ nm, $\sigma_{\text{inner}} = 0.1$ nm was found [24]. The most important difference between the two materials is the smaller inner tube RBM linewidths for the 60-DWCNT sample. In what follows, we discuss the properties of only the peapod based 60-DWCNT samples and will refer to these briefly as DWCNTs.

14.3.2 Energy dispersive Raman studies of DWCNTs

Electronic structure of DWCNTs

The diverging behavior of the electronic density of states of SWCNTs gives rise to a significant resonant Raman enhancement and a photoselective Raman scattering. The photoselectivity, combined with the multi-frequency Raman method enables a detailed study of the electronic structure of the SWCNTs. The photoselective scattering also holds for the inner tubes of the DWCNTs. The laser energy dependent response of the inner tube RBMs is shown in Fig. 14.7. For the red excitation RBM linewidths as small as 0.35 cm^{-1} were observed [24]. This is almost an order of magnitude smaller than reported previously on individual SWCNTs [32]. Related to the narrow linewidth of the vibrational modes, the resonant excitation for several lines is significant, resulting in Raman intensities almost 10 times larger than those from the outer tubes. This implies very sharp resonances between the Van Hove singularities. This issue is discussed in detail below. In addition to the sharp electronic resonances, the electron-phonon coupling is enhanced for small diameter tubes [33], which may also contribute to the observed signal enhancement of the inner tube vibrational modes [24].

The Kataura plot that is relevant for the current study is shown in Fig. 14.8. It describes the relation between the optical transitions and the tube diameters. It shows that when using red laser excitations (¡ 2 eV), nominally semiconducting inner tubes are expected to be observed. The

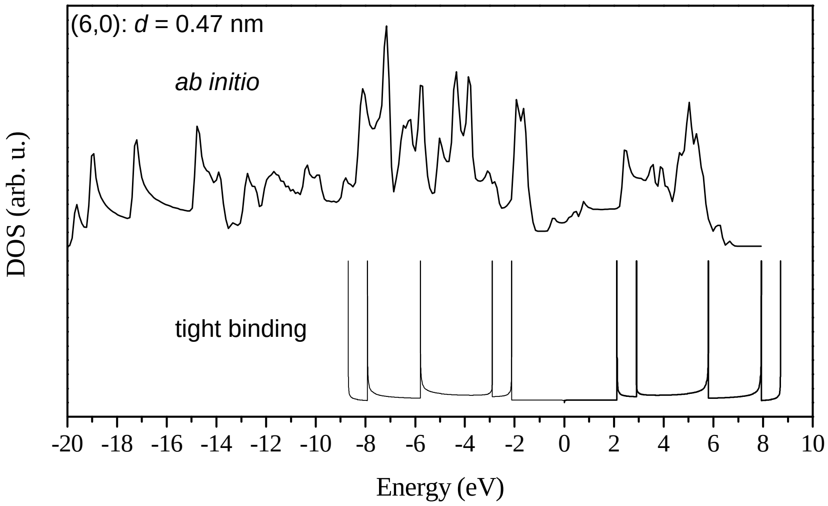

FIGURE 14.9. Electronic density of states for a small diameter, metallic nanotube using *ab initio* and tight-binding techniques. The additional structure seen in the *ab initio* calculations between the two first Van Hove singularities of the tight-binding method gives rise to resonances at excitation energies lower than E^m_{11}.

metallic inner tubes are expected to appear only for higher energy excitations, above 2.5 eV.

The presence of metallic tubes, as e.g. the (9,3) inner tube at the 647 nm laser excitation in Fig. 14.7 is unexpected as they should only be observable at significantly larger excitation energy when resonance with the E^m_{11} transition occurs. This proves that smaller energy optical transitions are present for small diameter nanotubes that are absent in the simplest tight-binding calculations. Fig. 14.9 compares the zone folded tight-binding and *ab initio* derived density of states (DOS) for a (6,0) metallic tube. The *ab initio* calculations show the presence of some structures between the lowest energy optical transitions of the tight-binding model, giving rise to the experimentally observed resonance. The observed difference between the *ab initio* and the tight-binding theory results from the finite curvature of the small diameter nanotubes. This curvature induces the mixing of the σ and the inward pointing π orbitals.

The width of the Van Hove singularities of the DOS of SWCNTs is a measure of their one-dimensional character. It can be measured from high resolution energy dispersive Raman studies. The results in the 700-750 nm excitation energy range are shown in Fig. 14.10. Dashed lines mark the Raman shift where the RBMs of two selected inner SWCNTs were followed for several laser excitations. The FWHM of the energy dependent inner tube intensities and thus the FWHM of the Van Hove singularities was found to be 60 meV. This value is very small and reflects the one dimensional character of the SWCNTs. However, this does not significantly differ from values obtained from CVD grown, individual SWCNTs in a previous study [34]. This shows that the high perfectness of the inner tubes as deduced from the phonon lifetimes has no influence on the width of the singularities in their DOS as compared to the non defect-free outer SWCNTs. It rather supports the enhancement of electron-phonon coupling for small diameter nanotubes as the origin for the signal enhancement. If, however, an enhanced electron phonon coupling is present for the small diameter tubes, one expects a range of interesting physical phenomena to arise for the small tube such as Peierls transition [35] or superconductivity [36]. Indeed, superconductivity has been observed with a critical transition temperature of T_c= 15 K in 0.4 nm diameter SWCNTs [37]. However, the relevance of such phenomena for the inner tubes embedded in DWCNTs is not yet settled and is currently being investigated.

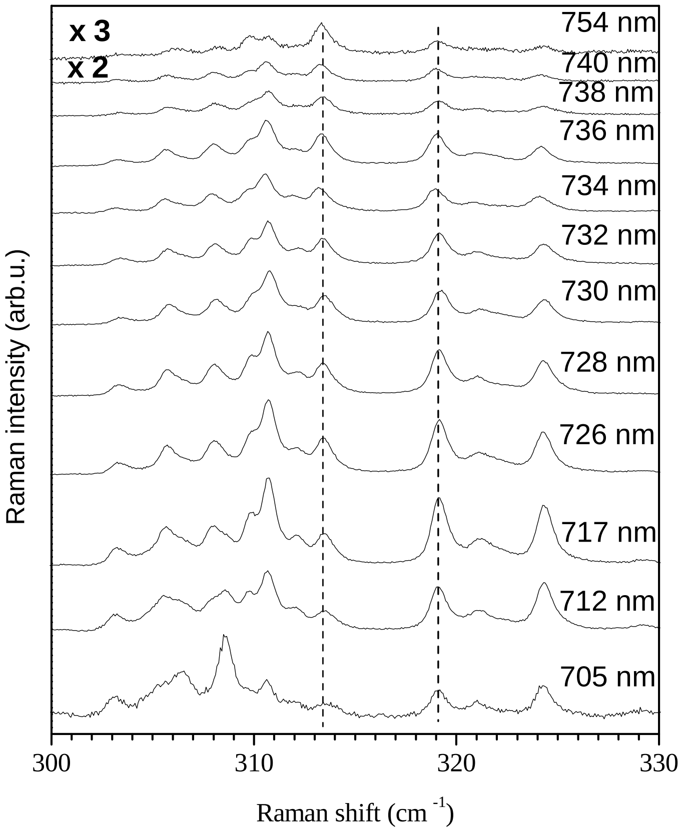

FIGURE 14.10. Energy dispersive Raman spectra of the DWCNT sample in the 700-750 nm excitation energy range. Dashed lines indicate the same inner tube RBM followed for several laser excitations. The spectra are normalized to the incident power.

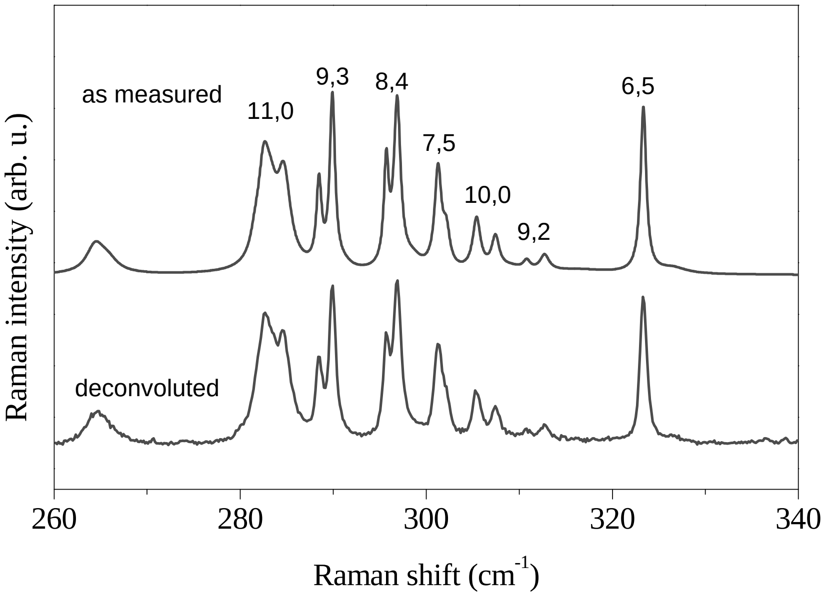

FIGURE 14.11. High resolution Raman spectra of inner tube RBMs of DWCNT at λ=647 nm laser excitation and 90 K. We also show the corresponding spectrum after deconvolution with the resolution of the spectrometer.

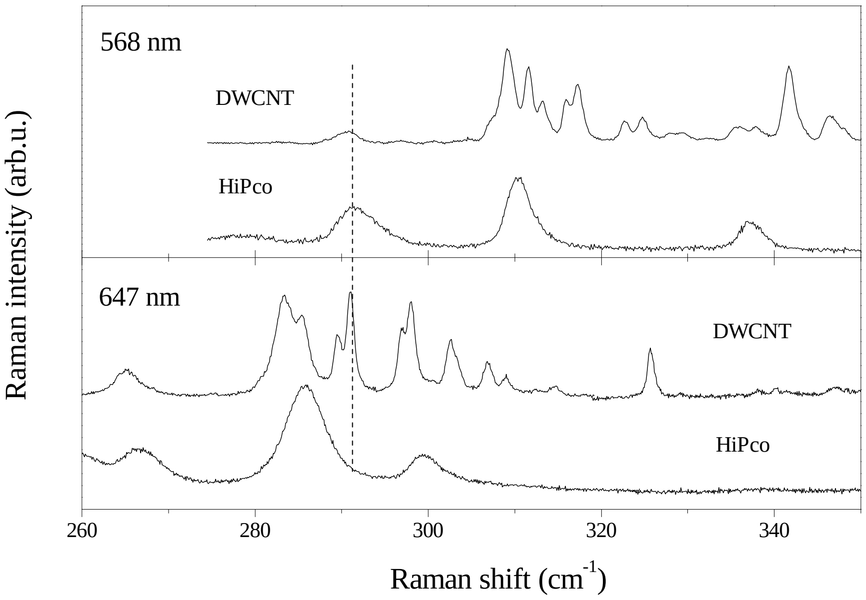

FIGURE 14.12. Comparison of the inner tube RBMs of a DWCNT sample and the RBMs of a sample prepared by the HiPco process at λ=568 nm and 647 nm laser energy. Both samples were measured at 90 K in the high resolution mode.

Splitting of the inner tube RBM response of DWCNTs

In addition to the well defined number of geometrically allowed inner tubes, a larger number of RBMs are observed. In Fig. 14.11 we show spectra measured in the high resolution mode at the 647 nm laser excitation at 90 K. The spectra after deconvolution with the resolution of the spectrometer are also shown. The resolution of the spectrometer contributes to an additional Gaussian broadening of the intrinsically Lorenztian RBM lineshapes. The width of the Gaussian was measured from the response of our apparatus to the exciting laser and was found to be 0.4-0.7 cm^{-1} depending on the laser energy. The presence of additional, split components is apparent in Fig. 14.11 for some tubes. Some RBMs split into even 3 and more components. This splitting is a natural consequence of the different number of geometrically allowed inner and outer tubes and is related to the interaction between the two shells of the DWCNTs. As the diameters of both the inner and outer tubes are discrete sequences, some inner tubes can be grown in outer tubes with different diameters. Then the difference in inner-outer tube wall distance gives rise to a different interaction that causes the observed splitting of the lines. A rough estimate yields that for the DWCNTs studied here, 40 geometrically allowed outer tubes accommodate 20 geometrically allowed inner tubes. As a consequence, on average splitting into two components is expected. This estimate, however, does not account for the magnitude of the splitting that is currently being further investigated both experimentally and theoretically [38].

In addition to the two-wall related splitting of the RBMs of inner tubes, further peculiarities can be observed. In Fig. 14.12 we compare the inner tube RBMs of a DWCNT sample with the RBMs of a small diameter SWCNT sample. The latter was a HiPco sample with a mean diameter and a variance of d =1.05 nm and σ=0.15 nm, respectively [39]. The figure shows this comparison for 568 nm and 647 nm laser excitation. The larger number of RBMs in the DWCNT sample as compared to the HiPco sample and the absence of splitting for the RBMs in the HiPco sample is observed. Broader RBM lines are observed in the HiPco sample, however this would not limit the observation of the splitting. As discussed above, the splitting is related to the two-shell nature of the DWCNT samples and thus its absence is natural in the HiPco sample. However, the absence of some RBMs corresponding to geometrically allowed tubes in the HiPco sample that are observed in the inner tube DWCNT spectrum is intriguing.

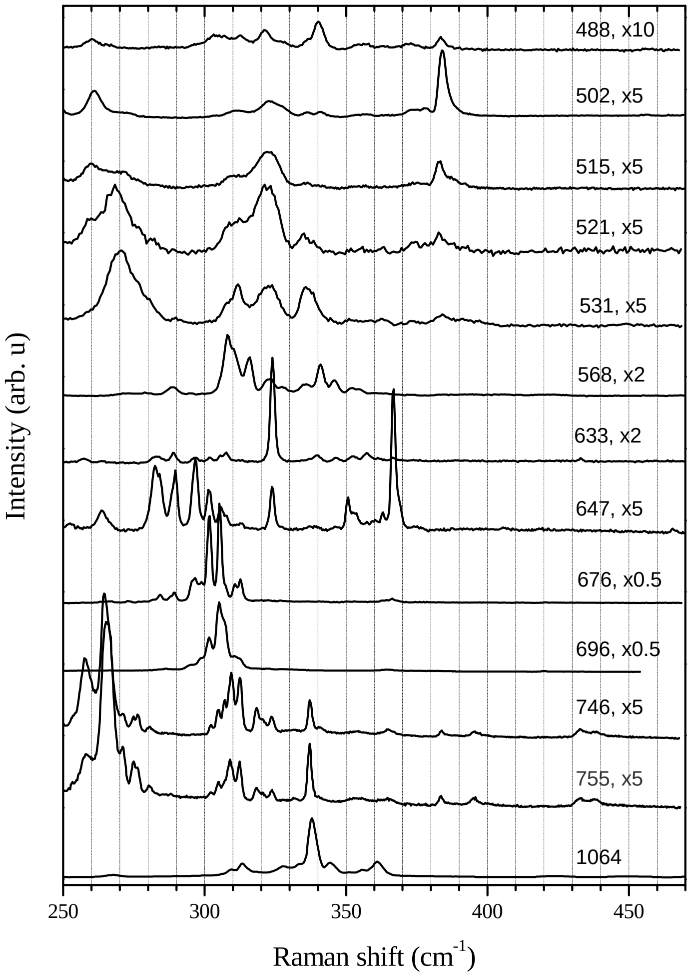

FIGURE 14.13. DWCNT RBM spectra measured at 90 K for several laser excitations.

The absence of geometrically allowed SWCNTs or the smaller number of optical transitions in the HiPco samples may explain for our observation. The dashed line in Fig. 14.12 shows an example for a tube RBM that is absent at 647 nm excitation from the HiPco spectrum, however appears at 568 nm excitation. Similar behavior was observed for other, missing HiPco RBM modes, i.e. the RBM modes of the SWCNTs of the HiPco samples are also present, although at much less number of laser lines. This clearly shows, that all the geometrically allowed SWCNTs are present both among the inner tubes and also in the HiPco sample, however, there is a significantly larger number of optical transitions for the inner tubes of the DWCNT sample. This is most probably related to a yet unexplained intricate interplay between the two shells of the DWCNT samples and calls for theoretical work on this issue. In addition to the larger number of lines observed in the inner tube RBM spectrum of DWCNTs, a slight downshift ranging from 2-3 cm^{-1} is also observed. This downshift is related to the different environment for an inner tube of the DWCNT and for an SWCNT in a HiPco sample. The earlier is surrounded by an outer tube, whereas the latter is embedded in bundles. These interactions give rise to a different value for the C_2 constant of the RBM mode frequencies. The broader linewidths observed in the HiPco sample underlines the highly perfect nature of the inner nanotubes.

Chiral index assignment for inner tubes

The reciprocal relation between the RBM frequencies and the tube diameters contributes to a significant spectral spread for the observed inner tube RBMs. This, together with the narrow linewidths observed for the inner tubes allows the accurate (n, m) indexing of the tubes. In Fig. 14.13, the inner tube RBMs measured at several laser lines are shown. The observation of a large

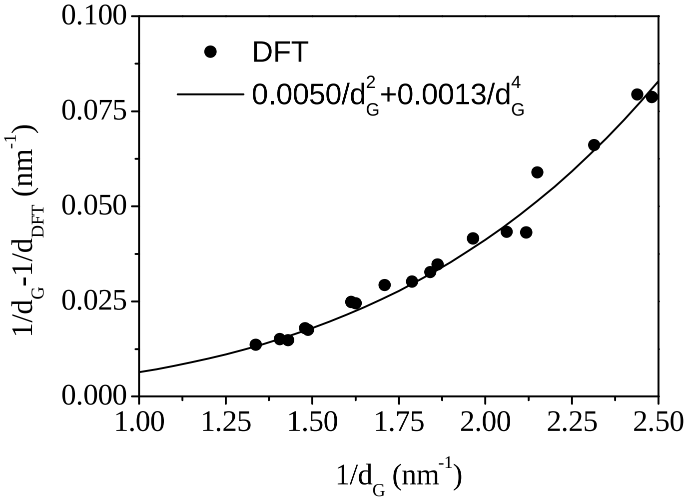

FIGURE 14.14. Difference between graphene and DFT derived inverse tube diameters. The solid line is a polynomial interpolation.

number of well defined RBMs allows the determination of RBM shifts corresponding to distinct inner tubes. The Raman shifts of observable inner tubes are summarized in Table. 14.1, together with the assigned chiral vectors, and tube diameters calculated with DFT methods. It was found that the diameters of small tubes, based on the lattice constant of graphene gives significant deviations as compared to the DFT calculated tube diameters [40].

In Fig. 14.14 we compare the inverse tube diameters calculated from the lattice constant of graphene and from a DFT calculation. A simple interpolation could be established: $1/d_{\mathrm{DFT}} = 1/d_{\mathrm{G}}$ - $\left(0.0050/d_{\mathrm{G}}^2 + 0.0013/d_{\mathrm{G}}^4\right)$, where d_{DFT} and d_{G} are the DFT and the graphene derived tube diameters, respectively, and d_{G} is expressed from the chiral indices as: $d_{\mathrm{G}} = 0.141\sqrt{3\left(m^2+n^2+mn\right)}/\pi$. The C_1 and C_2 constants of the RBM frequencies ν_{RBM}=$C_1/d_{\mathrm{DFT}} + C_2$ were determined from a linear regression and C_1=233 cm^{-1} nm and C_2=14 cm^{-1} were found.

TABLE 14.1. Inner tube RBM frequencies and tube diameters: (1) center of gravity line position of the RBM averaged from different laser excitations, (2) CNT chiral indices, (3) interpolated DFT determined tube diameters, (4) first and second tight-binding optical transition energies with γ_0= 2.9 eV, (5) theoretical RBM frequencies at the best fit with C_1=233 cm^{-1} nm and C_2= 14 cm^{-1}. ("n.i.": not identified), from [40].

ν_{RBM} exp. (cm^{-1})	(n,m)	d_{RBM} (nm)	E_{11}/E_{22} (eV)	ν_{RBM}th. (cm^{-1})
246.1	(11,3)	0.997	0.84/1.59	247.8
252.4	(12,1)	0.978	0.86/1.60	252.1
n.i.	(10,4)	0.975	2.36/4.21	252.9
257.6	(9,5)	0.960	0.84/1.73	256.8
260.5	(8,6)	0.950	0.87/1.69	259.2
n.i.	(11,2)	0.947	2.40/4.24	260
n.i.	(7,7)	0.947	2.52/4.54	260
n.i.	(12,0)	0.937	2.40/4.25	262.6
265.3	(10,3)	0.921	0.87/1.84	267
270.5	(11,1)	0.901	0.85/1.91	272.5
274.7	(9,4)	0.901	0.82/1.75	272.5
n.i.	(8,5)	0.888	2.61/4.60	276.5
280.2	(7,6)	0.881	0.93/1.85	278.5
282.3	(10,2)	0.871	0.97/1.78	281.6
284.0	(11,0)	0.860	0.98/1.80	284.9
289.1	(9,3)	0.846	2.67/4.63	289.4
296.1	(8,4)	0.828	0.98/2.00	295.4
298.9	(10,1)	0.824	2.70/4.65	296.7
301.9	(7,5)	0.817	1.01/1.95	299.2
304.0	(6,6)	0.813	2.90/5.02	300.5
306.5	(9,2)	0.794	1.01/2.15	307.3
311.7	(10,0)	0.783	1.02/2.22	311.6
317.2	(8,3)	0.771	1.09/2.02	316.1
319.8	(7,4)	0.756	3.00/5.07	322.5

Fig. 14.15 shows that no linear relationship could be established between the RBM frequencies and the graphene derived inverse tube diameters. However, a very reliable fit is obtained with small discrepancies between calculated and measured RBM frequency values when the DFT optimized tube diameters were used. It establishes that the reciprocal relationship between the RBM frequencies and the tube diameters, when the latter is properly calculated, is valid down to the smallest observable inner tubes. The value determined for the C_1 constant is not restricted to small diameter tubes only, however studies on larger diameter tubes have been lacking the precision that could be obtained from the inner tube analysis of DWCNTs. Therefore a direct comparison with previously determined values can not be performed. It has been pointed out above that the different environment for an inner tube and for an SWCNT in a bundle prevents a comparison of the respective C_2 parameters.

ν_{RBM} exp. (cm^{-1})	(n,m)	d_{RBM} (nm)	E_{11}/E_{22} (eV)	ν_{RBM}th. (cm^{-1})
323.0	(9,1)	0.748	1.13/2.05	325.8
327.9	(6,5)	0.748	1.09/2.17	325.8
336.7	(8,2)	0.719	3.06/5.09	338.3
340.3	(9,0)	0.706	3.08/5.10	344.1
345.8	(7,3)	0.697	1.15/2.41	348.2
353.8	(6,4)	0.684	1.21/2.30	354.6
358.5	(5,5)	0.680	3.37/5.52	356.8
364.9	(8,1)	0.671	1.19/2.60	361.4
374.5	(7,2)	0.643	1.32/2.38	376.3
383.5	(8,0)	0.629	1.36/2.40	384.4
389.3	(6,3)	0.624	3.52/5.54	387.3
395.6	(5,4)	0.615	1.33/2.63	393.2
405.8	(7,1)	0.595	3.58/5.55	405.9
422.0	(6,2)	0.569	1.40/3.00	423.8
432.9	(7,0)	0.553	1.43/3.22	435.7
438.1	(5,3)	0.553	1.52/2.79	435.7
444.5	(4,4)	0.547	4.10/5.80	439.9
462.1	(6,1)	0.519	1.66/2.87	463.1

14.4 Conclusion

In conclusion, the Raman studies of peapod based DWCNT materials have been reviewed. It was shown that this material has an unprecedently high perfectness related to the growth in the catalyst free environment. The growth mechanism is not fully understood and some alternative mechanisms have been discussed. A method is presented that enables the industrial scaling up of the DWCNT production. The properties of the DWCNT have been compared with a similar diameter SWCNT material, a HiPco sample.

The geometrically allowed small diameter tubes are present in both materials. However, due to the smaller number of optical transitions in the HiPco sample, a smaller number of RBM lines are observed. A splitting of the geometrically allowed inner tube RBMs in the DWCNT sample was observed. It was explained by the different shell-shell distance of inner-outer tube pairs with varying diameters. The sharp appearance of the inner tube RBMs and their relatively larger spectral spread allowed a chiral index assignment for a broad spectral range and Raman shifts. It was found that a linear relation could be established between the RBM frequencies and DFT determined tube diameters. The empirical constants relating the RBM frequencies and the tube diameters have been refined. Nevertheless, a direct comparison with values determined on free-standing or bundled SWCNTs is not straightforward.

The authors gratefully acknowledge J. Kürti, and V. Zólyomi for many fruitful discussions and for the DFT calculations. H. Kataura and Y. Achiba are acknowledged for providing some of the C_{60} peapod materials. We thank Hui-Ming Cheng for providing the CVD grown DWCNT sample. The authors gratefully acknowledge J. Bernardi for the TEM micrographs, A. Sen, Ch. Schaman, Th. Pichler, and Á. Kukovecz for their contributions to the Raman experiments. This work was supported by the Austrian Science Funds (FWF) project Nr. 14893 and by the EU projects NANOTEMP BIN2-2001-00580 and PATONN Marie-Curie MEIF-CT-2003-501099.

References

[1] S. Iijima, Nature **354**, 56 (1991).
[2] J. H. Hafner, C. L. Cheung, and C. M. Lieber, Nature **398**, 761 (1999).
[3] G. Z. Yue, Q. Qiu, B. Gao, Y. Cheng, J. Zhang, H. Shimoda, S. Chang, J. P. Lu, and O. Zhou, Appl. Phys. Lett. **81**, 355 (2002).

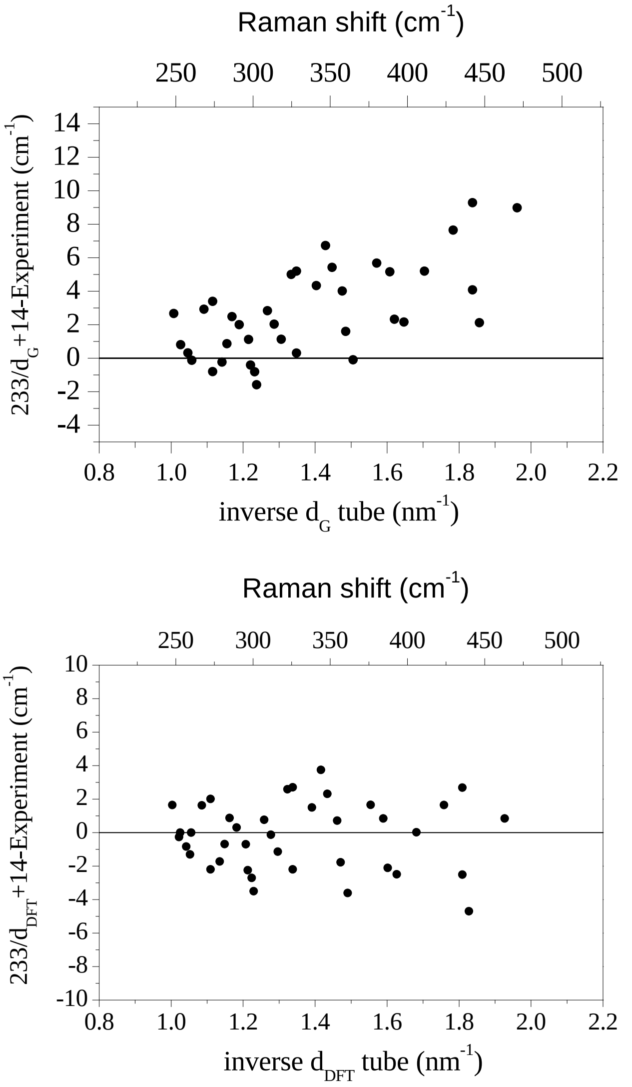

FIGURE 14.15. Difference between the calculated and measured RBM Raman shifts when the graphene derived (upper panel) and DFT optimized (lower panel) tube diameters were used.

[4] A. N. Obraztsov, I. Pavlovsky, A. P. Volkov, E. D. Obraztsova, A. L. Chuvilin, and V. L. Kuznetsov, J. Vac. Sci. Techn. B **18**, 1059 (2000).

[5] R. Saito, G. Dresselhaus, and M. Dresselhaus, *Physical Properties of Carbon Nanotubes* (Imperial College Press, 1998).

[6] D. Chattopadhyay, L. Galeska, and F. Papadimitrakopoulos, J. Am. Chem. Soc. **125**, 3370 (2003).

[7] R. Krupke, F. Hennrich, H. von Lohneysen, and M. M. Kappes, Science **301**, 344 (2003).

[8] Z. H. Chen, X. Du, M. H. Du, C. D. Rancken, H. P. Cheng, and A. G. Rinzler, Nano Lett. **3**, 1245 (2003).

[9] M. Zheng, A. Jagota, M. S. Strano, A. P. Santos, P. Barone, S. G. Chou, G. Diner, M. S. B. A. Dresselhaus, R. S. McLean, G. B. Onoa, et al., Science **302**, 1545 (2003).

[10] M. J. O'Connell, S. M. Bachilo, C. B. Huffman, V. C. Moore, M. S. Strano, E. H. Haroz, K. L. Rialon, P. J. Boul, W. H. Noon, C. Kittrell, et al., Science **297**, 593 (2002).

[11] B. W. Smith, M. Monthioux, and D. Luzzi, Chem. Phys. Lett. **315**, 31 (1999).

[12] B. W. Smith, M. Monthioux, and D. E. Luzzi, Nature **396**, 323 (1998).

[13] H. Kataura, Y. Maniwa, T. Kodama, K. Kikuchi, K. Hirahara, K. Suenaga, S. Iijima, S. Suzuki, Y. Achiba, and W. Krätschmer, Synthetic Met. **121**, 1195 (2001).

[14] S. Bandow, M. Takizawa, K. Hirahara, M. Yudasaka, and S. Iijima, Chem. Phys. Lett. **337**, 48 (2001).

[15] J. L. Hutchison, N. A. Kiselev, E. P. Krinichnaya, A. V. Krestinin, R. O. Loutfy, A. P. Morawsky, V. E. Muradyan, E. D. Obraztsova, J. Sloan, S. V. Terekhov, et al., Carbon **39**, 761 (2001).

[16] W. Ren, F. Li, J. Chen, S. Bai, and H.-M. Cheng, Chem. Phys. Lett. **359**, 196 (2002).

[17] H. Kuzmany, W. Plank, M. Hulman, C. Kramberger, A. Grüneis, T. Pichler, H. Peterlik, H. Kataura, and Y. Achiba, Eur. Phys. J. B **22**, 307 (2001).

[18] X. Liu, T. Pichler, M. Knupfer, M. S. Golden, J. Fink, H. Kataura, Y. Achiba, K. Hirahara, and

S. Iijima, Phys. Rev. B **65**, 045419 (2002).

[19] G. Kresse and D. Joubert, Phys. Rev. B **59**, 17581775 (1999).

[20] B. W. Smith and D. Luzzi, Chem. Phys. Lett. **321**, 169 (2000).

[21] M. Abe, H. Kataura, H. Kira, T. Kodama, S. Suzuki, Y. Achiba, K.-i. Kato, M. Takata, A. Fujiwara, K. Matsuda, et al., Phys. Rev. B **68**, 041405(R) (2003).

[22] M. Melle-Franco, H. Kuzmany, and F. Zerbetto, J. Phys. Chem. B **109**, 6986 (2003).

[23] S. Berber, Y.-K. Kwon, and D. Tománek, Phys. Rev. Lett. **88**, 185502 (2002).

[24] R. Pfeiffer, H. Kuzmany, C. Kramberger, C. Schaman, T. Pichler, H. Kataura, Y. Achiba, J. Kürti, and V. Zólyomi, Phys. Rev. Lett. **90**, 225501 (2003).

[25] S. Bandow, T. Hiraoka, T. Yumura, K. Hirahara, H. Shinohara, and S. Iijima, Chem. Phys. Lett. **384**, 320 (2004).

[26] S. W. Han, M. Yoon, S. Berber, N. Park, E. Osawa, J. Ihm, and D. Tománek, Phys. Rev. B **70**, 113402 (2004).

[27] Y. Zhao, B. I. Yakobson, and R. E. Smalley, Phys. Rev. Lett. **88**, 185501 (2002).

[28] K. Hirahara, K. Bandow, S. Suenaga, H. Kato, T. Okazaki, T. Shinohara, and S. Iijima, Phys. Rev. B **64**, 115420 (2001).

[29] F. Simon, A. Kukovecz, C. Kramberger, R. Pfeiffer, F. Hasi, H. Kuzmany, and H. Kataura, Phys. Rev. B **71**, 165439 (2005).

[30] F. Simon, H. Kuzmany, H. Rauf, T. Pichler, J. Bernardi, H. Peterlik, L. Korecz, F. Fülöp, and A. Jánossy, Chem. Phys. Lett. **383**, 362 (2003).

[31] F. Li, S. G. Chou, W. Ren, J. A. Gardecki, A. K. Swan, M. S. Ünlü, B. B. Goldberg, H.-M. Cheng, and M. S. Dresselhaus, J. Mater. Res. **18**, 1251 (2003).

[32] A. Jorio, R. Saito, J. H. Hafner, C. M. Lieber, M. Hunter, T. McClure, G. Dresselhaus, and M. S. Dresselhaus, Phys. Rev. Lett. **86**, 1118 (2001).

[33] M. Machón, S. Reich, J. M. Pruneda, C. Thomsen, and P. Ordejón, in *Proceedings of the IWEPNM* (2003), pp. 427–430.

[34] A. Jorio, A. G. Souza, G. Dresselhaus, M. S. Dresselhaus, R. Saito, J. H. Hafner, C. M. Lieber, F. M. Matinaga, M. S. S. Dantas, and M. A. Pimenta, Phys. Rev. B **63**, 245416 (2001).

[35] G. Grüner, *Density waves in solids* (Addison-Wesley Publishing Company, 1994).

[36] M. Tinkham, *Introduction to superconductivity* (Krieger Publishing Company, 1975).

[37] Z. K. Tang, L. Y. Zhang, N. Wang, X. X. Zhang, G. H. Wen, G. D. Li, J. N. Wang, C. T. Chan, and P. Sheng, Science **292**, 2462 (2001).

[38] R. Pfeiffer, C. Kramberger, F. Simon, H. Kuzmany, V. N. Popov, and H. Kataura, Eur. Phys. J. B **42**, 345 (2004).

[39] A. Kukovecz, C. Kramberger, V. Georgakilas, M. Prato, and H. Kuzmany, Eur. Phys. J. B **28**, 223 (2002).

[40] C. Kramberger, R. Pfeiffer, H. Kuzmany, V. Zólyomi, and J. Kürti, Phys. Rev. B **68**, 235404 (2003).

15

Studying single-wall carbon nanotubes through encapsulation: from optical methods till magnetic resonance

Ferenc Simon

Journal of Nanosciences and Nanotechnology **in Press**.

ABSTRACT Encapsulating fullerenes, magnetic fullerenes, ^{13}C isotope enriched fullerenes and organic solvents inside SWCNTs enables to yield unprecedented insight into their electronic, optical, and interfacial properties and to study SWCNT growth. In addition to customary methods of their studies such as e.g. optical absorption or Raman spectroscopy, these efforts enables to employ electron spin resonance (ESR) and nuclear magnetic resonance (NMR) spectroscopy. Encapsulated C_{60} fullerenes are transformed to inner tubes by a high temperature annealing. The diameter distribution of the inner tubes follow that of the outer one and their unique, low defect concentration makes them an ideal model system for high resolution and energy dependent Raman studies. The observation of Raman modes of individual inner-outer tube pairs allows to measure the inner-outer tube interaction strength that is also well described theoretically. Reversible closing and opening of SWCNT can be studied in a diameter selective manner by encapsulating C_{60} and transforming it to an inner tube. The growth of inner tubes can be achieved from ^{13}C enriched encapsulated organic solvents, which shows that the geometry of the fullerene does not play a particular role in the inner tube growth as it was originally thought. In addition, it opens new perspectives to explore the in-the-tube chemistry. Growth of inner tubes from ^{13}C enriched fullerenes provides a unique isotope engineered heteronuclear system, where the outer tubes contain natural carbon and the inner walls are controllably ^{13}C isotope enriched. The material enables to identify the vibrational modes of inner tubes which otherwise strongly overlap with the outer tube modes. The ^{13}C NMR signal of the material has an unprecedented specificity for the small diameter SWCNTs. Temperature and field dependent ^{13}C T_1 studies show a uniform metallic-like electronic state for all inner tubes rather than distributed metallic and isolating behavior. A low energy, 3 meV gap is observed that is tentatively assigned to a long sought Peierls transition in the small diameter SWCNTs. Encapsulating magnetic fullerenes, such as N@C_{60} and C_{59}N opens the way for local probe ESR studies of the electronic properties of the SWCNTs.

15.1 Introduction

The nano-era can be originated from the discovery of carbon nanotubes (CNTs) by Sumio Iijima in 1991 [1]. Before 1991, nanoscience and nanotechnology usually meant small clusters of atoms or molecules with seemingly of fundamental interest only. The originally discovered multi-wall CNTs were soon followed by the discovery of single-wall CNTs [2, 3], which are both believed to be of paramount importance for applications. The principal interest in CNTs comes from the fact that they contain carbon only and all carbons are locally sp^2 bound, like in graphite, which provides unique mechanical and transport properties. This, combined with their huge, >1000, aspect ratio (the diameters being 1-20 nm and their lengths over 1 micron), endows them with their enormous application potential. The not exhaustive list of applications includes field-emission displays (epxloiting their sharp tips) [4], cathode emitters for small sized x-ray tubes for medical applications [5], reinforcing elements for CNT-metal composites, tips for scanning probe microscopy [6], high current transmitting wires, cables for a future space elevator, elements of nano-transistors [7], and elements for quantum information processing [8].

Carbon nanotubes can be represented as rolled up graphene sheets, i.e. single layers of graphite. Depending on the number of coaxial carbon nanotubes, they are usually classified into multi-wall carbon nanotubes (MWCNTs) and single-wall carbon nanotubes (SWCNTs). Some general considerations have been clarified in the past 14 years of nanomaterial research related to these structures. MWCNTs are more homogeneous in their physical properties as the large number of coaxial tubes smears out individual tube properties. This makes them suitable candidates for applications where their nanometer size and the conducting properties can be exploited such as e.g. nanometer sized wires. In contrast, SWCNT materials are grown as an ensemble of weakly interacting tubes with different diameters. The physical properties of similar diameter SWCNTs can change dramatically as the electronic structure is very sensitive on the rolling-up direction, the so-called chiral vector [9, 10]. The chiral vector is characterized by the (n,m) vector components which denote the direction along which a graphene sheet is rolled up to form a nanotube. Depending on the chiral vector, SWCNTs can be metallic or semiconducting [10]. This provides a richer range of physical phenomena as compared to the MWCNTs, however significantly limits the range of applications. To date, neither the directed growth nor the controlled selection of SWCNTs with a well defined chiral vector has been performed successfully. Thus, their broad applicability is still awaiting. Correspondingly, current research is focused on the post-synthesis separation of SWCNTs with a narrow range of chiralities [11–14] or on methods which yield information that are specific to SWCNTs with different chiralities. Examples for the latter are the observation of chirality selective band-gap fluorescence in semiconducting SWCNTs [15] and chirality assigned resonant Raman scattering [16, 17].

Clearly, several fundamental questions need to be answered before all the benefits of these novel nanostructures could be fully exploited. Recent theoretical and experimental efforts focused on the understanding of the electronic and optical properties of single-wall carbon nanotubes. It has been long thought that the one-dimensional structure of SWCNTs renders their electronic properties inherently one-dimensional [9, 10]. This was suggested to result in a range of exotic correlated phenomena such as the Tomonaga-Luttinger (TLL) state [18], the Peierls transition [19, 20], ballistic transport [21], and bound excitions [22–25]. The presence of the TLL state is now firmly established [26–28], there is evidence for the ballistic transport properties [21] and there is growing experimental evidence for the presence of excitonic effects [29, 30]. The Peierls transition, however remains still to be seen.

An appealing tool to study the SWCNT properties originates from the discovery of fullerenes encapsulated inside SWCNTs by Smith, Monthioux, and Luzzi [31]. This peapod structure is particularly interesting as it combines two fundamental forms of carbon: fullerenes and carbon nanotubes. A high-resolution transmission electron microscopy (HR-TEM) image of a peapod is shown in Fig. 15.1. It was also shown that macroscopic filling with the fullerenes can be achieved [32, 33]. This, in principle, opens the way to encapsulate magnetic fullerenes which would enable

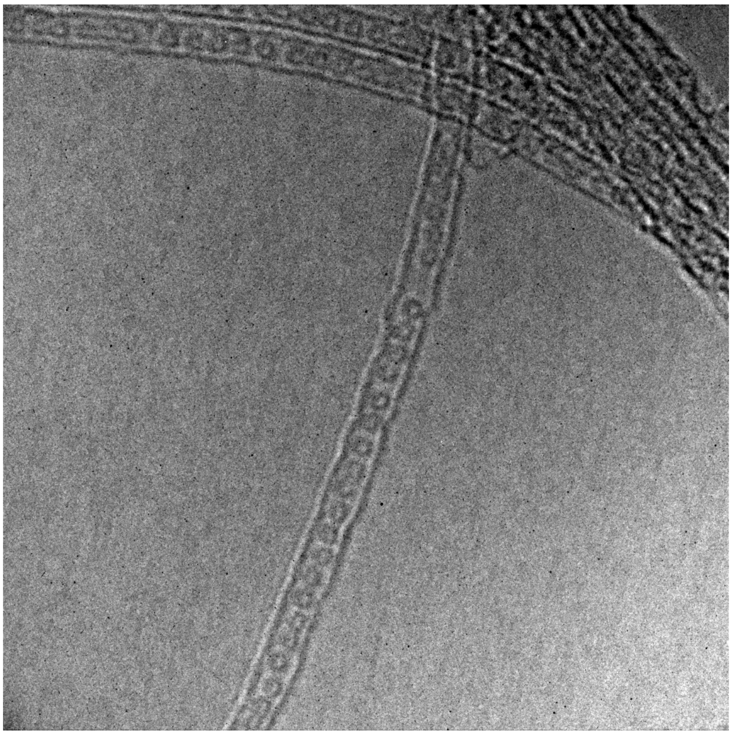

FIGURE 15.1. HR-TEM image of C_{60}@SWCNT peapods.

the study of the tube electronic properties using electron spin resonance as it is discussed in this review. Another interesting follow-up of the peapod structure discovery is that the encapsulated fullerenes can be fused into a smaller diameter inner tube [34, 35] thus producing a double-wall carbon nanotube (DWCNT). DWCNTs were first observed to form under intensive electron radiation [32] in a high resolution transmission electron microscope from C_{60} peapods. Following the synthesis of C_{60} peapods in macroscopic amounts [33], bulk quantities of the DWCNT material are available using a high temperature annealing method [35]. Alternatively, DWCNTs can be produced with usual synthesis methods such as arc-discharge [36] or CVD [37] under special conditions. According to the number of shells, DWCNTs are between SWCNTs and MWCNTs. Thus, one expects that DWCNTs may provide a material where improved mechanical stability as compared to SWCNTs coexists with the rich variety of electronic properties of SWCNTs. There are, of course, a number of yet unanswered questions e.g. if the outer tube properties are unaffected by the presence of the inner tube or if the commensurability of the tube structures plays a role. These questions should be answered before the successful application of these materials.

The inner tubes grown inside SWCNTs from peapods turned out to be a particularly interesting system as they are remarkably defect free which results in very long phonon life-times, i.e. very narrow vibrational modes [38]. In addition, their smaller diameters results in a larger energy spread, i.e. larger spectral splitting, for diameter dependent phonon modes such as e.g. the radial breathing mode (RBM). These two effects make the inner tubes very suitable to study diameter dependent physics of the small diameter tubes with precision. Here, we review how to employ the inner tubes as *probes* of the outer tube properties. The additional benefit of the inner tube growth from fullerenes is that the starting carbon source can be tailored at wish, e.g. when ^{13}C isotope enriched fullerenes are encapsulated inside the SWCNT host tubes, ^{13}C isotope enriched inner tubes are grown. In Fig. 15.2 we show the schematics of such a DWCNT.

Here, we review the efforts to study the SWCNTs properties through encapsulation using Raman and magnetic resonance spectroscopy. The reviewed phenomena include the precise characterization of diameter distribution of SWCNTs, the study of reversible hole engineering on the SWCNTs, study of the inner tube growth mechanism with the help of ^{13}C isotope labeling, the study of local density of states on the tubes using nuclear magnetic resonance (NMR) on the ^{13}C isotope enriched inner tubes, and the electron spin resonance (ESR) studies of the SWCNTs using encapsulated magnetic fullerenes. This review is organised as follows. First, we present the

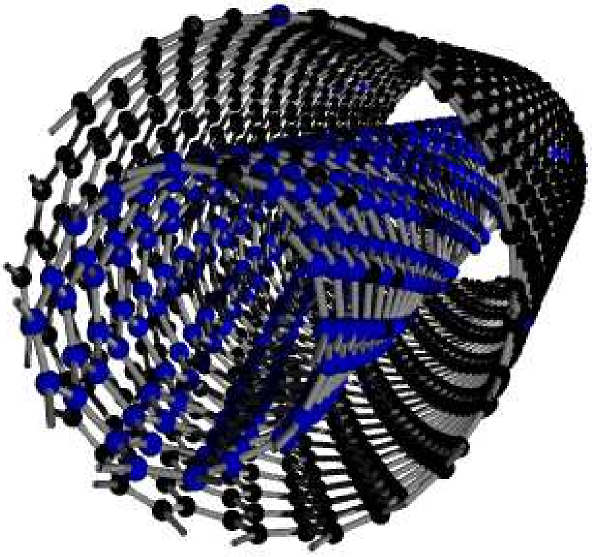

FIGURE 15.2. Schematic structure of an isotope engineered DWCNT with (14,6) outer and (6,4) inner tubes. ^{12}C and ^{13}C are shown in black and blue, respectively. The inner tube is 89 % ^{13}C enriched and the outer contains natural carbon (1.1 % ^{13}C abundance), which are randomly distributed for both shells.

general properties of DWCNTs using Raman, discuss the electronic and vibrational properties of the inner tubes, which are the probes in the subsequent studies. Second, we present the use of the inner tubes to probe the host outer tube diameter distribution and to study the opening and closing of holes on the outer tubes. Third, we present a study on the inner tube growth mechanism using isotope enriched carbon. Fourth, we discuss the NMR results on the isotope enriched inner tubes and in particular we present the observation of a low energy spin-gap in the density of states of SWCNTs. Fifth, we discuss the efforts related to studying the SWCNT properties by encapsulating magnetic fullerenes using ESR.

15.2 Experimental methods and sample preparation

15.2.1 Sample preparation

The starting SWCNT samples

SWCNTs from different sources and prepared by different methods were used in the studies described. Arc-discharge grown SWCNTs with 50 % supplier provided weight purity were purchased from Nanocarblab (Nanocarblab, Moscow, Russia) and laser ablation prepared SWCNTs with 10 % weight purity were purchased from Tubes@Rice (Tubes@Rice, Houston, USA). This latter material was purified through repeated steps of air oxidation and washing in HCl. Some laser ablation prepared and purified samples were obtained from H. Kataura. The purified samples are usuall well opened to enable fullerene encapsulation. If not, annealing in air at 450 °C for 0.5 hour makes them sufficiently open. The HiPco samples used as reference were purchased from CNI (Carbon Nanotechnologies Inc., Houston, USA). Most samples were used in the form of a buckypaper, which is prepared by filtering a suspension of SWCNTs. We found that commercially available SWCNTs already meet a required standard in respect of purity and quality. In addition, for the amount of experimental work described here, reproducible samples i.e. a large amount of SWCNTs from similar quality, were required. The commercial samples can meet this requirement, which compensates for their slightly inferior quality as compared to laboratory prepared ones.

Synthesis of peapods

Encapsulation of fullerenes at low temperatures inside SWCNTs (solvent method) was performed by sonicating the fullerene and opened SWCNT suspensions together in organic solvents following Refs. [39–42]. For fullerene encapsulation at high temperatures (the vapor method), the SWCNTs and the fullerenes were sealed under vacuum in a quartz ampoule and annealed at 650 °C for 2 hours [33]. Fullerenes enter the inside of the SWCNTs at this temperature due to their high vapor pressure that is maintained in the sealed environment. Non-encapsulated fullerenes were removed by dynamic vacuum annealing at the same temperature for 1 hour. High purity fullerenes were obtained from a commercial source (Hoechst AG, Frankfurt, Germany). The filling of SWCNTs with the fullerenes was characterized by observing the peapod structure in high-resolution transmission electron microscopy (HR-TEM), by x-ray studies of the one-dimensional array of fullerenes inside the SWCNTs and by the detection of the fullerene modes from the cages encapsulated inside the SWCNTs using Raman spectroscopy [33, 43].

Synthesis of DWCNTs

DWCNTs were prepared by two routes: from fullerene peapods and using chemical vapor deposition (CVD) growth technique [44]. The peapods were transformed to DWCNTs by a dynamic vacuum treatment at 1250 °C for 2 hours following Ref. [35]. Again, the DWCNT transformation was followed by HR-TEM and by the observation of the DWCNT structure factors using x-ray studies. In addition, new Raman modes emerge after the 1250 °C heat treatment particularly in a frequency range that is clearly upshifted from the outer tube RBMs.

For the CVD DWCNT growth, the catalyst was a modified version of the Fe/Mo/MgO system developed by Liu *et al.* [45] for SWCNT synthesis. The catalyst possessed a molar Fe:Mo:MgO ratio of 1:0.1:110. Nanotubes were synthesized in a fixed bed horizontal quartz tube reactor. The gas stream was a C_2H_2:Ar (10 cm^3/min:150 cm^3/min volumetric flow rate at ambient temperature and pressure) reaction mixture. The reactor was pushed into the furnace and kept there at 850 °C for 20 minutes. The catalyst was removed from the sample by dissolving in excess of concentrated HCl solution at room temperature. The remaining carbonaceous material was filtered and washed with distilled water and dried at 120 °C.

Synthesis of isotope engineered DWCNTs

Commercial ^{13}C isotope enriched fullerenes (MER Corp., Tucson, USA) were used to prepare fullerene peapods C_{60},C_{70}@SWCNT with enriched fullerenes. Two supplier specified grades of ^{13}C enriched fullerene mixtures were used: 25 and 89 %, whose values were slightly refined based on the Raman spectroscopy. The 25 % grade was nominally C_{60}, and the 89 % grade was nominally C_{70} with C_{60}/C_{70}/higher fullerene compositions of 75:20:5 and 12:88:$<$ 1, respectively. The above detailed standard routes were performed for the peapod and the DWCNT productions.

15.2.2 *Raman spectroscopy*

Raman spectra were measured with a Dilor xy triple spectrometer using various lines of an Ar/Kr laser, a He/Ne laser and a tunable Ti:sapphire and Rhodamin dye-laser in the 1.54-2.54 eV (805-488 nm) energy range. Tunable lasers allow to record the so-called Raman map [16, 17] i.e. to detect the SWCNT resonance energies through the Raman resonance enhancement [46], which ultimately allows the chiral index assignment. The spectra can be recorded in normal (NR) and high resolution (HR) mode, respectively ($\Delta\bar{\nu}_{\mathrm{NR}} = 1.3$ cm^{-1} for blue and $\Delta\bar{\nu}_{\mathrm{HR}} = 0.4$ cm^{-1} in the red). The samples in the form of bucky-paper are kept in dynamic vacuum and on a copper tip attached to a cryostat, which allows temperature variation in the 20-600 K temperature range. Raman spectroscopy was used to characterize the diameter distribution of the SWCNTs, to determine the peapod concentrations, and to monitor the DWCNT transformation of the peapod samples.

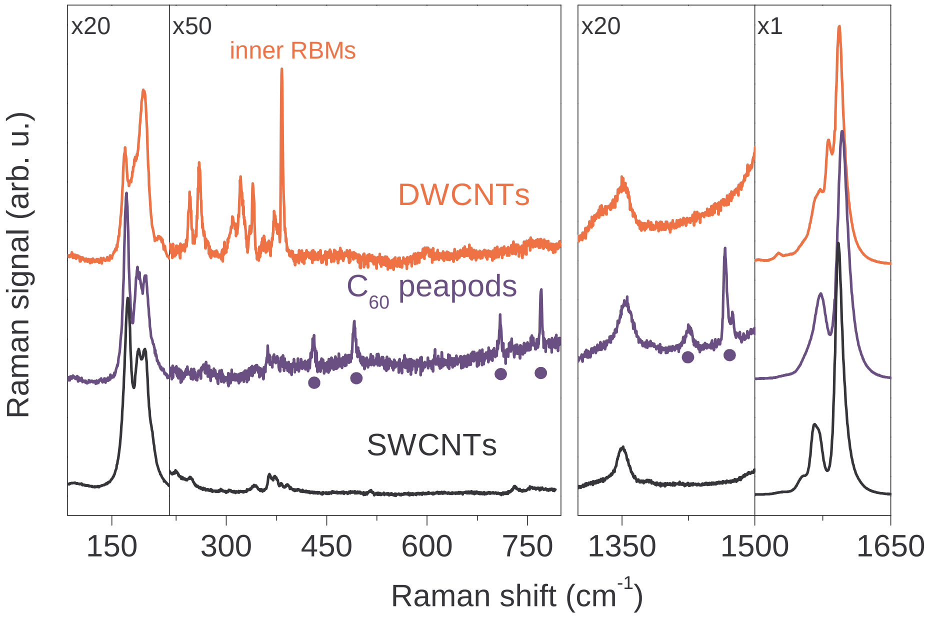

FIGURE 15.3. Transformation of fullerene peapods to DWCNTs as followed with Raman spectroscopy at 496.5 nm laser excitation and 90 K after Ref. [38]. The SWCNT Raman spectra (lower curve) is shown as reference. The fullerene related peapod modes (dots) in the middle curve disappear upon the heat treatment. Note the sharp RBMs appearing in the 250-450 cm^{-1} for the DWCNT sample.

15.2.3 Nuclear magnetic resonance

Nuclear magnetic resonance (NMR) is usually an excellent technique for probing the electronic properties at the Fermi level of metallic systems. The examples include conducting polymers, fullerenes, and high temperature superconductors. However the 1.1% natural abundance of ^{13}C with nuclear spin I=1/2 limits the sensitivity of such experiments. As a result, meaningful NMR experiments has to be performed on ^{13}C isotope enriched samples. NMR data were taken with the samples sealed in quartz tubes filled with a low pressure of high purity Helium gas [47]. We probed the low frequency spin dynamics (or low energy spin excitations, equivalently) of the inner-tubes using the spin lattice relaxation time, T_1, defined as the characteristic time it takes the ^{13}C nuclear magnetization to recover after saturation. The signal intensity after saturation, $M(t)$, was deduced by integrating the fast Fourier transform of half the spin-echo for different delay times, t.

15.2.4 Electron spin resonance

The peapod and the reference SWCNT materials were mixed with the ESR silent high purity SnO_2 in a mortar to separate the pieces of the conducting bucky-papers. The samples were sealed under dynamic vacuum. A typical microwave power of 10 μW and 0.01 mT magnetic field modulation at ambient temperature were used for the measurements in a Bruker Elexsys X-band spectrometer.

15.3 Results and discussion

15.3.1 Inner tubes in DWCNTs as local probes

Electronic and vibrational properties of DWCNTs

Encapsulating fullerenes and their transformation into inner tubes by the high temperature annealing process [35] provides a unique opportunity to study the properties of the host outer tubes.

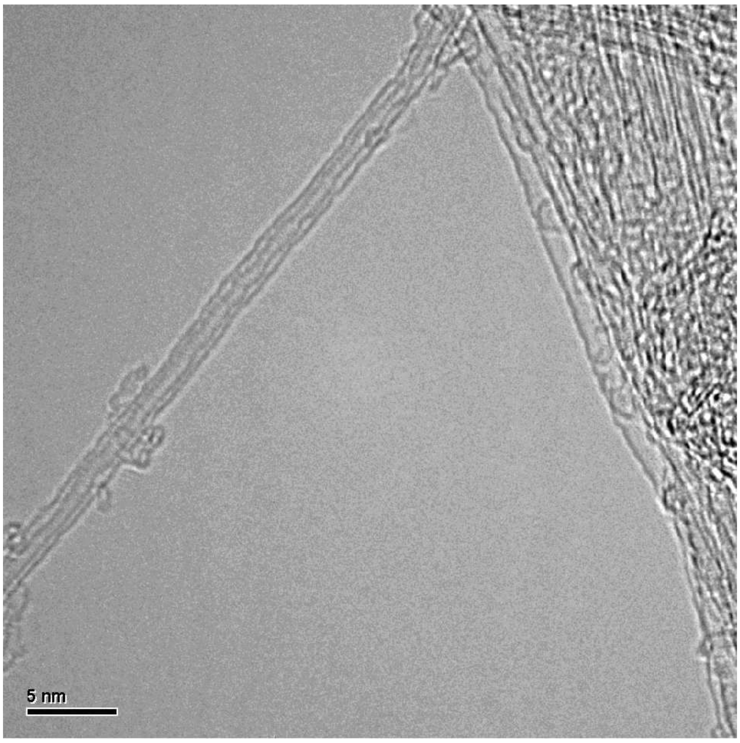

FIGURE 15.4. HR-TEM micrograph of a peapod template based DWCNT.

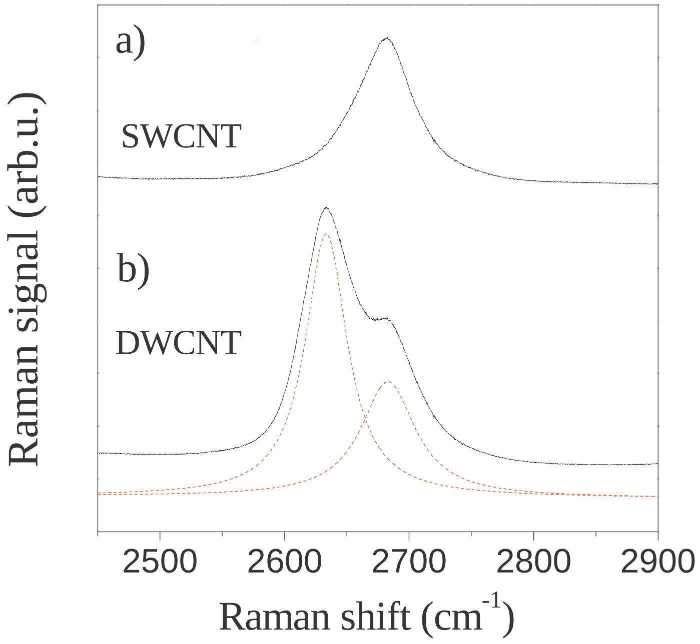

FIGURE 15.5. Raman spectra in the G' mode range of a) SWCNT and b) DWCNT samples at DWCNT 515 nm laser excitation. Dashed curves shows deconvolution to inner (lower frequency) and outer (higher frequency) tubes.

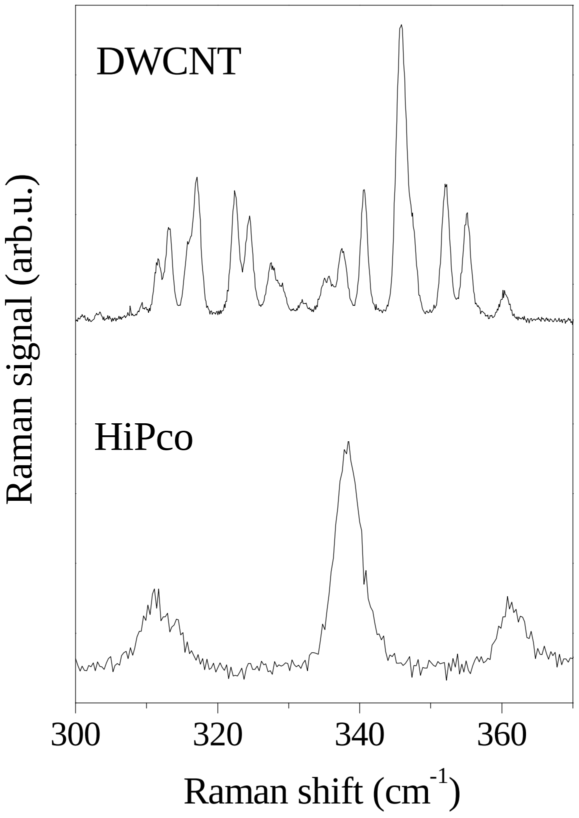

FIGURE 15.6. Raman spectra of the RBMs in DWCNT and HiPco (SWCNT) samples at 594 nm laser excitation and 90 K in the high resolution spectrometer mode.

In Fig. 15.3 we show the evolution of the SWCNT Raman spectrum upon C_{60} fullerene encapsulation and the DWCNT transformation after Ref. [38]. The series of sharp modes in the peapod spectrum, which are related to the encapsulated fullerenes [43], disappear upon the heat treatment and a series of sharp modes appear in the 250-450 cm^{-1} spectral range. The presence of inner tubes after this protocol have been independently confirmed by HR-TEM [34] and structures similar to that shown in Fig. 15.4 were observed. The small diameter tubes with $d \sim 0.7$ nm would have RBM modes in the $\sim$ 250-450 cm^{-1} spectral range, which clarifies the identification of these modes. The identification of the inner tube RBMs is possible due to the strong d dependence of this Raman mode [48].

The assignment of the dispersive SWCNT G' mode [10] mode to inner and outer tube modes was also possible due to the (weaker) diameter dependence and the high energy of this mode [49]. In Fig. 15.5, we show the energy dependence of this mode for DWCNTs. Clearly, the DWCNT G' mode consists of two components. Other modes, such as the SWCNT D and G modes are less diameter sensitive and assignment of inner and outer tube D and G modes requires the use of isotope enriched DWCNTs as shown below.

A variety of additional information can be gained about the inner tube properties when their RBMs are studied using the additive mode, i.e. high-resolution of the Raman spectrometer. In Fig. 15.6, we show the inner tube RBMs at 90 K with high-resolution in comparison with an SWCNT sample with similar tube diameter prepared by the HiPco process. Three striking observations are apparent in the comparison of the two spectra: i) there are a larger number of inner tube RBMs than geometrically allowed and they appear to cluster around the corresponding modes in the SWCNT sample, ii) the inner tube RBMs are on average an order of magnitude narrower than the SWCNT RBMs in the HiPco sample [38] and iii) the Raman intensity of the inner tubes is large in view of the $\sim$ 3 times less number of carbon atoms on them [49]. Points ii) and iii) are explained by the long phonon and quasi-particle life-times of inner tubes which are discussed further below.

Observation i), i.e. the clustering behavior of the observed inner tube RBMs around SWCNT RBMs, is further evidenced in energy dispersive Raman measurements. In Fig. 15.7, we show the

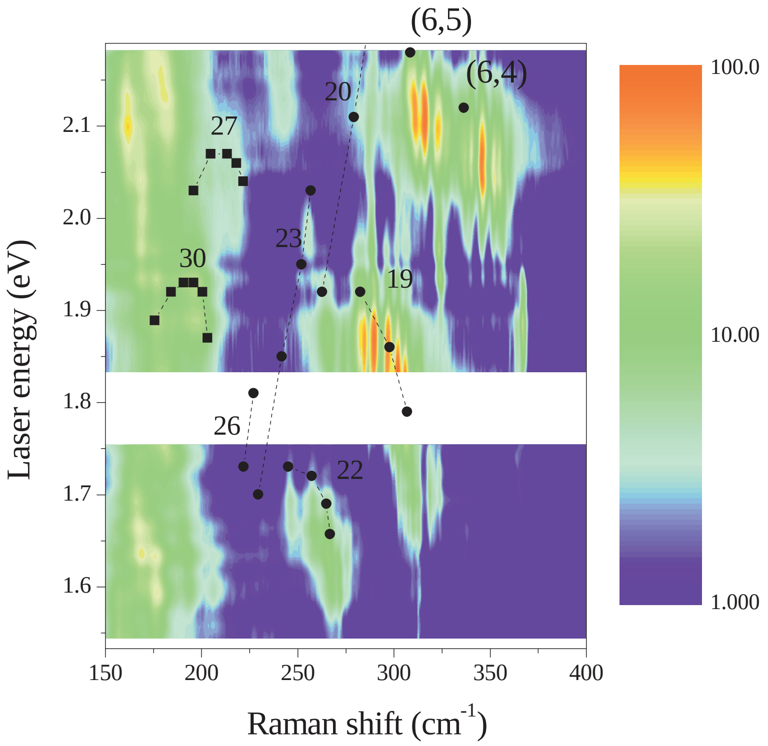

FIGURE 15.7. Raman map of DWCNTs after Ref. [50]. Circles and squares are the E^s_{22} and E^m_{11} peaks as measured in a HiPco sample [16], respectively. The family numbers and the chiral indexes for the (6,5) and (6,4) tubes are indicated. Dashed lines join chiralities in the same family. Laser excitation was not available in the missing area.

Raman map for the DWCNTs from Ref. [51]. The advantage of studying Raman maps is that the optical transition energies are also contained in addition to the Raman shifts. These two quantities uniquely identify the chirality of a nanotube [10, 52, 53]. The analogous Raman map for HiPco SWCNTs were measured by Fantini *et al.* [16] and Telg. *et al.* [17]. Their results are also shown in Fig. 15.7) with squares and circles for metallic and semiconducting tubes,respectively. It turns out that family patterns with $2n + m$ = const can be identified for which the tube resonance energies and Raman shifts are closely grouped together [15]. The comparison of the HiPco results and the DWCNT Raman map confirms the above statement, i.e. that a number of inner tube modes are observed for the DWCNT where only a few (or one) SWCNT chirality is present. This is best seen for the (6,5) and (6,4) chiralities which are well resolved from other modes.

In Fig. 15.8, we show the Raman maps for the two samples near the energy and Raman shift regions for the (6,5) and (6,4) tube modes [15–17]. The comparison of the Raman maps of the two kinds of samples shows that the corresponding tube modes are split into up to 15 components for the inner tube RBMs. This is explained by the inner-outer tube interaction in the DWCNT samples: an inner tube with a particular chirality can be grown in outer tubes with different diameters (chiralities). The varying inner-outer tube spacing can give rise to a different Raman shift for the split components. The large number of split components is a surprising result as it is expected that an inner tube with a given diameter is grown in maximum 1-2 outer tubes where its growth is energetically preferred.

To further prove the origin of the splitting and to quantify this effect, model calculations on the inner-outer tube interactions were performed [50, 54] following the continuum model of Popov and Henrard [55] that is discussed here. The DWCNT is represented by two nested cylinders with diameters d_{i} and d_{o} of the inner and outer shells, respectively. The inner-outer tube interaction is described by the Lennard-Jonnes (LJ) potential: the interaction between two points at a distance r on the two shells is given by

$$V(r) = 4\epsilon[(\sigma/r)^{12} - (\sigma/r)^{6}]\,, \tag{15.1}$$

where $\epsilon = 2.964\mathrm{meV}$ and $\sigma = 0.3407\mathrm{nm}$ are the parametrized values for graphite [56].

The inner tube RBM frequencies are obtained from the eigenvalues of the DWCNT dynamical

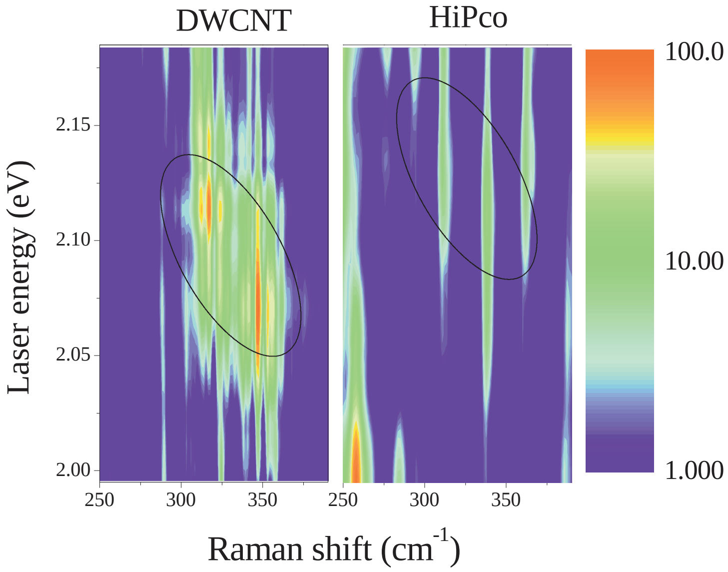

FIGURE 15.8. Raman map comparison of the (6,5) and (6,4) tube RBM ranges for DWCNT and SWCNT (HiPco) samples. Ellipsoids indicate the corresponding tube modes. Note the progressive transition energy downshift for the split components of the inner tubes and the 30 meV transition energy difference between the two kinds of samples, which are discussed in the text.

matrix written for the RBMs:

$$D = -\frac{1}{\sqrt{m_\mathrm{i} m_\mathrm{o}}} \begin{pmatrix} k_\mathrm{i} + \partial^2\Phi/\partial d_\mathrm{i}^2 & \partial^2\Phi/\partial d_\mathrm{i}\partial d_\mathrm{o} \\ \partial^2\Phi/\partial d_\mathrm{o}\partial d_\mathrm{i} & k_\mathrm{o} + \partial^2\Phi/\partial d_\mathrm{o}^2 \end{pmatrix} , \tag{15.2}$$

Here m_i and m_o are the masses (per unit length) and k_i and k_o are the force constants of the inner and outer shells, respectively. Φ is the inner-outer tube interaction energy. The force constants can be determined from the RBM frequencies for separate inner and outer SWCNTs using first principles calculations such as in Ref. [48]. The inner-outer tube interaction energy, Φ is a sum of the elastic energies of both tubes and the tube-tube interaction energy, E_{LJ}:

$$\Phi = Y_1\pi/2[d_{\mathrm{i},0}(\Delta d_\mathrm{i}/d_\mathrm{i})^2 + d_{\mathrm{o},0}(\Delta d_\mathrm{o}/d_\mathrm{o})^2] + E_\mathrm{LJ} \tag{15.3}$$

Here $d_{\mathrm{i},0}$ and $d_{\mathrm{o},0}$ are the diameters for separate inner and outer tubes, respectively and Δd_i and Δd_o are their changes in the DWCNTs. $Y_1 = Yd$, $Y = 1.06$ TPa is the graphene in-plane Young's modulus, and $d = 0.335$ nm is the tube wall thickness. The relaxed diameters of the inner and outer tubes are obtained from minimizing the Φ interaction energy.

In Fig. 15.9a, we show the calculated upshift of the inner tube RBMs for a (6,4) tube as a function of the diameter difference to various outer tubes. Clearly, up to 35 cm^{-1} Raman shift variations can be reproduced. The question remains, however whether such inner-outer tube diameter differences really appear in a sample. In Fig. 15.9b, we show the assumed Gaussian distribution for the outer tube abundance that was used for the simulation of an inner tube spectrum taking into account the effect of outer tubes. This simulation is shown in Fig. 15.9c. This procedure assumes equal Raman matrix elements for all members of a cluster which is justified by the inner tube having the same chirality. The calculated frequencies were scaled with a factor of 0.98. To get the best agreement between theory and experiment, the parameters of the Gaussian were $\omega_0 = 348.9$ cm^{-1} and $\sigma = 5.2$ cm^{-1}. For the intermediate frequencies, experiment and theory are in good agreement. For lower and higher frequencies, the components deviate from the experiment. The maximum of the simulated spectrum is found for a diameter difference of about $0.66 nm$, which is smaller than the experimental value of 0.72 nm reported in Refs. [57] and [58]. This shows, that the paramaterization of the LJ potential for graphite is not exact for the curved sp^2 networks of DWCNTs.

A progressive transition energy downshift for a given inner tube chirality for the split components with increasing Raman shifts is observed in Fig. 15.8. Similarly to the frequency upshift, this can be understood by an increasing interaction between the two shells for decreasing diameter difference. This interaction acts on the inner shell like a radial pressure. The pressure dependence

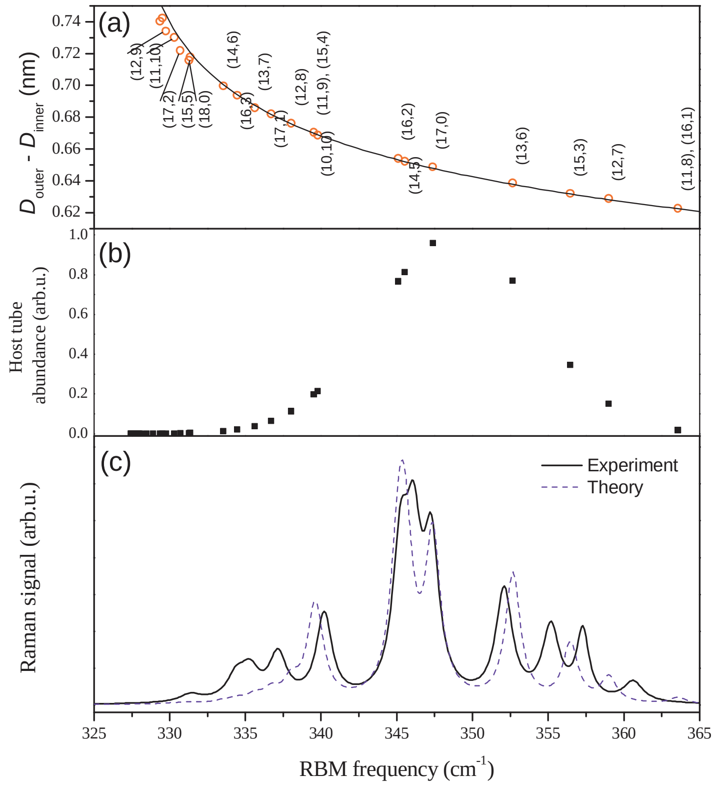

FIGURE 15.9. (a) RBM frequency of a (6, 4) inner tube as a function of the diameter difference to various outer tubes (indicated by their chiral vectors) after Ref. [51]. (b) The abundance of the corresponding outer tubes used in the model calculation. (c) Raman line pattern for the RBM of the (6, 4) inner tube as obtained from experiment (solid line) and from theory (dashed line) as described in the text.

of E_{22} for the $(6,4)$ and the $(6,5)$ inner tubes was calculated in Ref. [59] using an extended tight-binding method. The corresponding values are -7.8 meV/GPa and -2.5 meV/GPa. After Ref. [60], the frequencies shift with about 1.1 cm^{-1}/GPa. Thus one obtains -7.1 meV/cm^{-1} and -2.3 meV/cm^{-1}, respectively. The signs and the order of magnitude compare well with the experimental values. Additionally, one gets -3.6 meV/cm^{-1} from the measured pressure induced shift of the E_{22}^{S} transition [61] for a $(6,5)$ tube of -4 meV/GPa, which is very close the experimental value of -2.7 meV/cm^{-1}.

In summary, the splitting of the inner tube modes to a large number of components as compared to the SWCNTs with the same chiralities is explained by the possibility of finding the same inner tube in a large number of outer ones with different diameters. The varying shell to shell distance for different inner-outer tube pairs for a fixed inner tube gives rise to significant shifts in the vibrational and transition energies, which can be quantitatively explained.

Phonon and quasi-particle life-times in DWCNTs

Now, we turn to discussion of the observed very narrow line-widths of the RBMs. This is the most important property of the inner tube RBMs, which will be exploited throughout in this work. Intrinsic line-widths can be determined by deconvoluting the experimental spectra with the spectrometer response fit a Voigtian fit, whose Gaussian component describes the spectrometer resolution and the Lorentzian gives the intrinsic line-width. The Lorentzian component for some inner tube RBMs is as small as 0.4 cm^{-1} [38], which is an order or magnitude smaller than the values obtained for isolated individual tubes in a normal SWCNT sample [62]. The narrow line-widths, i.e. long phonon life-times of the inner tube RBMs was originally associated to the perfectness of the inner tubes grown from the peapod templates [38]. It was found, however, that inner tubes in chemical vapor deposition (CVD) grown DWCNTs have similarly small line-widths [44]. In Fig. 15.10, the high resolution spectra for the inner tube RBMs in CVD and peapod template grown DWCNTs is shown. This suggests, that the tube environment plays an important role in the magnitude of the observable RBM line-width.

The tube-tube interactions have been shown to give rise to up to ≈ 30 cm^{-1} extra shift to

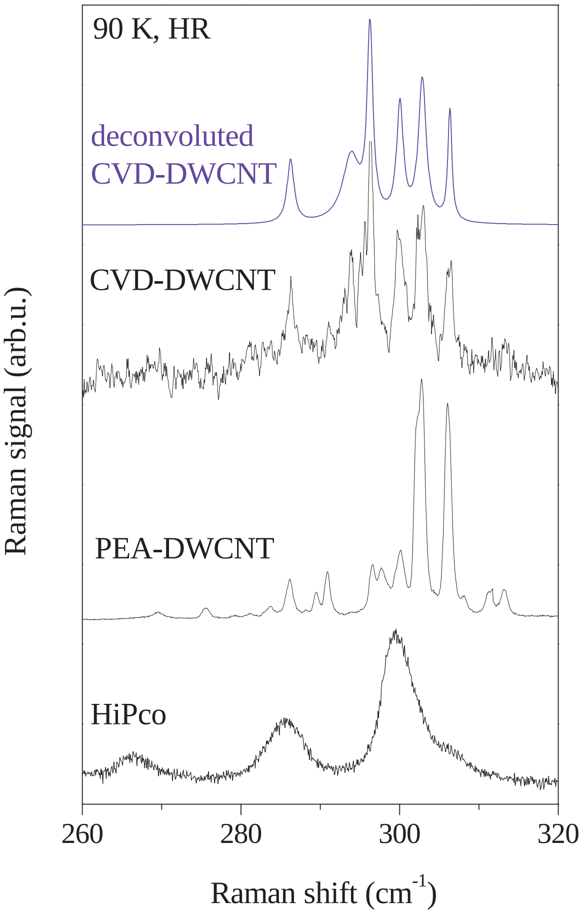

FIGURE 15.10. High resolution Raman spectra taken at 676 nm laser excitation and 90 K on the CVD- and PEA-DWCNT and an SWCNT reference (HiPco) sample after Ref. [44]. The deconvoluted spetrum is also shown for the CVD-DWCNT sample. The narrow line-widths indicate the long RBM phonon life-times of the inner tubes in both DWCNT materials.

the RBMs. The principal difference between SWCNTs and inner tubes in DWCNTs (irrespective whether these are CVD or peapod template grown) is the different surrounding of a small diameter SWCNT with a given chirality: for the SWCNT sample, each tube is surrounded by the ensemble of other SWCNTs. For a close packed hexagonal bundle structure [63], this involves 6 nearest neighbors with random chiralities. This causes an inhomogeneous broadening of the RBMs. However, the nearest-neighbor of an inner tube with a given chirality is an outer tube also with a well defined chirality. A given inner tube can be grown in several outer tubes with different diameters, however the chiralities of an inner-outer tube pair is always well defined, therefore the nearest neighbor interaction acting on an inner tube is also well-defined. As shown above, the interaction between most inner-outer tube pairs is strong enough to separate the inner tube RBMs from each-other thus giving rise to the well resolved split components of a given inner tube chirality [54].

In addition to the long phonon life-times of inner tubes, the life-time of optical excitations, i.e. the life-time of the quasi-particle associated with the Raman scattering is unexpectedly long. To demonstrate this, we compare the resonant Raman scattering data for an inner tube and a SWCNT with the same chirality. In Fig. 15.11 we show the energy profile of the resonant Raman scattering at some selected temperatures for two 6,4 tube modes: one is an inner tube in a DWCNT sample, the other is a SWCNT in a CoMoCAT sample. Such energy profiles are obtained by taking an energy (vertical) cross section of a Raman map such as shown in Fig. 15.8. The Raman intensities for a given excitation energy were obtained by fitting the spectra with Voigtian curves for the tube modes, whose Gaussian component accounts for the spectrometer resolution and whose Lorentzian for the intrinsic line-width. For the DWCNT sample, the strongest (6,4) inner tube component at 347 cm^{-1} and for the SWCNT CoMoCat sample the (6,4) tube mode at 337 cm^{-1} is shown. The temperature dependent resonant Raman data can be fitted with the conventional resonance Raman theory for Stokes Raman modes [46, 64]:

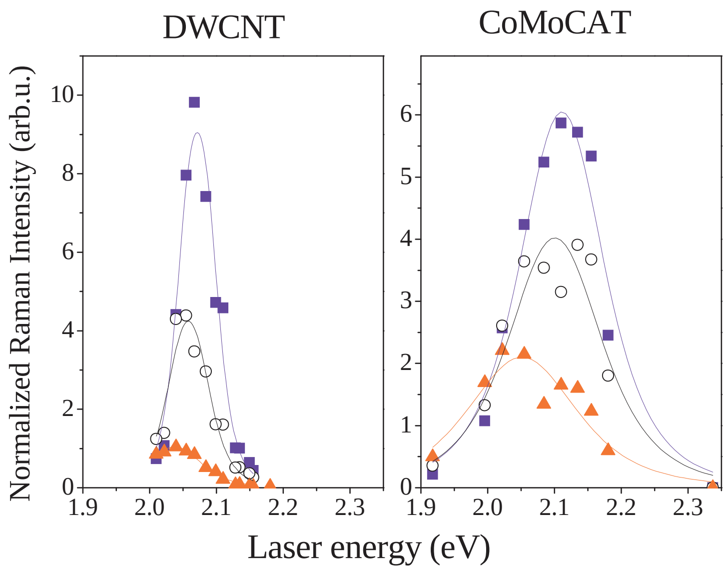

FIGURE 15.11. Temperature dependent Raman resonance profile for the (6,4) tubes in the DWCNT and SWCNT (CoMoCat) samples, ■: 90 K, ◯: 300 K, ▲: 600 K. For the DWCNT, the strongest, 347 cm^{-1} component is shown. Solid curves show fits with the resonant Raman theory as discussed in the text.

$$I(E_l) \propto \left| \frac{1}{(E_l - E_{ii} - i\Gamma)\,(E_l - E_{ph} - E_{ii} - i\Gamma)} \right|^2 \tag{15.4}$$

Here, the electronic density of states is assumed to be a Dirac function, the matrix elements describing the electron-phonon interactions are assumed to be identical for a tube with the same chirality irrespective of the surrounding and temperature independent and are dropped from the equation, E_l is the exciting laser energy, E_{ii} is the transition energy, E_{ph} is the phonon energy and Γ is the damping parameter, i.e. the inverse of the quasi-particle life-time. The temperature dependence of the resonant Raman scattering is included in the T dependence of E_{ii} and Γ. For the 6,4 chirality, the E_{22} optical transition is observed [51]. The fitted curves are shown with solid lines in Fig. 15.11.

Clearly, the resonance width is always smaller for the DWCNT than for the SWCNT sample. In other words, the life-time of the optically excited quasi-particle is longer lived for the DWCNT. This explains why very strong inner tube modes are observed as the resonant Raman intensity is proportional to Γ^4. The quasi-particle life-time is an important parameter for the application of carbon nanotubes in optoelectronic devices [24, 25]. As a result, DWCNTs appear to be superior in this respect than their one-walled counterparts.

Probing the SWCNT diameter distribution through inner tube growth

As discussed above, the Raman spectra of inner tubes have several advantages compared to that of the outer tubes: i) their RBMs have a $\sim$ factor 2 times larger splitting due to the smaller diameters, ii) the line-widths are about 10 times narrower. The larger spectral splitting and narrower line-widths of the inner tube RBMs enable to characterize the inner tube diameter distribution with a spectral resolution that is about 20 times larger as compared to the analysis on the outer tubes. To prove that studying the inner tubes can be exploited for the study of outer ones, here we show that there is a one-to-one correspondence between the inner and outer tube diameter distributions following Ref. [58].

In Fig. 15.12, we compare the inner tube RBM Raman spectra for four different DWCNT materials based on SWCNTs with different diameters and produced with different methods. The SWCNTs were two arc-discharge grown SWCNTs (SWCNT-N1 and N2) and two laser ablation grown tubes (SWCNT-R and SWCNT-L). The diameter distributions of the SWCNT materials were determined from Raman spectroscopy [64] giving $d_{\mathrm{N1}} = 1.50$ nm, $\sigma_{\mathrm{N1}} = 0.10$ nm, $d_{\mathrm{N2}} = 1.45$ nm, $\sigma_{\mathrm{N1}} = 0.10$ nm, $d_{\mathrm{R}} = 1.35$ nm, $\sigma_{\mathrm{R}} = 0.09$ nm, and $d_{\mathrm{L}} = 1.39$ nm, $\sigma_{\mathrm{L}} = 0.09$ nm for the mean diameters and the variances of the distributions, respectively.

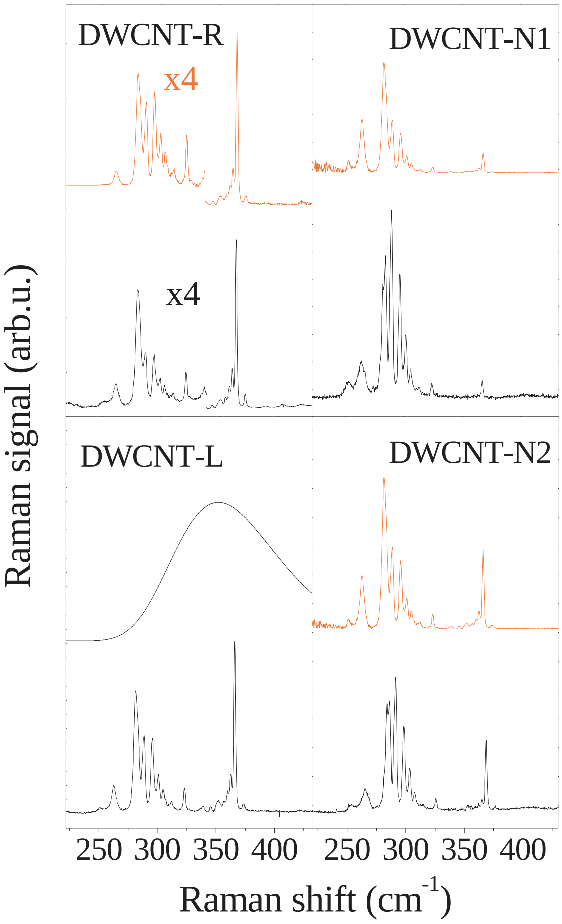

FIGURE 15.12. As measured Raman spectra of the inner nanotube RBMs for four DWCNT samples (lower curves in each quarter) at 647 nm laser excitation after Ref. [58]. The upper spectra (shown in red) are smart scaled from the lower left spectrum. The Gaussian diameter distribution is shown for the DWCNT-L sample.

The spectra shown are excited with a 647 nm laser that is representative for excitations with other laser energies. The RBMs of all the observable inner tubes, including the split components [38], can be found at the same position in all DWCNT samples within the ± 0.5 cm^{-1} experimental precision of the measurement for the whole laser energy range studied. This proves that vibrational modes of DWCNT samples are robust against the starting material.

As the four samples have different diameter distributions, the overall Raman patterns look different. However, scaling the patterns with the ratio of the distribution functions (smart scaling) allows to generate the overall pattern for all systems, starting from e.g. DWCNT-L in the bottom-left corner of Fig. 15.12. It was assumed that the inner tube diameter distributions follow a Gaussian function with a mean diameter 0.72 nm smaller than those of the outer tubes following Ref. [57] and with the same variance as the outer tubes. The empirical constants from Ref. [65] were used for the RBM mode Raman shift versus inner tube diameter expression. The corresponding Gaussian diameter distribution of inner tubes is shown for the DWCNT-L sample in Fig. 15.12. A good agreement between the experimental and simulated patterns for the DWCNT-R sample is observed. A somewhat less accurate agreement is observed for the DWCNT-N1, N2 samples, which may be related to the different growth method: arc discharge for the latter, as compared to laser ablation for the R and L samples. The observed agreement has important consequences for the understanding of the inner tube properties. As a result of the photoselectivity of the Raman experiment, it proves that the electronic structure of the inner tubes is identical in the different starting SWCNT materials.

The scaling of the inner tube Raman spectra with the outer tube distribution shows that the inner tube abundance follows that of the outer ones. This agrees with the findings of x-ray diffractomery on DWCNTs [57] and is natural consequence of the growth of inner tubes inside the outer tube hosts. As a result, the inner-outer tube diameter distributions are similar to that shown schematically in Fig. 15.13: the width of the inner outer tube distributions are the same,

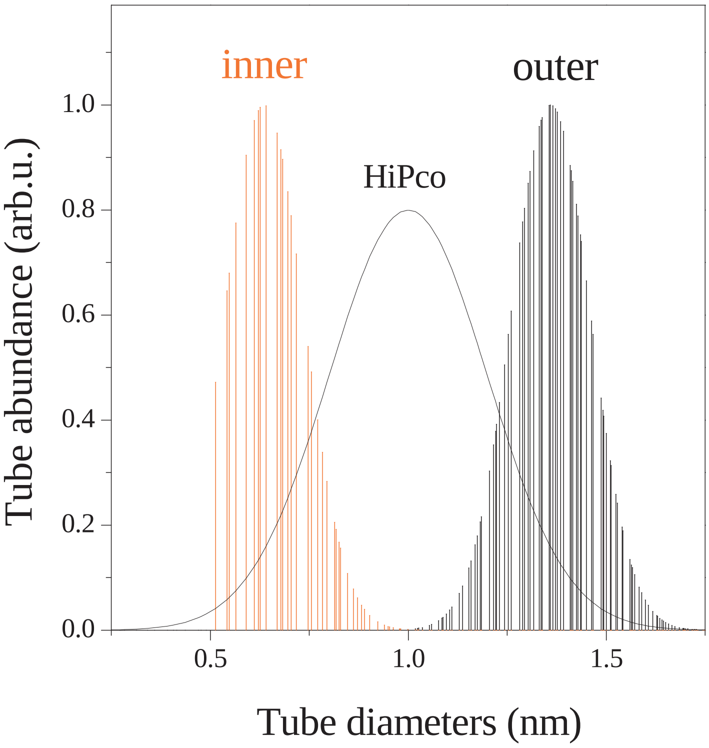

FIGURE 15.13. Schematic diameter distribution of inner and outer tubes. Vertical lines denote a tube with a given chirality. Inner-outer tube relative abundances are not to scale. Note the inner tube abundance cut-off at ~ 0.5 nm. The diameter distribution for a HiPco SWCNT sample is shown for comparison.

and the mean values differ by 0.72 nm. A cut-off in the inner tube diameter distribution was imposed at $d \approx 0.48$ nm due to the inability of C_{60} to enter into outer tubes smaller than 1.2 nm [66–68].

In summary, the RBM frequencies of inner tubes with neighboring diameters are on the average four times more separated from each other than those of the outer ones [65]. In addition, the outer tube RBMs have a typical FWHM of 10 cm^{-1} [62] as compared to the FWHM of the inner tube RBMs of 0.4-0.5 cm^{-1} [38]. As a result, the available spectral resolution is at least 20 times larger when the RBMs of the inner tubes are investigated. This allows to study chirality or at least diameter selective reactions of the outer tubes by analyzing the inner tube response.

Studying the reversible hole engineering using DWCNTs

Soon after the discovery of the peapods [31], it was recognized [33, 69] that opening the SWCNTs by oxidation in air or by treating in acids is a prerequisite for good filling. Good filling means a macroscopic filling where the peapods are observable not only by local microscopic means such as HR-TEM but also by spectroscopy such as Raman scattering. On the other hand, a heat treatment around 1000 °C was known to close the openings which results in a low or no fullerene filling. It was also shown that the geometrically possible maximum of filling can be achieved when purified SWCNTs were subject to a 450 °C heat treatment in flowing oxygen [70]. However, these studies have concerned the overall fullerene filling, with no knowledge on the precise dependence on the thermal treatment or tube diameter specificity.

The high diameter and chirality sensitivity of Raman spectroscopy for the inner tubes allows to study the behavior of tube openings when subject to different treatments. More precisely, openings which allow fullerenes to enter the tubes can be studied. This is achieved by studying the resulting inner tube RBM pattern when the outer tube host was subject to some closing or opening treatments prior to the fullerene encapsulation [71]. Annealing of as purchased or opened tubes was performed at various temperatures between 800 °C and 1200 °C in a sealed and evacuated quartz tube at a rest gas pressure of 10^{-6} mbar. Opening of the tubes was performed by exposure to air at various temperatures between 350 °C and 500 °C.

Figure 15.14 shows the Raman response of tubes after the standardized DWCNT transformation

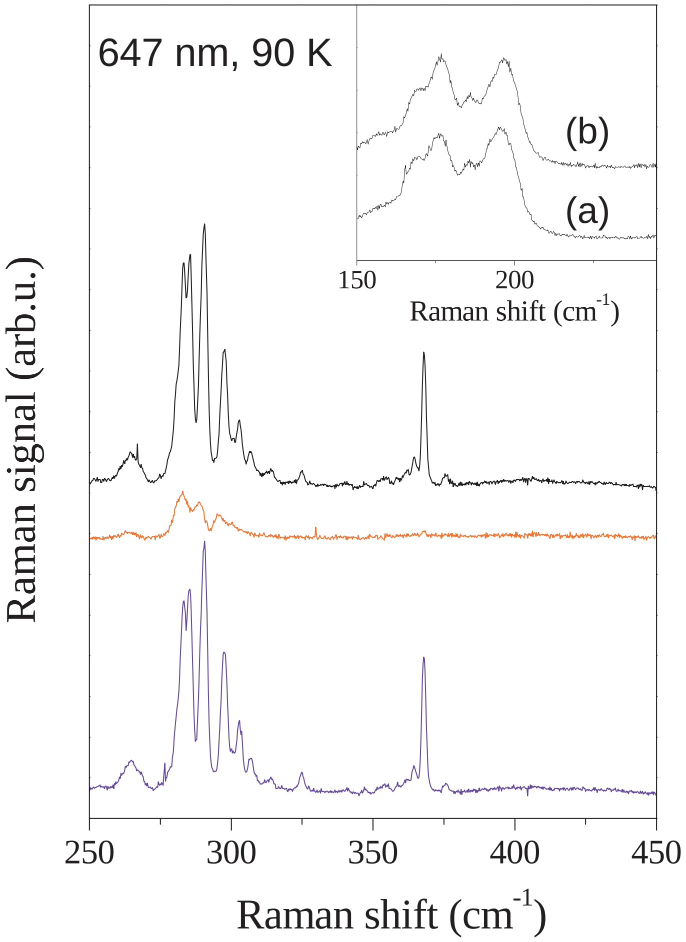

FIGURE 15.14. Raman spectra in the spectral range of the inner shell tube RBM for nanotubes after special pre-treatment after Ref. [71]. Bottom: after filling as purchased tubes with C_{60} and standard transformation; Center: after annealing the as purchased tubes at 1000 °C for two hours, filling with C_{60} and standard transformation; Top: after re-opening the annealed samples, filling with C_{60}, and standard transformation. All spectra recorded at 90 K for 647 nm excitation and normalized to the response of the outer tube RBM of the pristine tubes. Insert: the RBM of the outer tubes before (a) and after (b) annealing at 1000 °C.

conditions but different pre-treatment. Only the spectral range of the inner tube is shown in the main part of the figure. The spectrum at the center was recorded under identical conditions but the SWCNT was pre-annealed before the standardized filling and standardized transformation. Almost no response from inner shell tubes is observed for this material, which means no fullerenes had entered the tubes: the tubes were very efficiently closed by the annealing process. The small response just below 300 cm^{-1} could originate from some small leaks in the cage were a few C_{60} molecules or even more likely some carbon contamination had entered the primary tubes on a level which leads to less than 20 % inner tubes for the larger diameter tubes and less than 3 % for the smaller diameter tubes. The insert in Fig. 15.14 depicts the RBM response from the outer tubes before and after annealing. The two spectra are almost identical, which proves that no outer tube coalescence had occurred at the temperature applied. The spectrum at the top in Fig. 15.14 was recorded after reopening the annealed tubes at 500 °C on air and standard filling and transformation. The spectra derived from the pristine and from the reopened tubes are identical in all details. This means no dramatic damages by cutting a large number of holes into the sidewalls have happened. Consequently, the sidewalls of the tubes remain highly untouched by the opening process. Thus, it is suggested that fullerenes enter the tubes through holes at the tube ends.

The dependence of tube closing on annealing temperature and time was studied in more detail. Spectra for the RBM response were recorded for standard filling and standard transformation after various annealing temperatures and annealing times. The most important lines were evaluated with respect to their peak intensity. This intensity was related to the peak intensity of inner shell modes of DWCNTs grown from untreated starting material. This ratio is a quantitative measure for the fraction of tubes which remain open after the annealing procedure. I_0 and $I_{annealed}$ are the intensity for the pristine and annealed tubes after standard filling and transformation,

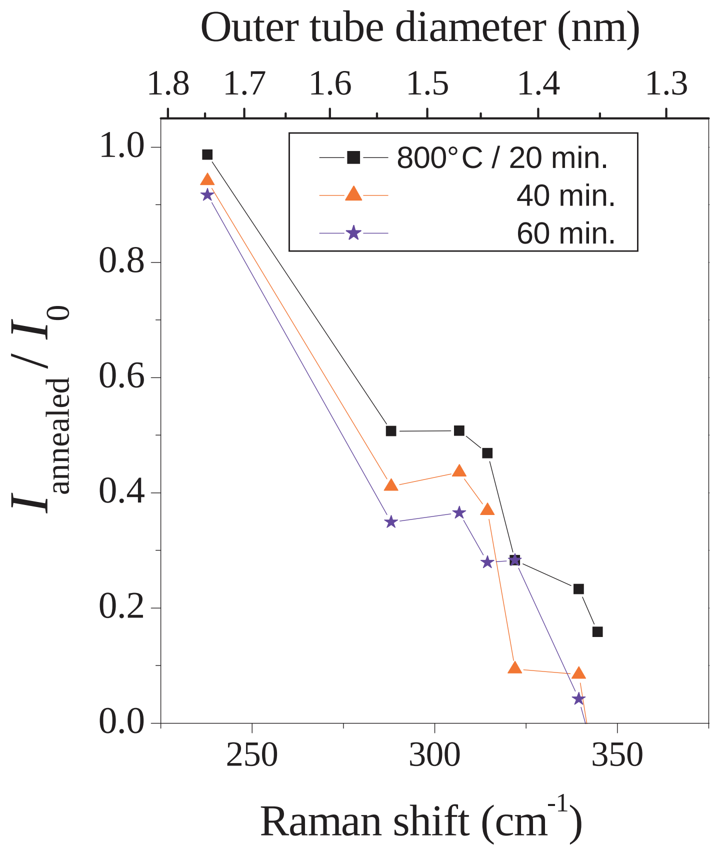

FIGURE 15.15. Relative intensities, I_{annealed}/I_0, of inner tube RBMs versus frequency (tube diameter) after various annealing conditions as indicated in the inserted legend after Ref. [71]. All spectra are normalized to the outer tube intensities. The upper scale shows the corresponding outer tube diameters.

respectively. Results are depicted in Fig. 15.15 for annealing at 800 °C (1073 K). A dramatic decrease of concentration for tubes remaining open after the annealing treatment is immediately recognized in Fig. 15.15 with decreasing tube diameter (increasing RBM frequency). For tubes with 1.8 nm diameter (240 cm^{-1}) 98 % remain open for a 20 min annealing at 800 °C whereas for the same annealing conditions and tubes with 1.3 nm diameter (345 cm^{-1}) only 15 % remain open.

This technique can also be used to study the diameter selective tube opening process. Fig. 15.16 depicts Raman spectra of the RBM recorded for 647 nm excitation for tubes which were closed at 1000 °C for two hours and then reopened by exposure to air at the temperatures indicated. As an overall result, the opening process becomes less and less efficient with decreasing temperature. However, the reduction in efficiency hardly depends on the tube diameter. The latter behavior is more evidently seen from an analysis of the response for the individual peaks as depicted in part (b) of Fig. 15.16. For opening at 500 °C 95 % of the closed tubes could be reopened, nominally independent of tube diameter. For opening at 400 °C only about 60 % of the tubes could be opened. Surprisingly, as plotted this fraction is even slightly decreasing with decreasing tube diameter. Similarly, for opening at 350 °C only 45 % of the tubes could be opened again, with a slight decrease of this fraction for small diameter tubes.

In summary, the reaction activity of holes in SWCNTs can be investigated by studying the process of filling the tubes with C_{60} fullerenes and transforming the latter to a set of small diameter inner tubes. Reversible closing and opening of the tubes can be achieved. The tube opening process is sensitive to temperature but insensitive to tube diameter. The almost identical Raman spectra for the pristine and for the opened tubes with respect to line positions, line-widths and line intensities suggest that the tube walls remain untouched and the holes for the tube filling are located at the tube ends. After tube closing, a small amount of inner tubes can be grown mostly in high defect areas of the tubes. In contrast to tube opening, the tube closing process is highly diameter sensitive.

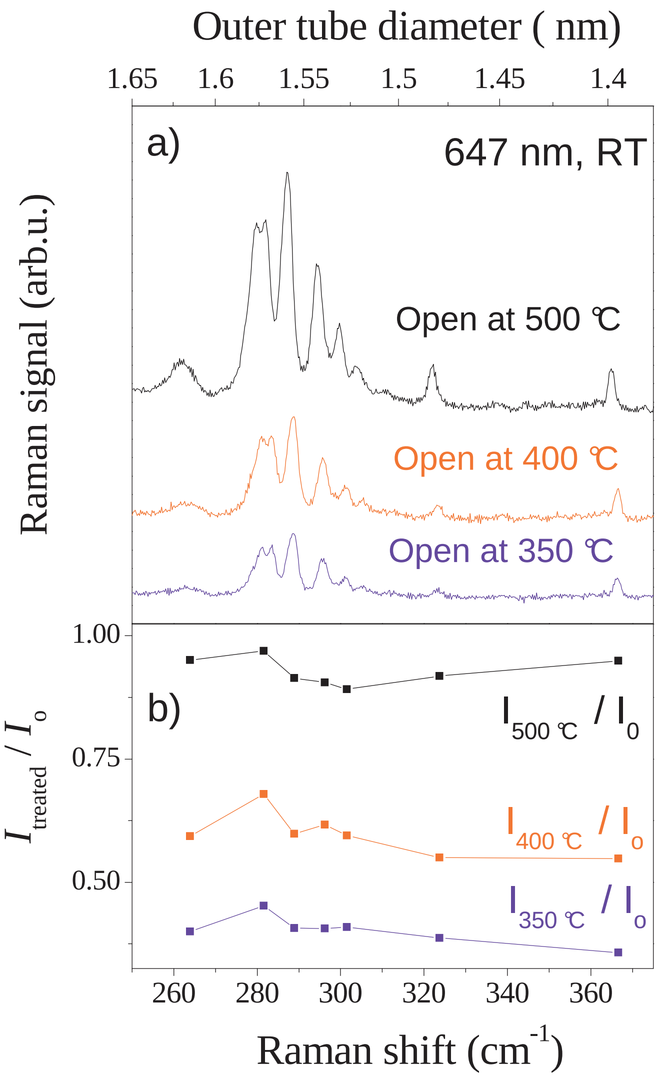

FIGURE 15.16. Raman response of the RBM of inner shell CNTs for standard filling and transformation procedures after the pristine tubes had been closed and re-opened at temperatures indicated (a). Part (b) depicts evaluated relative intensities versus Raman shift for the three different opening conditions. The upper scale provides outer tube diameters.

15.3.2 Growth mechanism of inner tubes studied by isotope labeling

The growth of inner tubes from fullerenes raises the question, whether the fullerene geometry plays an important role in the inner tube growth or it acts as a carbon source only. Theoretical results suggest the earlier possibility [72, 73]. In addition, it needs clarification whether carbon exchange occurs between the two tube walls. Here, we review ^{13}C isotope labeled studies aimed at answering these two open questions. ^{13}C is a naturally occurring isotope of carbon with 1.1 % abundance. In general, isotope substitution provides an important degree of freedom to study the effect of change in phonon energies while leaving the electronic properties unaffected. This have helped to unravel phenomena such as e.g. the phonon-mediated superconductivity [74].

First, we discuss the inner tube growth from isotope labeled fullerenes [47], and secondly we present the growth of inner tubes from isotope labeled organic solvents [75].

Commercial ^{13}C isotope enriched fullerenes with two different enrichment grades were used to grow isotope enriched inner tubes. Fullerene encapsulation [33] and inner tube growth was performed with the conventional methods [35]. This results in a compelling isotope engineered system: double-wall carbon nanotubes with ^{13}C isotope enriched inner walls and outer walls containing natural carbon [47].

In Fig. 15.17a, we show the inner tube RBM range Raman spectra for a natural DWCNT and two DWCNTs with differently enriched inner walls, 25 % and 89 %. These two latter samples are denoted as ^{13}C$_{25}$- and ^{13}C$_{89}$-DWCNT, respectively. The inner wall enrichment is taken from the nominal enrichment of the fullerenes used for the peapod production, whose value is slightly

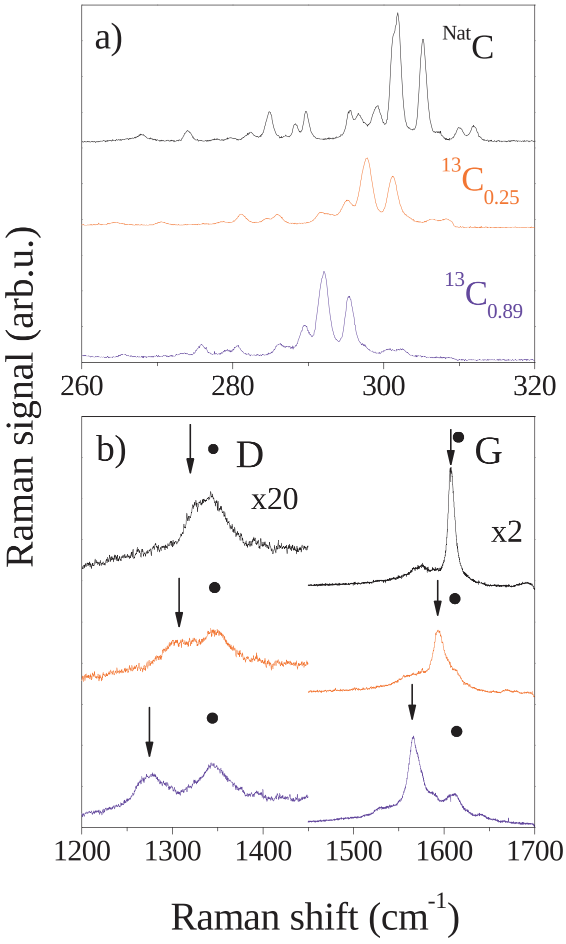

FIGURE 15.17. Raman spectra of DWCNTs with natural carbon and ^{13}C enriched inner tubes at 676 nm laser excitation and 90 K after Ref. [47]. The inner tube RBM (a) and D and G mode spectral ranges (b) are shown. Arrows and filled circles indicate the D (left) and G (right) modes corresponding to the inner and outer tubes, respectively.

refined based on the Raman data. An overall downshift of the inner tube RBMs is observed for the ^{13}C enriched materials accompanied by a broadening of the lines. The downshift is clear evidence for the effective ^{13}C enrichment of inner tubes. The magnitude of the enrichment and the origin of the broadening are discussed below.

The RBM lines are well separated for inner and outer tubes due to the $\nu_{\mathrm{RBM}} \propto 1/d$ relation and a mean inner tube diameter of $d \sim 0.7$ nm [57, 58]. However, other vibrational modes such as the defect induced D and the tangential G modes strongly overlap for inner and outer tubes. Arrows in Fig. 15.17b indicate a gradually downshifting component of the observed D and G modes. These components are assigned to the D and G modes of the inner tubes. The sharper appearance of the inner tube G mode, as compared to the response from the outer tubes, is related to the excitation of semiconducting inner tubes and metallic outer tubes [38, 58].

The shifts for the RBM, D and G modes can be analyzed for the two grades of enrichment. The average value of the relative shift for these modes was found to be $(\nu_0 - \nu)/\nu_0 = 0.0109(3)$ and 0.0322(3) for the $^{13}\mathrm{C}_{0.25}$- and $^{13}\mathrm{C}_{0.89}$-DWCNT samples, respectively. Here, ν_0 and ν are the Raman shifts of the same inner tube mode in the natural carbon and enriched materials, respectively. In the simplest continuum model, the shift originates from the increased mass of the inner tube walls. This gives $(\nu_0 - \nu)/\nu_0 = 1 - \sqrt{\frac{12+c_0}{12+c}}$, where c is the concentration of the ^{13}C enrichment on the inner tube, and $c_0 = 0.011$ is the natural abundance of ^{13}C in carbon. The resulting values of c are 0.277(7) and 0.824(8) for the 25 and 89 % samples, respectively.

The growth of isotope labeled inner tubes allows to address whether carbon exchange between the two walls occurs during the inner tube growth. In Fig. 15.18, we show the G’ spectral range for DWCNTs with natural carbon and ^{13}C enriched inner walls with 515 nm laser excitation. The G’ mode of DWCNTs is discussed in detail in Ref. [54] and it was introduced in Fig. 15.5: the

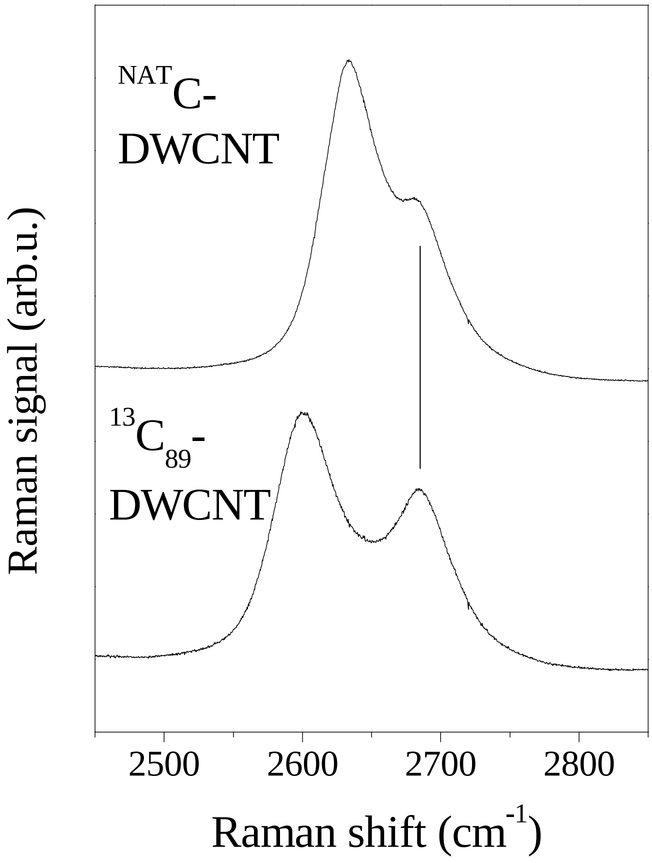

FIGURE 15.18. G' spectral range of DWCNTs with natural carbon and ^{13}C enriched inner walls with 515 nm laser excitation. Note the unchanged position of the outer tube G' mode indicated by a vertical line.

upper G' mode component corresponds to the outer tubes and the lower to the inner tubes. The outer tube G' components are unaffected by the ^{13}C enrichment within the 1 cm^{-1} experimental accuracy. This gives an upper limit to the extra ^{13}C in the outer wall of 1.4 %. This proves that there is no sizeable carbon exchange between the two walls as this would result in a measurable ^{13}C content on the outer wall, too. This is important for the contrast of the NMR signal between the two walls as it is discussed further below: were the outer shell also enriched, one could not obtain a reliable information about the density of states on the inner shell alone.

The narrow RBMs of inner tubes and the freedom to control their isotope enrichment allows to precisely compare the isotope related phonon energy changes in the experiment and in *ab-initio* calculations. This was performed by J. Kürti and V. Zólyomi in Ref. [47]. The validity of the above simple continuum model for the RBM frequencies was verified by performing first principles calculations on the (n,m)=(5,5) tube as an example. In the calculation, the Hessian matrix was determined by DFT using the Vienna Ab Initio Simulation Package [76]. Then, a large number of random ^{13}C distributions were generated and the RBM vibrational frequencies were determined from the diagonalization of the corresponding dynamical matrix for each individual distribution. The distribution of the resulting RBM frequencies can be approximated by a Gaussian where center and variance determine the isotope shifted RBM frequency and the spread in these frequencies. The difference between the shift determined from the continuum model and from the *ab-initio* calculations is below 1 %.

The broadening for the ^{13}C enriched inner tubes is best observed for the narrow RBMs. In Fig. 15.19a-b we show the RBMs of some inner tubes for the $^{\mathrm{Nat}}$C and ^{13}C$_{0.25}$ samples. Curves (1) are the line-shapes after deconvolution with the Gaussian response of our spectrometer. In Fig. 15.19a, the resulting line-shapes are Lorentzians, but in Fig. 15.19b, the line-shape still contains a Gaussian component, as discussed below. The FWHMs of the resulting line-shapes are 0.76(4), 0.76(4), 0.44(4), 0.54(4) and 1.28(6), 1.30(6), 1.12(6), 1.16(6) for the inner tube RBMs shown in Fig. 15.19 of the $^{\mathrm{Nat}}$C and ^{13}C$_{0.25}$ materials, respectively. The origin of the extra broadening is

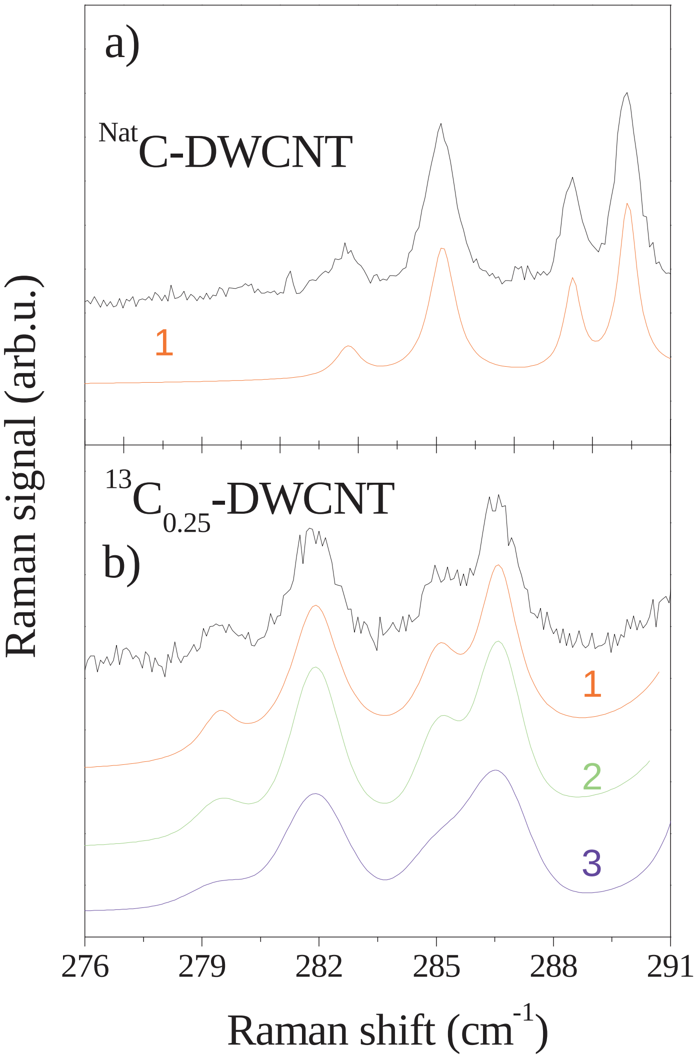

FIGURE 15.19. RBMs of some inner tubes at 676 nm laser excitation with 0.5 cm^{-1} spectral resolution. a) natural carbon-, b) 25 % ^{13}C enriched inner shell DWCNT after Ref. [47]. Curves are the line-shapes after deconvolution by the spectrometer response (1), the simulated line-shape with an extra Gaussian broadening to the intrinsic lines of the $^{\mathrm{Nat}}$C material (2), and the calculated line-shape (see text) (3).

due to the random distribution of ^{12}C and ^{13}C nuclei. Calculations indicate that the ratio between the half width of extra broadening and the shift, $\Delta\nu/\left(\nu_0-\nu\right)$, is approximately 0.19 for a 30 % ^{13}C enriched sample. The corresponding broadened line-shapes are shown in Fig. 15.19b as curve (3). When the magnitude of the Gaussian randomness related broadening was fit (curve (2) in Fig.15.19b), we found that $\Delta\nu/\left(\nu_0-\nu\right)=0.15$. Similar broadening was observed for the 89 % sample which can also be reproduced by the calculation.

The known characteristics of isotope labeled inner tubes allow to study the possibility of inner tube growth from non-fullerene carbon sources. For this purpose, we choose organic solvents containing aromatic rings, such as toluene and benzene. These are known to wet the carbon nanotubes and are appropriate solvents for fullerenes. As described in the following, the organic solvents indeed contribute to the inner tube growth, however only in the presence of C_{60} "stopper" molecules [75]. In the absence of co-encapsulated fullerenes the solvents alone give no inner tube.

The fullerene+organic solvents encapsulation was performed by dissolving typically 150 μg fullerenes in 100 μl solvents and then sonicating with 1 mg SWCNT in an Eppendorf tube for 1 h. The weight uptake of the SWCNT is ~15 % [47] that is shared between the solvent and the fullerenes. The peapod material was separated from the solvent by centrifuging and it was then greased on a sapphire substrate. The solvent prepared peapods were treated in dynamic vacuum at 1250 °C for 2 hours for the inner tube growth. The inner tube growth efficiency was found independent of the speed of warming.

The growth of inner tubes from the solvents can be best proven by the use of C_{60} containing natural carbon and a solvent mixture consisting of ^{13}C enriched and natural carbon containing

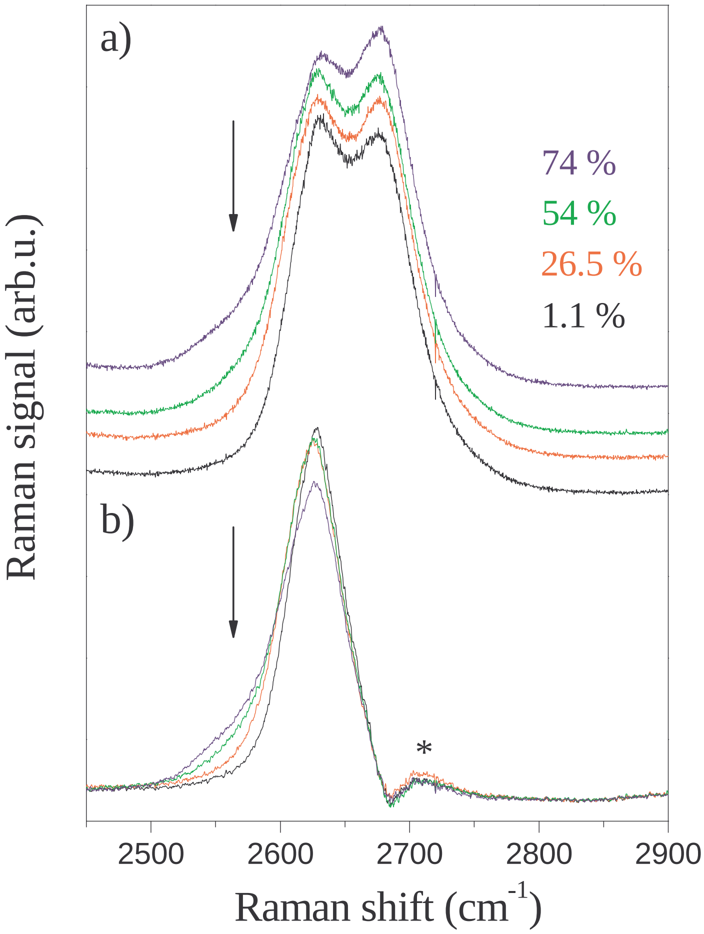

FIGURE 15.20. a) The G' mode of toluene+C_{60} peapod based DWCNTs with varying ^{13}C enrichment at 515 nm laser excitation. From top to bottom: 74 %, 54 %, 26.5 % and natural ^{13}C content. b) The G' mode of the inner tubes after subtracting the experimental SWCNT spectrum. A small residual peak is observed around 2710 cm^{-1} (denoted by an asterisk) due to the imperfect subtraction. Arrows indicate the spectral weight shifted toward lower frequencies.

solvents with varying concentrations. Toluene was a mixture of ring ^{13}C labeled ($^{13}C_6H_6$-$^{NAT}CH_3$) and natural toluene ($^{NAT}C_7H_8$). Benzene was a mixture of ^{13}C enriched and natural benzene. The labeled site was > 99 % ^{13}C labeled for both types of molecules. The ^{13}C content, x, of the solvent mixtures was calculated from the concentration of the two types of solvents and by taking into account the presence of the naturally enriched methyl-group for the toluene. In Fig. 15.20a, we show the G' modes of DWCNTs with varying ^{13}C labeled content in toluene+C_{60} based samples and in Fig. 15.20b, we show the same spectra after subtracting the outer SWCNT component. A shoulder appears for larger values of x on the low frequency side of the inner tube mode, whereas the outer tube mode is unchanged. Similar behavior was observed for the benzene+C_{60} based peapod samples (spectra not shown) although with a somewhat smaller spectral intensity of the shoulder. The appearance of this low frequency shoulder is evidence for the presence of a sizeable ^{13}C content in the inner tubes. This proves that the solvent indeed contributes to the inner tube formation as it is the only sizeable source of ^{13}C in the current samples. The appearance of the low frequency shoulder rather than the shift of the full mode indicates an inhomogeneous ^{13}C enrichment. A possible explanation is that smaller diameter nanotubes might be higher ^{13}C enriched as they retain the solvent better than larger tubes.

To quantify the ^{13}C enrichment of the inner tubes, the downshifted spectral weight of the inner tube G' mode was determined from the subtracted spectra in Fig. 15.21b. The subtraction does not give a flat background above 2685 cm^{-1}, however it is the same for all samples and has a small spectral weight, thus it does not affect the current analysis. The line-shapes strongly deviate from an ideal Lorentzian profile. Therefore the line positions cannot be determined by fitting, whereas the first moments are well defined quantities. The effective ^{13}C enrichment of the inner tubes, c, is calculated from $(\nu_0 - \nu)/\nu_0 = 1 - \sqrt{\frac{12+c_0}{12+c}}$, where ν_0 and ν are the first moments of the inner tube G' mode in the natural carbon and enriched materials, respectively, and $c_0 = 0.011$ is the

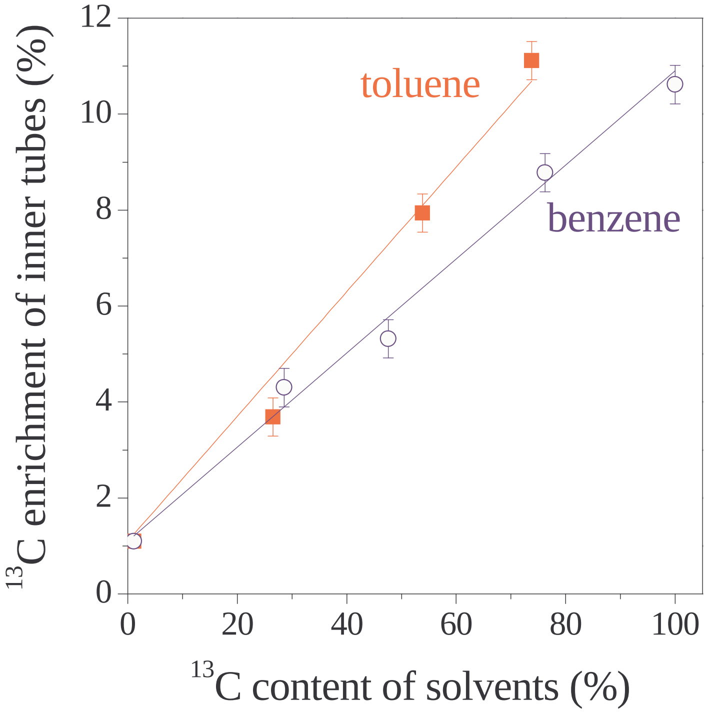

FIGURE 15.21. ^{13}C content of inner tubes based on the first moment analysis as explained in the text as a function of ^{13}C enrichment of benzene and toluene. Lines are linear fits to the data and are explained in the text.

natural abundance of ^{13}C in carbon. The validity of this "text-book formula" is discussed above and it was verified by *ab-initio* calculations for enriched inner tubes in Ref. [47]. In Fig. 15.21, we show the effective ^{13}C content in the inner tubes as a function of the ^{13}C content in the starting solvents. The scaling of the ^{13}C content of the inner tubes with that in the starting solvents proves that the source of the ^{13}C is indeed the solvents. The highest value of the relative shift for the toluene based material, $(\nu_0 - \nu)/\nu_0 = 0.0041(2)$, corresponds to about 11 cm^{-1} shift in the first moment of the inner tube mode. The shift in the radial breathing mode range (around 300 cm^{-1}) [52] would be only 1 cm^{-1}. This underlines why the high energy G' mode is convenient for the observation of the moderate ^{13}C enrichment of the inner tubes. When fit with a linear curve with $c_0 + A * x$, the slope, A directly measures the carbon fraction in the inner tubes that originates from the solvents.

The synthesis of inner tubes from organic solvent proves that any form of carbon that is encapsulated inside SWCNTs contributes to the growth of inner tubes. As mentioned above, inner tubes are not formed in the absence of fullerenes but whether the fullerene is C_{60} or C_{70} does not play a role. It suggests that fullerenes act only as a stopper to prevent the solvent from evaporating before the synthesis of the inner tube takes place. It also clarifies that the geometry of fullerenes do not play a distinguished role in the inner tube synthesis as it was originally suggested [72, 73]. It also proves that inner tube growth can be achieved irrespective of the carbon source, which opens a new prospective to explore the in-the-tube chemistry with other organic materials.

15.3.3 NMR studies on isotope engineered heteronuclear nanotubes

The growth of the "isotope engineered" nanotubes, i.e. DWCNTs with highly enriched inner wall allows to allows to study these samples with NMR with an unprecedented specificity for the small diameter carbon nanotubes. This allows a unique study of the electronic properties of such nanotubes. For normal SWCNTs, either grown from natural or ^{13}C enriched carbon, the NMR signal originates from all kinds of carbon like amorphous or graphitic carbon.

NMR allows to determine the macroscopic amount of enriched tubes in our sample as it is sensitive to the number of ^{13}C nuclei in the sample. In Fig. 15.22, we show the static and magic angle spinning spectra of ^{13}C enriched DWCNTs, and the static spectrum for the SWCNT material. The mass fraction which belongs to the highly enriched phase can be calculated from the integrated

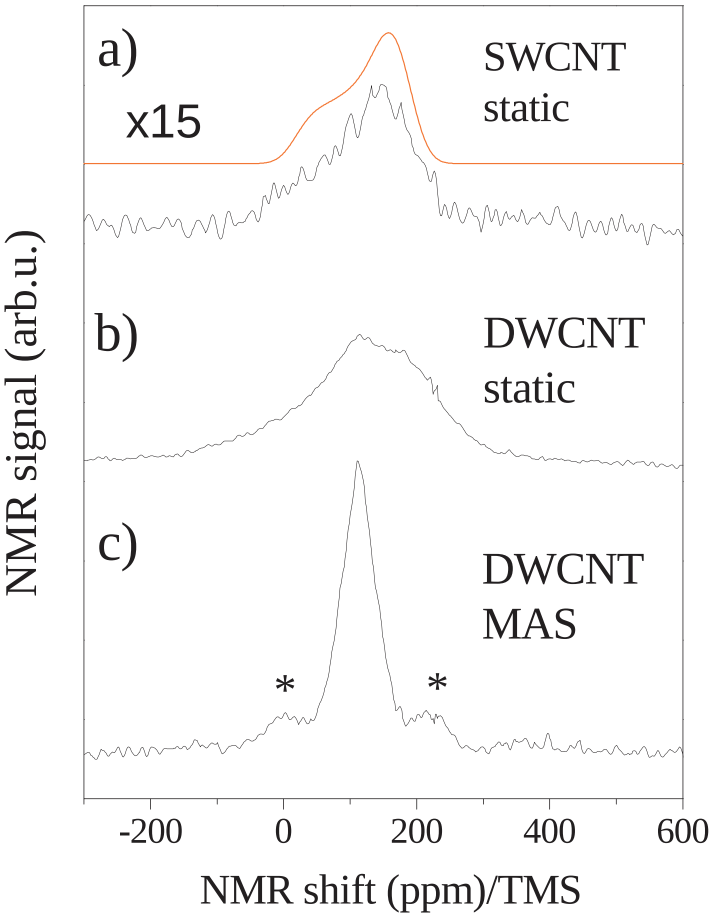

FIGURE 15.22. NMR spectra normalized by the total sample mass, taken with respect to the tetramethylsilane (TMS) shift Ref. [47]. (a) Static spectrum for non-enriched SWNT enlarged by 15. Smooth solid line is a chemical shift anisotropy powder pattern simulation with parameters published in the literature [77]. (b) Static and (c) MAS spectra of $^{13}C_{0.89}$-DWCNT, respectively. Asterisks show the sidebands at the 8 kHz spinning frequency.

signal intensity by comparing it to the signal intensity of the 89 % ^{13}C enriched fullerene material. We found that the mass fraction of the highly enriched phase relative to the total sample mass is 13(4) %. The expected mass ratio of inner tubes as compared to the total sample mass is 15 %, which is obtained from the SWCNT purity (50 %), ~70 % volume filling for peapod samples [70], and the mass ratio of encapsulated fullerenes to the mass of the SWCNTs. Thus, the measured mass fraction of the highly enriched phase is very similar to that of the calculated mass fraction of inner tubes. This suggests that the NMR signal comes nominally from the inner tubes, and other carbon phases such as amorphous or graphitic carbon are non ^{13}C enriched.

The typical chemical shift anisotropy (CSA) powder pattern is observed for the SWCNT sample in agreement with previous reports [77, 78]. However, the static DWCNT spectrum cannot be explained with a simple CSA powder pattern even if the spectrum is dominated by the inner tube signal. The complicated structure of the spectrum suggests that the chemical shift tensor parameters are highly distributed for the inner tubes. It is the result of the higher curvature of inner tubes as compared to the outer ones: the variance of the diameter distribution is the same for the inner and outer tubes [79] but the corresponding bonding angles show a larger variation [80]. In addition, the residual line-width in the MAS experiment, which is a measure of the sample inhomogeneity, is 60(3) ppm, i.e. about twice as large as the ~35 ppm found previously for SWCNT samples [77, 78]. The isotropic line position, determined from the MAS measurement, is 111(2) ppm. This value is significantly smaller than the isotropic shift of the SWCNT samples of 125 ppm [77, 78]. However, recent theoretical *ab-initio* calculations have successfully explained this anomalous isotropic chemical shift [81]. It was found that diamagnetic demagnetizing currents on the outer walls cause the diamagnetic shift of the inner tube NMR signal.

In addition to the measurement of the line position, the dynamics of the nuclear relaxation is a sensitive probe of the local electronic properties [83]. The electronic properties of the nanotubes

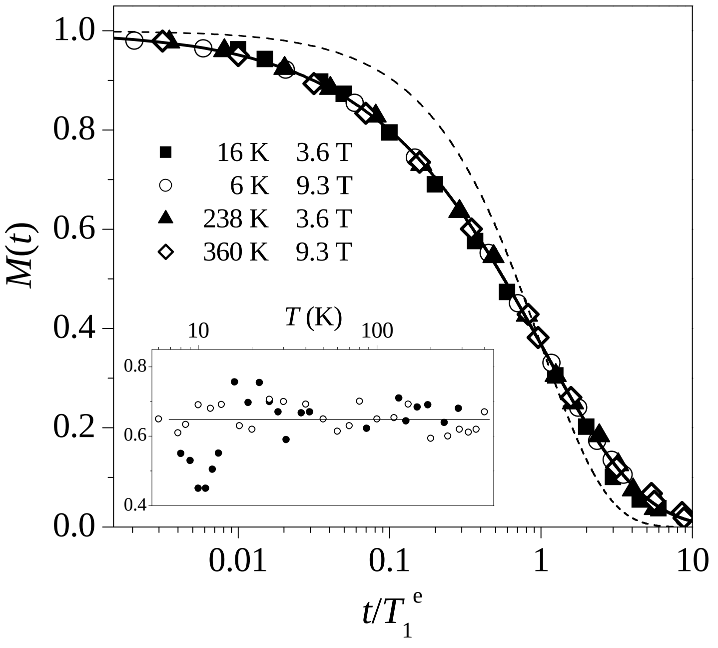

FIGURE 15.23. Reduced nuclear magnetization recovery, $M(t)$, as a function of the scaled delay time t/T_1^e (see Eq. (15.5)), for various temperature and magnetic field values after Ref. [82]. Both axes are dimensionless. Solid curve shows stretched exponential fit with $\beta = 0.65$ and dashed curve shows single exponential with $\beta = 1$. Inset shows temperature dependence of the best fit values of β at 3.6 Tesla (•) and 9.3 Tesla (○), and average value of the data set $\beta = 0.65$ (solid line).

was probed using the spin lattice relaxation time, T_1, defined as the characteristic time it takes the ^{13}C nuclear magnetization to recover after saturation [82]. The signal intensity after saturation, $S(t)$, was deduced by integrating the fast Fourier transform of half the spin-echo for different delay times t. The data were taken with excitation pulse lengths $\pi/2 = 3.0$ μs and short pulse separation times of $\tau = 15$ μs [83]. The value of T_1 was obtained by fitting the t dependence of $S(t)$ to the form $S(t) = S_a - S_b \cdot M(t)$, where $S_a \simeq S_b$ (> 0) are arbitrary signal amplitudes, and

$$M(t) = \exp\left[- (t/T_1^e)^{\beta}\right], \tag{15.5}$$

is the reduced magnetization recovery of the ^{13}C nuclear spins. Fig. 15.23 shows the results of $M(t)$ for the inner-tubes as a function of the scaled delay time t/T_1^e, under various experimental conditions listed in the Figure. We find that $M(t)$ does not follow the single exponential form with $\beta = 1$ (dashed line), but instead fits well to a stretched exponential form with $\beta \simeq 0.65(5)$, implying a distribution in the relaxation times T_1. The data in Fig. 15.23 is displayed on a semi-log scale for the time axis in order to emphasize the data for earlier decay times and to illustrate the collapse of the data set for the upper 90 % of the NMR signal. For a broad range of experimental conditions, the upper 90 % of the $M(t)$ data is consistent with constant $\beta \simeq 0.65(5)$ (see inset), implying a field and temperature independent underlying distribution in T_1. The lower 10 % of the $M(t)$ data, corresponding to longer delay times, comes from the non-enriched outer-walls which have much longer relaxation times under similar experimental conditions [77, 78].

The collapse of the data set in Fig. 15.23 to Eq. (15.5) with constant $\beta = 0.65(5)$ is a remarkable experimental observation. From an experimental point of view, it implies that all one needs in order to characterize the T and H dependence of the underlying T_1 distribution is the bulk (or average) value, T_1^e (Eq. (15.5)). From an interpretational point of view, it implies that each inner-tube in the powder sample has a different value of T_1, yet *all* the T_1 components and therefore all the inner-tubes follow the same T and H dependence within experimental uncertainty. This finding is in contrast to earlier reports in SWCNTs where $M(t)$ fits well to a bi-exponential distribution, 1/3 of which had a short T_1 value characteristic of fast relaxation from metallic tubes, and the remaining 2/3 had long T_1 corresponding to the semiconducting tubes [77, 78, 84, 85], as expected from a macroscopic sample of SWCNTs with random chiralities. The data for the inner-tubes in DWCNTs differ in that a similar bi-exponential fit to $M(t)$ is inconsistent with the shape of the recovery in Fig. 15.23. Furthermore, if there were 1/3 metallic and 2/3 truly semi-conducting inner-tubes in the DWCNT sample, one would expect the ratio of T_1 between semiconducting and

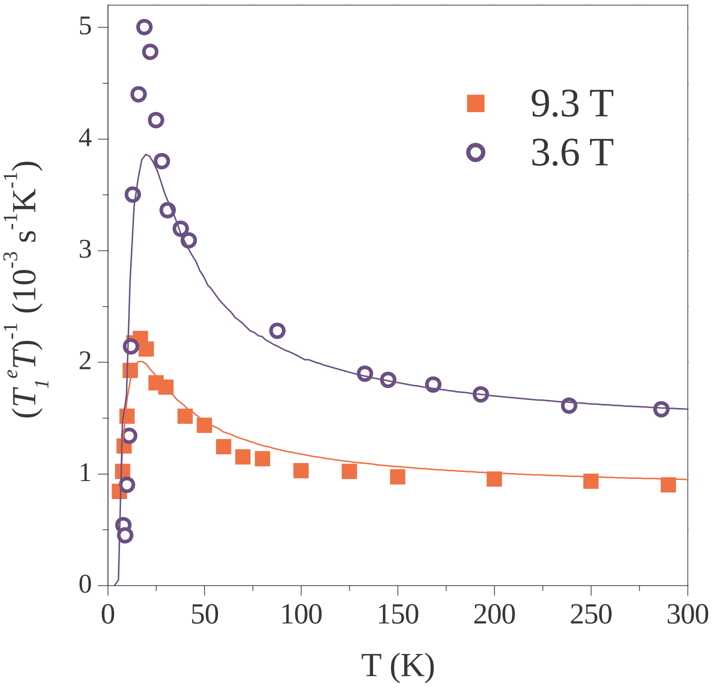

FIGURE 15.24. Temperature dependence of spin-lattice relaxation rate divided by temperature, $1/T_1^e T$, in units of ($10^3\times$ s^{-1} K^{-1}) after Ref. [82]. Grey curves are best fits to Eq. (15.7) with $2\Delta = 46.8(40.2)$ K for $H = 3.6(9.3)$ Tesla, respectively.

metallic tubes to increase exponentially with decreasing T below the semiconducting gap ($\sim$ 5000 K), and therefore one would expect an increasingly large change in the underlying distribution in T_1 with decreasing T. This change would manifest itself as a large change in the shape of the $M(t)$, however this is not the case as shown in Fig. 15.23. The possibility of two components in T_1 with different T dependence can therefore be ruled out, and instead it could be concluded that all T_1 components (corresponding to distinct inner-tubes) exhibit the same T and H dependence within experimental scattering.

With these arguments, the bulk average T_1^e defined in Eq. (15.5) can be considered and its uniform T and H dependence can be followed. The $M(t)$ data can be fitted with the constant exponent $\beta = 0.65(5)$, which reduces unnecessary experimental scattering in T_1^e. In Fig. 15.24 we show the temperature dependence of $1/T_1^e T$ in for two different values of the external magnetic field H. The data can be separated into two temperature regimes; the high temperature regime $\gtrsim$ 150 K, and the low T regime $\lesssim$ 150 K. At high temperatures, $1/T_1^e T$ is independent of T which indicates a metallic state [83] for all of the inner tubes. A strong magnetic field dependence for T_1 was also observed, which was explained by a 1D spin diffusion mechanism for T_1 [82].

The origin of the unusual T dependence of $1/T_1^e T$ in the low temperature regime ($\lesssim$ 150 K) is very peculiar. Some trivial explanations can be ruled out as its origin. Firstly, one can rule out the possibility of an activation type mechanism where T_1 is dominated by fluctuating hyperfine fields with a characteristic time scale τ which increases with decreasing T (i.e. glassy slowing). This would result in a peaked relaxation with a strongly field dependent peak value [83], which is clearly not the case. Furthermore at low T, $1/T_1^e T$ drops below its high temperature value, which rules out the possibility of a T independent component in $1/T_1^e T$ plus an activated component on top. Secondly, the possibility of a simple $1/T$ Curie-like T dependence in $1/T_1^e T$ as a result of paramagnetic centers in the sample can be ruled out. This can be inferred from the pronounced gap in $1/T_1^e T$, together with the fact that no loss of ^{13}C NMR signal intensity in the entire temperature range of the experiment was observed. This implies that all the ^{13}C nuclei measure a gap in the spin excitation spectrum which cannot be explained by a Curie-like mechanism.

Following these considerations, one is lead to consider the simplest possible explanation for the experimental data in a non-interacting electron model of a 1D semiconductor with a small secondary gap (SG). The SG may be a result of the finite inner-wall curvature [9, 86–88]. The $1/T_1^e T$ data can be fitted using this non-interacting model with only one free parameter, the

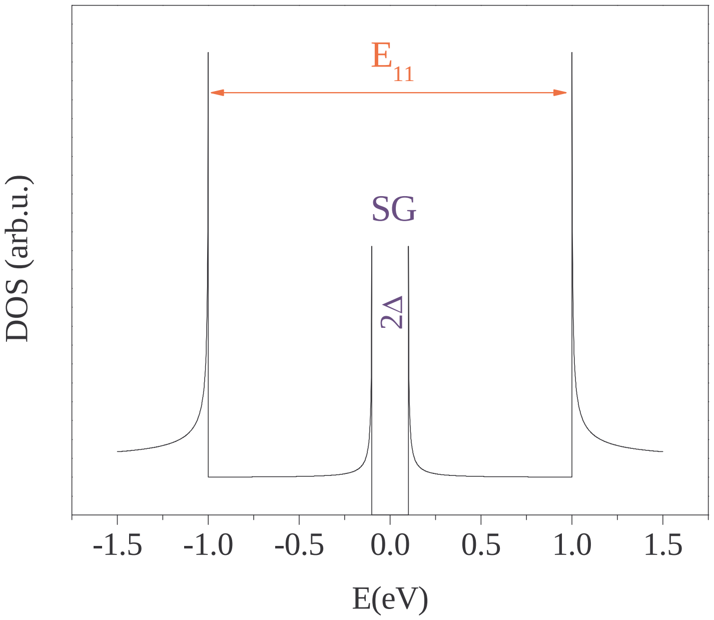

FIGURE 15.25. Schematics of the density of states proposed to explain the relaxation results. A small energy, 2Δ a few meV secondary gap opens at the Fermi level of metallic inner tubes, which is displayed not to scale. Note the van Hove singularities (vHs) at ±Δ. The unaffected vHs of the original band structure are shown for the first optical transition (E_{11}).

homogeneous SG, 2Δ. The normalized form of the gapped 1D density-of-states $n(E)$

$$n(E) \;=\; \begin{cases} \frac{E}{\sqrt{E^2-\Delta^2}} & \text{for } |E| > \Delta \\ 0 & \text{otherwise} \end{cases} \tag{15.6}$$

here, E is taken with respect to the Fermi energy). The total DOS of an inner tube is shown schematically in Fig. 15.25. Eq. (15.6) is used to calculate $1/T_1^eT$ [89] as such

$$\frac{1}{T_1^eT} \;=\; \alpha(\omega)\int_{-\infty}^{\infty} n(E)n(E+\omega)\left(-\frac{\delta f}{\delta E}\right)dE, \tag{15.7}$$

where E and ω are in temperature units for clarity, f is the Fermi function $f = [\exp(E/T)+1]^{-1}$, and the amplitude factor $\alpha(\omega)$ is the high temperature value for $1/T_1^eT$. The results of the best fit of the data to Eq. (15.7) are presented in Fig. 15.24, where $2\Delta = 43(3)$ K ($\equiv 3.7$ meV) is H independent within experimental scattering between 9.3 and 3.6 Tesla. We note that at the largest external field of 9.3 Tesla, $\omega = 4.5$ mK $\ll \Delta, T$, however, ω must be retained inside the integral. This is a direct consequence of the one dimensionality which gives a logarithmic divergence inside the integral (solved numerically) of the form $\ln(T/\omega)$ for $T \lesssim \Delta$. At the lowest temperatures T ($\lesssim 5$ K), T_1^e ($\gtrsim 300$ s) becomes so long that the low energy excitations specific to the homogeneous properties of the inner-tubes become inefficient, and other excitations take over, possibly defect related. In such cases we find that the recovery shape is no longer universal and the underlying distribution in T_1 is smoothed out, possibly due to spin-diffusion effects.

The origin of the experimentally observed gap still remains to be clarified. Tight binding calculations predict that applied magnetic fields can induce SG's of similar magnitude for metallic SWCNT [90]. However, such a scenario can be excluded due to the absence of any field dependence of the gap. The NMR data would be more consistent with a curvature induced SG for metallic tubes [9, 86–88], however for the typical inner-tubes the predicted values, ∼ 100 meV, are over an order of magnitude larger than our experimental data. Other scenarios, such as quantization of levels due to finite short lengths of the nanotubes could be considered as well, however, in all these cases a behaviour independent of tube size and chirality is certainly not expected.

This suggests that electron-electron interactions play an important roled for the metallic inner tubes. It has been predicted that electron-electron correlations and a Tomonaga-Luttinger (TLL) state leads to an increase in $1/T_1T$ with decreasing T [91], which is a direct consequence of the 1D electronic state. The correlated 1D nature may also lead to a Pierels instability [10] with the

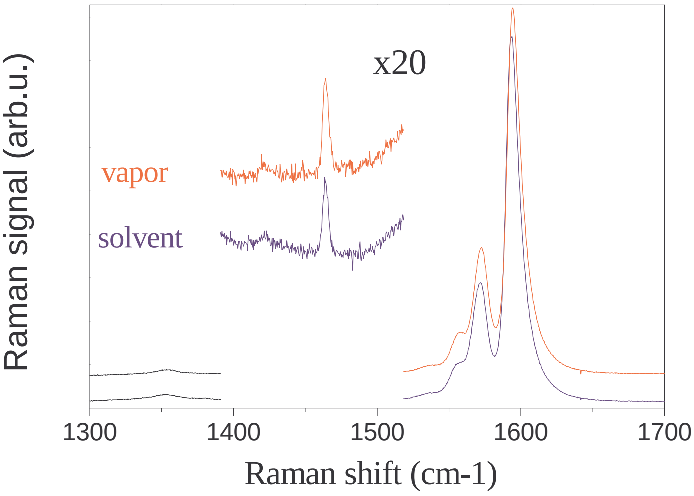

FIGURE 15.26. Raman spectra of vapor and solvent filled C_{60}@SWCNT at 488 nm excitation and 90 K after Ref. [40]. The spectra are normalized to the amplitude of the SWCNT G mode.

opening of a small collective gap 2Δ and a sharp drop in $1/T_1T$ below $\Delta \sim 20$ K. Therefore, the presence of both a TLL state and a Pierels instability could possibly account for the data.

Summarizing the NMR studies on DWCNTs, it was shown that T_1 has a similar T and H dependence for all the inner-tubes have, with no indication of a metallic/semiconducting separation due to chirality distributions. At high temperatures ($T \gtrsim 150$ K) $1/T_1^eT$ of the inner tubes exhibit a metallic 1D spin diffusion state. Below ~150 K, $1/T_1^eT$ increases dramatically with decreasing T, and a gap in the spin excitation spectrum is found below $\Delta \simeq 20$ K. A 1D correlated state was suggested to be responsible for the opening of a small collective gap in the excitations, possibly a Pierels instability [10, 52]. Certainly, theoretical work on the electronic properties of inner wall nanotubes in DWCNT, and on the incidence of 1D correlation effects are needed to clarify the exact nature of the ground states.

15.3.4 ESR studies on encapsulated magnetic fullerenes

Observation of the intrinsic ESR signal of pristine SWCNTs remains elusive [92, 93]. Now, it is generally believed that intrinsic ESR of the tubes can not be observed as conduction electrons on metallic tubes are relaxed by defects too fast to be observable. In addition, one always observes a number of ESR active species in a sample, such as graphitic carbon or magnetic catalyst particles, which prevent a meaningful analysis of the signal. In contrast, local probe studies could still allow an ESR study of tubes, provided the local spin probe can be selectively attached to the tubes. This goal can be achieved by using magnetic fullerenes, such as e.g. N@C_{60} or C_{59}N, since fullerenes are known to be selectively encapsulated inside SWCNTs [31] and can be washed from the outside using organic solvents [33]. As the properties and handling of the two magnetic fullerenes are quite different, the synthesis of the corresponding peapods and the results are discussed separately.

N@C_{60} is an air stable fullerene [94] but decays rapidly above ~ 200 °C [95] which prevents the use of the conventional vapor method of peapod preparation which requires temperatures above 400 °C. To overcome this limitation and to allow in general the synthesis of temperature sensitive peapod materials, low temperature peapod synthesis (solvent method) was developed independently by four groups [39–42]. These methods share the common idea of mixing the opened SWCNTs with C_{60} in a solvent with low fullerene solubility such as methanol [39] or n-pentane [40]. The encapsulation is efficient as it is energetically preferred for C_{60} to enter the tubes rather than staying in the solution. After the solvent filling, excess fullerenes can be removed by sonication in toluene, which is a good fullerene solvent as it was found that fullerenes enter the tube irreversibly. HR-TEM has shown an abundant filling with the fullerenes [39, 41] but here we discuss macroscopic characterizations using Raman spectroscopy, which has proven that peapods prepared by the solvent method are equivalent to the vapor prepared peapods.

In Fig. 15.26, we show the comparison of the Raman spectra of vapor- and solvent-filled C_{60}

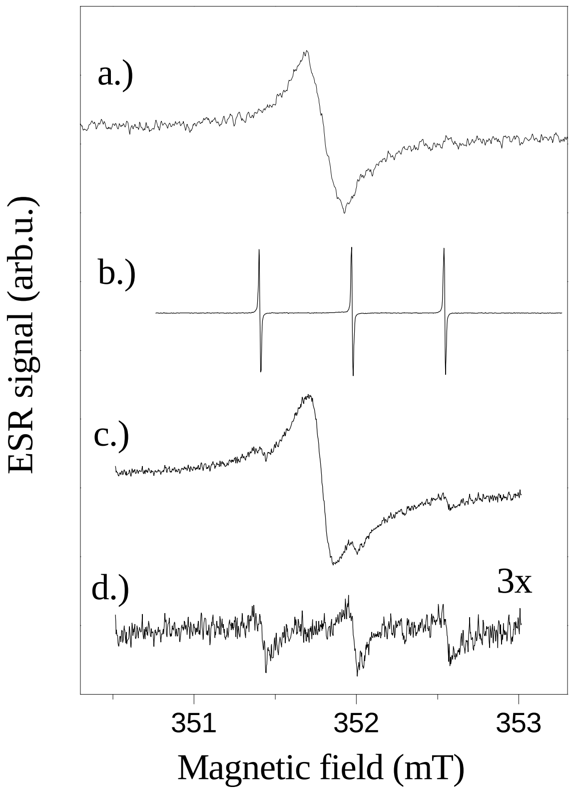

FIGURE 15.27. X-band electron spin resonance spectrum of the a.) pristine SWCNT, b.) crystalline N@C_{60}:C_{60}, c.) (N@C_{60}:C_{60})@SWCNT and d.) the triplet component of the (N@C_{60}:C_{60})@SWCNT ESR spectrum at ambient temperature after Ref. [40].

peapod samples. The Raman spectra of peapod samples in the plotted frequency range consist of the SWCNT G and D modes at 1590 and 1355 cm^{-1}, respectively and narrow lines related to the Raman active modes of the C_{60} inside the SWCNT [33, 43]. We show enlarged the most significant Raman active line of C_{60} peapod, the $A_g(2)$ mode. We observe a single $A_g(2)$ line at 1466 cm^{-1} for both peapod materials which is consistent with the relatively large, $d = 1.4$ nm, tube diameter [49]. The observation of the 1466 cm^{-1} C_{60} $A_g(2)$ mode is characteristic [43] for the encapsulated C_{60}. Its observation for the solvent prepared sample with the same intensity as for the vapor prepared sample proves the effective macroscopic filling. The absence of an extra line at 1469 cm^{-1}, that is the Raman shift of the $A_g(2)$ of crystalline C_{60} is evidence that no C_{60} is present apart from those encapsulated in the nanotubes.

The low temperature synthesis allows to encapsulate the N@C_{60} fullerene. The N@C_{60}:C_{60} endohedral fullerene: fullerene solid solution can be produced in a N_2 arc-discharge tube following Ref. [96] with a typical yield of a few 10 ppm [97]. In Fig. 15.27., the ESR spectra of the starting SWCNT, (N@C_{60}:C_{60})@SWCNT, and N@C_{60}:C_{60} are shown. The ESR spectrum of the pristine SWCNT for the magnetic field range shown is dominated by a signal that is assigned to some residual carbonaceous material, probably graphite. Fig. 15.27c. shows, that after the solvent encapsulation of N@C_{60}:C_{60} in the NCL-SWCNT, a hyperfine N triplet ESR is observed, similar to that in pristine N@C_{60}:C_{60}, superimposed on the broad signal present in the pristine nanotube material. Fig. 15.27d. shows the triplet component of this signal after subtracting the signal observed in pristine SWCNT. The hiperfine triplet in N@C_{60}:C_{60} is the result of the overlap of the $^4S_{3/2}$ state of the three 2p electrons of the N atom and the ^{14}N nucleus, with nuclear spin, $I = 1$. The isotropic hyperfine coupling of N@C_{60}:C_{60} is unusually high as a result of the strongly compressed N atomic $2p^3$ orbitals in the C_{60} cage thus it unambiguously identifies this material [94]. The hyperfine coupling constant observed for the triplet structure in the encapsulated material, $A = 0.57 \pm 0.01$ mT, agrees within experimental precision with that observed in N@C_{60}:C_{60} [94], which proves that the encapsulated material is (N@C_{60}:C_{60})@SWCNT. The ESR line-width for the encapsulated material, $\Delta H_{pp} = 0.07$ mT, is significantly larger than the resolution limited ΔH_{pp} =0.01 mT in the pristine N@C_{60}:C_{60} material, the lines being Lorentzian. The most prob-

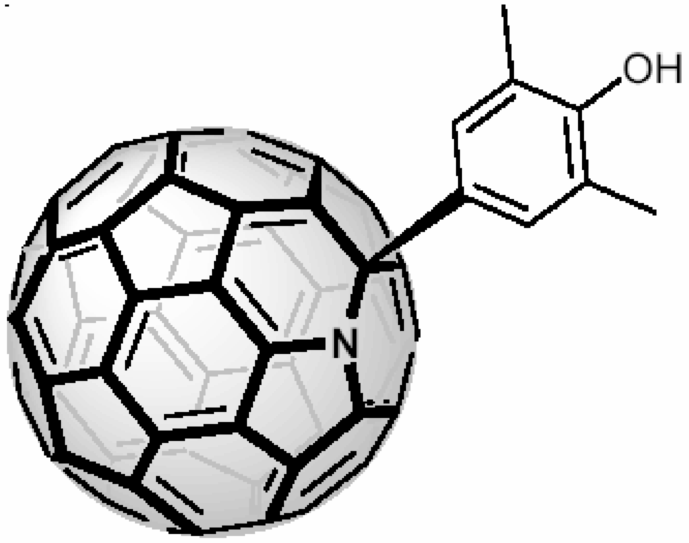

FIGURE 15.28. Schematic structure of the 4-Hydroxy-3,5-dimethyl-phenyl- hydroazafullerene.

able cause for the broadening is static magnetic fields from residual magnetic impurities in the SWCNT [77]. The ESR signal intensity is proportional to the number of N spins, and this allows the quantitative comparison of N concentrations in (N@C_{60}:C_{60})@SWCNT and N@C_{60}:C_{60}. Taking the filling value from the EELS measurement, we obtain that the N spin concentration in (N@C_{60}:C_{60})@SWCNT is ∼2.5 times smaller than in the starting N@C_{60}:C_{60} material. This cannot be due to a loss of N spins during the synthesis as N@C_{60}:C_{60} is stable below 100 °C and N loss becomes rapid above 220 °C only [95]. However, the observed difference may be caused by the limited accuracy of the ESR intensity measurement also caused by microwave losses as the conducting bucky-paper pieces are separated from each-other in a poorly controlled way.

As seen from the ESR results on encapsulated N@C_{60}, relatively limited information can be deduced about the tubes themselves. This stems from the fact that the N spins are well shielded in N@C_{60} [98] and are thus are relatively insensitive to the SWCNT properties. In contrast, N@C_{60}@SWCNT peapods might find another application as building elements of a quantum computer as proposed by Harneit *et al.* [8]. A better candidate for magnetic fullerene encapsulation is the $C_{59}N$ monomer radical as here the unpaired electron is on the cage and is a sensitive probe of the environment. This material can be chemically prepared [99], however it forms a non-magnetic dimer crystal $(C_{59}N)_2$. It appears as a spinless monomer in an adduct form [100] or attached to surface dangling bonds [101]. The magnetic $C_{59}N$ monomer radical is air sensitive but it can be stabilized as a radical when it is dilutely mixed in C_{60}[102]. As a result, a different strategy has to be followed to encapsulate $C_{59}N$ inside SWCNT, which is discussed in the following along with preliminary ESR results.

To obtain $C_{59}N$ peapods, air stable $C_{59}N$ derivatives, ($C_{59}N$-der in the following) were prepared chemically by A. Hirsch and F. Hauke following standard synthesis routes [100, 103]. The $C_{59}N$-der was 4-Hydroxy-3,5-dimethyl-phenyl-hydroazafullerene whose structure is shown in Fig. 15.28. The $C_{59}N$ derivatives were encapsulated either pure or mixed with C_{60} as $C_{59}N$-der:C_{60} with 1:9 concentrations using a modified version of the low temperature encapsulation method. In brief, the mixture of the dissolved fullerenes and SWCNTs were sonicated in toluene and filtered. It is expected that the $C_{59}N$ monomer radical can be obtained after a heat treatment in dynamic vacuum, which is discussed below.

Raman spectroscopy was performed to characterize the SWCNT filling with the $C_{59}N$-der. In Fig. 15.29, the Raman spectra of the pristine and encapsulated $C_{59}N$-der is shown. The Raman spectra of the peapod sample (lower curve in Fig. 15.29) in the plotted frequency range consist of the SWCNT G modes around 1550 cm^{-1} and additional lines related to the Raman active modes of the encapsulated azafullerene derivative [43]. The major Raman modes of the pristine $C_{59}N$-der are similar to those of the $(C_{59}N)_2$ dimer [104]. The strongest mode is observed at 1459.2 cm^{-1}

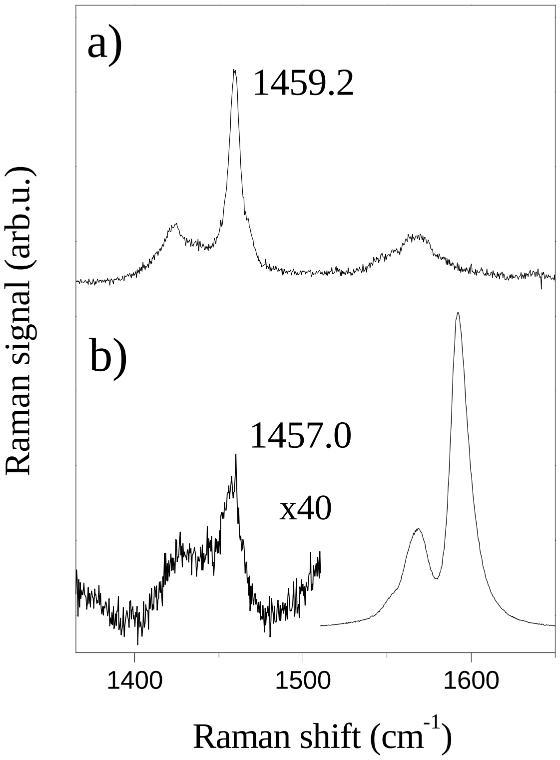

FIGURE 15.29. Tangential mode of the Raman spectra of the C_{59}N-der before (a) and after encapsulation (b) excited with a 488 nm laser. Labels mark the position of the strongest C_{59}N-der mode in the two samples. The Raman G-mode of SWCNT dominates the peapod spectrum in the 1550-1650 cm^{-1} range.

which is derived from the C_{60} $A_g(2)$ mode and is downshifted to 1457 cm^{-1} after the encapsulation procedure. The 2.2 cm^{-1} downshift proves the encapsulation of the molecule inside the SWCNT.

When encapsulated inside SWCNTs, the corresponding $A_g(2)$ mode of C_{60} downshifts with 3 cm^{-1} , which is assigned to the softening of the C_{60} $A_g(2)$ vibrational mode due to the interaction between the ball and the SWCNT wall [43]. The slight difference between the downshift for the azafullerene and for the C_{60} peapods might be attributed to the different structure of the two molecules. The encapsulation also manifests in a line broadening: the main component of the 1457 cm^{-1} mode is broadened from 4.5 cm^{-1} FWHM in the pristine material to 10 cm^{-1} FWHM in the encapsulated one. This is similar to the values found for encapsulated C_{60} [43].

The integrated intensity of the observed $A_g(2)$ derived mode of the C_{59}N is approximately 5 times larger than that of a C_{60} peapod prepared identically when normalized by the SWCNT G mode intensity. This, however, can not be used to measure the encapsulation efficiency as Raman intensities depend on the strength of the Raman resonance enhancement and the Raman scattering matrix elements [46]. For C_{60} peapods the Raman signal was calibrated with independent and carbon number sensitive measurements: EELS studies gave the total number of C_{60} related and non-C_{60} related carbons [70] and the mass of encapsulated C_{60}s was determined from NMR studies using ^{13}C enriched fullerenes [47, 82]. In the current case, neither methods can be employed and we determined the filling efficiency for the azafullerene by encapsulating a mixture of the azafullerene and C_{60}.

In Fig. 15.30., the Raman spectra of the encapsulated C_{59}N-der:C_{60} mixture with weight ratios of 1:9 in the starting solvent is shown. The Raman spectrum of the encapsulated mixture was simulated with a weighted sum of the separately recorded spectra for encapsulated C_{59}N-der and C_{60}. The best agreement between the simulated and the experimental spectra is for a C_{59}N-der content of 0.12(2). This value is close to the expected value of 0.1 and it proves that the azafullerene enters the tubes with the same efficiency as C_{60}.

In Fig. 15.31, we show the ESR spectra of the encapsulated mixture, (C_{59}N-der:C_{60})@SWCNT, after 700 °C vacuum annealing. The spectra of C_{59}N:C_{60}, a C_{59}N monomer embedded in C_{60} [102], is also shown for comparison. A triplet structure similar to that in C_{59}N:C_{60} is observed in the heat-treated (C_{59}N-der:C_{60})@SWCNT overlapping with a broader line. The broader component is

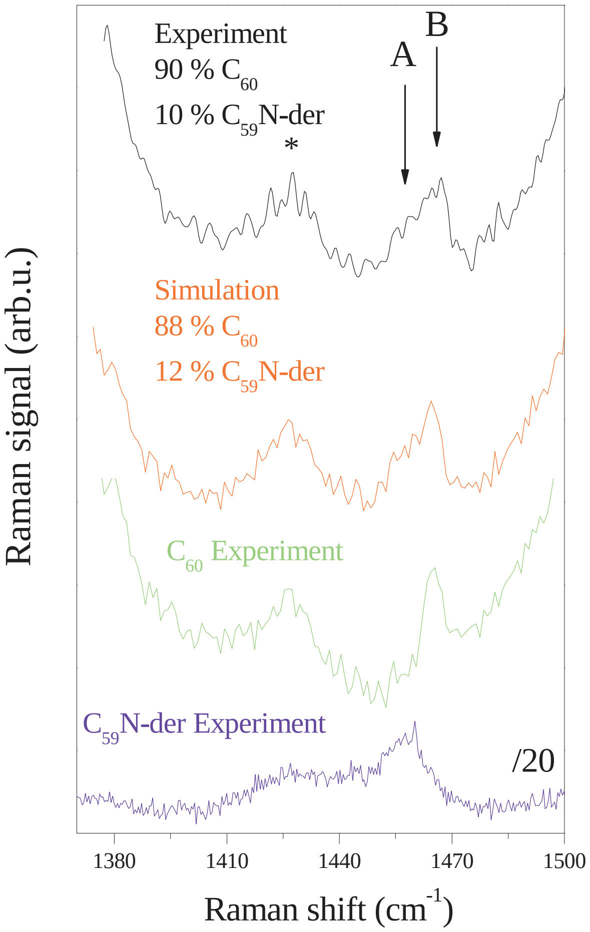

FIGURE 15.30. Raman spectra of the encapsulated $C_{59}N$-der:C_{60} mixture at the 488 nm laser excitation. The spectra for the $C_{59}N$-der and C_{60} peapods is shown together with their weighted sum as explained in the text. A and B mark the components coming nominally from the superposing two phases. The asterisk marks a mode that is present in the pristine SWCNT material. Note the different scale for the $C_{59}N$-der peapod material.

present in reference samples without encapsulated azafullerenes and is identified as a side-product. The broad line was numerically deconvoluted from the triplet component by fitting Lorentzian for all the signal. In Fig. 15.31 a fit for the triplet component is shown with solid lines. However, the triplet pattern appears only after the 700 °C vacuum annealing.

The ESR spectra of $C_{59}N$:C_{60} is well understood [102]: at room temperature it consists of a triplet pattern due to the hyperfine interaction with the ^{14}N nucleus ($I = 1$) and a series of doublet peaks due to the interaction of the electron delocalized over the entire fullerene cage with ^{13}C nuclei ($I = 1/2$). The isotropic hyperfine coupling, A_{iso}=0.370(4) of the triplet pattern in ($C_{59}N$-der:C_{60})@SWCNT closely agree with those found for $C_{59}N$ monomers in solvents A_{iso}=0.373 [105] and A_{iso}=0.37 [106] or A_{iso}=0.363(1) in the C_{60} matrix [102]. This proves that after the 700 °C heat treatment, a sizeable amount of rotating $C_{59}N$ monomer radicals are present in the sample. This is not surprising in the view of the ability to form $C_{59}N$ monomers from $C_{59}N$ at similar temperatures [107], however the current process is not reversible and the remnants of the side-groups are probably removed by the dynamic pumping. Although, the production of $C_{59}N$ monomers inside SWCNTs was proved, further work is required to understand the spectral details, to improve the background to triplet signal ratio, and in particular temperature dependent studies are required to study the tube properties.

15.4 Summary

In summary, we reviewed how molecules encapsulated inside SWCNTs can be used to study various properties of the tubes themselves. Inner tubes grown from encapsulated fullerenes were shown to be an excellent probe of diameter dependent reactions on the outer tubes. Inner tubes grown from isotope labeled fullerenes and organic solvents allowed to understand the role of

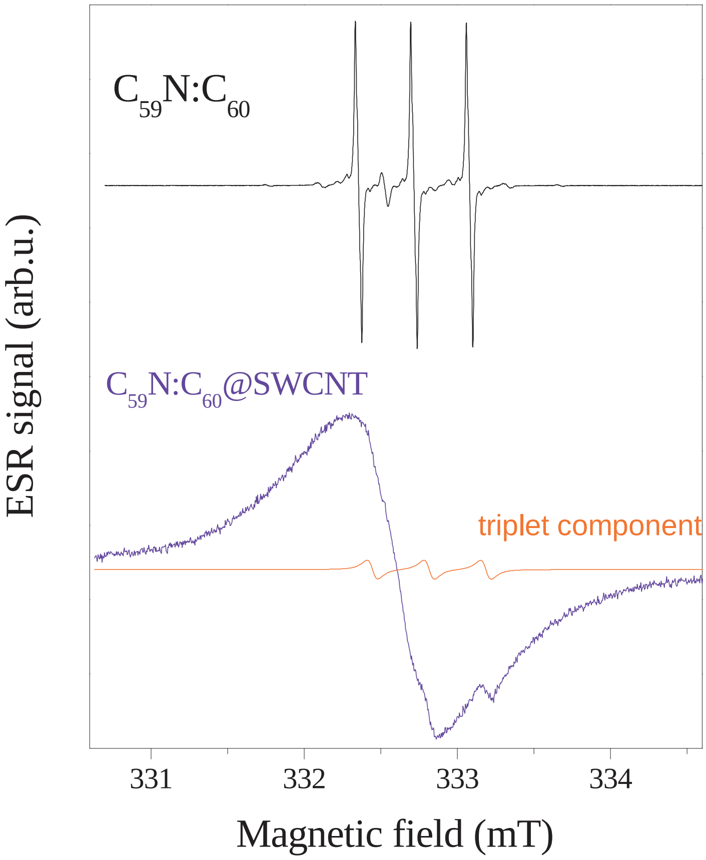

FIGURE 15.31. ESR spectra of crystalline $C_{59}N:C_{60}$ (a) and ($C_{59}N:C_{60}$)@SWCNT obtained by annealing the ($C_{59}N$-der:C_{60})@SWCNT. A solid curve shows the triplet component after deconvolution from the total ESR signal.

the different carbon phases in the growth of the inner tubes. In addition, isotope labeled inner tubes were shown to yield an unparalleled precision to study the density of states near the Fermi level using NMR. It was reviewed how magnetic fullerenes can be encapsulated inside SWCNTs yielding linear spin chains with sizeable spin concentrations and also to allow ESR studies of the tube properties.

15.5 Acknowledgements

This work was supported by the Austrian Science Funds (FWF) project Nr. 17345, by the Hungarian State Grants No. TS049881, F61733 and NK60984 by the EU projects BIN2-2001-00580, and MERG-CT-2005-022103 and by the Zoltán Magyary fellowship. The author is particularly grateful to Hans Kuzmany and Rudolf Pfeiffer for their participation in the discussed works, for the stimulating discussions and for the critical comments on the manuscript. Á. Kukovecz, Z. Kónya, T. Pichler, H. Rauf, C. Kramberger, F. Hasi, E. Obraztsova, H. Alloul, P. M. Singer, J. Bernardi, P. Wzietek, F. Fülöp, A. Rockenbauer, A. Jánossy, F. Hauke, A. Hirsch, V. N. Popov, V. Zólyomi and J. Kürti are acknowledged for their participation in the reviewed works. Ch. Schaman is acknowledged for preparing some of the figures.

†Present address: Budapest University of Technology and Economics, Institute of Physics and Solids in Magnetic Fields Research Group of the Hungarian Academy of Sciences, H-1521, Budapest P.O.Box 91, Hungary

References

[1] S. Iijima, Nature **354**, 56 (1991).
[2] S. Iijima and T. Ichihashi, Nature **363**, 603 (1993).

[3] D. S. Bethune, C. H. Kiang, M. S. DeVries, G. Gorman, S. R., and R. Beyers, Nature **363**, 605 (1993).

[4] A. N. Obraztsov, I. Pavlovsky, A. P. Volkov, E. D. Obraztsova, A. L. Chuvilin, and V. L. Kuznetsov, J. Vac. Sci. Techn. B **18**, 1059 (2000).

[5] G. Z. Yue, Q. Qiu, B. Gao, Y. Cheng, J. Zhang, H. Shimoda, S. Chang, J. P. Lu, and O. Zhou, Appl. Phys. Lett. **81**, 355 (2002).

[6] J. H. Hafner, C. L. Cheung, and C. M. Lieber, Nature **398**, 761 (1999).

[7] A. Bachtold, P. Hadley, T. Nakanishi, and C. Dekker, Science **294**, 1317 (2001).

[8] W. Harneit, C. Meyer, A. Weidinger, D. Suter, and J. Twamley, Phys. St. Solidi B **233**, 453 (2002).

[9] N. Hamada, S. Sawada, and A. Oshiyama, Phys. Rev. Lett. **68**, 1579.1581 (1992).

[10] R. Saito, G. Dresselhaus, and M. Dresselhaus, *Physical Properties of Carbon Nanotubes* (Imperial College Press, 1998).

[11] D. Chattopadhyay, L. Galeska, and F. Papadimitrakopoulos, J. Am. Chem. Soc. **125**, 3370 (2003).

[12] R. Krupke, F. Hennrich, H. von Lohneysen, and M. M. Kappes, Science **301**, 344 (2003).

[13] Z. H. Chen, X. Du, M. H. Du, C. D. Rancken, H. P. Cheng, and A. G. Rinzler, Nano Lett. **3**, 1245 (2003).

[14] M. Zheng, A. Jagota, M. S. Strano, A. P. Santos, P. Barone, S. G. Chou, G. Diner, M. S. B. A. Dresselhaus, R. S. McLean, G. B. Onoa, et al., Science **302**, 1545 (2003).

[15] S. M. Bachilo, M. S. Strano, C. Kittrell, R. H. Hauge, R. E. Smalley, and R. B. Weisman, Science **298**, 2361 (2002).

[16] C. Fantini, A. Jorio, M. Souza, M. S. Strano, M. S. Dresselhaus, and M. A. Pimenta, Phys. Rev. Lett. **93**, 147406 (2004).

[17] H. Telg, J. Maultzsch, S. Reich, F. Hennrich, and C. Thomsen, Phys. Rev. Lett. **93**, 177401 (2004).

[18] R. Egger and A. O. Gogolin, Nature **79**, 50825085 (1997).

[19] K. P. Bohnen, R. Heid, H. J. Liu, and C. T. Chan, Phys. Rev. Lett. **93**, 245501 (2004).

[20] D. Connétable, G.-M. Rignanese, J.-C. Charlier, and X. Blase, Phys. Rev. Lett. **94**, 015503 (2005).

[21] S. J. Tans, M. H. Devoret, H. Dai, A. Thess, R. E. Smalley, L. J. Geerligs, and C. Dekker, Nature **386**, 474 (1997).

[22] C. Kane and E. Mele, Phys. Rev. Lett. **90**, 207401 (2003).

[23] C. D. Spataru, S. Ismail-Beigi, L. X. Benedict, and S. G. Louie, Phys. Rev. Lett. **92**, 077402 (2004).

[24] V. Perebeinos, J. Tersoff, and P. Avouris, Phys. Phys. Lett. **92**, 257402 (2004).

[25] V. Perebeinos, J. Tersoff, and P. Avouris, Phys. Phys. Lett. **94**, 027402 (2005).

[26] M. Bockrath, D. H. Cobden, J. Lu, R. A. G., R. E. Smalley, L. Balents, and P. L. McEuen, Nature **397**, 598 (1999).

[27] H. Ishii, H. Kataura, H. Shiozawa, H. Yoshioka, H. Otsubo, Y. Takayama, T. Miyahara, S. Suzuki, Y. Achiba, M. Nakatake, et al., Nature **426**, 540 (2003).

[28] H. Rauf, T. Pichler, M. Knupfer, J. Fink, and H. Kataura, Phys. Rev. Lett. **93**, 096805 (2004).

[29] F. Wang, G. Dukovic, , L. E. Brus, and T. F. Heinz, Science **308**, 838 (2005).

[30] J. Maultzsch, R. Pomraenke, S. Reich, E. Chang, D. Prezzi, A. Ruini, E. Molinari, M. S. Strano, C. Thomsen, and C. Lienau, Phys. Rev. B **72**, 241402 (2005).

[31] B. W. Smith, M. Monthioux, and D. E. Luzzi, Nature **396**, 323 (1998).

[32] B. W. Smith, M. Monthioux, and D. Luzzi, Chem. Phys. Lett. **315**, 31 (1999).

[33] H. Kataura, Y. Maniwa, T. Kodama, K. Kikuchi, K. Hirahara, K. Suenaga, S. Iijima, S. Suzuki, Y. Achiba, and W. Krätschmer, Synthetic Met. **121**, 1195 (2001).

[34] B. W. Smith and D. Luzzi, Chem. Phys. Lett. **321**, 169 (2000).

[35] S. Bandow, M. Takizawa, K. Hirahara, M. Yudasaka, and S. Iijima, Chem. Phys. Lett. **337**, 48 (2001).

[36] J. L. Hutchison, N. A. Kiselev, E. P. Krinichnaya, A. V. Krestinin, R. O. Loutfy, A. P. Morawsky, V. E. Muradyan, E. D. Obraztsova, J. Sloan, S. V. Terekhov, et al., Carbon **39**, 761 (2001).

[37] W. Ren, F. Li, J. Chen, S. Bai, and H.-M. Cheng, Chem. Phys. Lett. **359**, 196 (2002).

[38] R. Pfeiffer, H. Kuzmany, C. Kramberger, C. Schaman, T. Pichler, H. Kataura, Y. Achiba, J. Kürti, and V. Zólyomi, Phys. Rev. Lett. **90**, 225501 (2003).

[39] M. Yudasaka, K. Ajima, K. Suenaga, T. Ichihashi, A. Hashimoto, and S. Iijima, Chem. Phys. Lett. **380**, 42 (2003).

[40] F. Simon, H. Kuzmany, H. Rauf, T. Pichler, J. Bernardi, H. Peterlik, L. Korecz, F. Fülöp, and A. Jánossy, Chem. Phys. Lett. **383**, 362 (2004).

[41] M. Monthioux and L. Noé, in *XVIIIth International Winterschool on Electronic Properties of Novel Materials.* (2004), aIP Proceedings.

[42] A. N. Khlobystov, D. A. Britz, J. W. Wang, S. A. O'Neil, M. Poliakoff, and G. A. D. Briggs, J. Mat. Chem. **14**, 2852 (2004).

[43] T. Pichler, H. Kuzmany, H. Kataura, and Y. Achiba, Phys. Rev. Lett. **87**, 267401 (2001).

[44] F. Simon, H. Kukovecz, H. Rauf, T. Pichler, J. Bernardi, H. Peterlik, L. Korecz, F. Fülöp, and A. Jánossy, Chem. Phys. Lett. **413**, 506 (2005).

[45] B. C. Liu, S. C. Lyu, S. I. Jung, H. K. Kang, C.-W. Yang, J. W. Park, P. C.Y., and C. J. Lee, Chem. Phys. Lett. **383**, 104 (2004).

[46] H. Kuzmany, *Solid-State Spectroscopy, An Introduction* (Springer Verlag, Berlin, 1998).

[47] F. Simon, C. Kramberger, R. Pfeiffer, H. Kuzmany, J. Zólyomi, V. Kürti, P. M. Singer, and H. Alloul, Phys. Rev. Lett. **95**, 017401 (2005).

[48] J. Kürti, G. Kresse, and H. Kuzmany, Phys. Rev. B **58**, R8869 (1998).

[49] R. Pfeiffer, H. Kuzmany, T. Pichler, H. Kataura, Y. Achiba, M. Melle-Franco, and F. Zerbetto, Phys. Rev. B **69**, 035404 (2004).

[50] R. Pfeiffer, H. Kuzmany, F. Simon, S. N. Bokova, and E. Obraztsova, Phys. Rev. B **71**, 155409 (2005).

[51] R. Pfeiffer, F. Simon, H. Kuzmany, and V. N. Popov, Phys. Rev. B **72**, 161404 (2005).

[52] M. S. Dresselhaus, G. Dresselhaus, and P. Avouris, *Carbon Nanotubes: Synthesis, Structure, Properties, and Applications* (Springer, Berlin, Heidelberg, New York, 2001).

[53] H. Kataura, Y. Kumazawa, Y. Maniwa, I. Umezu, S. Suzuki, Y. Ohtsuka, and Y. Achiba, Synthetic Met. **103**, 2555 (1999).

[54] R. Pfeiffer, C. Kramberger, F. Simon, H. Kuzmany, V. N. Popov, and H. Kataura, Eur. Phys. J. B **42**, 345 (2004).

[55] V. N. Popov and L. Henrard, Phys. Rev. B **65**, 235415 (2002).

[56] J. P. Lu, X.-P. Li, and R. M. Martin, Phys. Rev. Lett. **68**, 1551 (1992).

[57] M. Abe, H. Kataura, H. Kira, T. Kodama, S. Suzuki, Y. Achiba, K.-i. Kato, M. Takata, A. Fujiwara, K. Matsuda, et al., Phys. Rev. B **68**, 041405(R) (2003).

[58] F. Simon, A. Kukovecz, C. Kramberger, R. Pfeiffer, F. Hasi, H. Kuzmany, and H. Kataura, Phys. Rev. B **71**, 165439 (2005).

[59] V. N. Popov, New J. Phys. **6**, 17 (2004).

[60] U. D. Venkateswaran, D. L. Masica, G. U. Sumanasekera, C. A. Furtado, U. J. Kim, and P. C. Eklund, Phys. Rev. B **68**, 241406(R) (2003).

[61] J. Wu, W. Walukiewicz, W. Shan, E. Bourret-Courchesne, J. W. Ager III, K. M. Yu, E. E. Haller, K. Kissell, S. M. Bachilo, R. B. Weisman, et al., Phys. Rev. Lett. **93**, 017404 (2004).

[62] A. Jorio, R. Saito, J. H. Hafner, C. M. Lieber, M. Hunter, T. McClure, G. Dresselhaus, and M. S. Dresselhaus, Phys. Rev. Lett. **86**, 1118 (2001).

[63] A. Thess, R. Lee, P. Nikolaev, H. Dai, P. Petit, J. Robert, C. Xu, Y. H. Lee, S. G. Kim, A. G. Rinzler, et al., Science **273**, 483 (1996).

[64] H. Kuzmany, W. Plank, M. Hulman, C. Kramberger, A. Grüneis, T. Pichler, H. Peterlik, H. Kataura, and Y. Achiba, Eur. Phys. J. B **22**, 307 (2001).

[65] C. Kramberger, R. Pfeiffer, H. Kuzmany, V. Zólyomi, and J. Kürti, Phys. Rev. B **68**, 235404 (2003).

[66] M. Melle-Franco, H. Kuzmany, and F. Zerbetto, J. Phys. Chem. B **109**, 6986 (2003).

[67] S. Berber, Y.-K. Kwon, and D. Tománek, Phys. Rev. Lett. **88**, 185502 (2002).

[68] M. Otani, S. Okada, and A. Oshiyama, Phys. Rev. B **68**, 125424 (2003).

[69] B. W. Smith and D. E. Luzzi, Chem. Phys. Lett. **321**, 169 (2000).

[70] X. Liu, T. Pichler, M. Knupfer, M. S. Golden, J. Fink, H. Kataura, Y. Achiba, K. Hirahara, and S. Iijima, Phys. Rev. B **65**, 045419 (2002).

[71] F. Hasi, F. Simon, and H. Kuzmany, J. Nanosci. Nanotechn. **5**, 1785 (2005).

[72] Y. Zhao, B. I. Yakobson, and R. E. Smalley, Phys. Rev. Lett. **88**, 185501 (2002).

[73] S. W. Han, M. Yoon, S. Berber, N. Park, E. Osawa, J. Ihm, and D. Tománek, Phys. Rev. B **70**, 113402 (2004).

[74] J. Bardeen, L. N. Cooper, and J. R. Schrieffer, Phys. Rev. **108**, 1175 (1957).

[75] F. Simon and H. Kuzmany, *Growth of single wall carbon nanotubes from ^{13}C isotope labelled organic solvents inside single wall carbon nanotube hosts*, cond-mat/0603477.

[76] G. Kresse and D. Joubert, Phys. Rev. B **59**, 17581775 (1999).

[77] X.-P. Tang, A. Kleinhammes, H. Shimoda, L. Fleming, K. Y. Bennoune, S. Sinha, C. Bower, O. Zhou, and Y. Wu, Science **288**, 492 (2000).

[78] C. Goze-Bac, S. Latil, P. Lauginie, V. Jourdain, J. Conard, L. Duclaux, A. Rubio, and P. Bernier, Carbon **40**, 1825 (2002).

[79] F. Simon, R. Pfeiffer, C. Kramberger, M. Holzweber, and H. Kuzmany, *The Raman response of double wall carbon nanotubes* (Springer New York, 2005), pp. 203–224.

[80] J. Kürti, V. Zólyomi, M. Kertész, and S. Guangyu, New. J. Phys. **5**, 125.1125.21 (2003).

[81] M. A. L. Marques, M. d'Avezac, and F. Mauri, *Magnetic response of carbon nanotubes from ab initio*

calculations, cond-mat/0510197.

[82] P. M. Singer, P. Wzietek, H. Alloul, F. Simon, and H. Kuzmany, Phys. Rev. Lett. **95**, 236403 (2005).

[83] C. P. Slichter, *Principles of Magnetic Resonance* (Spinger-Verlag, New York, 1989), 3rd ed.

[84] H. Shimoda, B. Gao, X. P. Tang, A. Kleinhammes, L. Fleming, Y. Wu, and O. Zhou, Phys. Rev. Lett. **88**, 15502 (2002).

[85] A. Kleinhammes, S.-H. Mao, X.-J. Yang, X.-P. Tang, H. Shimoda, J. P. Lu, O. Zhou, and Y. Wu, Phys. Rev. B **68**, 75418 (2003).

[86] C. Kane and E. Mele, Phys. Rev. Lett. **78**, 1932 (1997).

[87] J. Mintmire and C. White, Phys. Rev. Lett. **81**, 2506 (1998).

[88] V. Zólyomi and J. Kürti, Phys. Rev. B **70**, 085403 (2004).

[89] T. Moriya, J. Phys. Soc. Jpn. **18**, 516 (1963).

[90] J. P. Lu, Phys. Rev. B **74**, 1123 (1995).

[91] H. Yoshioka, J. Phys. Chem. Solids. **63**, 1281 (2002).

[92] A. S. Claye, N. M. Nemes, A. Jánossy, and J. E. Fischer, Phys. Rev. B **62**, 4845 (2000).

[93] J.-P. Salvetat, T. Fehér, C. LHuillier, F. Beuneu, and L. Forró, Phys. Rev. B **72**, 075440 (2005).

[94] T. Almeida Murphy, T. Pawlik, A. Weidinger, M. Hhne, R. Alcala, and J.-M. Spaeth, Phys. Rev. Lett. **77**, 1075 (1996).

[95] M. Waiblinger, K. Lips, W. Harneit, A. Weidinger, E. Dietel, and A. Hirsch, Phys. Rev. B **64**, 159901 (2001).

[96] B. Pietzak, M. Waiblinger, T. Murphy, A. Weidinger, M. Hohne, E. Dietel, and A. Hirsch, Chem. Phys. Lett. **279**, 259 (1997).

[97] A. Jánossy, S. Pekker, F. Fülöp, F. Simon, and G. Oszlányi, in *Proceedings of the IWEPNM* (2000), p. 199.

[98] K.-P. Dinse, Phys. Chem. Chem. Phys. **4**, 5442 (2002).

[99] J. C. Hummelen, B. Knight, J. Pavlovich, R. Gonzalez, and F. Wudl, Science **269**, 1554 (1995).

[100] J. C. Hummelen, C. Bellavia-Lund, and F. Wudl, *Heterofullerenes* (Springer, Berlin, Heidelberg, 1999), vol. 199, p. 93.

[101] M. J. Butcher, F. H. Jones, P. H. Beton, P. Moriarty, B. N. Cotier, M. D. Upward, K. Prassides, K. Kordatos, N. Tagmatarchis, F. Wudl, et al., Phys. Rev. Lett. **83**, 3478 (1999).

[102] F. Fülöp, A. Rockenbauer, F. Simon, S. Pekker, L. Korecz, S. Garaj, and A. Jánossy, Chem. Phys. Lett. **334**, 223 (2001).

[103] A. Hirsch and B. Nuber, Acc. Chem. Res. **32**, 795 (1999).

[104] H. Kuzmany, W. Plank, J. Winter, O. Dubay, N. Tagmatarchis, and K. Prassides, Phys. Rev. B **60**, 1005 (1999).

[105] K. Hasharoni, C. Bellavia-Lund, M. Keshavarz-K, G. Srdanov, and F. Wudl, J. Am. Chem. Soc. **119**, 11128 (1997).

[106] A. Gruss, K.-P. Dinse, A. Hirsch, B. Nuber, and U. Reuther, J. Am. Chem. Soc. **119**, 8728 (1997).

[107] F. Simon, D. Arčon, N. Tagmatarchis, S. Garaj, L. Forró, and K. Prassides, J. Phys. Chem. A. **103**, 6969 (1999).

16

Publikationsnachweise und Druckzusagen

Available online at www.sciencedirect.com

SCIENCE DIRECT®

Chemical Physics Letters 383 (2004) 362–367

CHEMICAL PHYSICS LETTERS

www.elsevier.com/locate/cplett

Low temperature fullerene encapsulation in single wall carbon nanotubes: synthesis of N@C_{60}@SWCNT

F. Simon [a,*], H. Kuzmany [a], H. Rauf [b], T. Pichler [b], J. Bernardi [c], H. Peterlik [a], L. Korecz [d], F. Fülöp [d], A. Jánossy [d]

[a] *Institut für Materialphysik, Universität Wien, Strudlhofgasse 4, A-1090 Vienna, Austria*
[b] *Institut für Festkörper und Werkstoffforschung, P.O. Box 270016, D-01171, Dresden, Germany*
[c] *University Service Centre for Transmission Electron Microscopy (USTEM), Technische Universität Wien, Wiedner Hauptstrasse 8-10/052, A-1040 Vienna, Austria*
[d] *Institute of Physics and Solids in Magnetic Fields Research Group of the Hungarian Academy of Sciences, Budapest University of Technology and Economics, H-1521, P.O. Box 91, Budapest, Hungary*

Received 6 October 2003; in final form 13 November 2003

Abstract

High filling of single wall carbon nanotubes (SWCNT) with C_{60} and C_{70} fullerenes from solvent is reported at temperatures as low as 69 °C. A 2-h long refluxing in *n*-hexane of the mixture of the fullerene and SWCNT results in a high yield of C_{60},C_{70}@SWCNT, fullerene peapod, material. The peapod filling is characterized by TEM, Raman and electron energy loss spectroscopy and X-ray scattering. We applied the method to synthesize the temperature sensitive (N@C_{60}:C_{60})@SWCNT as proved by electron spin resonance spectroscopy. The solvent prepared peapod samples can be transformed to double walled nanotubes enabling a high yield and industrially scalable production of DWCNT.

1. Introduction

Nanostructures based on carbon nanotubes [1] have been in the forefront of nanomaterial research in the last decade. Single wall carbon nanotube (SWCNT) is an even more exciting material as it represents the perfect, one-dimensional form of carbon. Fullerene encapsulating SWCNTs have attracted considerable interest after the discovery of C_{60}@SWCNT peapods [2]. More recently, several molecules have been successfully inserted into the interior of tubes such as other fullerenes, endohedral metallofullerenes or alkali halides [3]. It is believed that the inside filled structures can alter or enhance the mechanical and electronic properties of the SWCNTs or may allow the fine tuning of these parameters. However, all these synthesis methods required treatment at relatively high temperatures above 400 °C. In particular, the peapod synthesis requires the heat treatment of SWCNT and fullerenes sealed together under vacuum, a method that appears impractical for large scale production purposes. Another important trend is the study of the behavior of the encapsulated materials under special conditions. It was recently shown that fullerene peapods are transformed into a double wall carbon nanotube (DWCNT) structure after high temperature annealing [4]. The fullerenes coalesce into an inner nanotube, which leaves the electronic properties unaffected but is expected to significantly enhance the mechanical properties of the tube system. This enhanced mechanical stability makes DWCNTs promising candidates for applications such as future electronics, probe tips for scanning probe microscopy, field emission devices and many more. Our aim in the current study was twofold: (i) development of a peapod synthesis method that allows the use of low temperatures in order to obtain encapsulated materials which do not survive the usual high temperature synthesis meth-

---

[*] Corresponding author. Fax: +43-1-4277-51375.
E-mail address: fsimon@ap.univie.ac.at (F. Simon).

0009-2614/$ - see front matter © 2003 Elsevier B.V. All rights reserved.
doi:10.1016/j.cplett.2003.11.039

Chapter 3

Available online at www.sciencedirect.com
SCIENCE DIRECT®
Chemical Physics Letters 404 (2005) 85–89
CHEMICAL PHYSICS LETTERS
www.elsevier.com/locate/cplett

Highly ^{13}C isotope enriched azafullerene, $C_{59}N$, for nuclear spin labelling

F. Simon [a,*], F. Fülöp [b], A. Rockenbauer [b,c], L. Korecz [b,c], H. Kuzmany [a]

[a] *Institut für Materialphysik, Universität Wien, Strudlhofgasse 4, AT-1090 Wien, Austria*
[b] *Budapest University of Technology and Economics, Institute of Physics and Solids in Magnetic Fields Research Group of the Hungarian Academy of Sciences, H-1521, Budapest, P.O. Box 91, Hungary*
[c] *Chemical Research Center of the Hungarian Academy of Sciences, P.O. Box 17, Budapest H-1525, Hungary*

Received 17 November 2004; in final form 3 January 2005

Abstract

Synthesis of highly ^{13}C isotope enriched azafullerene, $C_{59}N$ embedded in C_{60} is reported. ^{13}C enriched fullerenes, produced with the Krätschmer–Huffmann process, were subject to a N_2 discharge that produces $C_{59}N$ with a low probability. Raman spectroscopy indicates a homogeneous ^{13}C distribution. Electron spin resonance measurement (ESR) proves that the $C_{59}N$ concentration, 0.2%, is similar as in non-enriched fullerenes. The ESR spectrum is simulated accurately with the known ^{14}N and ^{13}C hyperfine coupling constants. The material enables the nuclear spin-labelling of heterofullerene complexes with a potential for biological applications. It might also find applications as a building element for quantum computation.

1. Introduction

Isotope controlled synthesis (ICS) of molecular nanostructures provides an important degree of freedom to characterize fundamental and application oriented properties. ICS is generally considered as a tool to, e.g., enhance nuclear magnetic resonance signals, to provide improved information when specific isotope labelling is possible or to trace biological processes using radioactive nuclei. For fullerenes [1], ICS was applied to improve the NMR data [2], to identify the origin of different vibrational modes in crystalline C_{60} [3], and to yield an insight into underlying physical phenomenon such as the mechanism of the superconductivity in alkali doped fullerides [4] by means of ^{13}C enrichment. More recently, ^{13}C enriched fullerenes were used to produce ^{13}C enriched single wall carbon nanotubes [5].

Properties of fullerenes can be also studied through the synthesis of on-ball doped modifications. The $C_{59}N$ or $C_{59}B$ heterofullerenes were predicted to provide a doping opportunity for C_{60} [6,7]. In general, heterofullerenes possess a rich chemistry due to their enhanced reactivity as compared to pristine fullerenes [7]. The $C_{59}N$ azafullerene can be synthesized in macroscopic amounts [7,8] and in a solid form it is an insulator consisting of $(C_{59}N)_2$ dimer units where the extra electrons are localized in the dimer bonds as singlet states [9]. The $C_{59}N$ monomer radical can be observed by light [10,11] or thermal induced homolysis of $(C_{59}N)_2$ [12] or when the $C_{59}N$ monomer is embedded in a low concentration in the C_{60} crystal [13]. This $C_{59}N$:C_{60} solid solution was synthesized in a discharge tube designed for the production of N@C_{60} [13]. The advantages of the latter synthesis method over the chemical synthesis [8] are its relative simplicity and the ability of providing an isotope control option by changing the $^{14}N_2$ gas to $^{15}N_2$. Recently, it was shown that the extra electron on the $C_{59}N$ is transferred toward the C_{60}'s at high

---

[*] Corresponding author. Fax: +43 1 4277 51375.
E-mail address: fsimon@ap.univie.ac.at (F. Simon).

0009-2614/$ - see front matter © 2005 Elsevier B.V. All rights reserved.
doi:10.1016/j.cplett.2005.01.056

Chapter 4

ELSEVIER

Available online at www.sciencedirect.com
SCIENCE DIRECT®

Carbon 44 (2006) 1958–1962

CARBON

www.elsevier.com/locate/carbon

Encapsulating $C_{59}N$ azafullerene derivatives inside single-wall carbon nanotubes

F. Simon [a,*], H. Kuzmany [a], J. Bernardi [b], F. Hauke [c], A. Hirsch [c]

[a] *Institut für Materialphysik, Universität Wien, Strudlhofgasse 4, A-1090 Wien, Austria*
[b] *University Service Centre for Transmission Electron Microscopy (USTEM), Technische Universität Wien, Wiedner Hauptstrasse 8-10/052, A-1040 Wien, Austria*
[c] *Institut für Organische Chemie der Friedrich Alexander Universität, Erlangen-Nürnberg, Henkestrasse 42, D-91054 Erlangen, Germany*

Received 11 October 2005; accepted 1 February 2006
Available online 20 March 2006

Abstract

Filling of single-wall carbon nanotubes with $C_{59}N$ azafullerene derivatives is reported from toluene solvent at ambient temperature. The filling is characterized by high-resolution transmission electron microscopy and Raman spectroscopy. The filling efficiency is the same as for C_{60} fullerenes and the tube-azafullerene interaction is similar to the tube-C_{60} interaction. Vacuum annealing of the encapsulated azafullerene results in the growth of inner tubes, however no spectroscopic signature of nitrogen built in the inner walls is detected.

Keywords: Carbon nanotubes; Fullerene; Electron microscopy; Raman spectroscopy

1. Introduction

The hollow space inside single-wall carbon nanotubes (SWCNTs) have attracted considerable attention recently. The field was opened by the discovery of C_{60} fullerenes encapsulated inside SWCNTs, the peapods [1]. Later it was found that chemical reactions can take place inside the tube such as charging induced polymerization [2] or fusion of the C_{60} spheres to inner tubes [3,4]. The resulting inner tubes in the double-wall carbon nanotubes (DWCNTs) were shown to be exceptionally defect free [5] which apostrophizes the inside the of the tube as “nano-clean-room chemical reactor”. We recently found that chemical reactions are not restricted to fullerenes but organic solvents such as benzene or toluene can also participate.[1] The breakthrough to further explore the in-the-tube chemistry was the discovery of encapsulating fullerenes or fullerene derivatives at ambient temperatures [6–10]. Conventional peapod synthesis involves heating the sample above 400–500 °C [11,12], which most fullerene derivatives do not tolerate. $C_{59}N$, the on-ball nitrogen doped modification of fullerenes, has a rich chemistry due to its enhanced reactivity as compared to pristine fullerenes and can be synthesized in macroscopic amounts chemically [13,14]. The electronic state of $C_{59}N$ and its derivatives is strongly modified compared to C_{60} [15]. Encapsulating azafullerene peapods would be advantageous as they are expected to go preferably inside the SWCNTs similarly to all-carbon fullerenes, however their sizeable dipole moment adds a further degree of freedom for their applications such as e.g. ambipolar transistor [16]. In addition, the presence of the nitrogen enables to explore the in-the-tube chemistry with heteroatoms.

Here, we present the encapsulation of azafullerene derivatives inside SWCNTs. We use a low temperature synthesis method at ambient conditions. The encapsulation is proven by high-resolution transmission microscopy and Raman

---

[*] Corresponding author.
E-mail addresses: ferenc.simon@univie.ac.at, simon@esr1.fkf.bme.hu (F. Simon).

[1] Simon F, Kuzmany H. Unpublished result.

0008-6223/$ - see front matter © 2006 Elsevier Ltd. All rights reserved.
doi:10.1016/j.carbon.2006.02.001

Chapter 5

PHYSICAL REVIEW B **71**, 165439 (2005)

Diameter selective reaction processes of single-wall carbon nanotubes

F. Simon, Á. Kukovecz,* C. Kramberger, R. Pfeiffer, F. Hasi, and H. Kuzmany
Institut für Materialphysik, Universität Wien, Strudlhofgasse 4, A-1090 Wien, Austria

H. Kataura
Department of Physics, Tokyo Metropolitan University, Tokyo, Japan

(Received 11 November 2004; published 29 April 2005)

A method is presented which allows the study of diameter selective reactions in single-wall carbon nanotubes with an unprecedented accuracy. It is based on the transformation of fullerene peapods into double-wall carbon nanotubes and the study of the resulting diameter distribution of the inner nanotubes with Raman spectroscopy. This yields a spectral resolution increase of about 40 for the modes of different tubes. The method is demonstrated for the diameter selective healing of nanotube defects and yield from C_{70} peapod samples. The growth of very small diameter inner tubes from C_{70} peapods is demonstrated, which challenges the models of inner nanotube formation. An anomalous absence of middiameter inner tubes is explained by the suppressed amount of C_{70} peapods in the transition region between standing and lying C_{70} configurations.

DOI: 10.1103/PhysRevB.71.165439 PACS number(s): 61.46.+w, 78.30.Na

I. INTRODUCTION

Nanostructures based on carbon nanotubes[1] have been in the forefront of nanomaterial research in the past decade. However, there still remains a number of open questions before one of the most promising candidates, namely single-wall carbon nanotubes (SWCNTs), will have wide-spread applications. The major obstacle is the large number of electronically different nanotubes produced with varying diameters and chiralities.[2] Directed growth or separation efforts are hindered by the lack of accurate chiral vector identification methods in bulk samples. In addition, little is known about chirality and diameter sensitive reactions. Band-gap fluorescence was successfully applied to assign chiral indices to semiconducting SWCNTs.[3] Similarly, assignment of small diameter nanotubes to chiral vectors was performed in double-wall carbon nanotubes (DWCNTs) using Raman spectroscopy.[4,5] DWCNTs are SWCNTs containing a coaxial, smaller diameter CNT. The material is produced from fullerenes encapsulated in SWCNT (peapods[6]) by a high-temperature treatment.[7] The growth process in such systems is of fundamental interest, since it proceeds without catalytic particle support.

The growth process of DWCNTs from fullerene peapods is not yet understood. Computer simulations have suggested that C_{60}@SWCNT based DWCNTs are formed by Stone-Wales transformations from C_{60} dimer precursors at high temperature by cycloaddition.[8,9] The free rotation of C_{60} molecules is a prerequisite for the dimer formation as it enables the molecules to have facing double bonds. The ellipsoidal shaped C_{70} were found to be present in both standing or lying configurations, i.e., with the longer C_{70} axis perpendicular or parallel to the tube axis.[10,11]

At first glance, the above-mentioned assignment by Raman spectroscopy of the inner tubes in DWCNTs is not applicable to study properties of the outer tubes. However, we show in this paper that the assignment of chiralities to the inner tubes of DWCNTs is a new and so far unique tool for a diameter selective or even chirality selective analysis of the outer tube reactions. This possibility originates from the correlation between inner and outer tube abundances and from the robustness of this correlation against the different types of SWCNTs used for the inner tube growth. Due to the larger spectral splitting and narrower linewidths of the inner tube radial breathing modes,[4] the inner tube diameter distribution can be characterized with a spectral resolution that is about 40 times larger as compared to the analysis of the outer tubes. Thus, the analysis of the inner tubes allows the characterization of diameter selective reactions in the starting material with an unprecedented accuracy. The method is demonstrated on the diameter selective healing of the SWCNT openings. A dramatic exception in the equivalency of the C_{60} and C_{70} grown tubes is also presented for the $d \approx 0.67$ nm inner nanotubes for which the corresponding outer tubes are on the border between lying and standing C_{70} configurations.

II. EXPERIMENTAL DETAILS

C_{60} and C_{70} based DWCNTs (60-DWCNT and 70-DWCNT, respectively) were prepared from two arc-discharge grown commercial SWCNTs (SWCNT-N1 and N2 from Nanocarblab, Russia) and two laser ablation grown tubes. From the latter, one was commercial (SWCNT-R from Tubes@Rice, Houston, TX) and the other was laboratory-prepared (SWCNT-L). The SWCNT-N1,N2 materials were purified to 50% by the manufacturer. SWCNT-R and SWCNT-L materials were purified following Ref. 12. Peapod samples were prepared by annealing SWCNT with C_{60} in a quartz tube following Ref. 12 and were transformed to DWCNT at high temperature following Ref. 7. The diameter distributions of the SWCNT materials were determined from Raman spectroscopy[13] giving $d_{N1} = 1.50$ nm, $\sigma_{N1} = 0.10$ nm, $d_{N2} = 1.45$ nm, $\sigma_{N2} = 0.10$ nm, $d_R = 1.35$ nm, $\sigma_R = 0.09$ nm, and $d_L = 1.39$ nm, $\sigma_L = 0.09$ nm for the mean diameters and the variances of the distributions, respectively. The results described here were observed for all samples. Multifre-

Journal of
Nanoscience and Nanotechnology
Vol. 5, 1785–1791, 2005

Reversible Hole Engineering for Single-Wall Carbon Nanotubes

F. Hasi, F. Simon,* and H. Kuzmany

Institut für Materialphysik, Universität Wien, A-1090 Wien, Strudlhofgasse 4, Austria

Experimental results are provided for reversible generation of holes on single-wall carbon nanotubes and their closing by temperature treatment. The generation of the holes was analyzed by checking the amount of C_{60} fullerenes that can be filled into the tubes and subsequently transformed to an inner-shell tube. The concentration of the latter was determined from the Raman response of the radial breathing mode. The tube opening process was performed by exposure of the tubes to air at elevated temperatures. This process was found to be independent from the tube diameters. In contrast, the tube closing process was found to depend strongly of the tube diameter. For large diameter tubes ($d = 1.8$ nm) the activation energy was 1.7 eV whereas for the small diameter tubes this energy was only 0.33 eV. Optimum conditions for tube closing were found to be one hour at 800 °C or 10 minutes at 1000 °C. From the almost identical Raman spectra for the tubes before and after engineering, a predominant generation of the holes at the tube ends is concluded.

Keywords: Single-Wall Carbon Nanotubes, Raman Spectroscopy, Filling of Nanotubes, Peapods, Purification, Controlled Oxidation, Diameter Control.

1. INTRODUCTION

The inside of carbon cages has been attracting the interest of chemists and physicists ever since the discovery of the fullerenes in 1985 by Kroto et al.[1] To develop an endohedral or concave chemistry was one of the dreams of the scientists in the early days of fullerene research. New materials and new chemical reactions, which do not exist outside the cages, were expected to be discovered. It was indeed demonstrated in a large number of experiments that atoms or even groups of atoms can be encaged into the fullerenes[2–4] and revealed so far unobserved systems. However, a reversible opening, filling and re-closing of the cages was not possible. Only very recently such a process was demonstrated to operate for the filling of a fullerene cage with hydrogen atoms.[5] In contrast to this, filling of carbon nanotubes had been demonstrated already in 1994[6] shortly after the discovery of the tubes.[7] At that time, filling of multi-wall carbon nanotubes was studied in some detail. Since the inner diameter of such tubes is rather large, of the order of 10 to 20 nm, fillers such as lead or iron was expected and was observed to behave almost like bulk material. The situation changed when Smith et al. discovered the filling of single wall carbon nanotubes (SWCNTs) with C_{60} fullerenes[8] by electron beam irradiation. The resulting structures were called peapods. Shortly later it was reported by several groups that different types of fullerenes, including higher fullerenes or endohedral fullerenes can be filled into the SWCNTs[9–11] if the tubes were treated in a special way in order to generate holes in the side walls or to open the caps of the tubes. The filling of the SWCNTs attracted considerable attention, since the inner diameter of the tubes is at least an order of magnitude smaller than the inner diameter of the multi-wall tubes and reaches values where quantum confinement becomes noticeable. Also, the highly shielded inside of the tubes were demonstrated to provide clean room conditions where highly defect free material can be grown.[12] Special recipes were reported for efficient filling but it turned out that any cleaning of the as grown tube material by chemical etching allows for filling with fullerenes or other inorganic or organic material. Attractive forces between the fullerenes and the inside of the cages were considered as the driving mechanism for the filling process. However, details of the

---

*Author to whom correspondence should be addressed.

Chapter 7

Available online at www.sciencedirect.com
SCIENCE DIRECT®
Chemical Physics Letters 425 (2006) 85–88
CHEMICAL PHYSICS LETTERS
www.elsevier.com/locate/cplett

Growth of single wall carbon nanotubes from ^{13}C isotope labelled organic solvents inside single wall carbon nanotube hosts

Ferenc Simon *, Hans Kuzmany

Institut für Materialphysik, Universität Wien, Strudlhofgasse 4, A-1090 Wien, Austria

Received 16 March 2006; in final form 22 April 2006
Available online 5 May 2006

Abstract

We present the growth of single wall carbon nanotubes (SWCNTs) from organic solvents such as benzene and toluene inside a host SWCNT. The solvents encapsulated in SWCNTs are transformed to an inner tube when subject to a heat treatment under dynamic vacuum at 1270 °C. We used isotope labeling of the different carbon sources to prove that the source of the inner tubes is indeed the solvent. Our results put constraints on the models explaining the inner tube growth and provides a simple alternative for the fullerene based inner tube growth. It also provides the possibility to study a completely new field of in-the-tube chemistry.

1. Introduction

Catalyst free growth of single wall carbon nanotubes (SWCNT) has been intensively attempted since their discovery in 1993 [1,2]. The efforts resulted in novel nanostructures such as, e.g. the nano-horns [3] but the metal catalyst-free synthesis remains elusive. Recently, catalyst free growth of SWCNTs was achieved from fullerenes encapsulated in SWCNTs, when these so-called peapods [4] are subject to a high temperature annealing at 1270 °C [5,6].

In this Letter, the synthesis of inner tubes is reported from ^{13}C isotope labeled organic solvents such as benzene and toluene encapsulated in SWCNTs. This is demonstrated to work when fullerenes are co-encapsulated preventing the solvents from evaporation. Isotope labeling proves unambiguously that the solvents contribute to the inner tubes and gives a measure on the yield. The current result opens new perspectives for the catalyst free synthesis of SWCNTs in other confined environments such as zeolite [7] and allows further exploration of the in-the-tube chemistry.

2. Experimental

2.1. Sample preparation

Commercial SWCNT material (50 weight % purity, Nanocarblab), fullerenes (C_{60} and C_{70}) of natural carbon (Hoechst AG), benzene and toluene (Sigma–Aldrich) and isotope labeled benzene and toluene (Euriso-Top SA) were used. In the following, we denote these two latter compounds as solvents even though their primarily role is being precursors of a chemical process. The purification of the SWCNTs by the supplier in the form of repeated air oxidation at 400 °C and acid washing results in purified and opened SWCNTs. The tube diameter distribution was determined from Raman spectroscopy [8] and we obtained $d = 1.40$ nm and $\sigma = 0.10$ nm for the mean diameter and the variance of the Gaussian distribution, respectively. Vapor filling with fullerenes was performed by subjecting the SWCNT flakes to fullerene vapor in a sealed quartz ampoule at 650 °C following Ref. [9]. Non-encapsulated

---

[*] Corresponding author. Present address: Department of Experimental Physics, Budapest University of Technology and Economics, Institute of Physics and Solids in Magnetic Fields Research Group of the Hungarian Academy of Sciences, H-1521, Budapest P.O. Box 91, Hungary. Fax: +36 1 463 3819.

E-mail address: ferenc.simon@univie.ac.at (F. Simon).

0009-2614/$ - see front matter © 2006 Elsevier B.V. All rights reserved.
doi:10.1016/j.cplett.2006.04.094

Chapter 8

ELSEVIER
Available online at www.sciencedirect.com
SCIENCE DIRECT®
Chemical Physics Letters 413 (2005) 506–511
CHEMICAL PHYSICS LETTERS
www.elsevier.com/locate/cplett

Highly perfect inner tubes in CVD grown double-wall carbon nanotubes

F. Simon [a,*], Á. Kukovecz [b], Z. Kónya [b], R. Pfeiffer [a], H. Kuzmany [a]

[a] *Institut für Materialphysik, Universität Wien, Strudlhofgasse 4, AT-1090 Wien, Austria*
[b] *Department of Applied and Environmental Chemistry, University of Szeged, Rerrich B. ter 1, H-6720 Szeged, Hungary*

Received 15 June 2005; in final form 1 August 2005
Available online 30 August 2005

Abstract

The synthesis of double-wall carbon nanotubes (DWCNTs) with highly unperturbed inner shells is reported using the catalytic vapor deposition method. Temperature dependent and high resolution Raman measurements show an enhanced phonon life-time of the inner tubes with respect to the outer ones and similar diameter SWCNTs. This proves that the inner tubes are unperturbed similar to the inner tubes in peapod-grown DWCNTs. The presence of the outer tube is argued to protect the inner tube from interaction with impurities and also to stabilize the growth of defect free inner tubes. The current material underlines the application potential of DWCNTs.

1. Introduction

Double-wall carbon nanotubes (DWCNTs) are on the borderline between single-wall (SWCNTs) and multi-wall carbon nanotubes (MWCNTs). As a result, they share common features with both classes of materials. Generally, SWCNTs are considered to be of fundamental interest and MWCNTs are known to be more application-friendly. SWCNTs exhibit a number of compelling physical properties such as superconductivity [1], the Tomonaga-Luttinger liquid state [2,3] and a predicted Peierls state [4,5]. DWCNTs are fundamentally interesting as their physical properties are determined by the well defined inner and outer tube chiralities [6,7] and are candidates for applications such as, e.g., reinforcing composites or scanning microscopy probeheads due to the improved elastic properties as compared to the SWCNTs but still of smaller diameter than MWCNTs. In addition, the small diameter inner tubes enable us to study the behavior of highly curved nanostructures such as curvature induced deviations from the electronic structure of graphite [8,9].

DWCNTs can be grown from fullerenes encapsulated inside SWCNTs, peapods [10] (PEA-DWCNTs) by a high temperature treatment [11,12] without any catalysts. Raman studies on the inner tubes in PEA-DWCNTs indicated at least an order of magnitude longer phonon life-times, i.e., narrower line-widths, as compared to the outer tubes [6]. This was associated with the highly unperturbed nature of the inner tubes that are grown in the nano clean-room interior of SWCNTs. The defect content of the tube shells is crucial for applications such as the possibility of ballistic transport and improved mechanical properties.

An alternative DWCNT synthesis is based on catalytic SWCNT growth methods such as arc-discharge [13] and catalytic chemical vapor deposition (CCVD) methods [14–20]. So far, Raman studies on such samples have given a similar linewidth for the inner and outer tubes indicating comparable number of defects for the two shells [14,17–19,21]. However, no low temperature

---

[*] Corresponding author. Fax: +43 1 4277 51375.
E-mail address: fsimon@ap.univie.ac.at (F. Simon).

0009-2614/$ - see front matter © 2005 Elsevier B.V. All rights reserved.
doi:10.1016/j.cplett.2005.08.036

Chapter 9

Eur. Phys. J. B **42**, 345–350 (2004)
DOI: 10.1140/epjb/e2004-00389-0

THE EUROPEAN
PHYSICAL JOURNAL B

Interaction between concentric tubes in DWCNTs

R. Pfeiffer[1,a], Ch. Kramberger[1,2], F. Simon[1], H. Kuzmany[1], V.N. Popov[3], and H. Kataura[4]

[1] Institut für Materialphysik, Universität Wien, Strudlhofgasse 4, 1090 Wien, Austria
[2] Leibniz Institute of Solid State and Materials Research Dresden, Helmholtzstrasse 20, 01069 Dresden, Germany
[3] Faculty of Physics, University of Sofia, Sofia, Bulgaria
[4] AIST, Central 4, Higashi 1-1-1, Tsukuba, 305-8562 Ibaraki, Japan

Received 14 June 2004 / Received in final form 15 September 2004

Abstract. A detailed investigation of the Raman response of the inner tube radial breathing modes (RBMs) in double-wall carbon nanotubes is reported. It revealed that the number of observed RBMs is two to three times larger than the number of possible tubes in the studied frequency range. This unexpected increase in Raman lines is attributed to a splitting of the inner tube response. It originates from the possibility that one type of inner tubes may form in different types of outer tubes. In this case, a splitting of lines results since the inner tube RBM frequency depends on the diameter of the outer tube. Finally, a comparison of the inner tube RBMs and the RBMs of tubes in bundles gave clear evidence for a stronger interaction between tubes in a bundle as compared to the interaction between inner and outer tubes.

PACS. 81.07.De Nanotubes – 81.05.Tp Fullerenes and related materials – 78.30.Na Fullerenes and related materials

1 Introduction

Single-wall carbon nanotubes (SWCNTs) [1, 2] have attracted a lot of scientific interest over the last decade due to their unique structural and electronic properties. In 1998, Smith et al. [3] discovered that fullerenes can be encapsulated in SWCNTs, forming so-called peapods [4–6]. By annealing the peapods at high temperatures in a dynamic vacuum the enclosed C_{60} peas transform into SWCNTs within the outer tubes, thus producing double-wall carbon nanotubes (DWCNTs) [7, 8]. The growth process of the inner tubes is a new route for the formation of SWCNTs under shielded conditions in the absence of any additional catalyst.

A detailed Raman study of the radial breathing modes (RBMs) of the inner tubes revealed intrinsic linewidths down to 0.4 cm^{-1} [9]. These small linewidths indicate long phonon lifetimes and therefore highly defect free inner tubes. Thus, they are a direct experimental evidence for a nano-cleanroom reactor on the inside of SWCNTs.

Peapod grown DWCNTs are also interesting from another point of view. Usually, they are produced from standard SWCNTs with diameters around 1.4 nm. Taking into account the van der Waals interaction between the walls this means that the diameters of the inner shell tubes are around 0.7 nm. For these tubes the possible diameters can no longer be assumed to form a quasi-continuum. Additionally, due to the inverse relation between RBM frequency and diameter, the spectral distance between the RBMs of different inner tube types is (with few exceptions) much larger than between different outer tube RBMs. This opens the possibility to study the properties of individual SWCNTs in a bulk sample. A first application of this was the assignment of the chiral vectors to all inner tubes [10].

Studying the Raman response of the inner tube RBMs in high resolution at 20 K revealed that the number of observed lines is about two to three times larger than the number of geometrically allowed inner tubes. In the following, we show that this unexpected increase of Raman lines can be attributed to a splitting of the response from the inner tubes. This splitting originates from the possibility for one inner tube type to form in several outer tube types (with different diameters) and the fact that the RBM frequency of the inner tube depends on the diameter of the encapsulating parent tube. A quantitative explanation for the splitting was obtained by calculating the RBM frequencies of the inner tubes as a function of the outer tube diameter within a continuum model. Using two different scenarios regarding the possible inner-outer shell pairs, we compared the splitting obtained from the simulation with the experimentally obtained splitting. From this we conclude that not only the best fitting inner tubes are formed.

2 Experimental

The starting material for the DWCNTs were C_{60} peapods (in the form of bucky paper), produced by a previously described method [5]. The mean diameter of the assumed Gaussian diameter distribution of the outer tubes was 1.39(2) nm with a variance of 0.1 nm, as determined from

---

[a] e-mail: `rpfei@ap.univie.ac.at`

Chapter 10

PHYSICAL REVIEW B **71**, 155409 (2005)

Resonance Raman scattering from phonon overtones in double-wall carbon nanotubes

R. Pfeiffer,[1] H. Kuzmany,[1] F. Simon,[1] S. N. Bokova,[2] and E. Obraztsova[2]
[1]*Universität Wien, Institut für Materialphysik, Strudlhofgasse 4, A-1090 Wien, Austria*
[2]*Natural Sciences Center of A. M. Prokhorov General Physics Institute of Russian Academy of Sciences, 38 Vavilov Street, 119991 Moscow, Russia*

(Received 13 September 2004; revised manuscript received 22 December 2004; published 15 April 2005)

The resonance behavior and the dispersion of the G′ line in double-wall carbon nanotubes were investigated by multifrequency Raman scattering. Using a large number of laser lines for excitation, the dispersion for the response from the inner tubes and from the outer tubes was found to be 85 and 99 cm^{-1}/eV, respectively. The reduction of the dispersion for the inner tubes is a consequence of their high curvature and suggests a flattening of the phonon dispersion at the K point in the Brillouin zone. The frequency position for the G′ line of the inner tubes for a given laser energy was likewise strongly reduced as compared to values expected from tubes with standard diameter. This was again assigned to the strong curvature of the small-diameter inner tubes. Finally, the G′ line scattering cross sections for the outer tubes and for the inner tubes revealed resonances according to the transitions between the corresponding Van Hove singularities. The response from the inner tubes was particularly strong, in good agreement with the expected resonance enhancement resulting from their high curvature.

DOI: 10.1103/PhysRevB.71.155409 PACS number(s): 78.67.Ch, 61.46.+w, 78.30.Na, 63.20.Dj

I. INTRODUCTION

Single-wall carbon nanotubes (SWCNTs) have been attracting considerable interest for a number of years as they are very good examples for one-dimensional systems on the one hand and exhibit a high application potential on the other hand.[1–3] Recently, particular attention has been dedicated to double-wall carbon nanotubes (DWCNTs). Such systems are of special interest if the inner shell tubes are grown from fullerenes encapsulated into the primary outer shell tubes (so-called peapods[4]).[5] On heating to temperatures as high as 1250 °C, the fullerenes in the peapods transform into inner shell tubes with a high degree of perfectness.[6]

Peapod grown DWCNTs are exceptional for several reasons. Normally, peapods are obtained from SWCNTs with mean tube diameters between 1.3 and 1.5 nm. Since the intertube distance in the DWCNTs is about 0.35 nm (the interlayer distance in graphite), the diameters of the inner shell tubes are around 0.7 nm, coming close to SWCNTs grown in zeolites.[7,8] The diameter distribution of the inner tubes is expected to follow roughly the distribution of the outer ones, except for a cutoff below 0.5 nm.[9] This cutoff is a consequence of the rather large size of the fullerenes which cannot enter tubes with diameters smaller than about 1.2 nm.

Referring to applications, DWCNTs share the advantages of multiwall tubes in a sense that they are rather stiff and properties from the two shells average out. Conversely, they still have some advantages of SWCNTs, e.g., small diameters and low weight. For fundamental research, the very small radii of the inner tubes are of particular interest. Additionally, the unit cells become small enough to allow for application of density-functional calculations. Such calculations are indeed necessary to describe the physical properties as a consequence of the high curvature of the narrow tubes.

One of the famous and important properties of the SWCNTs is their electronic structure. Due to the one-dimensional nature of the tubes, the electronic density of states is jammed into Van Hove singularities (VHSs). Within a simple tight-binding approximation, optical transitions are between VHSs symmetric to the Fermi level. The transition energies for semiconducting and metallic tubes are assigned as E_{ii}^{S} and E_{ii}^{M}, respectively. In a linear approximation, these energies scale with $1/D$, where D is the tube diameter.[10] In a refined description, the trigonal warping of constant energy contours and the influence of the chirality must be considered.[10] Symmetry-adapted nonorthogonal tight-binding calculations yield more precise results with lower transition energies and a stronger deviation from a $1/D$ law since tube curvature is included.[11] In addition, the exact values for the electronic energies are modulated by excitonic effects, particularly for the low i transitions[12] and by the effect of bundling or dressing with surfactants. Finally, and certainly of particular importance for very small inner shell tubes, the influence of the curvature must be considered explicitly. If the tube diameters become significantly lower than 1 nm, characteristic differences in the electronic structure as compared to tight-binding results were reported from *ab initio* calculations.[13]

A plot of the transition energies versus tube diameter for all geometrically allowed tubes, known as the Kataura plot,[14] is very helpful and important to understand optical and resonance Raman effects. The plot depicted in Fig. 1, with the inverse tube diameter used on the abscissa, is based on calculations by Popov.[11] The calculated energies from this work were subsequently scaled to match the experimental ones of Fantini *et al.*[15] and Weisman and Bachilo[16] (obtained from HiPco tubes dispersed in aqueous solution and wrapped in SDS). The scaling factors for each transition and SWCNT type (metallic as well as semiconducting type I and II) depended linearly on the inverse tube diameter. The horizontally hatched area marks the range of laser energies used in our experiments. The vertically hatched areas mark the diameter distribution of the outer (left) and inner tubes (right), respectively.

Chapter 11

RAPID COMMUNICATIONS

PHYSICAL REVIEW B **72**, 161404(R) (2005)

Fine structure of the radial breathing mode of double-wall carbon nanotubes

R. Pfeiffer,[1] F. Simon,[1] H. Kuzmany,[1] and V. N. Popov[2]
[1]*Institut für Materialphysik, Universität Wien, Strudlhofgasse 4, 1090 Wien, Austria*
[2]*Faculty of Physics, University of Sofia, Sofia, Bulgaria*

(Received 19 August 2005; published 24 October 2005)

The analysis of the Raman scattering cross section of the radial breathing modes of double-wall carbon nanotubes allowed us to determine the optical transitions of the inner tubes. The Raman lines are found to cluster into species with similar resonance behavior. The lowest components of the clusters correspond well to sodium sodecyl sulfate wrapped high pressure carbon monoxide grown tubes. Each cluster represents one particular inner tube inside different outer tubes and each member of the clusters represents one well-defined pair of inner and outer tubes. The number of components in one cluster increases with the decreasing inner tube diameter and can be as high as 14 spread over 30 cm^{-1}. This suggests a lot of variation in the diameter difference of inner-outer tube pairs.

DOI: 10.1103/PhysRevB.72.161404 PACS number(s): 78.67.Ch, 63.20.Dj, 78.30.Na, 78.66.Tr

Double-wall carbon nanotubes (DWCNTs) are interesting structures in the family of carbon nanophases, especially when they are grown by the annealing of so-called peapods, i.e., single-wall carbon nanotubes (SWCNTs) filled with fullerenes.[1] The outer tubes diameter of such DWCNTs are of the same small size (around 1.4 nm) as it is typical for SWCNTs. This means, they provide the same spatial resolution for sensors or the same field enhancement for electron emitters as the latter but exhibit a higher stiffness. The inner tubes, with typical diameters of 0.7 nm, have a rather high curvature and are thus expected to exhibit significant deviations from graphene with respect to their mechanical and electronic properties. Amongst others, the electron-phonon coupling is expected to considerably increase as compared to graphene, which might result in superconductivity or a Peierls transition. Also, the concentric layers in the DWCNTs represent curved graphite sheets with an interesting van der Waals–type interaction and DWCNTs are well-defined model materials for multiwall CNTs. Finally, by filling SWCNTs with isotope labeled fullerenes it is possible to produce DWCNTs with ^{13}C enriched inner and normal ^{12}C outer tubes.[2]

The peapod-grown DWCNTs attracted additional interest as the inner tubes are grown in an highly unperturbed environment and thus exhibit unusual narrow lines for the radial breathing mode (RBM) Raman response.[3] In this sense, the inside of the outer tubes has been termed a "nano-clean-room." Moreover, the Raman signal from the RBMs of the inner tubes exhibits strong resonance enhancement and the observed number of lines is larger than the number of geometrically allowed species.[4]

Similar to the outer tubes, the geometric and electronic properties of the inner tubes are uniquely determined by their chiral vectors (m,n), along which the graphene layers are rolled up into tubes.[5] Due to the quasi-one-dimensionality of the tubes, the electronic states are jammed into Van Hove singularities (VHSs). Recent experiments suggest that the optical transitions of semiconducting (E_{ii}^{S}) and metallic (E_{ii}^{M}) tubes arise from excitonic states close to the VHSs instead from the VHSs as such.[6] These transition energies scatter around lines with slopes proportional to the inverse tube diameter $1/D$. Refined calculations revealed considerable curvature corrections to the transition energies, especially for small diameter tubes.[7–9] Experimental information on these effects has recently been obtained from the Raman and luminescence measurements of HiPco (high pressure carbon monoxide grown) tubes with a mean diameter of about 1 nm.[10–12] The pattern of the deviation from the linear relation between E_{ii} and $1/D$ can be categorized into tube families with respect to $2m+n=\mathrm{const}$. There are the metallic tubes with $2m+n\equiv 0$ (mod 3) and two types of semiconducting tubes with $2m+n\equiv 1$ (mod 3) (SI) and $2m+n\equiv 2$ (mod 3) (SII). For the E_{22}^{S} transition, the SI tubes deviate strongly from the linear relation towards lower transition energies whereas the SII tubes exhibit a smaller deviation towards higher transition energies. In all cases zigzaglike tubes close to $(m,0)$ show the largest deviation from the linear relationship.

The RBM frequencies also scale roughly as $1/D$ and have therefore been used repeatedly for the structural analysis of SWCNTs, particularly with respect to the diameter distribution. By analyzing the Raman cross section of the RBMs it is possible to determine chiralities and electronic transition energies of CNTs.[11,12]

Here, we present the results of resonance Raman measurements in the RBM range of DWCNTs. These measurements unraveled the optical transitions of the inner tubes which cannot be accessed by optical and scanning probe experiments. Using a contour plot where the Raman cross section is plotted over a two-dimensional grid of RBM frequency and laser excitation energy, we found a well-expressed fine structure in the resonance pattern. An analysis of this pattern showed a clustering of the inner tubes RBMs near the HiPco transition energies and frequencies. The clusters start around the HiPco frequencies and extend up to 30 cm^{-1} to higher frequencies. They consist of up to 14 well-expressed components. Each cluster represents one particular inner tube inside different outer tubes and each member of the clusters represents a well-defined pair of one inner tube in one outer tube. Within one cluster, the transition energies

1098-0121/2005/72(16)/161404(4)/$23.00

Chapter 12

PRL **95,** 017401 (2005) PHYSICAL REVIEW LETTERS week ending 1 JULY 2005

Isotope Engineering of Carbon Nanotube Systems

F. Simon, Ch. Kramberger,* R. Pfeiffer, and H. Kuzmany
Institut für Materialphysik, Universität Wien, Strudlhofgasse 4, A-1090 Wien, Austria

V. Zólyomi and J. Kürti
Department of Biological Physics, Eötvös University Budapest, Pázmány Péter sétány 1/A, H-1117 Budapest, Hungary

P. M. Singer and H. Alloul
Laboratoire de Physique des Solides, UMR 8502, Université Paris-Sud, 91405 Orsay, France

(Received 15 June 2004; published 27 June 2005)

The synthesis of a unique isotope engineered system, double-wall carbon nanotubes with natural carbon outer and highly ^{13}C enriched inner walls, is reported from isotope enriched fullerenes encapsulated in single-wall carbon nanotubes (SWCNTs). The material allows the observation of the *D* line of the highly defect-free inner tubes that can be related to a curvature induced enhancement of the electron-phonon coupling. *Ab initio* calculations explain the inhomogeneous broadening of inner tube Raman modes due to the distribution of different isotopes. Nuclear magnetic resonance shows a significant contrast of the isotope enriched inner SWCNTs compared to other carbon phases and provides a macroscopic measure of the inner tube mass content. The high curvature of the small diameter inner tubes manifests in an increased distribution of the chemical shift tensor components.

DOI: 10.1103/PhysRevLett.95.017401 PACS numbers: 78.30.Na, 61.46.+w, 76.60.−k

Isotope engineering (IE) of materials provides an important degree of freedom for both fundamental studies and applications. The change in phonon energies upon isotope substitution, while leaving the electronic properties unaffected, has been used to identify vibrational modes [1–3] and gave insight into underlying fundamental mechanisms, such as phonon-mediated superconductivity [4]. Applications of IE involve, for instance, the controlled doping of isotope engineered Si heterostructures by means of neutron irradiation [5], fabrication of mononuclear devices with controlled heat conducting properties [6], and the basic architecture for spintronics and quantum computing [7]. Recently, single-wall carbon nanotubes (SWCNTs) have been intensively studied as a result of their anticipated applicability and the unique physical properties related to their quasi-one-dimensional electronic structure. Examples include the presence of Van Hove singularities in the density of states [8] and the Luttinger liquid behavior [9]. IE of carbon nanotubes using isotope enriched graphite as the starting material was attempted in order to allow NMR spectroscopy [10,11]. However, the NMR studies have been hampered by the fact that the ^{13}C NMR active nuclei can be found in all species of carbons, e.g., amorphous or graphitic carbon, inevitably present even in the purified SWCNT materials, and no nanotube selective enrichment or purification could be achieved until now. Vibrational spectroscopy is suitable to study the effect of IE. For SWCNTs, Raman spectroscopy has proven to be convenient to characterize their electronic and structural properties. In addition, Raman studies on double-wall carbon nanotubes (DWCNTs) [12,13], synthesized from fullerenes encapsulated inside the tubes (fullerene peapods) [14], provide a unique opportunity to study the small diameter inner tubes.

In this Letter, we report the preparation and study of a unique hybrid carbon nanotube material. It consists of DWCNTs where the inner tube contains ^{13}C with a controlled level of enrichment, whereas the outer tube remains natural carbon. This material is obtained by filling a host SWCNT with isotopes labeled C_{60} or C_{70} fullerenes and transforming the resulting peapods to an inner tube by high temperature annealing. Raman scattering reveals an unexpected strong response from the *D* line of the inner tubes, even though the latter are highly defect free [13]. Even at the high temperature of the peapod transformation, no exchange of carbon between the inner and outer shell is observed. The random distribution of ^{13}C atoms in the wall of the inner tube leads to a line broadening which is quantitatively explained. In contrast with nonisotope enriched tubes, the present material is an excellent object for NMR spectroscopy. This allows the measurement of the mass fraction of a material encapsulated in carbon nanotubes for the first time. The effect of high curvature is demonstrated for the small diameter inner tubes from unusual NMR line shapes.

Commercial SWCNTs (50 weight % purity, Nanocarblab, Moscow, Russia), ^{13}C isotope enriched fullerenes (MER Corp., Tucson, USA), and C_{60} of natural carbon (Hoechst AG, Frankfurt, Germany) were used to prepare fullerene peapods C_{60}, C_{70}@SWCNT. The Gaussian tube diameter distribution was determined from Raman spectroscopy [15] and revealed $d = 1.40$ nm and $\sigma = 0.10$ nm for the mean diameter and the variance, respectively. We used two grades of ^{13}C enriched fullerene mixtures: 25% and 89%, whose values are slightly refined

Chapter 13

PRL **95,** 236403 (2005) PHYSICAL REVIEW LETTERS week ending 2 DECEMBER 2005

NMR Evidence for Gapped Spin Excitations in Metallic Carbon Nanotubes

P. M. Singer,[1] P. Wzietek,[1] H. Alloul,[1] F. Simon,[2] and H. Kuzmany[2]
[1]*Laboratoire de Physique des Solides, UMR 8502, Université Paris-Sud, 91405 Orsay, France*
[2]*Institut für Materialphysik, Universität Wien, Strudlhofgasse 4, A-1090 Wien, Austria*

(Received 11 August 2005; published 29 November 2005)

We report on the spin dynamics of ^{13}C isotope enriched inner walls in double-wall carbon nanotubes using ^{13}C nuclear magnetic resonance. Contrary to expectations, we find that our data set implies that the spin-lattice relaxation time (T_1) has the same temperature (T) and magnetic field (H) dependence for most of the inner-wall nanotubes detected by NMR. In the high-temperature regime ($T \gtrsim 150$ K), we find that the T and H dependence of $1/T_1T$ is consistent with a 1D metallic chain. For $T \lesssim 150$ K we find a significant increase in $1/T_1T$ with decreasing T, followed by a sharp drop below $\simeq 20$ K. The data clearly indicate the formation of a gap in the spin excitation spectrum, where the gap value $2\Delta \simeq 40$ K ($\equiv$3.7 meV) is H independent.

DOI: 10.1103/PhysRevLett.95.236403 PACS numbers: 71.20.Tx, 61.46.+w, 73.22.−f, 76.60.−k

The electronic properties of carbon nanotubes have been of a topic of intense investigation ever since their discovery in the early 1990s. According to band-structure calculations, the basic electronic structure of single-wall carbon nanotubes (SWCNT) is expected to depend on the chiral wrapping vector (n, m) across the graphene plane, where tubes for which $(2n + m)/3 =$ integer are metallic, while all other tubes are semiconducting [1–4] with a large ~1 eV gap [5]. While STM and transport measurements on *isolated* tubes demonstrate the diversity of tube properties, significant measurements on *macroscopic* amounts of tubes are only possible in selected cases. Photoemission spectroscopy (PES) measurements on metallic tubes in bundles [6,7] suggest that strong electron-electron correlations can lead to a Tomonaga-Luttinger-liquid (TLL) state. Recently, double-wall carbon nanotubes (DWCNT) have been synthesized by filling SWCNT with fullerenes (so-called "peapods" [8]) followed by a high-temperature reaction which merges the fullerenes into inner tubes [9,10]. These DWCNT have some exceptional properties since the inner tubes are accommodated in a highly shielded environment under clean room conditions [11]. Raman experiments performed even on bucky paper material allows one to detect some significant properties of these inner tubes due to their small diameter (high curvature).

Nuclear magnetic resonance (NMR) is usually an excellent technique for probing the electronic properties at the Fermi level of metallic systems; take for instance conducting polymers, fullerenes, and high-temperature superconductors to mention a few. However the 1.1% natural abundance of ^{13}C with nuclear spin $I = 1/2$ limits the sensitivity of such experiments. Data taken on SWCNT essentially evidence a large distribution of properties since samples of identical tubes are presently out of reach. In this Letter, selective enrichment of the inner shells using ^{13}C isotope enriched fullerenes [12,13] in the peapod synthesis route is used to probe the specific properties of the inner tubes. The ^{13}C enrichment allows us to increase the ^{13}C NMR sensitivity by 2 orders of magnitude, and furthermore achieve *selective* ^{13}C enrichment of the inner shells alone. This provides us with the possibility of singling out the electronic properties of these inner tubes for the first time. We show that, although these tubes are distributed in diameter and chirality, their electronic properties display a strikingly homogeneous behavior. The magnetic properties of these inner-wall nanotubes behave as for a 1D metal at room T, but exhibit a pronounced gap below $\simeq 20$ K. This unexpected result reveals that this specific macroscopic collection of carbon nanotubes is an object displaying original physical properties worth studying in more detail with macroscopic experimental techniques.

All ^{13}C NMR data in this Letter were taken with the sample sealed in a 6 mm diameter glass tube filled with 200 mbar of high purity helium gas. Details of the synthesis techniques and various independent experimental evidences for the formation of 89% ^{13}C isotope enriched inner walls inside natural 1.1% ^{13}C enriched outer walls are reported elsewhere [12]. We probed the low frequency spin dynamics (or low energy spin excitations, equivalently) of the inner tubes using the spin-lattice relaxation time, T_1, defined as the characteristic time it takes the ^{13}C nuclear magnetization to recover after saturation. The signal intensity after saturation $S(t)$ was deduced by integrating the fast Fourier transform of half the spin echo for different delay times t. All data were taken with excitation pulse lengths $\pi/2 = 3.0\ \mu$s and short pulse separation times of $\tau = 15\ \mu$s [14]. We obtained the value of T_1 by fitting the t dependence of $S(t)$ to the form $S(t) = S_a - S_b M(t)$, where $S_a \simeq S_b$ (>0) are arbitrary signal amplitudes, and

$$M(t) = \exp[-(t/T_1^e)^\beta] \qquad (1)$$

is the reduced magnetization recovery of the ^{13}C nuclear spins. Figure 1 shows the results of $M(t)$ for the inner tubes as a function of the scaled delay time t/T_1^e, under various

Chapter 14

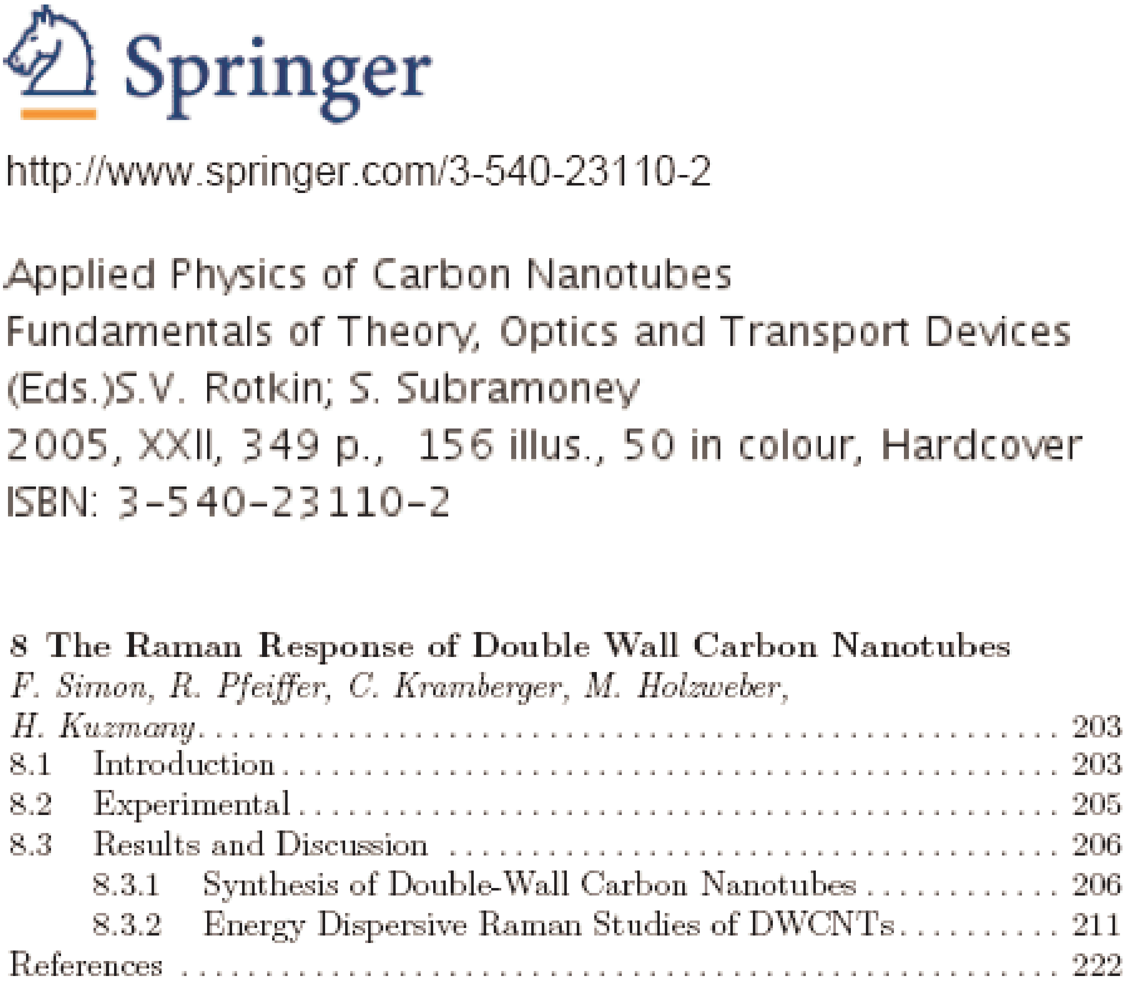

Springer
http://www.springer.com/3-540-23110-2

Applied Physics of Carbon Nanotubes
Fundamentals of Theory, Optics and Transport Devices
(Eds.)S.V. Rotkin; S. Subramoney
2005, XXII, 349 p., 156 illus., 50 in colour, Hardcover
ISBN: 3-540-23110-2

Chapter 15

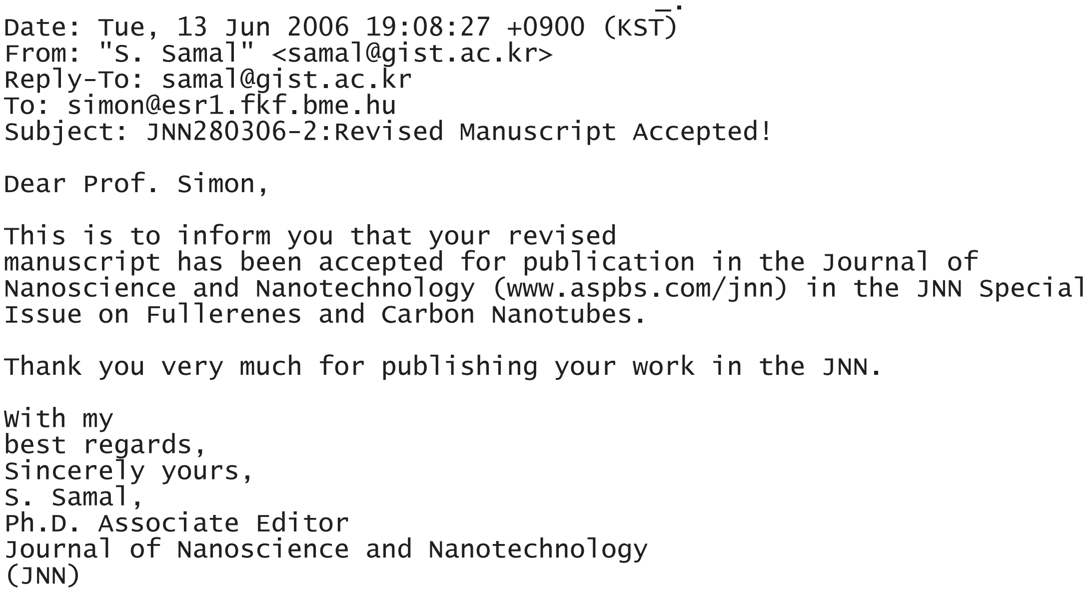

Date: Tue, 13 Jun 2006 19:08:27 +0900 (KST)
From: "S. Samal" <samal@gist.ac.kr>
Reply-To: samal@gist.ac.kr
To: simon@esr1.fkf.bme.hu
Subject: JNN280306-2:Revised Manuscript Accepted!

Dear Prof. Simon,

This is to inform you that your revised
manuscript has been accepted for publication in the Journal of
Nanoscience and Nanotechnology (www.aspbs.com/jnn) in the JNN Special
Issue on Fullerenes and Carbon Nanotubes.

Thank you very much for publishing your work in the JNN.

With my
best regards,
Sincerely yours,
S. Samal,
Ph.D. Associate Editor
Journal of Nanoscience and Nanotechnology
(JNN)